Gas-Phase Conversions of Glycerol to Methanol Over Ceria-Based Catalysts

Thesis submitted in accordance with the requirement of Cardiff University for the degree of Doctor of Philosophy

Louise R. Smith

School of Chemistry

Cardiff University

2020

Summary of Thesis

The conversion of aqueous glycerol feedstocks to methanol has been investigated in the gas phase using metal oxide catalysts, at atmospheric pressures and in the absence of an external reductant. Whilst preliminary investigations included catalyst free conditions and the use of MgO, most studies were performed with CeO_2. A complex product distribution was obtained over all catalysts, with hydroxyacetone identified as the major intermediate in the conversion of glycerol to methanol. Investigations into the carbon balance showed the presence of high molecular weight products, likely formed through condensation reactions, highlighting the difficulty in selectively converting concentrated glycerol feedstocks. The use of ceria nanostructures with different exposed surface planes showed a strong dependency between product distribution and ceria surface, with the (111) surface found to be beneficial for methanol productivity. A significant increase in previously reported methanol STYs, with a 50 wt.% glycerol feedstock, was obtained over a polyhedral ceria nanostructured catalyst, with a value of 201 $g_{MeOH}\ h^{-1}\ kg^{-1}_{cat}$, corresponding to 24.5 % methanol selectivity. Additionally, mechanistic differences across the catalysts showed a strong correlation existed between high hydroxyacetone STYs at low conversion and high methanol STYs at high conversion. The addition of copper and cobalt dopants did not improve the selectivity towards methanol at high conversion, despite the increase in hydroxyacetone at low conversion, particularly over $CuCeO_x$. This was likely due to the conversion of methanol leading to an increased selectivity to CO and H_2. Whilst the addition of dopants were not beneficial to methanol production, they were beneficial for the conversion of glycerol to acetaldehyde and H_2, which could provide an alternative route for glycerol valorisation.

Acknowledgments

First and foremost, I would like to extend my sincerest gratitude to Prof. Graham Hutchings and Prof. Stuart Taylor for not only giving me the opportunity to undertake a PhD within the CCI, but for all the supervision, guidance, and additional opportunities along the way. I have greatly enjoyed both my research, and my time in the group and will be forever grateful for the experience.

A massive thank you must also go to Dr Nicholas Dummer and Dr Mark Douthwaite. Nick, you have been there from the start of my PhD to the end and I am so grateful for all the supervision and advice you have given me over the past four years. I have no doubt that this thesis would not be what it is today without your input. Mark, thank you so much for everything you have done since joining the project. I am so grateful for all the support you have given me over the past few years! To Dr Dave Willock, thank you for all your insights during the green methanol meetings, and your patience when answering my sometimes very silly questions about computational chemistry! A special thanks also goes to Dr Paul Smith, thank you for all the comprehensive training you provided me with. I would also like to thank Prof. Donald Bethell, Prof. David Knight and Prof. Mark Howard for their insights into the complex chemistry which is reported throughout this thesis. Many stimulating discussions have taken place over the past few years and your knowledge and experience has been invaluable throughout the course of the project. I am incredibly appreciative for the time you have all taken to help further the project, thank you.

I am grateful to numerous members of the Chemistry Department for their help and expertise throughout the course of this work. I must extend a huge thanks to the team in workshop, particularly Steve Morris and Lee Wescombe, for all the help with any reactor issues. Thank you to Dr Tom Davies for the help and expertise with TEM, and to Tom Williams for assistance with LC-MS. A special thanks also goes to Dr Greg Shaw, thank you for all of your help, and for your calming ways in a crisis!

I would also like to extend a massive thank you to Anthony, thank you for always loving and supporting me. It hasn't always been an easy journey, but you've always been by my side every step of the way. A special thanks should also go to Rose, thanks for always bringing a smile to my face! Finally, I must thank my parents, to whom I owe everything. Dad, I really wish you were here to read this thesis, but I know how proud you would be. Thank you for always supporting and encouraging me to be my best. Mum, thank you for everything, I could not have done this without you. Your love, support, and guidance have got me through the most difficult of times and I will always be grateful for everything you have done for me.

Abbreviations and units

1,2-PD – 1,2-propanediol

1,3-PD – 1,3-propanediol

2,3-BD – 2,3-butanedione

% - Percent

°C – Degrees Celsius

Å – Angstrom (10^{-10} meters)

AA – Allyl alcohol

ACA - Acetaldehyde

ACE – Acetone

ACR - Acrolein

a.u. – Arbitrary units

BET – Brunauer, Emmet and Teller

CeO_2 – Cerium oxide (ceria)

CHN – Carbon, hydrogen and nitrogen

COx – Carbon oxides (CO/CO2)

DFT – Density functional theory

DRIFTS – Diffuse reflectance infrared fourier transform spectroscopy

DTA – Differential thermal analysis

EG – Ethylene glycol

EtOH – EthanolFID – Flame ionisation detector

FT-IR – Fourier transform infrared spectroscopy

FWHM – Full-width half-maximum

g – Gram

GC – Gas chromatography

GHSV – Gas hourly space velocity

GLY - Glycerol

h – Hours

HA – Hydroxyacetone

IR – Infrared

K – Kelvin

kg – Kilogram (10^3 g)

M – Molar (mol dm^{-3})

MeOH - Methanol

MFC – Mass Flow Controllers

mg – Milligram (10^{-3} g)

MgO – Magnesium oxide

min – Minutes

mL – Millilitre (10^{-3} L)

µm – Micrometre (10^{-6} m)

mol – Moles

MS – Mass spectrometry

nm – Nanometre (10^{-9} m)

PXRD – Powder X-ray diffraction

SEM – Scanning electron microscopy

SiC – Silicon carbide

STEM – Scanning transmission electron microscopy

STY – Space time yield

SV – Space velocity

TCD – Thermal conductivity detector

TGA – Thermogravimetric analysis

TEM – Transmission electron microscopy

TPD – Temperature programmed desorption

TPO – Temperature programmed oxidation

TPR – Temperature programmed reduction

wt. - % Weight percent

XPS – X-ray photoelectron spectroscopy

XRD – X-ray diffraction

Publication list

The following publications were produced throughout the duration of this thesis:

- **Smith, L. R.**; Smith, P. J.; Mugford, K. S.; Douthwaite, M.; Dummer, N. F.; Willock, D. J.; Howard, M.; Knight, D. W.; Taylor, S. H.; Hutchings, G. J., Catalysis Science & Technology 2019, 9 (6), 1464-1475.

- Smith, P. J.; **Smith, L.**; Dummer, N. F.; Douthwaite, M.; Willock, D. J.; Howard, M.; Knight, D. W.; Taylor, S. H.; Hutchings, G. J., Energies 2019, 12 (7), 1359.

- Sainna, M. A.; Nanavati, S.; Black, C.; **Smith, L. R.**; Mugford, K.; Jenkins, H. J.; Douthwaite, M.; Dummer, N. F.; Catlow, R. C. A.; Hutchings, G.; Taylor, S. H.; Logsdail, A. J.; Willock, D. J., Faraday Discussions 2020.

- Devlia, J.; **Smith, L.**; Douthwaite, M.; Taylor, S. H.; Willock, D. J.; Hutchings, G. J.; Dummer, N. F., Philosophical Transactions of the Royal Society A: Mathematical, Physical and Engineering Sciences 2020, 378 (2176), 20200059.

- **Smith, L. R.;** Sainna, M. A.; Douthwaite, M.; Davies, T. E.; Dummer, N. F.; Willock, D. J.; Knight, D. W.; Catlow, C. R. A.; Taylor, S. H.; Hutchings, G. J., ACS Catalysis 2021, 11 (8), 4893-4907.

Contents

Chapter 1

Introduction

1.1 Context and motivation

Increasing environmental, political and economic concerns surrounding society's heavy dependency on fossil-based sources, both for fuels and as building blocks for commodity chemicals, has been a major driving force for research into alternative, sustainable feedstocks. Biomass was the earliest and dominant power source until the 20th century, and biobased materials, including dyes, synthetic fibres, and solvents, were of great industrial importance; although throughout the 20th century, fossil-based resources largely displaced biobased sources in both the production of fuels and chemical building blocks.[1] However, rising global energy consumption, resulting in increasing demands on finite crude oil derived products, has had dramatic effects on the price of crude oil.[2-4] Additionally, the serious concerns surrounding the environmental consequences of our heavy dependence on fossil fuels and the resulting rising greenhouse gas emissions has prompted widespread interest in renewable fuel sources. Renewable sources have been widely implemented within the power sector, with hydropower, wind, bioenergy and solar photovoltaics providing approximately 23.5 % of all electricity generated worldwide in 2015.[5] Despite this, the transportation sector still has a heavy dependence on petroleum-based liquid fuels.

The transportation sector has high energy demands, accounting for 29 % of all energy consumption in 2015, secondary only to the heating and cooling industry in terms of end-use sector energy usage, with 96 % of the transport sector's energy use derived from petroleum products, accounting for 64.7 % of the world's total oil consumption.[5] In 2015, only 3.1 % of the transport sector's energy demand was fulfilled by renewable energy and comprised of 1.6 % bioethanol, 0.8 % biodiesel, 0.4 % other liquid biofuels, 0.3 % renewable electricity and >0.1 % biomethane. Whilst renewable electricity and hydrogen fuel cells are attractive prospects for the transportation sector, technological barriers have prevented their widespread implementation thus far. Alternatively, liquid biofuels, such as biodiesel and bioethanol, can provide renewable transportation fuels that are compatible with current technologies, and do not require significant changes to transport infrastructure or internal combustion engines.[6]

As a renewable carbon source, biomass provides the only sustainable alternative to fossil-based sources for the production of platform chemicals and liquid transportation fuels. Consequently, the biorefinery concept has been extensively examined over recent years.[7-10]

The concept of a biorefinery is analogous to a traditional crude oil refinery and has been described by the US National Renewable Energy Laboratory (NERL) as a facility that integrates biomass conversion processes, resulting in the production of chemicals, fuels and power from biomass.[11, 12] Typically, a range of technologies are required to separate biomass (in the form of wood, plant matter, agricultural waste etc.) into its chemical components, generally: Lignocellulose, triglycerides, and mixed organic residues.[9] The latter generally arises from municipal solid waste such as manure and waste from fruit and vegetable industries, often with highly contaminated feedstocks, thus, mixed organic residues are often more suitable for biogas production through anaerobic digestion processes than as feeds to produce chemicals or higher biofuels. Triglycerides, derived from plant and animal-based fats and oils, are widely used in the production of biodiesel; this will be discussed in detail later in this Chapter. Lignocellulosic biomass, often referred to as lignocellulose, is the major component of biomass, and is composed of cellulose (40 – 50 %), hemicellulose (25 – 35 %) and lignin (15 – 20 %). Lignocellulose can therefore be considered the most abundant organic carbon source on Earth, which provides enormous opportunities for valorisation and has led to extensive research in this area. [13-17] It should, however, be noted, that the complex nature of the feedstock has provided additional challenges and barriers which must be overcome, before wider implementation of lignocellulosic-based processes are achieved.

Since the introduction of the internal combustion engine alcohols have been used as fuels, although their application was largely displaced by petroleum derivatives throughout the 1900s.[18] Whilst bioethanol, generally produced through sugar fermentation, is the most widely used biofuel, the use of other low molecular weight alcohols, either as fuel additives or direct fuels, has gained significant popularity over recent years. This is due to the potentially lower emissions upon their combustion, the cost of the fuels and overall enhancement in energy efficiency.[19] In addition to its use as a fuel and fuel additive, methanol (MeOH) is a versatile C_1 chemical of huge industrial importance, used in the production of formaldehyde, acetic acid, methyl methacrylate and methyl tert-butyl ether, amongst other chemicals.[20] MeOH is produced on an industrial scale through a syngas route ($CO + 2H_2 \rightleftarrows CH_3OH$), generally over copper-zinc oxide catalysts, with carbon dioxide hydrogenation ($CO_2 + 3H_2 \rightleftarrows CH_3OH + H_2O$) and water-gas shift ($CO + H_2O \rightleftarrows CO_2 + H_2$) reactions occurring simultaneously.[21] Syngas can be produced through fossil-based resources, for example, through coal gasification or steam reforming of natural gas or alternatively, syngas can be obtained through biomass *via* gasification. The direct hydrogenation of carbon dioxide for MeOH production is highly desirable, not only as it involves removing a potent greenhouse gas from the environment, but also, provides a renewable fuel.[22] That said, the requirement for high purity H_2 for the direct conversion of

CO_2 to MeOH can be difficult to acquire from biobased-sources,[23, 24] thus novel, sustainable routes for the production of MeOH without the need for an external H_2 source are highly desirable.

In 2004, the US Department of Energy identified a number of target chemicals that could be produced through the biorefining processes.[25] One of these target chemicals was glycerol (GLY), a C_3 triol and the simplest sugar alcohol. GLY was identified for such an application due to the extensive literature investigating its valorisation, multiple product applicability, potential for direct substitution, high potential as a platform chemical, possibility of industrial scale-up and wide availability.[26] GLY availability has dramatically increased over the past two decades due to the significant increase in biodiesel production, a process by which GLY is the major by-product formed. Consequently, significant research efforts have been undertaken to develop routes for the effective conversion of GLY to other important commodity chemicals.

A recent discovery by the Hutchings group showed that aqueous GLY could be converted to MeOH over basic or reducible oxides, such as magnesium oxide (MgO) or ceria (CeO_2) in a simple vapour phase process, without the requirement for an external reductant.[27] This is a highly desirable reaction, with the potential to convert a waste product from commercial biodiesel synthesis into a major commodity chemical. There is also scope for the MeOH produced to be recycled into the biodiesel synthesis process, as MeOH is a key reagent., which is also used in the production of biodiesel. This thesis aims to further explore this process, building on the foundation provided by Hutchings and co-workers.[27] The work herein is focussed on providing greater insights into the conversion of GLY to MeOH, with a focus on CeO_2 based catalysts. Throughout the following chapter, the importance of this conversion will be established through first discussing the production of GLY in commercial biodiesel synthesis and the subsequent effect on the GLY economy. Current research efforts regarding GLY valorisation will then be reviewed, focussing on dehydration and hydrogenolysis, due to their relevance in this process. An overview of catalysis by ceria will be provided, highlighting the versatile nature of the material as a catalyst. Finally, the aims of the thesis will be fully established.

1.2 Biodiesel production and the glycerol economy

With the exception of bioethanol, biodiesel is the most widely used renewable liquid fuel, with an annual production expected to exceed 40 million litres in 2020.[28] Biodiesel is produced *via* a transesterification reaction between triglycerides and an alcohol, typically MeOH, giving fatty acid methyl esters (biodiesel or FAMEs) in an approximate yield of 90 wt. %, with crude GLY produced as a by-product, accounting for 10 wt. % of the total product

yield. Throughout the following section, an overview of biodiesel production will be given, with a focus on the nature of GLY produced through this route.

1.2.1 Transesterification for biodiesel production

As described above, the production of biodiesel involves the transesterification of triglycerides with an alcohol in the presence of a catalyst to produce fatty acid alkyl esters. Alcohols used in biodiesel production typically include MeOH, EtOH, PrOH and BuOH. MeOH and EtOH are most commonly used, with MeOH the preferred alcohol due to its low cost and advantageous chemical properties, such as high polarity and fast rate of reaction with triglycerides.[29] Triglycerides can be categorized as glycerol esters, comprised of a GLY backbone esterified with three fatty acid moieties. Throughout the transesterification process, the GLY backbone of a triglyceride is displaced by three equivalents of MeOH, generating three molecules of fatty acid methyl esters and one molecule of GLY formed as a by-product. As the transesterification reaction is reversible, an excess of MeOH is typically used to shift the equilibrium to favour the products.[30] The process generally utilises a catalyst to improve product yields and reaction rates;[29] an overview of the catalysts used for biodiesel production is summarised in Table 1.

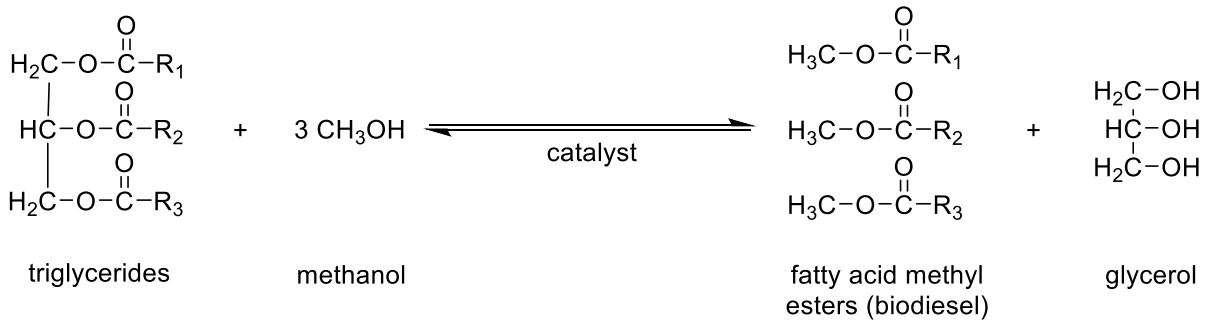

Figure 1. Transesterification reaction between triglycerides and MeOH to produce biodiesel and glycerol

The most widely used catalysts for transesterification are homogeneous alkaline catalysts such as NaOH or KOH, preferred for their low cost and high catalytic activity.[30] Alkali metal alkoxides such as CH_3ONa are also highly active for transesterification and can result in yields > 98 % under short reaction times (30 mins).[31] Alkali hydroxides, such as NaOH, are generally highly hygroscopic and generate water when dissolved in MeOH, thus, careful handling is required to avoid any undesirable reduction in biodiesel yield. Homogeneous alkali catalysts are highly sensitive to saponification, or soap formation, which can form through reaction of free fatty acids (FFA) with the catalyst, as illustrated in Figure 2.[30] Saponification is detrimental to biodiesel production, lowering yields and resulting in the removal of the active catalyst from the system, requiring the addition of further catalyst to maintain activity. Consequently, free fatty acid levels must be kept to a minimum, if high levels of FFA are present in the feedstock, a pre-treatment is required before base catalysed transesterification can take place.

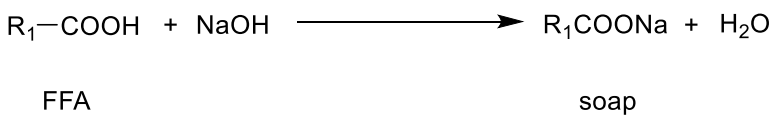

Figure 2. Side reaction between free fatty acids (FFA) and catalyst to form soap and water

Additionally, water, whether present in the original feed or formed through saponification, is detrimental to the transesterification process as triglyceride hydrolysis can occur, generating free fatty acids (Figure 3). Whilst basic heterogeneous catalysts can circumvent some of the issues associated with homogeneous catalysts, a lower rate of reaction is typically observed, and diffusion limitations can occur. Whilst base catalysed transesterification reactions are most commonly used industrially, strict feedstock requirements exist due to the sensitivity of the catalyst to FFA and water, necessitating feedstock pre-treatment of unrefined or crude feedstocks.

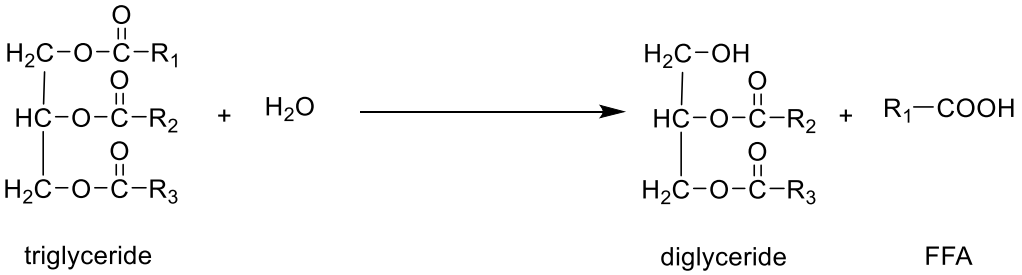

Figure 3. Triglyceride hydrolysis generating free fatty acids

Whilst base catalysed transesterifications are more widely used due to their superior reaction rates, acid catalysts offer the advantage of catalysing esterification and transesterification simultaneously, allowing crude feedstocks with high levels of FFA to be used. The acid catalysts often utilized for this include homogeneous mineral acids such as H_2SO_4 and HCl, although the rate of acid catalysed transesterification is estimated to be *ca.* 4000 times slower than with homogeneous alkali catalysts;[32] for this reason, acid catalysed transesterification has received limited attention, despite its applicability with low grade feedstocks. The use of enzymatic catalysts for transesterification has also been the focus of significant research efforts over previous years.[33-38]

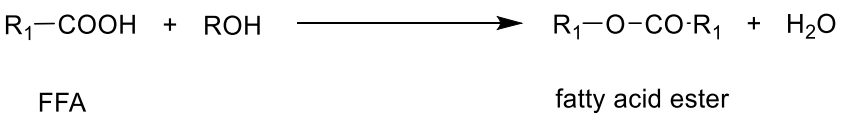

Figure 4. Acid catalysed FFA esterification

Whilst biodiesel production has been widely implemented, significant socioeconomic and environmental concerns have been raised. One of the primary concerns surrounds the use of arable land to grow crops for direct use in biofuel production and the impact this can have on food security and prices. Furthermore, issues also arise surrounding losses in biodiversity, deforestation and water consumption, amongst others.[39-41] Consequently, the

production of biodiesel from virgin feedstocks can contribute to some of the issues it was intended to negate, thus the use of waste feedstocks, such as used cooking oils and animal tallow, has been the focus of significant research efforts in recent years.[42-45] The use of waste materials for biodiesel is highly desirable and satisfies most of the aforementioned environmental concerns. In addition to the environmental benefits of utilising waste as a feedstock for this process, significant economic advantages are also associated. However, waste feedstocks can provide additional challenges throughout biodiesel production, with a pre-purification stage necessary in certain circumstances. As described earlier, the presence of FFAs and water can be detrimental to the most commonly used homogeneous alkaline catalysts, thus, flexibility with regards to the catalyst system employed is often required with waste feedstocks. Despite this, the use of non-virgin feedstocks has been successfully realised with more than 80 % of UK biodiesel derived from waste cooking oil in 2019.[46]

Table 1. Advantages and disadvantages of different catalyst types for biodiesel production and feedstock suitability with different catalyst systems.[47, 48]				
Type of catalyst	***Feedstock***	***Yield (%)***	***Advantages of catalyst***	***Disadvantages of catalyst***
Homogeneous basic e.g. NaOH, KOH, CH_3Ona	Pre-treated/refined vegetable oils	96-98	High catalytic activity, low cost, favourable reaction kinetics, modest operating conditions	Low FFA required so pre-treatment often required, anhydrous conditions required, saponification, difficult catalyst separation and recyclability
Heterogeneous basic e.g. CaO, MgO, KOH/Al_2O_3	Pre-treated/refined vegetable oils	< 90	Easy catalyst separation, non-corrosive, high selectivity, long catalyst lifetimes, environmentally benign	Low FFA requirement, anhydrous conditions, high molar ratio of alcohol to oil requirement, high reaction temperature and pressure, diffusion limitations, higher cost
Homogeneous acid e.g. H_2SO_4, HCl	Pre-treated/refined vegetable oils and waste and crude vegetable oils	≤ 99	Catalyses esterification and transesterification simultaneously, suitable for high FFA content feedstocks, no saponification	Corrosion of reactor/equipment from catalysts, difficult catalyst separation and recyclability, slow rate of reaction, long reaction times, biodiesel neutralisation often required
Heterogeneous acid e.g. SBA-15, HPA	Pre-treated/refined vegetable oils and waste and crude vegetable oils	< 90	Catalyses esterification and transesterification simultaneously, suitable for high FFA content feedstocks, no saponification, environmentally benign	Very slow rates of reaction, high cost, diffusion limitations
Enzymatic e.g. Candida antarctica fraction B lipase,	Pre-treated/refined vegetable oils and waste and crude vegetable oils	99	Avoids soap formation, easy purification, mild reaction conditions	Slow reaction rates, high costs, can be denatured by MeOH

1.2.2 Crude glycerol composition and purification

Phase separation occurs throughout the transesterification process, with GLY falling to the bottom of the reaction vessel owing to its higher density. Since residual GLY and MeOH are removed from the biodiesel product by water washing, large quantities of water are present in the crude GLY obtained. The GLY product also contains numerous other impurities including unrecovered alcohol, FAMEs, glycerides, FFA, soap, ash and catalyst residue. As described above, numerous feedstocks and a variety of catalysts can be used in the production of biodiesel and thus, the composition of crude GLY can vary widely according to the triglyceride feedstock and the transesterification process operating conditions. The highly heterogeneous nature of crude GLY provides additional challenges regarding its effective utilisation; not only do numerous impurities exist, the nature and quantities of these impurities fluctuates between GLY batches, with this variability providing a barrier to its use on a commercial scale.

Numerous studies into the composition of crude GLY have been performed. Hassan *et al.* performed analysis on 11 crude GLY samples obtained from 8 Australian biodiesel manufacturers.[49] The GLY content was found to range between 38.4 – 96.5%, with an average of 72.4%. Large variations in pH were observed, with values between 2.0 and 10.8 recorded. A study by Li and co-workers was performed to investigate the chemical composition of 5 crude GLY samples, although it should be noted that all samples were sourced from the same provider. There was significant variation in the composition of the samples, with GLY content ranging from 22.9 – 63.0%; notable differences also existed in the amounts of MeOH, water, soap, FAMEs and glycerides detected, leading the authors to highlight the importance of crude GLY characterisation prior to its conversion or application.[50]

The method of purification undoubtably varies depending on the reaction conditions and catalyst used throughout the biodiesel process but can simply be summarised as follows:[51]

1) *Neutralisation* – Free fatty acids and salts are removed by precipitation. In the use of an alkali catalyst, a strong acid such as H_2SO_4 or H_3PO_4 is added; this typically releases free fatty acid molecules from soap and reacts with catalyst residue to give salt and water. Generally, three layers are formed, the FFA layer rises to the top where it can be skimmed off whilst inorganic salts fall to the bottom, leaving a GLY-rich middle layer.
2) *Methanol removal* – Since an excess of MeOH is typically used throughout FAMEs production, residual MeOH is contained within the crude GLY phase. MeOH can be easily removed through evaporation processes, through utilization of an evaporator

or flash units. Some residual water will also be removed this way, although this will depend on the conditions used for MeOH recovery.

3) *Purification and refining* - the high boiling point of GLY (290 °C at atmospheric pressure) necessitates the use of high temperature vacuum distillation. Since GLY can undergo polymerisation and thermal degradation at elevated temperatures, distillation must be performed under vacuum to minimise thermal reactions. Whilst distillation is a well-established technique, the high energy requirement to achieve GLY vaporisation makes it a costly process, requiring large-scale operation to achieve cost-efficiency. Alternative technologies to vacuum distillation include membrane separation technologies and adsorption techniques utilizing activated carbons or ion exchange resins.

Crude GLY purification is an expensive process that is often economically unfeasible for small-to-medium sized biodiesel producers, thus crude GLY produced through biodiesel is typically a low value product.[52] Additionally, the heterogeneity of crude GLY, with huge variations reported across providers, results in the need for both characterisation and purification of crude GLY feedstocks prior to further application.

1.2.3 The effect of biodiesel on the glycerol economy

As shown in Figure 1, GLY is produced as a by-product of biodiesel production and accounts for approximately 10 wt.% of the total product yield. Since GLY is produced alongside biodiesel, the rapid expansion of the biodiesel market over the past two decades has had significant effects on GLY supply drivers, as shown in Figure 5. GLY was traditionally produced through fatty acids and saponification, with the GLY by-product providing additional revenues to the soap manufacturing. However, the biodiesel industry is now the biggest supplier of GLY.[53] Annual crude GLY production *via* biodiesel increased from *ca.* 200,000 tonnes in 2003 to > 2 million tonnes in 2012, with traditional GLY markets unable to absorb the dramatic surplus.

High purity GLY has numerous applications in several industries, including food and drink, cosmetics and pharmaceuticals, however, the high levels of impurities present in biodiesel-derived GLY often prevent its direct use in the majority of traditional applications. Prior to use, GLY must first be refined to an acceptable purity level, this can then be sold as "technical-grade" GLY at a low price or refined further to produce GLY sufficiently pure for uses in the food and pharmaceutical industries.[54] The rapid increase in GLY availability has had a dramatic effect on the price of both refined and crude GLY; the price of refined (99.5 %) GLY dropped from €4000/tonne in 2000 to €450/tonne in 2010.[53] The price of crude GLY has fallen to such an extent that it has become a waste product with such low econmic value it is often used as cattle feed or incinerated as a low-energy content fuel.

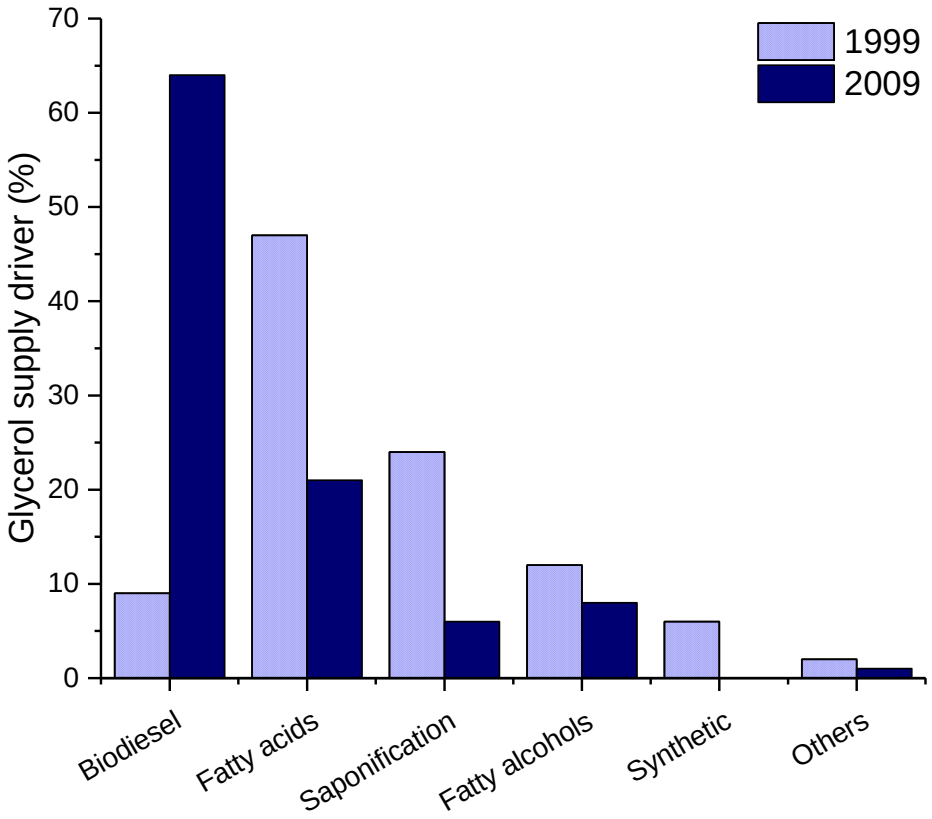

Figure 5. Changes in glycerol supply drivers from 1999 to 2009.[54]

Since GLY is produced predominantly as a by-product of the biodiesel industry, its supply is independent of market demands. Consequently, in order to add value to the GLY by-product, the end-product needs to be economic despite fluctuations in GLY supply and price. The conversion of the crude GLY by-product to higher value products, such as high purity GLY, through refining and purification processes, or other value added chemicals, including propanediols, acrolein, dihydroxyacetone and MeOH, through catalytic transformations, offers an attractive prospect to enhance the overall profitability of biodiesel production.[54]

1.2.4 Direct utilisation of crude glycerol

Whilst there are limited examples for the direct use of crude glycerol feeds, the examples which do exist are often for low value products and thus, provide limited economic benefit. The conversion of glycerol to value added products, also known as glycerol valorisation, is essential to help ensure the profitability of the biodiesel market, whilst also reducing our dependency on fossil-based feedstocks. Whilst enormous efforts into efficient GLY conversions have been performed, the vast majority employ high purity GLY as a feedstock. As described in the preceding sections, the composition of crude GLY can vary significantly from batch to batch, depending on several operating factors.

Crude GLY has been identified as an alternative to ethylene glycol (EG) as a renewable cement additive that can improve grinding and handling properties while enhancing the strength of the cement.[55] Crude GLY is often of such low economic value that it is incinerated

for energy, however, it provides low energy value as a fuel, thus this is not a desirable use. Similarly, crude GLY can be used to supplement animal feed,[56] due to the ability of ruminant creatures to better tolerate MeOH impurities, although this is another low value application, which is highly susceptible to market fluctuations.

Biological transformations of crude GLY to numerous high-value chemicals, such as 1,3-propanediol, n-butanol and dihydroxyacetone, have been widely explored and extensively studied.[57-61] Whilst successful biological transformations of crude GLY have been demonstrated, the required biocatalysts are often expensive. Furthermore, their sensitive nature and requirement for fairly dilute GLY feedstocks often results in low catalyst productivity. The impurities present in crude GLY can inhibit cell growth during fermentation, particularly when more concentrated GLY feedstocks are utilised, resulting in low transformation efficiency.[62]

Numerous investigations into the use of crude GLY for chemocatalytic transformations have been undertaken, although in many cases, the catalytic performance reported with crude GLY feedstocks was far inferior to that achieved with high purity GLY.[63] The use of crude GLY will be reviewed where relevant in section 1.3. Briefly, the impurities present can result in catalyst poisoning, an increase in char production and a reduction in desired product yields.[62] Furthermore, inorganic contaminants can provide additional difficulties surrounding the use of crude feedstocks for gas phase GLY conversions; as GLY is vaporised, inorganic sediments are deposited which can result in reactor fouling and associated blockages, making the direct transformation of crude GLY a challenging process.

1.3 Glycerol valorisation

Whilst the concept of a glycerol-based biorefinery is highly desirable due to the vast scale of GLY production, limited information surrounding the feasibility of utilising crude GLY as a feedstock is available. As described above, the composition of crude GLY can vary widely depending on the operating conditions and triglyceride feedstocks used. Recently, a techno-economic assessment of a GLY biorefinery was performed to determine the profitability of GLY valorisation reactions through an integrated facility, based on previously reported processes.[64] The process model involved the use of a crude feedstock with an initial GLY purification stage whereby the removal of ash, water, MeOH and MONG (matter organic, non-glycerol) was modelled. Whilst the purified-to-crude GLY ratio of 0.81 was accounted for, the cost of the actual purification stage was not included in the overall profitability assessment.

As described earlier, the conversion of GLY to value added products can provide significant economic and environmental benefits; the direct conversion of crude GLY is therefore highly desirable. Despite this, the complex nature and heterogeneity of crude GLY

feedstocks mean that the vast majority of chemocatalytic GLY transformations have been performed with high purity GLY allowing any impurity effects to be discounted. Consequently, the literature findings discussed below can be assumed to have utilised high purity GLY unless explicitly stated otherwise.

As a C_3 triol, GLY can undergo a wide variety of chemocatalytic transformations with numerous comprehensive reviews highlighting significant developments in GLY valorisation.[54, 65-81] Examples of some of the chemical transformations possible for GLY are shown in Figure 6. Dehydration, reduction, oxidation, gasification, esterification, etherification, oligomerisation, carboxylation and chlorination strategies have been widely explored and are attractive options for GLY valorisation. As mentioned earlier, the aim of this thesis is to further investigate the conversion of GLY to MeOH over simple oxide catalysts without the addition of an external hydrogen source. Consequently, the ensuing review of GLY valorisation will be limited to dehydration and hydrogenolysis reactions, due to their relevance by way of the reaction conditions used and products observed.

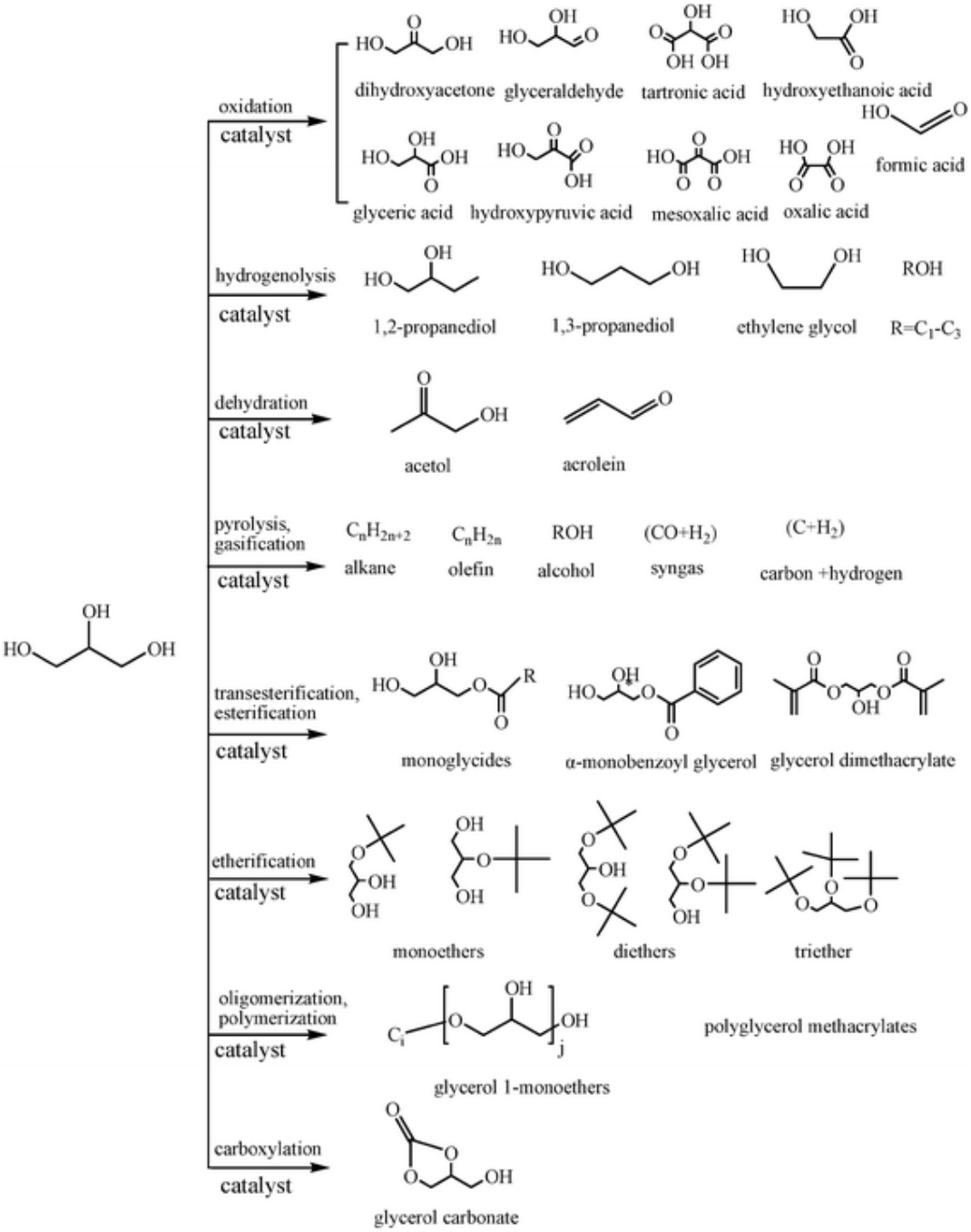

Figure 6. Chemocatalytic glycerol conversions to value added chemicals. Figure reproduced from Chem. Soc. Rev., 2008, 37, 527-549 - Reproduced by permission of The Royal Society of Chemistry

1.3.1 Glycerol to methanol

As briefly discussed, a recent publication by the Hutchings group demonstrated the conversion of aqueous GLY to MeOH in a one-step process over simple metal oxide catalysts such as MgO (magnesium oxide) or CeO_2 (cerium(IV) oxide, ceria).[27] No external reductant was added to the reaction and reactions performed with D_2O in place of H_2O, displayed a significant kinetic isotope effect, leading to the conclusion that water was acting as the hydrogen source required to produce MeOH. Similarly, investigations performed with $^{18}OH_2$

did not lead to the presence of ^{18}O-MeOH, confirming GLY, not water, as the oxygen source for MeOH.

A GLY conversion of 26 % was achieved with a corresponding MeOH selectivity of 41 % at a reaction temperature of 300 °C with a 10 wt.% GLY feedstock, over an MgO catalyst. The catalytic activity could be maintained by increasing the GLY concentration to 30 wt.% with a proportional increase in catalyst mass, and activity was demonstrated to be stable over a 35-hour time period. Attempts to improve GLY conversion through increasing the reaction temperature and/or catalyst mass were unsuccessful. Under the above reaction conditions, remarkably similar levels of GLY conversion (27 %) and MeOH selectivity (41 %) were achieved over a CeO_2 catalyst, however, increasing the reaction temperature to 400 °C resulted in full GLY conversion, whilst MeOH selectivity reached a maximum of 60 % at 380 °C.

In addition to MeOH, other observed products included hydroxyacetone (HA), acetaldehyde (ACA), ethanol (EtOH), acrolein (ACR), ethylene glycol (EG), propionaldehyde, allyl alcohol (AA), 2,3-butanedione (2,3-BD), acetone (ACE) and CO_2, with the proposed reaction scheme shown in Figure 7. Products such as MeOH, EtOH, ACE, and ACR were found to be unreactive throughout the process when used as reactants and thus, are considered to be terminal products. Interestingly, when other oxygenates were explored as feedstocks for MeOH production, it was found that MeOH was formed from 1,3-propanediol (1,3-PD) and EG but not from 1-propanol or 2-propanol, suggesting more than one hydroxyl group is crucial for MeOH formation.

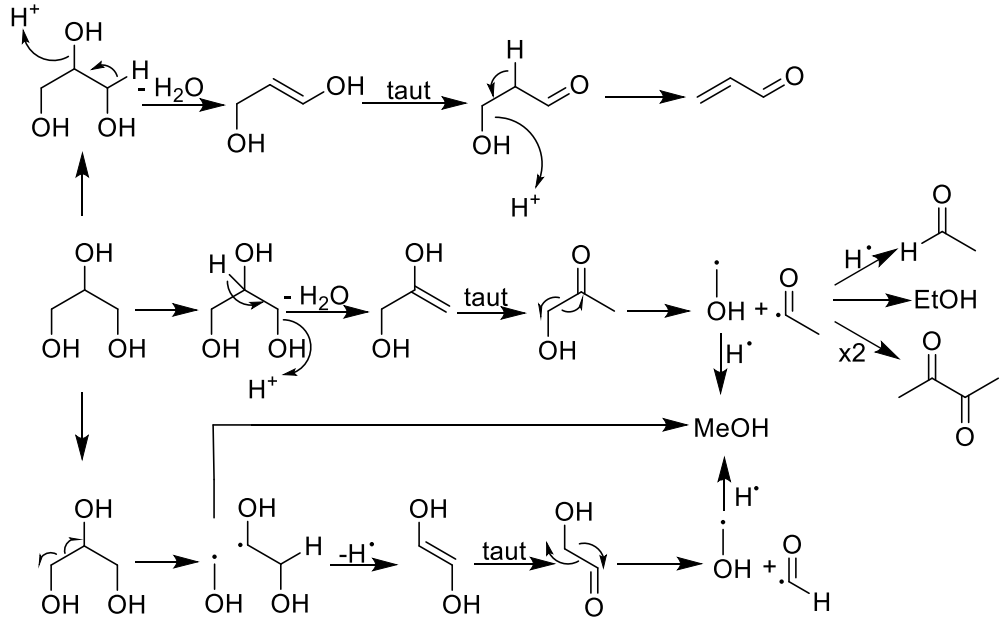

Figure 7. Proposed reaction scheme for the formation of methanol from glycerol. Figure reproduced from Nature Chem, 2015, 7, 1028–1032. Copyright © 2015, Springer Nature.

The major pathway involved the dehydration of GLY to HA, initiated through the loss of a terminal hydroxyl group followed by a subsequent tautomerization. The radical fragmentation of HA lead to the formation of MeOH and acetyl radicals, producing MeOH and ACA, respectively, with ethanol produced through the reduction of ACA. The presence of 2,3-BD provided good support to the proposed mechanism, since a C_4 ketone seems unlikely to form from GLY, other than through a C_2 coupling mechanism.

A second, more minor route for MeOH production was also identified, and is shown as the bottom pathway in Figure 7. This involved the radical fragmentation of GLY to yield a MeOH radical and an EG radical, the latter of which, either gained a hydrogen radical to make EG or lost a hydrogen radical to give glycolaldehyde. Analogous to the fragmentation of HA, glycolaldehyde could further fragment, giving another MeOH radical along with a formaldehyde radical, both of which could be further reduced to MeOH. In addition to the pathways responsible for MeOH production, an additional pathway was observed, whereby GLY undergoes a double dehydration reaction to give ACR, a well-established process which is typically acid catalysed.[82-84]

The reactions discussed above were performed with high purity GLY. Crude GLY was obtained from Biodiesel Amsterdam BV and simply purified by treating the aqueous GLY phase with activated carbon, prior to use as a feedstock over a ceria catalyst. The catalyst proved to be tolerant to impurities in the feed, even with a 50 wt.% GLY solution, although it should be noted that GLY conversion, MeOH selectivity and corresponding space time yield were slightly lower using crude feedstocks than with high purity counterparts. These results offer a novel route to produce MeOH from crude GLY. Since MeOH is required for biodiesel production, and GLY is a by-product of the process, this offers a sustainable recycling route for crude GLY.

The conversion of GLY to MeOH has also been demonstrated in a process known as the Supermethanol concept, which is an integrated process combining GLY reforming in supercritical water (RSCW) with MeOH production from syngas.[85] Typically, GLY reforming is performed over a Ni based catalyst at reaction temperatures between 675 – 725 °C and pressures of 240 – 270 bar.[86] Following catalytic reforming, the gas stream is subsequently converted to MeOH over a $Cu/ZnO/Al_2O_3$ catalyst at temperatures of 195 – 245 °C and pressures between 240 – 270 bar. Whilst MeOH yields of *ca.* 60 % have been reported, the conditions required for the integrated process are incredibly harsh.[85] Furthermore, the CO/CO_2 ratio of the gas obtained from RSCW needs to be carefully controlled in order to maximise MeOH yields, adding further complexity to the process.

In addition to the aforementioned processes, MeOH has frequently been reported as a by-product during GLY dehydration and hydrogenolysis reactions. MeOH production *via* these routes is discussed in the subsequent sections, where appropriate.

1.3.2 Glycerol to ethanol

The conversion of GLY to EtOH in a simple gas phase process, without the addition of an eternal H-source, has very recently been reported.[87] Over a caesium-promoted ZSM-5(1500) catalyst, an EtOH selectivity of 91 mol.% was observed over a period of 50-hours on stream; a significant drop in GLY conversion occurred in the first twenty hours, but this stabilised at *ca.* 40 % for the remaining reaction time. EtOH was proposed to form through GLY *via* consecutive monodehydration-radical fragmentation-transfer hydrogenation reactions, as shown in Figure 8.

In agreement with the mechanism proposed by Haider, the authors suggested that HA, formed through GLY dehydration, undergoes a radical fragmentation process to yield MeOH and ACA radicals. EtOH production was attributed to the reduction of the acetyl radical, with ACA reduction excluded as a route to EtOH in the process. The use of MeOH as a reactant led to the formation of EtOH as the only detected liquid phase product. As such, MeOH was suggested to dehydrate, forming the corresponding methyl carbene and water. The rates observed for the MeOH methylation were however comparatively low, suggesting that this route was fairly minor.

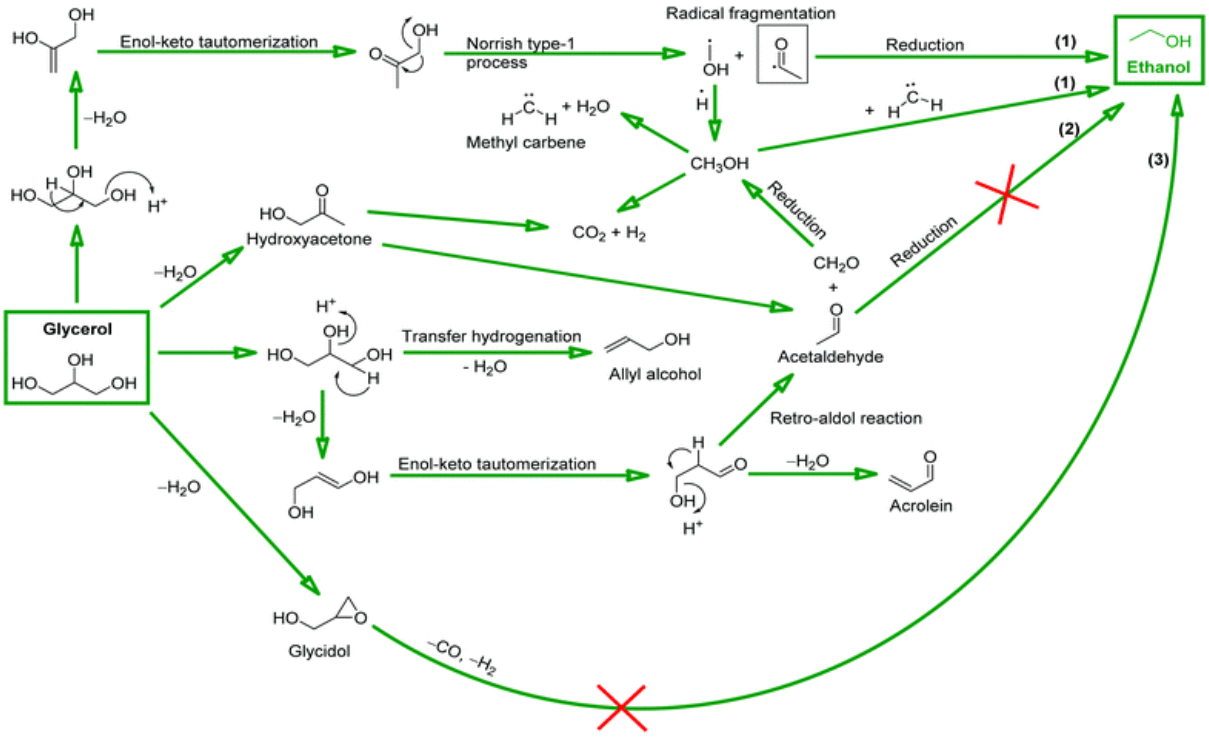

Figure 8. Proposed mechanism for the gas phase conversion of glycerol to ethanol. Figure reproduced from Green Chem., 2020, 22, 753-765 - Reproduced by permission of The Royal Society of Chemistry.

The authors attributed the remarkable EtOH selectivity observed over the 20 wt.% CsZSM-5(1500) catalyst to a suitable density of basic sites accompanied by a total absence of acid sites. The small zeolite crystallite size and synergistic interaction between caesium and the zeolite support were also suggested to promote desired reaction selectivity. Over a 20 wt.% CsZSM-5(30) catalyst, the major products formed were HA, glycidol and AA. Post-reaction analysis of the catalysts showed significant levels of coke were deposited over 20 wt.% CsZSM-5(30), whereas modest coking was observed over 20 wt.% CsZSM-5(1500). The different levels of carbon deposition that occurred across the two materials was attributed to the acid sites which were present in 20 wt.% CsZSM-5(30) but not in 20 wt.% CsZSM-5(1500). This highlighted the importance of carefully controlling the acid-base properties of the catalyst in order the control product distribution.

1.3.3 Dehydration

As described above, HA was identified as an intermediate in the gas phase conversions of GLY to both MeOH and ethanol.[27, 87] Since HA is a GLY dehydration product, initiated through the loss of a terminal hydroxyl group, the process of GLY dehydration will be examined in more detail. Alternatively, GLY dehydration can occur *via* the secondary hydroxyl group, giving 3-hydroxypropanal, a highly reactive molecule that typically dehydrates further to yield ACR, thus GLY dehydration will be discussed in wider context.

GLY dehydration to ACR is one of the most widely studied GLY valorisation reactions, due to the industrial importance of ACR. As the simplest unsaturated aldehyde, ACR is a valuable intermediate, which can be converted to the polymer precursor, acrylonitrile, by ammoxidation. Traditionally produced from propene, which is obtained from fossil fuel-based sources, the production of ACR *via* GLY dehydration offers a sustainable route to an important platform chemical. Over recent years, extensive investigations into GLY dehydration as a route to ACR have been performed; comprehensive reviews regarding GLY dehydration have been published providing detailed insights into reaction mechanisms and the current state of the art situation.[76, 77]

The dehydration of GLY to ACR is not a new reaction, with Sabatier investigating gas phase GLY dehydration as early as 1918.[88] Complete conversion of GLY in the gas phase over alumina and uranium oxide catalysts was achieved at reaction temperatures of 360 and 350 °C respectively, with ethene and CO detected as by-products alongside ACR, due to further decomposition of the latter. The first patent regarding the conversion of GLY to ACR was published in 1930 whereby an ACR yield of *ca.* 75% was obtained in the gas phase over a supported lithium phosphate catalyst.[89] In 1934 Shell patented a process for the aqueous phase GLY dehydration in the presence of sulfuric acid at a reaction temperature of 190 °C, achieving an ACR yield of close to 50 %.[90] Hoyt and Manninen also investigated liquid phase

GLY dehydration, this time with a clay-supported phosphoric acid catalyst in a petroleum oil reaction medium, allowing for a reaction temperature of >300 °C which achieved an ACR yield of *ca*. 72 %.[91]

Despite the early works surrounding GLY dehydration to ACR, no significant efforts to further develop the process took place until the 1990s, coinciding with increased GLY supplies through biodiesel production. A patent published by Neher *et al.* reported that ACR yields of up to 70 % at reaction temperatures above 300 °C were achievable over an alumina supported phosphoric acid catalyst.[92] HA (acetol) was the main by-product of the process, with a yield of *ca.* 10 %. The authors highlighted the importance of catalyst acidity, with a Hammett acidity function of < +2 required, with a preference for catalysts with H_0 < -3.

Bühler *et al.* investigated GLY decomposition in near- and sub-critical water, at temperatures between 350 and 475 °C and pressures between 250 – 450 bar, whereby obtained products included MeOH, ACA, propionaldehyde, ACR, AA, formaldehyde, CO, CO_2 and H_2.[93] Overall non-Arrhenius behaviour was observed which, along with the product distribution, led the authors to propose two alternative competing pathways, as shown in Figure 9. An ionic pathway and a free radical pathway were proposed, the former of which was favoured at lower temperature and/or higher pressure. The radical pathway was preferred under higher temperature and/or low pressure. Whilst products such as MeOH, AA and propionaldehyde were only produced through radical pathways, most products including ACR, ACA, formaldehyde, CO_x and H_2 could be produced through both ionic and radical routes.

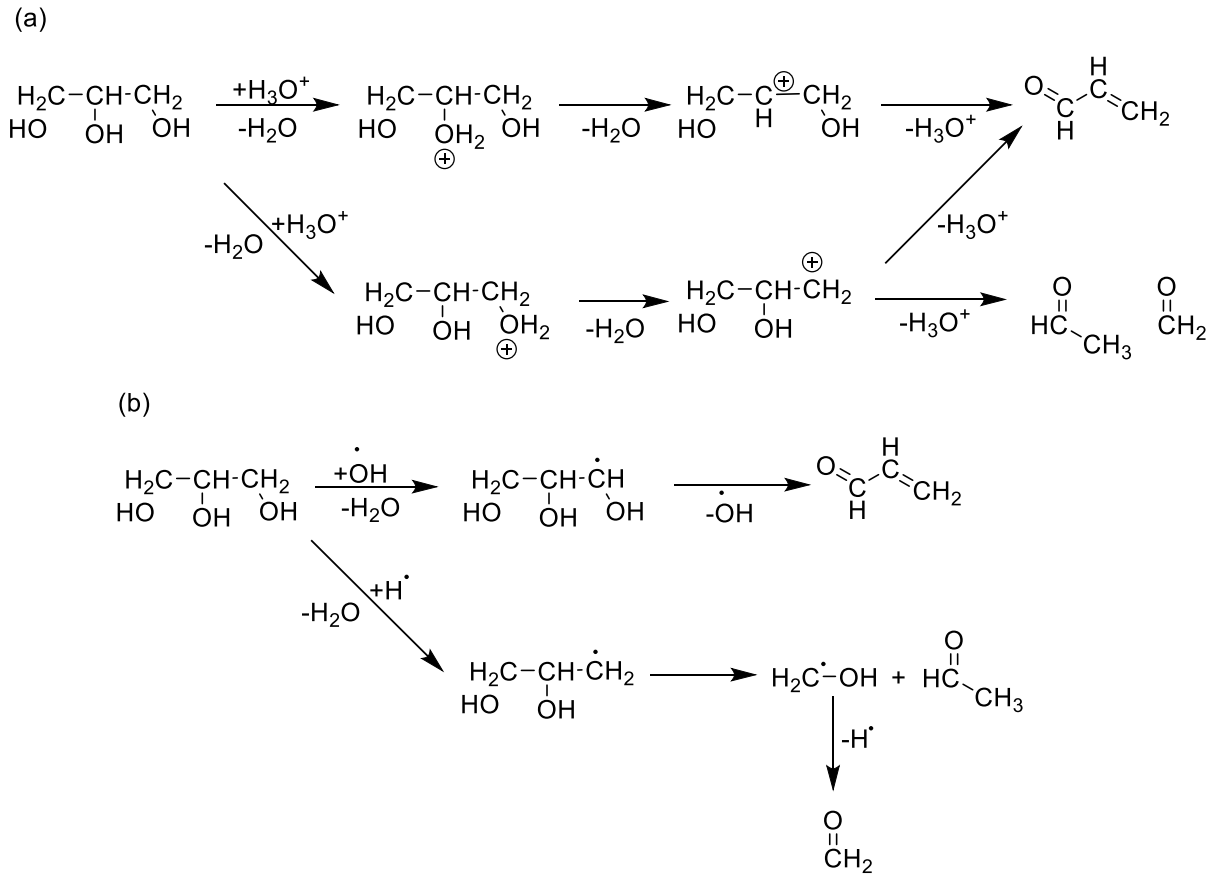

Figure 9. Reaction pathways to the formation of acrolein considering *a*) an ionic pathway and (*b*) a radical pathway, as suggested by Bühler *et al.*[93]

Whilst GLY dehydration to yield ACR can be performed in both the vapour and liquid phase, gas phase reactions can be advantageous for product separation. Additionally, liquid phase reactions involve near-, sub- or super-critical conditions, which when combined with acid catalysis, can result in significant corrosion. This ultimately results in increase capital costs and requires substantial investment in specialist equipment. For such reasons gas phase GLY dehydrations are preferable from an industrial perspective, particularly when considering the scale of GLY supplies.[77] Consequently, the majority of dehydration studies have been performed in the vapour phase.

A formal reaction scheme for vapour phase GLY dehydration was suggested by Tsukuda *et al.* who explored silica supported heteropolyacids as catalysts for the reaction.[83] Protonation of a secondary hydroxyl group in GLY leads to elimination of a H_3O^+ molecule, forming an enol intermediate which readily tautomerises to 3-hydroxypropanal. As a highly reactive species, 3-hydroxypropanal was not detected in the reaction stream due to its rapid dehydration to ACR. Alternatively, protonation at the terminal positions results in the formation of HA, again through an enol intermediate. The presence of ACA as a product was attributed to the decomposition of 3-hydroxypropanal through a retro-aldol reaction, also generating formaldehyde. ACA is easily oxidised to acetic acid. Other detected products included ACE, propionaldehyde, and EtOH, which could be attributed to HA

dehydroxylation, and ACR and ACA reductions, respectively. The authors also highlighted the importance of the initial loss of the secondary hydroxyl group for high ACR selectivity.

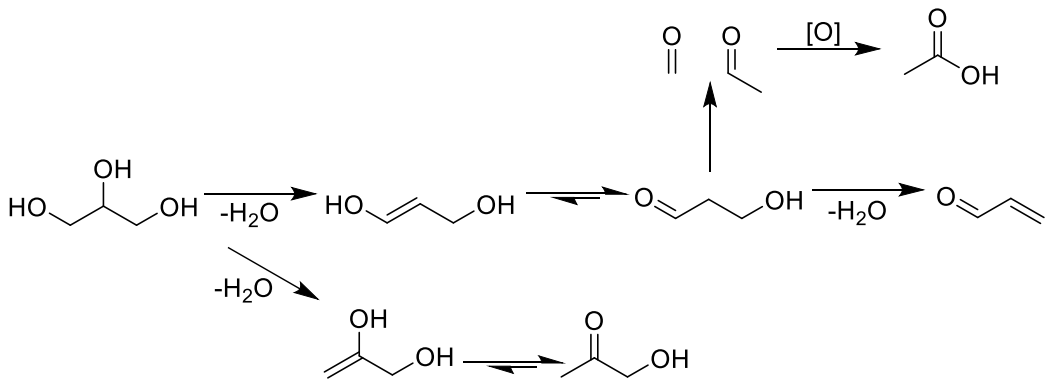

Figure 10. Probable reaction routes over silica supported heteropoly acids, published by Tsukuda *et al.*[83]

Building on the work by Neher, Chai *et al.* investigated the role of catalyst acidity and basicity on ACR selectivity.[94] Materials were classified as bases, weak and medium strength acids, strong acids and very strong acids, according to their Hammett acidity (H_0) or basicity (H_-) which was measured by titration with various Hammett indicators. It was found that strong acid catalysts ($-8.2 \leq H_0 \leq -3.0$) were most selective to ACR. The use of stronger acids ($H_0 \leq -8.2$) resulted in reduced ACR selectivity due to an increase in secondary reactions which can consume produced ACR. The strongest acid catalysts showed significant levels of carbon deposition and were found to be highly selective for the conversion of ACR to coke, which also resulted in significant catalyst deactivation. Basic and weak and medium strength acidic catalysts both showed low selectivity to ACR, suggesting that is not the primary reaction pathway over these materials. These findings were in agreement with the earlier scheme proposed by Tsukuda *et al.*[83] 1,2-PD and MeOH were also detected over basic materials, which were attributed to the reduction of HA and formaldehyde, respectively. Similarly, the presence of AA was attributed to ACR reduction.

A comprehensive reaction network was reported by Corma and co-workers, who studied the gas conversion of aqueous GLY feedstocks (20 – 85 wt.%) over zeolite catalysts.[84] Very high levels of GLY conversion were observed and the main oxygenates produced were ACR, ACA, ACE, AA and HA. Trace amounts of MeOH, EtOH, methacrolein, methyl vinyl ketone and C_2-C_4 unidentified compounds were also detected. Other observed products included CO, CO_2, C_1-C_4 alkanes, C_2-C_4 alkenes, C_5^+ hydrocarbons (including BTX) and coke. To better understand the nature of the products observed from GLY, several of the major products were used as reactants. HA was found to be very reactive in the system, although it was less reactive than GLY; additionally, the product distribution differed significantly from that obtained from a GLY feedstock. More ACE and acids (including acetic, propionic and acrylic acid) were produced from HA, along with a significant amount of unidentified high

molecular weight products and a lower selectivity to ACA was observed. No ACR was detected from HA, indicative of the two distinctive, independent pathways of GLY dehydration. One of these pathways involved the loss of the secondary hydroxyl group to yield ACR *via* a 3-hydroxypropanal intermediate. The other, involved the loss of a terminal hydroxyl group to yield HA. ACE was attributed to the hydrodeoxygenation of HA, which could proceed through a 1,2-PD intermediate (although that was not detected as a product). The high selectivity to acids observed from HA was explained by the isomerisation of HA to propionic acid. The use of 1,2-PD as a feedstock led to similar product distributions to those obtained from HA; a high selectivity to ACE was obtained through a direct dehydration reaction.

AA and ACE were also used as feedstocks. While similar reactivities were observed for GLY and AA, ACE was found to be much less reactive, reaching only 30 % conversion at 500 °C under the same operating conditions. Both AA and ACE showed high selectivity to olefins, but with AA more selective to propene and ethene, and ACE more selective to butenes. Significant quantities of CO_2 and acetic acid were also produced from ACE. A high selectivity to coke was obtained from AA, as well as pentenes, BTX compounds and high molecular weight products; aromatics were attributed to the condensation of olefins produced *in situ*, which could further react with *in situ* produced aromatics leading to the formation of coke. Similarly, a high selectivity to coke was obtained from a propionic acid feed.

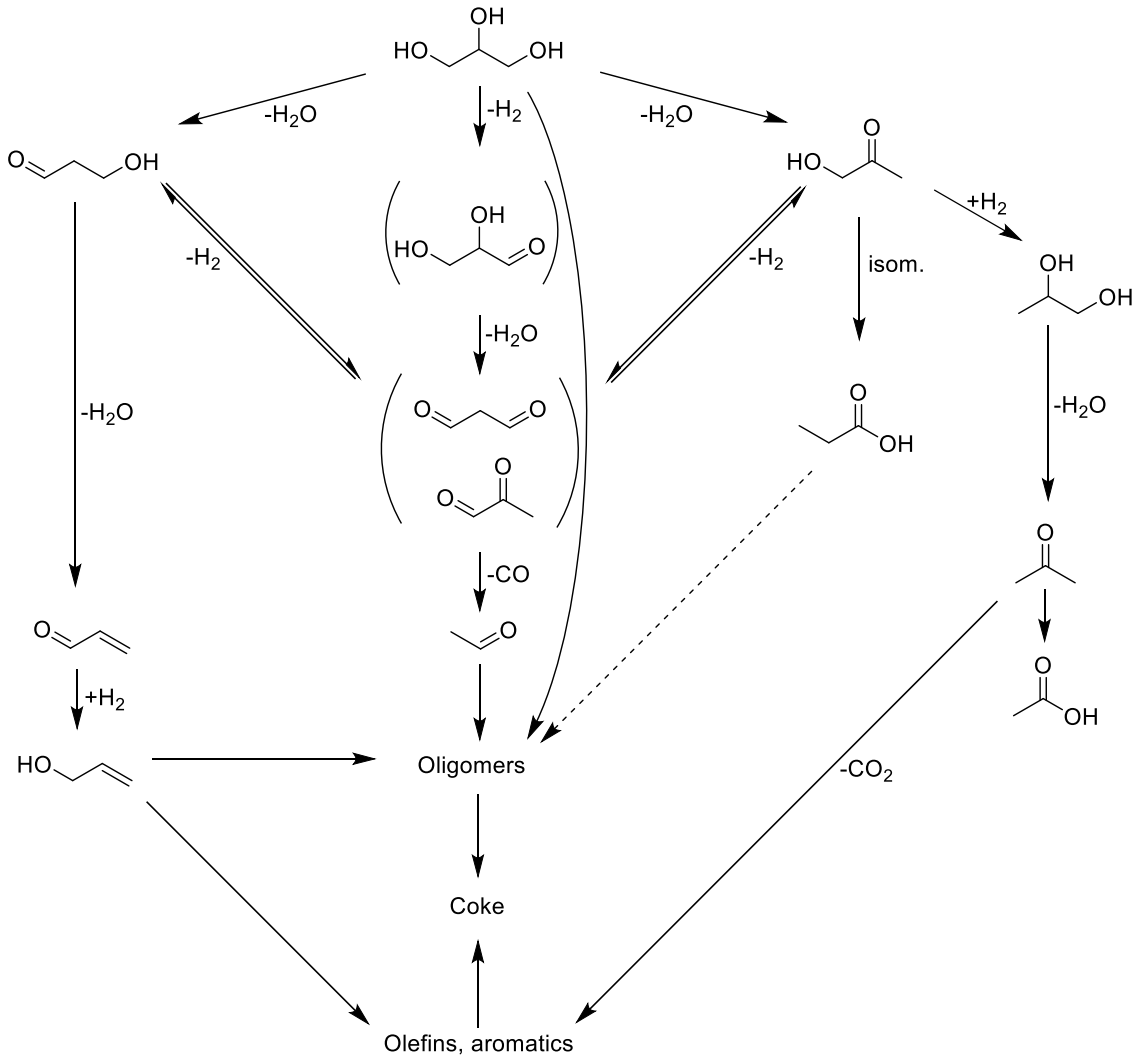

Figure 11. Reaction network of glycerol/water mixtures over zeolite materials, initially published by Corma and co-workers.[84]

Kozhevnikov and co-workers provided further mechanistic insight into GLY dehydration.[95] With the use of a caesium heteropolysalt catalyst (CsPW), a GLY conversion of 100% was achieved, with an ACR selectivity of 98%, although significant reduction in GLY conversion occurred after an initial time-on-stream period of 1 hour. This significant reduction in activity was attributed to heavy catalyst coking. Platinum group metal dopants were explored in an attempt to reduce catalyst deactivation by carbon deposition and an enhanced stability was observed for a 0.5% Pd/CsPW catalyst, resulting in an ACR selectivity of 96% at 79% GLY conversion after a period of 5 hours on stream. CsPW was then compared with a Zn(II)–Cr(III) (1:1) mixed oxide (Zn-Cr oxide) catalyst, in an attempt to further understand the role of acid sites on subsequent mechanisms of GLY dehydration. Characterisation of the acid sites by pyridine DRIFTS evidenced that the CsPW material possessed strong Brønsted acidic character. On the contrary, the Zn-Cr oxide was determined to contain only Lewis acidic sites. Lower GLY activity was achieved over Zn-Cr oxide compared with CsPW, which was attributed to the lower total acidity. In contrast to

CsPW, where ACR was the major product obtained with a selectivity of 98 % (or 94% after 5 hours on stream), much lower ACR selectivity was observed over Zn-Cr oxide (30-34%), with HA selectivity greater than or equal to that of ACR. The authors proposed that ACR formed on Brønsted acid sites, with HA forming on Lewis acid sites (Figures 12 and 13, respectively). Thus, the ACR produced over the Zn-Cr oxide catalyst was attributed to the conversion of Lewis acid sites to Brønsted acid sites by the large excess of steam present. The authors concluded that Lewis acid catalysts have a higher activation energy than Brønsted acid catalysts and thus, require higher operation temperatures. The authors also suggested that Lewis acid catalysts are fairly selective for the conversion of GLY to HA, the major by-product in the conversion of GLY to ACR.

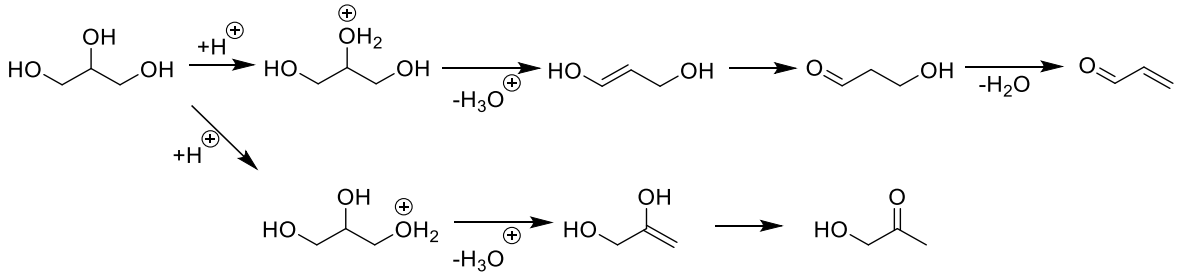

Figure 12. Mechanism of glycerol dehydration over Brønsted acid sites, as proposed by Kozhevnikov and co-workers[95]

The application of Brønsted acidic catalysts results in GLY protonation; given that there are no steric constraints surrounding proton transfer, protonation typically occurs at the secondary hydroxyl group due to its stronger partial negative charge. Following protonation, H_3O^+ leaves to produce 1,3-dihydroxypropene which tautomerises to 3-hydroxypropanal before undergoing further dehydration to ACR. Whilst protonation of the secondary hydroxyl group is favourable, protonation of a primary hydroxyl group can also occur leading to HA formation in the presence of Brønsted acid catalysts.

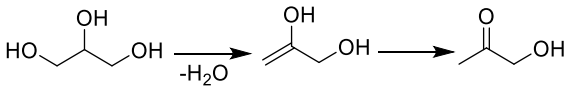

Figure 13. Mechanism of glycerol dehyration over Lewis acid sites, as proposed by Kozhevnikov and co-workers[95]

Alternatively, the interaction of GLY with Lewis acid sites is affected by steric constraints and thus, interaction of the terminal hydroxyl group is more favourable than that of the secondary hydroxyl group. Subsequently, a terminal OH group is transferred to metal ion Lewis acid site, with a proton from the secondary carbon atom in GLY migrating to the bridging atom of the metal oxide, giving the hydrated form of the Lewis acid catalyst alongside 2,3-dihydroxypropene which tautomerises to HA.

More recently, a detailed reaction mechanism for GLY dehydration was published by Martinuzzi *et al.*, who identified numerous by-products which could be formed over an

industrial solid acid catalyst; none of these by-products had not previously been reported.[96] An incredibly complex reaction scheme was proposed, with numerous competing pathways identified. Products such as 3-methyl-2-cyclopenten-1-one and phenol showed the C-C bond forming reactions occurred alongside C-C cleavage; cyclopentenes were proposed to form through aldol-condensation reactions between ACA and ACE, whereas phenol was attributed solely to ACA. Another larger product which has been previously identified was 1,3,5-dioxan-5-ol, attributed to the cyclization of GLY and formaldehyde. Additionally, formaldehyde reduction was responsible for the MeOH detected, whilst an analogous reaction occurred with ACA to generate EtOH.

GLY dehydration over basic catalysts was investigated by Kinage *et al.* due to the fact that that most acidic catalysts also contain basic sites.[97] In contrast to acidic catalysts whereby dehydration is the initial step, GLY dehydrogenation initially occurs over basic materials. The resulting glyceraldehyde (2,3-dihydroxypropanal) molecule subsequently dehydrates to give 2-hydroxyacrylaldehyde which is then reduced to HA. Alternatively, glyceraldehyde can undergo a retro-aldol reaction to produce formaldehyde and hydroxyacetaldehyde. These two products can subsequently undergo reduction to MeOH and EG, respectively. The base catalysed mechanism of GLY dehydration explains the high HA selectivity observed by Chai *et al.* over basic catalysts.

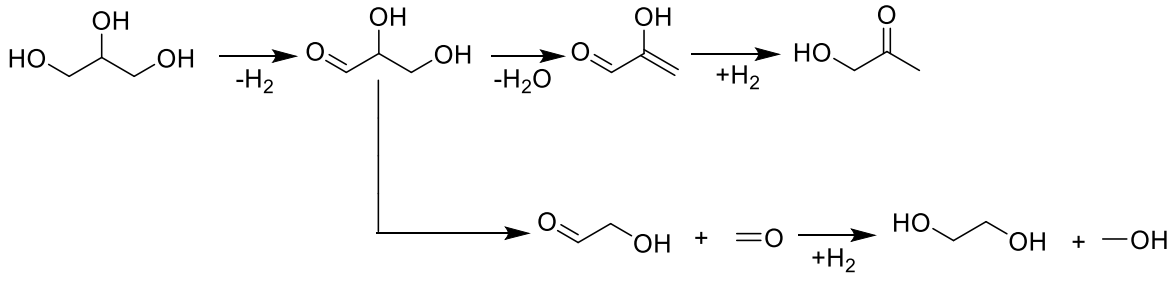

Figure 14. Mechanism of glycerol dehydration over basic sites, as proposed by Kinage *et al.*[97]

Further investigations into GLY dehydration over basic catalysts have been performed with lanthanum-based materials at reaction temperatures between 300 – 700 °C.[98] Over La_2O_3 and $LaNiO_3$, HA was predominantly formed at reaction temperatures of 400 and 500 °C and significant quantities of EG, MeOH and 1,2-PD also observed. The dehydration to HA was proposed to proceed through an enol intermediate, with 1,2-PD attributed to subsequent reduction of HA. The mechanism proposed for the formation of EG and MeOH was in agreement with that proposed by Kinage *et al.*,[97] initiated by GLY dehydrogenation to glyceraldehyde. The authors attributed the enhanced MeOH and EG selectivities observed over La_2O_3 to its increased basicity, which favoured C-C cleavage of glyceraldehyde. At reaction temperatures exceeding 500 °C, gas phase products were dominant due to GLY reforming ($C_3H_8O_3 \rightarrow 3CO + 4H_2$) and water gas shift ($CO + H_2O \rightarrow CO_2 + H_2$) reactions. Interestingly, a particularly poor carbon balance was obtained at a reaction temperature of

300 °C. This was attributed to the presence of high molecular weight products, with oligomeric species composed of up to twelve GLY monomers detected by mass spectrometry. Polyglycerols and other polymer residues have previously been reported in both liquid and gas phase over basic materials.[99, 100]

A HA yield of 76 % was reported by Batiot-Dupeyrat and co-workers over a La_2CuO_4 catalyst at a reaction temperature of 260 °C, in a further study into the use of lanthanum-based materials.[101] Results showed that metallic copper was not the active species for GLY dehydration and its presence promoted carbon deposition leading to catalyst deactivation. The high activity of La_2CuO_4 compared with Cu_2O and La_2O_3 was attributed to a cooperative interaction between lanthanum and copper ions which was proposed to benefit the reaction. Whilst Cu^{2+} was shown to be reduced to Cu^{+} under the reaction conditions, the activity of Cu_2O was significantly lower than that of La_2CuO_4, leading the authors to suggest that an interaction between Cu^{+} and La^{3+} was beneficial to the reaction. High catalyst stability was exhibited; no significant loss of activity observed over 20 hours on stream, which the authors suggested could be due to the absence of catalyst acidity.

The above findings were in contrast with a study performed by Sato *et al.*, who investigated the use of copper catalysts for gas phase polyol conversions.[102] A reduced copper catalyst was found to be effective for GLY dehydration to HA, with a HA selectivity exceeding 90 % obtained over a Cu-Al_2O_3 catalyst at a reaction temperature of 250 °C. Metallic copper was suggested to provide the active sites for GLY dehydration, although the authors acknowledged the need to further investigate the role of the support in the process.

Recently, copper-based catalysts have been further explored through the use of Cu-MgF_2, Cu-MgO, Cu-MgFOH and La_2CuO_4 materials.[103] Unlike the earlier study involving La_2CuO_4 which was performed in the absence of water, an 80 wt.% GLY feedstock in water was used throughout this investigation. The authors showed that as weak Lewis acid sites, Cu^{2+} was not responsible for GLY dehydration. Metallic copper was acknowledged to provide an active site for dehydration, through the formation of Cu-alkoxide species. In this study, Cu^{+} was therefore proposed to be the active species. The low activity of Cu-MgO and CuMgFOH catalysts was attributed to low levels or absence of Cu^{+} species, whereas the high stability of Cu-MgF_2 was attributed to the high stability of Cu in the +1 oxidation state.

GLY dehydration has also been investigated by computational methods. Nimlos *et al.* performed detailed theoretical studies in to the dehydration of GLY.[104] It was found that neutral GLY can dehydrate *via* a 1,2-elimination mechanism to yield ACR and HA through 1,3-dihydroxypropene and 2,3-dihydroxypropene intermediates; activation barriers of 71 and 73 kcal mol^{-1} were calculated for each pathway, respectively. Alternatively, a lower activation barrier of 65 kcal mol^{-1} was calculated for a 1,3-dehydration mechanism, which

leads to the formation of formaldehyde, vinyl alcohol and water. A smaller energy barrier was calculated for vinyl alcohol tautomerisation compared with the dehydration step, so ACA is readily produced *via* a 1,3-dehydration mechanism. The high activation barriers for the dehydration of neat GLY indicate that the process can only occur at relatively high temperatures. Alternatively, much lower activation barriers were calculated for the dehydration of protonated GLY. A barrier of 21 kcal mol^{-1} was calculated for a pinacol rearrangement mechanism (hydride transfer) and 25 kcal mol^{-1} for a substitution mechanism involving glycidol; an epoxide intermediate.

Sun *et al.* also used density functional theory (DFT) to probe the mechanism of GLY dehydration.[105] They focussed on the dehydration of neutral GLY to glycidol; a route not considered by Nimlos *et al.*, where an activation barrier of *ca.* 59 kcal mol^{-1} was calculated. This further evidenced that high temperatures are required for neutral GLY dehydration. This mechanism was revisited by Stolz and co-workers.[106] It was found that neutral GLY dehydrates to glycidol *via* a 1,2-elimination mechanism, with an activation barrier of 67 kcal mol^{-1}. Glycidol is converted to 3-hydroxypropanal through a rapid ring opening step, whereby the H atom present on the C_1 atom in glycidol is transferred to the secondary C atom concurrently with the formation of a carbonyl group. Once formed, 3-hydroxpropanal can undergo decomposition through a retro-aldol mechanism, to form water, formaldehyde and vinyl alcohol. The latter of these products rapidly tautomerises to ACA. Alternatively, 3-hydroxypropanal can undergo a dehydration step, yielding ACR and water. In terms of barrier height, 3-hydroxypropanal decomposition to formaldehyde and vinyl alcohol is most favourable, with a barrier of 35 kcal mol^{-1}; decomposition to ACR however, was calculated to have a barrier height of 54 kcal mol^{-1}. The dehydration reaction was proposed to be driven by the acidity of the H atom on the α-C atom whereas the retro-aldol reaction is driven by the acidity of the hydroxyl group. Since the hydroxyl group possesses higher acidity than the H on α-C, a lower activation barrier is obtained for decomposition versus the dehydration pathway.

Given that dehydration through activation of a terminal hydroxyl group would result in HA formation and dehydration through activation at the secondary hydroxyl group results in ACR production; statistically speaking, the possibility for HA formation is double that of ACR, due to the two terminal and one secondary hydroxyl groups in GLY. However, the work by Corma[84] and FT-IR investigations,[107] demonstrated that a high selectivity to ACR could be achieved over H-ZSM-5 suggesting favourable loss of the secondary hydroxyl group. GLY dehydration over H-ZSM5 was investigated by computational methods by Kongpatpanicha *et al.*[108] It was found that the first dehydration step was the rate determining step for both ACR and HA formation, which had intrinsic activation energies of 42.5 and 42.3 kcal mol^{-1}, respectively. These results suggest that there is competition between loss of a terminal and

secondary hydroxyl group. In the step following the initial dehydration an enol, is formed through the alkoxide returning the proton; the activation energy for this in the case of ACR (i.e. 1,3-dihydroxypropene formation from the alkoxide) is 19.7 kcal mol^{-1}, whereas the activation energy in the case of HA (i.e. 2,3-dihydroxypropene formation from the alkoxide) is 26.8 kcal mol^{-1}. The activation energy difference of 7.1 kcal mol^{-1} for the enol formation explains the kinetic favourability of ACR formation over HA formation. It should be noted that the final energy observed is lower for HA (-27.2 kcal mol^{-1}) and ACR (-17.1 kcal mol^{-1}), meaning that ACR formation is kinetically favourable, whilst HA formation is more favourable thermodynamically.[77]

1.3.4 Hydrogenolysis

The most common route for the conversion of GLY to diols or mono-alcohols is through hydrogenolysis, with GLY hydrogenolysis having been widely explored over recent years.[67, 74, 78, 109-112] Hydrogenolysis describes a reaction whereby the addition of hydrogen results in the cleavage of C-C or C-X bonds, where X represents a heteroatom. Generally, GLY hydrogenolysis involves the removal of one H_2O molecule following the addition of a H_2 molecule through cleavage of a C-O bond; the competing reaction (C-C cleavage) can lead to the formation of EG and MeOH. As a saturated triol, GLY has a higher O/C ratio than most chemical feedstocks, thus hydrogenolysis is an attractive prospect for GLY valorisation.[113]

1.3.4.1 Diols

Much of the research surrounding GLY hydrogenolysis has focussed on the production of the C_3 diols; 1,2-PD and 1,3-PD, both of which are valuable chemical intermediates traditionally produced from fossil-based sources.[65, 79, 109, 111, 114, 115] Currently 1,2-PD is produced from propylene oxide, whereas 1,3-PD is produced from ethylene oxide (Shell) or ACR (Degussa-DuPont). A significant challenge surrounding the selective hydrogenolysis of GLY to propanediols is the need for selective C-O bond cleavage over C-C cleavage. An additional challenge surrounding the selective production of 1,3-PD exists, due to steric hinderance, and the more favourable cleavage of a primary hydroxyl group.[116]

The conversion of GLY to 1,2-PD has been widely explored, with numerous reports of yields exceeding 90 % .[67, 117] 1,2-PD is widely used in the cosmetics, food and tobacco industries, and provides a non-toxic alternative for anti-freeze.[109] High 1,2-PD selectivities have been reported in the liquid phase using precious metals, base metals and bimetallic catalysts,[67] but particularly promising results have been reported through vapor-phase GLY hydrogenolysis over copper-based catalysts. Gradient temperatures systems have been utilised to facilitate the dehydration and hydrogenation steps, which occur simultaneously during GLY hydrogenolysis, to take place at different temperatures since lower temperatures favouring hydrogenation.[118, 119] Cu-based catalysts have shown high stability

for 1,2-PD production; yields in excess of 96 % have been demonstrated .[67, 118-120] High H_2 pressures are also often employed to shift the equilibrium towards 1,2-PD but exceptional selectivity to 1,2-PD have been demonstrated at atmospheric H_2 pressures.[118, 119]

GLY hydrogenolysis to 1,2-PD is widely accepted to proceed through one of three mechanisms: Dehydration-hydrogenation, dehydrogenation-dehydration-hydrogenation, and direct hydrogenolysis.[109] The dehydration-hydrogenation route is typically acid catalysed. For this a HA intermediate is formed *via* dehydration, before subsequent reduction to 1,2-PD. 1-propanol and 2-propanol are typically observed as by-products in such reactions, which can both form from sequential 1,2-PD reduction. Alternatively, 1,3-PD can also be formed through the hydrogenation of 3-hydroxypropanal if dehydration occurs at the secondary position, although the probability of 1,3-PD formation is low due to enhanced stability of HA vs. 3-hydroxypropanal.[121]

Alternatively, under neutral or basic conditions, GLY hydrogenolysis typically occurs through a dehydrogenation-dehydration-hydrogenation mechanism. Seminal work by Montassier *et al.* using ruthenium-based catalysts showed that GLY predominantly dehydrogenates to glyceraldehyde over metal sites before dehydrating to pyruvaldehyde *via* a 2-hydroxyacrylaldehyde intermediate on basic sites; pyruvaldehyde hydrogenation then occurs sequentially on metal sites through a HA intermediate.[121, 122]

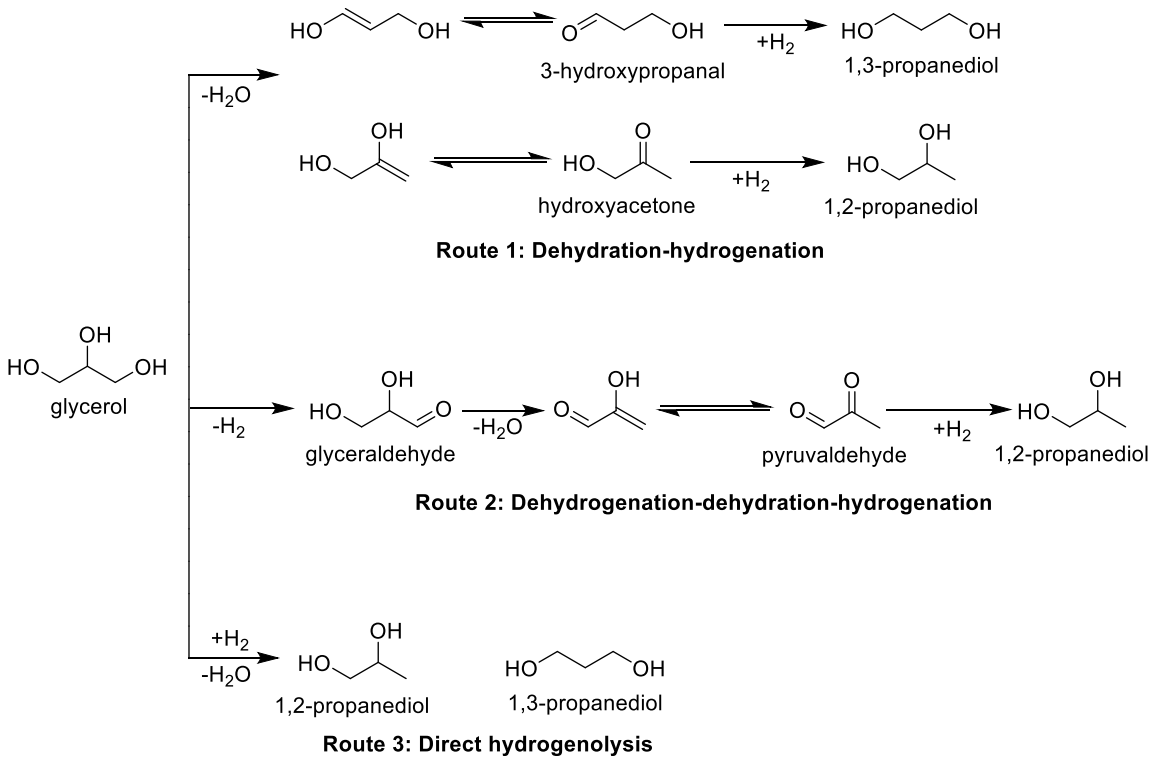

Figure 15. Proposed mechanisms of glycerol hydrogenolysis. Figure adapted from RSC Adv., 2015, 5, 74611-74268 - Reproduced by permission of The Royal Society of Chemistry.

Direct GLY hydrogenolysis was recently proposed by Tomishige *et al.*, over Ir-ReO_x/SiO_2 catalysts.[123, 124] GLY adsorption can occur to form two alkoxides, 1,3-dihydroxyisopropoxide and 2,3-dihydroxypropoxide, which activates the hydride in the 3-position and 2-position, respectively. Elimination at the terminal position then yields 1,2-PD with 1,3-PD formed through elimination at the secondary position. The hydride attack on 2,3-dihydroxypropoxide occurs through a 6-membered transition state which is more stable than the 7-membered transition state formed with 1,3-dihydroxyisopropoxide and thus, 1,3-PD was formed predominantly through this mechanism with a maximum selectivity of 58.9 % observed.[123] Additionally, 1,3-PD reduction to 1-PrOH is unlikely to occur since this would involve the formation of an unfavourable 7-membered transition state. As such, any 1,2-PD formed *in situ* underwent ready hydrogenolysis, due to its ability to form a stable transition state.

1,3-PD is the highest value GLY hydrogenolysis products, with great industrial importance. 1,3-PD is used as a monomer in the production of polypropylene terephthalate, PPT, a biodegradable polymer, synthesised through the condensation of 1,3-PD and terephthalic acid. As such, the development of direct GLY hydrogenolysis provides great promise to produce 1,3-PD from GLY. Whilst GLY to 1,3PD can proceed through hydrogenation of a 3-hydroxypropanal (3-HPA) intermediate (Figure 15), low yields of 1,3-PD are typically obtained. 3-HPA is a GLY dehydration product formed through the loss of the secondary hydroxyl group and typically requires a Brønsted acid catalyst. Whilst increasing reaction temperature favours the initial dehydration step, 3-HPA is highly reactive and readily dehydrates to ACR. As such, reaction temperatures must be kept relatively low to suppress this competitive reaction. High H_2 pressures promote 3-HPA hydrogenation over dehydration but preventing further reduction to 1-propanol is difficult, making 1,3-PD selectively a challenge. The relatively low temperature and high H_2 pressures required provide an additional challenge to continuous flow processes due to the low volatility and difficulty vaporising GLY under these conditions, thus, the majority of studies have been performed under batch conditions.

Under basic conditions, EG and MeOH can also be formed through GLY hydrogenolysis.[125, 126] Whilst 1,2-PD can be formed through a dehydrogenation-dehydration-hydrogenation mechanism, glyceraldehyde can undergo a retro-aldol reaction on basic sites to give glyceraldehyde and formaldehyde which are then hydrogenated over metal sites to give EG and MeOH, respectively. Alternatively, decarbonylation can occur over metal sites giving EG and CO. Methane is often produced through the reduction of MeOH and CO formed throughout the process.

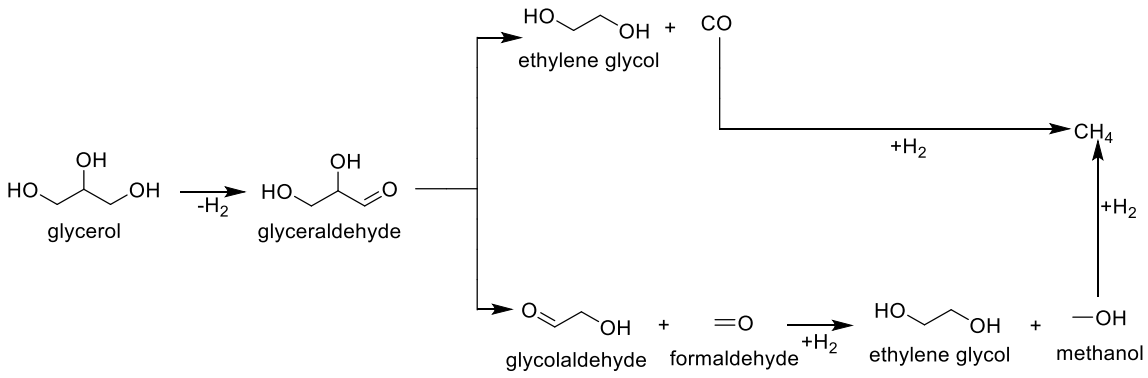

Figure 16. Proposed mechanism for ethylene glycol and methanol through glycerol hydrogenolysis, suggested by Montassier *et al.*[121, 125]

As discussed previously, despite the fact high selectivity to 1,2-PD has been demonstrated at atmospheric hydrogen pressure,[118, 119] high H_2 pressures are often used.[127-130] Since H_2 is typically produced from fossil-based sourced using energy intensive processes and given the inherent hazards surrounding the transport, storage and usage of high pressure H_2, the *in-situ* generation of H_2 during hydrogenolysis is highly desirable. One option for this is through partial GLY reforming ($C_3H_8O_3 + 3H_2O \rightarrow 3CO_2 + 7H_2$), whereby hydrogen formed is used for GLY hydrogenolysis leading to the overall production of 1,2-PD, HA, CO_2, CO, H_2O and H_2. While this methodology is advantageous, the1,2-PD yields produced in this way are typically lower than those obtained in hydrogen environments.[131] Catalytic transfer hydrogenation (CTH) is a process whereby hydrogen is transferred from a donor molecule to an acceptor molecule, and provides an alternative means of introducing the hydrogen required for hydrogenolysis.[115] 2-propanol and formic acid have been widely explored as hydrogen donor molecules, with selectivities in excess of 90 % reported.[132-136] Whilst CTH provides an attractive route for GLY hydrogenolysis, it should be noted that the hydrogen donor molecules are often of significantly higher value than crude GLY. As such, the economic feasibility of this route must be considered for it to be viable on a larger scale.

1.3.4.2 Mono-alcohols

The majority of mono-alcohols produced from GLY have been reported as by-products formed through the sequential reduction of desired diol products.[67, 109, 137, 138] However, Friedrich and co-workers have reported the conversion of GLY to mono-alcohols over Ni catalysts supported on silica or alumina.[139] A total mono-alcohol selectivity of 54.5 % was observed over Ni/Al_2O_3 compared with 68.5 % over Ni/SiO_2 at a reaction temperature of 320 °C with 60 bar H_2 and a 60 wt.% GLY feedstock (GHSV of 1060 h^{-1}). The superior performance exhibited by Ni/SiO_2 was attributed to the increased density of Ni sites when compared with Ni/Al_2O_3, which was postulated to be attributed to weaker metal-support interactions.

Further work was performed by the Friedrich group into the use of molybdenum and tungsten-based catalysts for the production of mono-alcohols from GLY.[140] Significantly increased activities were observed for the alumina supported catalysts compared to the previously investigated supported silica catalysts. The enhanced 'activity' of these catalysts was attributed to the increased Brønsted acidity of the alumina catalysts. Both increasing reaction temperature and the H_2: GLY ratio favoured the formation of mono-alcohols at the expense of diols; mainly 1,2-PD and EG. A total lower alcohol selectivity of 85.4 % was obtained over 10 wt.% W/Al_2O_3 catalyst at a reaction temperature of 325 °C with 60 bar H_2 and a H_2: GLY ratio of 2: 1. Under these reaction conditions, both Mo/Al_2O_3 and W/Al_2O_3 showed reasonable MeOH selectivity (> 30 mol.%) due to the propensity for C-C cleavage.

The production of MeOH *via* GLY hydrogenolysis has also been reported under batch conditions.[141] Whilst the patent successfully demonstrated the conversion of GLY to MeOH over a number of supported-metal catalysts, Ru/graphite in particular was shown to result in excellent MeOH selectivities. The superior performance of Ru/graphite was attributed to the high propensity for C-C cleavage coupled with minimal C-O cleavage. MeOH selectivity was, however, found to significantly decrease with increasing GLY conversion which would present a challenge to a larger scale application of this process.

1.4 Catalysis by ceria

Comprising approximately 0.0046 wt.% of the Earth's crust, cerium is the most abundant of the rare earth elements and has a higher natural abundancy than elements such as tin and copper.[142] Cerium dioxide, also known as ceria (CeO_2), has been widely researched and has extensive applications in the field of heterogeneous catalysis, both as a catalyst and a catalyst support. There have been more than 35,000 publications on the topic of ceria since 1995, with the number of publications generally increasing year on year (Figure 17). Additionally, publications relating to ceria-based catalysis steadily increased, highlighting the importance of ceria in catalytic applications.

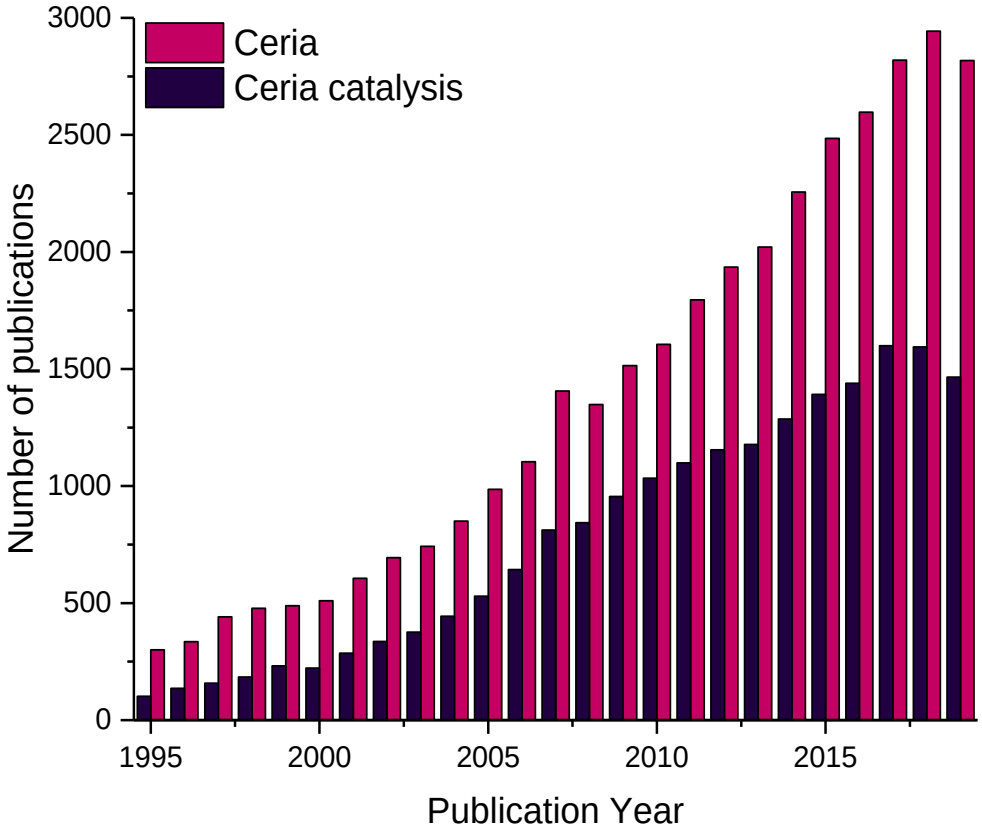

Figure 17. The number of publications related to "ceria or CeO_2" and "ceria or CeO_2 catalysis" between 1995 and 2019. (Source: Web of Science, 17 Dec 2019)

Numerous comprehensive reviews have been published, highlighting recent advancements in the catalytic applications of ceria based materials.[142-150]

1.4.1 Structure and properties

Element number 58, cerium has an electron configuration of $[Xe]4f^25d^06s^2$ and can occupy both the +4 and +3 oxidation states. The stoichiometric oxides of cerium are therefore CeO_2 and Ce_2O_3, although intermediate phases with a range of CeO_2-Ce_2O_3 compositions are also known.[151] The overall stoichiometry of cerium oxides is dependent on temperature and oxygen pressure, with Ce_2O_3 readily oxidised to CeO_2. The stoichiometric oxide, CeO_2, has a fluorite (CaF_2) crystal structure, with the space group *Fm3m*. The unit cell consists of a face-centred-cubic (FCC) arrangement of cerium cations which are bonded to eight nearest neighbour oxygen anions, in a Ce-O_8 cubic structure. The oxygen anions are tetrahedrally coordinated to four nearest neighbour cerium cations, in a simple cubic arrangement embedded in the unit cell, forming an O-Ce_4 tetrahedron.

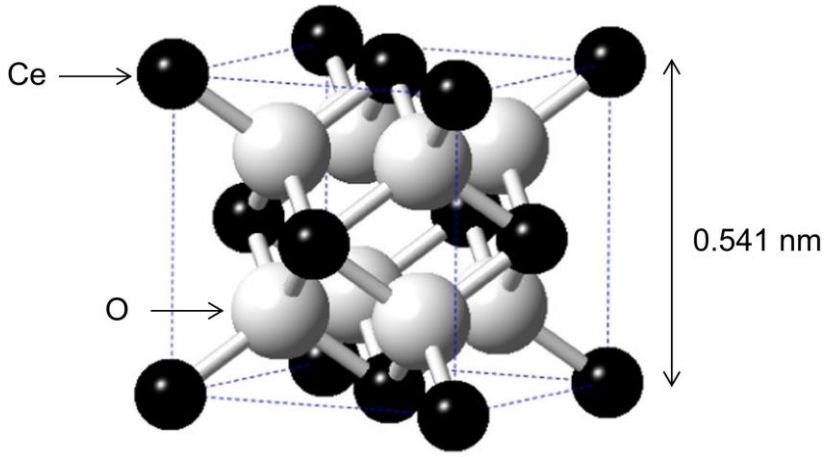

Figure 18. The unit cell of CeO_2. The black spheres are Ce and the white spheres are O. The spheres have been drawn at 50% space filling to allow the Ce-O bond to be seen. Figure reproduced from Surf. Sci. Rep., 2015, 70, 42-85. Copyright © 2014 Elsevier B.V.

Both intrinsic and extrinsic defects exist in ceria. Intrinsic defects can be induced through thermal disorder or reaction with an external atmosphere (i.e. through redox processes) whereas. extrinsic defects are typically induced through the addition of aliovalent dopants or impurities.[152] Intrinsic defects are observed in both stoichiometric and non-stoichiometric ceria, although higher defect densities are typically observed for non-stoichiometric ceria. Intrinsic defects can be classified as Frenkel or Schottky defects. Frenkel defects occur when an ion is displaced from its lattice position and becomes lodged in an interstitial site, creating a vacancy at the original lattice location and an interstitial defect. Schottky defects occur when oppositely charge ions leave their lattice sites creating vacancies. Vacancies form in stoichiometric units to maintain an overall neutral charge.

The following defects can be thermally generated and do not involve reaction with an external environment:

$$O_o \leftrightarrow O_i'' + V_{ö} \qquad \text{Eq. 1}$$

ΔE = 3.2 eV

O_o represents oxygen at its lattice site, O''_i represents a doubly positively charge oxygen vacancy and $V_{ö}$ is a doubly negative oxygen interstitial.

$$Ce_{Ce} \leftrightarrow Ce_i^{\cdots\cdot} + V_{Ce}'''' \qquad \text{Eq. 2}$$

ΔE = 11.1 eV

Ce_{Ce} indicates Ce at its lattice site, $Ce_i^{\cdots\cdot}$ indicates a cerium ion (Ce^{4+}) in an interstitial site, $V_{Ce}^{''''}$ represents a cerium vacancy.

$$Ce_{Ce} + 2O_o \leftrightarrow V_{Ce}'''' + V_{ö} + CeO_2 \qquad \text{Eq. 3}$$

ΔE = 3.5 eV

Equations 1 and 2 are representative of oxygen and cerium Frenkel defects, respectively, whereas equation 3 is representative of a Schottky defect. From the variation in ΔE values, it can be seen that anionic Frenkel type defects are dominant in ceria, leading to pairs of oxygen vacancies in lattice sites and oxygen anions lodged in interstitial sites. This was supported by neutron diffraction experiments which showed higher atomic displacement parameters for O anions compared with Ce cations, indicating higher anion mobility.[153] It should be noted that the density of these thermally generated defects is typically low and does not result in deviation from a stoichiometric composition.

Under reducing conditions, a high density of defects can be formed; upon reduction, there is a higher ratio of metal to anion *i.e.* ceria has a cation/anion ratio greater than 0.5. The principle way in which ceria can accommodate this change in composition is through oxygen vacancies which compensate the holes formed on reduction. The removal of oxygen from the lattice results in an overall positive charge, with an additional two electrons required per oxygen ion removed to maintain charge neutrality. These electrons are associated with cerium, changing the charge from +4 to +3. The effective charge of the anion vacancies is positive, thus neutralising the negatively charged holes. This can be written as:

$$CeO_2 \leftrightarrow CeO_{2-x} + \frac{x}{2}O_{2(g)}\ (x < 0.5) \qquad \text{Eq. 4}$$

The defect reaction can be written as:

$$CeO_2 \leftrightarrow 2xCe'_{Ce} + (1-2x)Ce_{Ce} + xV_{\ddot{o}} + (2-x)O_o\ \frac{1}{2}xO_{2(g)} \qquad \text{Eq. 5}$$

This implies that as x moles of atomic oxygen are removed from the ceria lattice, the corresponding quantity of oxygen anion sites are occupied by oxygen vacancies, leaving 2-x moles of O^{2-} anions in their original positions. On the cation side, 2x moles of Ce^{3+} are formed (Ce'_{Ce}) leaving 1-2x moles of Ce^{4+}.

Alternatively, cation interstitials may be formed through the transfer of a cerium ion from the surface to an interstitial position, which is accompanied by the removal of two O^{2-} anions into the gas phase. This can be written as:

$$(1+x)\ CeO_2 \leftrightarrow Ce_{1+x}O_2 + x\ O_{2(g)}\ (x < 0.33) \qquad \text{Eq. 6}$$

Whilst equation 6 describes the removal of oxygen into the gas phase which occurs alongside the formation of cerium interstitials, it does not adequately describe the localisation of electrons. Two possibilities exist, either through the formation of Ce^{3+} (eq. 7) or Ce^{4+} (eq. 8) interstitials.

$$(1-x)CeO_2 \leftrightarrow xCe_i^{\cdots} + 3xCe'_{Ce} + (1-3x)Ce_{Ce} + 2O_o + xO_{2(g)} \qquad \text{Eq. 7}$$

$$(1-x)CeO_2 \leftrightarrow xCe_i^{\cdots\cdot} + 4xCe'_{Ce} + (1-4x)Ce_{Ce} + 2O_o + xO_{2(g)} \qquad \text{Eq. 8}$$

The cubic fluorite structure can be maintained in non-stoichiometric ceria, CeO_{2-x}, with the fluorite structure reportedly maintained at (O/Ce) ratios as low as 1.71,[154, 155] although the Ce-O phase is dependent on both temperature and oxygen pressure.[156] Generally, an increase in lattice parameter is observed upon increasing values of x in CeO_{2-x}; the ionic radius of Ce^{4+} with a coordination number of 8 is $r(Ce^{4+}, 8) = 0.97$ Å, whereas the ionic radius of Ce^{3+} with the same coordination number is significantly larger $r(Ce^{3+}, 8) = 1.14$ Å,[157] resulting in lattice expansion.[158] It should be noted that the effects of lattice parameter are somewhat complicated by the presence of two competing effects; whilst the substitution of Ce^{4+} with Ce^{3+} can result in lattice expansion, lattice contraction is often observed with decreasing crystallite size, due to increasing pressure between the crystallite and its external atmosphere arising as a result of increased surface/volume ratios, thus the lattice parameter, particularly in nanoscale ceria, requires careful evaluation.[159, 160]

1.4.2 Redox properties

As described in the preceding section, ceria can possess intrinsic defects including anionic Frenkel defects whereby O^{2-} anions are present in interstitial sites, leaving oxygen vacancies at the lattice sites. Alternatively, under net reducing conditions (i.e. a hydrogen rich environment), Ce^{4+} can be reduced to Ce^{3+} which is accompanied by a release of oxygen into the gas phase. This reducibility allows ceria to act as an oxygen reservoir, by releasing oxygen under reducing conditions, or storing oxygen under oxidising conditions, and is known as oxygen storage capacity (OSC).[161] These redox properties have been widely exploited, with ceria-based catalysts successfully employed industrially, most widely as three-way catalysts (TWCs).[143]

Temperature programmed reduction (TPR) has been widely used to study the reduction behaviour of ceria-based materials, most commonly with H_2 as a probe molecule.[162] Generally, this technique involves the heating of a sample at a constant heating rate under a hydrogen atmosphere, while the consumption of any hydrogen is monitored and recorded as a function of temperature. The reduction of ceria is accepted to occur *via* a stepwise process, whereby surface layers of Ce^{4+} are initially reduced, with reduction of the bulk species occurring at higher temperature, which is reflected in the bimodal peak distribution typically observed during H_2-TPR experiments of CeO_2. The following mechanism for ceria reduction has been proposed: (i) H_2 surface dissociation leading to hydroxyl formation, (ii) water desorption through recombination of -OH and -H with simultaneous Ce^{4+} to Ce^{3+} reduction, leading to the formation of oxygen vacancies, (iii) diffusion of oxygen vacancies into the bulk.[163, 164]

Trovarelli and co-workers have proposed a revision to the two-step reduction model.[162, 165, 166] A linear relationship between the intensity of the first reduction peak and the surface

area of ceria was found, with negligible hydrogen consumption detected below 700 °C for low temperature ceria. Additionally, it was found that the reduction profiles could be modelled by assuming kinetic control across the entire temperature range, with the TPR profile not controlled by oxygen diffusion rates. The authors gave the following interpretation for the observed bimodal distribution: The first peak is due to hydrogen consumption occurring with the reduction of smaller ceria crystallites, which are reduced at lower temperatures. These smaller crystallites can be thermodynamically reduced to a high degree with the degree of reduction limited kinetically, either by the rate of hydrogen dissociation or formation of anionic defects. Consequently, the shape of the initial reduction peak is governed by the effects of sintering, resulting in a loss in surface area, and the kinetics of reduction. Upon increasing temperature, morphological changes occur leading to crystallite growth. The decrease in surface area observed at *ca.* 650 °C, the temperature at which no H_2 consumption typically occurs, indicates the presence of large ceria crystallite. As such, the high temperature reduction peak was concluded to represent the reduction profile of larger crystallites similarly to the lower temperature reduction of smaller crystallites.

The OSC of ceria is crucial to its application as a TWC, in addition to other applications.[143, 161, 167, 168] OSC can broadly be classified into two categories: (i) total OSC; the total amount of oxygen that can be extracted from ceria at a given temperature and (ii) dynamic OSC; the amount of readily available, reactive oxygen. Whilst the former is a measurement carried out under thermodynamic equilibria, the latter is related to the kinetics of reduction. TPR measurements are kinetically controlled, but the overall high temperature H_2 consumption is close to thermodynamic control. Thus, the total H_2 consumption measured by TPR is sometimes used as a measure of total OSC. Conversely, dynamic OSC much better represents behaviour under realistic operating conditions, with rapid alternating between reducing and oxidising environments. This typically involves alternating pulse injections of reducing agents (H_2 or CO) and oxidising agents (O_2, H_2O, CO_2) at given frequencies, to study the ability of the material to undergo fast redox cycling.[161, 162, 169]

Numerous studies have identified improvements to the redox properties of ceria through the introduction of dopants, with numerous classes of dopants explored. In addition to the intrinsic defects already discussed, the addition of dopants can induce the formation of extrinsic defects. The precise nature of the extrinsic defect is dependent on the nature of the dopant. Tetravalent dopants, e.g. Zr^{4+} or Hf^{4+}, have been widely reviewed and are demonstrated to increase OSC; the cation dopant differs in ionic radius to the parent Ce^{4+} cation thus, its introduction results in a distortion of the ceria lattice and results in an, increase in oxygen mobility. Limited attention has been given to higher valence dopants, e.g. Nb^{5+} and Ta^{5+}, due to their poor solubility in the ceria lattice.[170, 171] Alternatively, lower

valent dopants, particularly trivalent dopants, have been extensively explored. The use of trivalent dopants, such as Sm^{3+} and Gd^{3+}, are well known to increase ionic conductivity and thus have received considerable attention in the development of ceria-based electrolytes for solid oxide fuel cells.

Whilst numerous dopant types can have investigated, transition metal (TM) dopants have received considerable attention in recent years, in part due to their low cost and high relative abundance. The use of copper, manganese, cobalt, iron and nickel dopants have been shown to improve catalytic activity for a number of reactions including CO oxidation,[172-175] soot combustion,[175, 176] CO_2 hydrogenation,[177] and acetylene hydrogenation.[178, 179] Significant changes in the physicochemical properties of ceria are often observed through the addition of TM dopants. Increases in catalyst surface area, defect formation and reducibility are often observed and are widely acknowledged to be responsible for the increased catalytic activity.

1.4.3 Acid-base properties

In addition to exceptional redox properties, ceria also possesses versatile acid-base properties which can vary depending on preparation methods and catalyst pre-treatment. Whilst theoretical calculations have shown there may be some degree of covalency,[180, 181] CeO_2 is considered to be a purely ionic compound comprised of Ce^{4+} and O^{2-} ions, with cerium cations classified as Lewis acidic sites and oxygen anions classified as Lewis base sites, in line with Lewis acid-base theory.[182] Numerous techniques to investigate the acid-base chemistry of metal oxides such as ceria have been developed,[183] including titration methods,[184-186] vapour phase adsorption of probe molecules,[187-189] and model reactions which are known to be acid or base catalysed.[190, 191]

An early study by Yamaguchi *et al.* showed no correlation between the redox properties of ceria and the catalytic activity for 1-butene isomerisation, although significant loss of catalytic activity was observed upon the addition of CO_2 and NH_3, which can bind to basic and acidic sites, respectively. This led the authors to conclude that ceria's acid-base sites were the active site for the reaction.[192] This was further explored by Duprez and co-workers, who investigated a number of model reactions to evaluate the acid-base properties of numerous metal oxides.[193] Surface acidity was explored through 3,3-dimethylbut-1-ene isomerization, methylene cyclohexane isomerization and cyclohexanol dehydration to cyclohexene; CO_2 chemisorption and the ratio of cyclohexanone to cyclohexene were used to probe surface basicity. Ceria was found to possess strong levels of basicity for surface O^{2-} anions, but only very weak Lewis acidity was measured for Ce^{4+} cations.

A comprehensive evaluation of infrared spectroscopies for the assessment of surface basicity of metal oxides was performed by Lavalley.[194] The use of a CO probe molecule

showed the presence of highly basic O^{2-}; similar findings were observed with CO_2 and SO_2 probe molecule, although it was noted that these probe molecules can also result in oxidation of a partially reduced surface and surface reduction, respectively. Further works showed high levels of basicity in both reduced and unreduced ceria, and weak Lewis acidity was also reported.[182] The use of both NH_3 and pyridine as probe molecules confirmed that ceria possessed Lewis acid sites, in contrast to both Al_2O_3 and MgO, which were found to possess Brønsted acidity, and no acidic nature, respectively.[195] A CD_3CN probe showed weak levels of acidity in ceria. Strong basic sites were determined through the use of CO_2 and $CHCl_3$ probes, which was in agreement with nitrobenbenze adsorption experiments.

The experimental reports above were complemented by a thorough DFT investigation into the chemistry of acid-base pairs on metal oxide surfaces.[196] In addition to the basic nature of O^{2-}, it was also found that oxygen vacancies are also Lewis base sites. The formation of oxygen vacancies results in the production of unpaired electrons, and the subsequent reduction of Ce^{4+} to Ce^{3+} which have reduced Lewis acidity. These findings imply that an increase in the defect density of ceria could result in increased Lewis basicity and decreased Lewis acidity.

1.4.4 Low index surfaces and catalysis

The most thermodynamically stable ceria surfaces are the low index surfaces, which are the (111), (110) and (100). The surfaces are examples of the Tasker classification of ionic crystal surfaces[197] and have been extensively studied in recent years. This system followed the discovery by Mai *et al.* that ceria nanocrystals with well-defined crystal planes can be readily synthesised through simple hydrothermal methods.[198] Ceria nanostructures with well-defined morphologies have been widely reported[199-207] and typically include CeO_2 nanocubes, nanorods and nanopolyhedra, which possess exposed (100), (110), and (111) and (100) facets, respectively. Whereas bulk CeO_2 has coordination numbers of 8 and 4 for Ce and O, respectively, all three low index surfaces have lower coordination numbers, i.e. higher degrees of coordinative unsaturation which can greatly influence chemical reactivity.

CeO_2(111) is a type 2 surface, which is oxygen terminated with a repeating O-Ce-O-O-Ce-O structure. Whilst each plane is charged, the O-Ce-O layer is charge neutral and arranged in a symmetrical configuration leading to no net dipole overall. On this surface, both Ce and O have a single coordinatively unsaturated site or coordination vacancy (*CUS*), with coordination numbers of 7 and 3, respectively. CeO_2(110) is a type 1 surface which exposes both cerium cations and oxygen anions; each plane has no charge due to the stoichiometric balance of cations and anions and each plane is compositionally identical, leading to a neutral surface. On the (110) surface, Ce cations have 2 coordination vacancies (*CUS*) while O anions have a single coordination vacancy. This gives rise to coordination numbers of 6

and 3 respectively. CeO_2(100) is a type 3 surface which has a Ce-O-Ce-O layer structure, with half the amount of Ce in each layer as there is O in the adjacent layer. The surface comprises of alternately charged planes with a repeating unit of two layers, leading to a dipole which is perpendicular to the surface. The Ce(100) surface has the highest degree of coordinatively unsaturated sites across the low index ceria surfaces, with both Ce and O having 2 coordination vacancies and coordination numbers of 6 and 2, respectively.

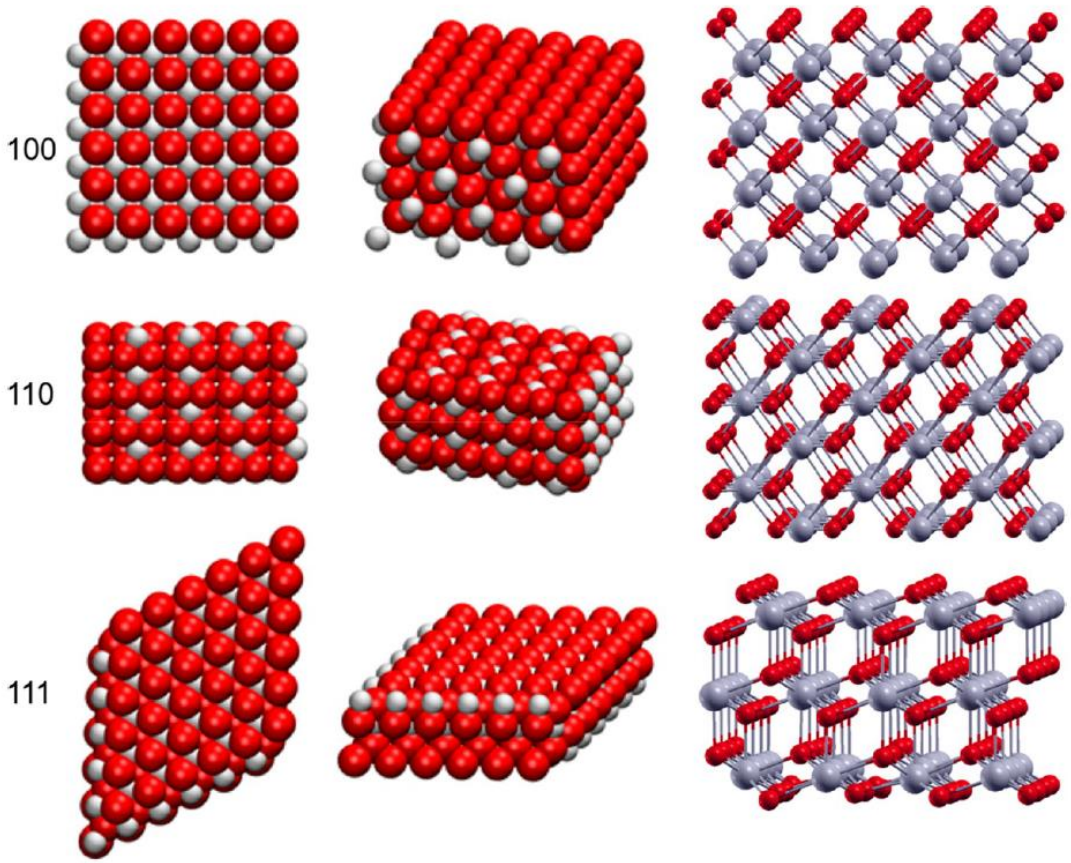

Figure 19. Top, side, and perspective view of CeO2 (100), (110), and (111) surfaces. Grey and red spheres represent cerium and oxygen ions, respectively. Adapted with permission from ACS Catal., 2017, 7, 4716−4735. Copyright © (2017) American Chemical Society.

Numerous computational studies have been performed to better understand the structure and stability of the low index ceria surfaces.[181, 208-212] A DFT-GGA+U study performed by Islam and co-workers found the surface energies to be 44, 67 and 90 meV $Å^{-2}$ (0.71, 1.06 and 1.44 J m^{-2}) for ceria (111), (110) and (100) surfaces, respectively. Significant levels of surface reconstruction were reported for Ce(100) due to the instability associated with the high energy surface. Based on the surface energies, the order of surface stability was found to be (111) > (110) > (100), which was in full agreement with previously published works from other groups.[181, 208, 212]

As described in section 1.3.1, ceria has rich defect chemistry. A number of theoretical studies have investigated the energy for oxygen vacancy formation. Defect formation was calculated

to be most favourable for Ce(110), followed by (100), with (111) the least favourable.[150, 180, 181, 208, 213] The effect of surface termination on defect sites has also been explored by Raman spectroscopy,[214] a widely established technique for the investigation of ceria-based materials.[215-219] Briefly, the authors showed that the defect density was of the order; rods > cubes > octahedra, reflecting the energy for defect formation of (110) < (100) < (111). Further probing showed these defects were most likely Frenkel-type oxygen defects, whereby anions are relocated from their lattice positions to interstitial sites. Since Raman spectroscopy is not solely a surface technique, it was suggested that the surface termination also affected the density of defect sites in the subsurface and bulk structures. Under reducing conditions, a similar density of Ce^{3+} cations and oxygen vacancies was observed across the rods and cubes, with a negligible defect density observed for the octahedra.

A study was performed by Désaunay *et al.* into the surface dependency of H_2 oxidation over ceria nanocrystals.[220] TPR analysis and the corresponding Kissinger plots showed the reactivity of hydrogen to be of the order cubes > rods > octahedra, with activation energies of 70 ± 20, 130 ± 20 and 430 ± 50 kJ mol^{-1} calculated from surface reduction temperatures of 391, 458 and 540 °C, respectively. This trend was analogous to surface stability, with the least stable (100) surface the most easily reduced, although this doesn't reflect previously published trends for the energies of defect formation. The authors acknowledged large degrees of experimental error in the activation energy calculations due to the exponential dependency of the gradient in the Kissinger plot, but were confident in the overall order of reducibility of ceria. Whilst the surface termination was demonstrated to have significant effects on the surface reduction temperature, no attempts were made to quantify hydrogen oxidation throughout the process and as such, no conclusions could be drawn on the effect of ceria surface on hydrogen consumption.

The effect of surface termination on the acid-base properties of ceria nanostructures was explored by Wu *et al.*[221] The differing degrees of coordinatively unsaturated sites suggest significant difference in surface acidity and basicity will be observed, with the theoretical acidity of Ce^{4+} in the order (100) ≈ (110) > (111) whereas the basicity of surface O^{2-} should follow the order (100) > (110) ≈ (111). The use of CO_2, $CHCl_3$ and CD_3CN probe molecules showed basicity followed the order rods > cubes >> octahedra, which reflect the order (110) > (100) >> (111). Pyridine and CD_3CN probes were used to assess the acidity of the nanostructures; whilst Lewis acid sites were detected, the strength of the sites were low, and no surface dependency was observed. The discrepancy between acidity and basicity as predicted by *cus* status and the experimental findings, led the authors to derive a number of conclusions. The increased basicity observed for the rods was attributed to the higher defect density compared with the cubes; as described earlier oxygen vacancies can act as Lewis base sites and thus, a high density of defects can increase surface basicity. Additionally, the

formation of oxygen vacancies is accompanied by the reduction of Ce cations; since Ce^{3+} are weaker Lewis acid sites than Ce^{4+}, the presence of oxygen defects results in reduced surface acidity. As such, the higher defect densities measured for the rods and cubes, compared with the octahedra, was concluded to be responsible for the reduced acidity observed. These findings highlight that the surface dependency of acid and base sites on ceria nanostructures are strongly influenced by both the degree of coordinative unsaturated surface sites and defect density.

The effect of morphology has been widely examined for numerous catalytic applications where ceria is employed as a catalyst support; this topic has been comprehensively explored and will not be further discussed.[222-228] Since the physicochemical properties of ceria can be greatly influenced by morphology and surface termination, it is not surprising that catalytic activities can also be significantly affected by surface termination.

The oxygen storage capacity (OSC) of the morphologically controlled materials was also investigated by Mai *et al.*, where it was found that the OSC was limited to the surface for the polyhedral samples. This is in contrast to the cubes and the rods, where the OSC involves both surface and bulk structures.[198] The effect of surface termination on CO oxidation was also studied by Overbury and co-workers, who found that the order of CO oxidation was in agreement with lattice oxygen reactivity and followed the trend rods > cubes >> octahedra.[229] Lattice oxygen reactivities showed an opposite trend to the theoretical energies of defect formation, which is (110) < (100) < (111), highlighting the role of defects in the mobility of oxygen species in oxidation reactions over ceria based materials. Similar findings were made by Liu *et al.* who investigated the use of ceria rods for CO oxidation and found a direct relationship between the concentration of defects and the catalytic activity.[204]

Similarly to CO oxidation, soot combustion also follows a Mars-van-Krevelen mechanism, which involves a reaction between the lattice oxygen in ceria and a substrate.[230, 231] Trovarelli and co-workers reported shape-dependent activity of soot combustion over ceria nanostructures.[232] The surface area normalised rates of soot oxidation showed enhanced activity for rods and cubes compared with conventional nanocrystalline ceria, attributed to the presence of more reactive (110) and (100) planes. Comparable findings were made in other oxidation reactions, including naphthalene,[200] xylene[233] and toluene.[234] The increased catalytic activity observed in oxidation reactions over nanorods and nanocubes, predominantly exposing the (110) and (100) surfaces, respectively, is typically ascribed to the enhanced OSC of the materials arising from increased levels of oxygen vacancies and surface defects.[200, 233, 234]

Whilst it has been shown that oxidation reactions can benefit from the presence of (100) and (110) surfaces due to their lower energies for defect formation, an investigation by the

Pérez-Ramírez group showed opposite-face sensitivity for oxidation and hydrogenation reactions; the latter was favoured over the (111) surface.[235] This was attributed to the lower levels of oxygen vacancies found in CeO_2_(111) planes, as a consequence of the higher energy for defect formation compared with other low index ceria surfaces. The proposed mechanism for acetylene hydrogenation over ceria involves the stabilisation of reactive species by surface oxygen atoms to prevent oligomerisation and thus, a negative correlation between OSC and the rate of acetylene hydrogenation was observed. Since CeO_2_(100) has a much higher propensity for defects and surface oxygen vacancies, a significantly lower hydrogenation activity was reported for ceria cubes. Similar findings were made by Zhou *et al.* whereby enhanced propene and propyne hydrogenation were observed over the (111) surface, accredited to the lower density of oxygen vacancies, along with an increased density of hydroxyl species.[236, 237] Catalytic dephosphorylation over ceria nanostructures was also found to follow the trend (111) > (110) > (100). It was proposed that this dependence may show a correlation with the Lewis acidity of Ce^{4+} cations, although the presence of differing densities of oxygen vacancies made it difficult to fully confirm the role of acidity in the reaction.

In addition to the surface-dependent activity observed in oxidation and hydrogenation reactions, morphologically dependent catalytic activity and selectivity has also been observed for a variety of reactions over ceria-based catalysts, which has been attributed to differences in reactivity and acid-base properties of ceria nanostructures with different exposed surface planes.[238-244] In the formylation of amines using dimethylformamide as the formylation agent, it was found that the (110) facet, exposed in ceria rods, was most active surface for the formylation of benzyl amine to benzyl amide. This was attributed to the increased basicity found in Ce_(110) as a consequence of the *cus* status and higher density of oxygen defects, which can also act as Lewis base sites.[244] A similar trend was observed in the synthesis of α,β-unsaturated ketones *via* C-C coupling of primary alcohols and ketones. Here, the enhanced activity observed over the ceria rods was attributed to a cooperative effect between surface basicity and redox centres.[245]

An investigation into the one-pot synthesis of 1,3-PD *via* Prins condensation and hydrolysis reactions over ceria catalysts showed the (111) surface to be most active for the reaction; a strong correlation between the number of surface oxygen atoms per gram of ceria and the catalytic activity was observed, with 1,3-butanediol yield in the order (111) > (110) > (100).[241] Similar findings were made by Corma and co-workers during an investigation into the phosgene-free synthesis of polyurethanes from dimethyl carbonate (DMC) and diaminotoluene (DAT).[246] As predicted by DFT calculations, selective DMC dissociation occurred selectively over the (111), and to a lesser extent, the (110) surface. Alternatively, over the (100) surface, two undesired DMC dissociation reactions were also possible,

leading to the formation of unwanted by-products and thus reducing the yield of the final N,N'-dicarbamoylated product. A trend of (111) > (110) > (100) was also reported by Snell et al., who investigated the effect of crystal facet on acetic acid ketonization over ceria catalysts.

1.5 Thesis aims

The recent discovery that GLY could be converted to MeOH in a simple one-step process provides a new and sustainable route to the production of MeOH.[27] The MeOH produced could subsequently be used in the biodiesel process to produce FAMEs, thus, converting the major by-product from the process into a starting material and increasing the overall sustainability and economic viability of the process. Whilst it was shown that vaporised aqueous GLY feedstocks could be converted to MeOH over simple metal oxide catalysts, such as MgO and CeO_2, numerous by-products were also detected alongside MeOH. A concern relating to this would be that these by-products could hinder the direct use of MeOH in the transesterification process. Additionally, the preliminary report focussed on the use of highly dilute GLY feedstocks, leading to low levels of catalyst productivity despite the high MeOH product selectivities reported. When more concentrated GLY feedstocks were investigated, no substantial difference in MeOH productivity was reported, despite the potential for significant increases. The highly reactive nature of GLY makes the selective conversion of concentrated GLY feedstocks challenging. However, the vast quantity of GLY produced annually, and the low market value of crude GLY necessitate high levels of catalyst productivity, to ensure economic desirability and industrial relevance.

This thesis aims to further explore the gas phase conversion of GLY to MeOH, with a focus on ceria-based catalysts. The following chapter will describe the methods and techniques used throughout the results chapters. A description of the methods used to prepare the catalysts examined throughout the thesis is given, followed by overviews of the techniques used to characterise said catalysts. Finally, a comprehensive explanation of catalyst testing protocols is provided, detailing the analysis protocol and any calculations used when assessing catalytic activity.

Initially, the use of both MgO and CeO_2 are further explored. Following an investigation into GLY conversions under catalyst free conditions, reaction conditions such as reaction temperature, GLY concentration and reaction time are explored over a basic MgO catalyst. Additional product analysis is performed in order to gain a better understanding of the complex product mixture and close the carbon balance. Similar product analysis is discussed, following reactions with a reducible CeO_2 catalyst. The effect of certain physicochemical properties such as surface area, crystallite size and defect density on product distributions over CeO_2 catalysts are also investigated.

The second results chapter is focussed on the use of nanostructured ceria catalysts with well-defined morphologies for the conversion of GLY to MeOH. CeO_2 nanocrystals with cubic, rod-like and polyhedral morphologies were synthesised, predominantly exposing (100), (110) and (100), and (111) and (100) surface planes, respectively. Comprehensive characterisation of the materials is undertaken to gain a greater understanding of how defect, redox and acid-base properties are affected by morphology, and how this may subsequently influence GLY reactivity. The catalytic activity of the materials is initially explored, followed by studies performed at constant GLY conversion to establish the effect of ceria morphology on both catalytic activity and product selectivity.

Throughout the final results chapter, the use of copper- and cobalt-doped ceria catalysts are investigated. Doped and undoped ceria, prepared by precipitation and citric acid combustion methods, are fully characterised and the effect of the preparation method on the physicochemical properties of the materials is examined. Subsequently, the effect of dopant addition on the product distribution and MeOH space time yield is explored. Furthermore, additional investigations into the feasibility of reducing unwanted by-products, such as aldehydic species, using in-situ generated hydrogen gas is discussed.

Finally, overall conclusions surrounding the use of ceria-based catalysts for the conversion of GLY to MeOH will be given. During this chapter, findings from this thesis will be used to make suggestions for further work to be performed where appropriate in order to further the foundations presented herein.

1.6 References

1. A. J. Ragauskas, C. K. Williams, B. H. Davison, G. Britovsek, J. Cairney, C. A. Eckert, W. J. Frederick, J. P. Hallett, D. J. Leak, C. L. Liotta, J. R. Mielenz, R. Murphy, R. Templer and T. Tschaplinski, *Science*, 2006, **311**, 484-489.
2. A. Guillouzouic-Le Corff, *Energy Economics*, 2018, **75**, 547-559.
3. R. Alquist and L. Kilian, *Journal of Applied Econometrics*, 2010, **25**, 539-573.
4. S. Shafiee and E. Topal, *Energy Policy*, 2009, **37**, 181-189.
5. IRENA, *Renewable Energy Policies in a Time of Transition*, 2018.
6. D. M. Alonso, J. Q. Bond and J. A. Dumesic, *Green Chemistry*, 2010, **12**, 1493-1513.
7. G. Taylor, *Energy Policy*, 2008, **36**, 4406-4409.
8. J. H. Clark, V. Budarin, F. E. I. Deswarte, J. J. E. Hardy, F. M. Kerton, A. J. Hunt, R. Luque, D. J. Macquarrie, K. Milkowski, A. Rodriguez, O. Samuel, S. J. Tavener, R. J. White and A. J. Wilson, *Green Chemistry*, 2006, **8**, 853-860.
9. F. Cherubini, *Energy Conversion and Management*, 2010, **51**, 1412-1421.
10. A. R. C. Morais and R. Bogel-Lukasik, *Sustainable Chemical Processes*, 2013, **1**, 18.
11. C. W. L. R. Lynd, M. Laser, D. Johnson, R. Landucci, *Strategic Biorefinery Analysis: Analysis of Biorefineries*, Report NREL/SR-510-35578, 2005.
12. J. N. Chheda, G. W. Huber and J. A. Dumesic, *Angewandte Chemie International Edition*, 2007, **46**, 7164-7183.
13. R. Rinaldi and F. Schüth, *ChemSusChem*, 2009, **2**, 1096-1107.
14. W. Den, V. K. Sharma, M. Lee, G. Nadadur and R. S. Varma, *Frontiers in Chemistry*, 2018, **6**.
15. F. H. Isikgor and C. R. Becer, *Polymer Chemistry*, 2015, **6**, 4497-4559.

16. A. K. Chandel, V. K. Garlapati, A. K. Singh, F. A. F. Antunes and S. S. da Silva, *Bioresource Technology*, 2018, **264**, 370-381.
17. G. De Bhowmick, A. K. Sarmah and R. Sen, *Bioresource Technology*, 2018, **247**, 1144-1154.
18. H. Rothman, R. Greenshields and F. Rosillo Calle, *The alcohol economy: fuel ethanol and the Brazilian experience*, Frances Pinter (Publishers), London, 1983.
19. V. R. Surisetty, A. K. Dalai and J. Kozinski, *Applied Catalysis A: General*, 2011, **404**, 1-11.
20. F. Dalena, A. Senatore, M. Basile, S. Knani, A. Basile and A. Iulianelli, *Membranes*, 2018, **8**, 98.
21. D. Sheldon, *Johnson Matthey Technology Review*, 2017, **61**, 172-182.
22. K. Ahmad and S. Upadhyayula, *Sustainable Energy & Fuels*, 2019, **3**, 2509-2520.
23. A. Boretti, *International Journal of Hydrogen Energy*, 2013, **38**, 1806-1812.
24. J. Turner, G. Sverdrup, M. K. Mann, P.-C. Maness, B. Kroposki, M. Ghirardi, R. J. Evans and D. Blake, *International Journal of Energy Research*, 2008, **32**, 379-407.
25. T. Werpy and G. Petersen, *Top Value Added Chemicals from Biomass: Volume I -- Results of Screening for Potential Candidates from Sugars and Synthesis Gas*, Report DOE/GO-102004-1992; TRN: US200427%%671 United States 10.2172/15008859 TRN: US200427%%671 NREL English, ; National Renewable Energy Lab., Golden, CO (US), 2004.
26. J. J. Bozell and G. R. Petersen, *Green Chemistry*, 2010, **12**, 539-554.
27. M. H. Haider, N. F. Dummer, D. W. Knight, R. L. Jenkins, M. Howard, J. Moulijn, S. H. Taylor and G. J. Hutchings, *Nature Chemistry*, 2015, **7**, 1028.
28. OECD/FAO, *OECD-FAO Agricultural Outlook 2017-2026*, Paris, 2017.
29. F. Ma and M. A. Hanna, *Bioresource Technology*, 1999, **70**, 1-15.
30. J.-S. Lee and S. Saka, *Bioresource Technology*, 2010, **101**, 7191-7200.
31. G. Vicente, M. Martínez and J. Aracil, *Bioresource Technology*, 2004, **92**, 297-305.
32. M. W. Formo, *Journal of the American Oil Chemists Society*, 1954, **31**, 548-559.
33. C.-H. Liu, C.-C. Huang, Y.-W. Wang, D.-J. Lee and J.-S. Chang, *Applied Energy*, 2012, **100**, 41-46.
34. A. Gog, M. Roman, M. Toşa, C. Paizs and F. D. Irimie, *Renewable Energy*, 2012, **39**, 10-16.
35. B. Norjannah, H. C. Ong, H. H. Masjuki, J. C. Juan and W. T. Chong, *RSC Advances*, 2016, **6**, 60034-60055.
36. T. A. Andrade, M. Errico and K. V. Christensen, *Bioresource Technology*, 2017, **243**, 366-374.
37. L. Fjerbaek, K. V. Christensen and B. Norddahl, *Biotechnology and Bioengineering*, 2009, **102**, 1298-1315.
38. A. Gusniah, H. Veny and F. Hamzah, *Industrial & Engineering Chemistry Research*, 2019, **58**, 581-589.
39. A. Gasparatos, P. Stromberg and K. Takeuchi, *Animal Frontiers*, 2013, **3**, 12-26.
40. R. A. Lee and J.-M. Lavoie, *Animal Frontiers*, 2013, **3**, 6-11.
41. M. Hajjari, M. Tabatabaei, M. Aghbashlo and H. Ghanavati, *Renewable and Sustainable Energy Reviews*, 2017, **72**, 445-464.
42. A. Gaeta-Bernardi and V. Parente, *Renewable Energy*, 2016, **86**, 1422-1432.
43. J. Abbas, S. Hussain, M. J. Iqbal, H. Nadeem, M. Qasim, S. Hina and F. Hafeez, *Environmental Technology*, 2016, **37**, 2082-2087.
44. R. L. Skaggs, A. M. Coleman, T. E. Seiple and A. R. Milbrandt, *Renewable and Sustainable Energy Reviews*, 2018, **82**, 2640-2651.
45. P. Upham, P. Thornley, J. Tomei and P. Boucher, *Journal of Cleaner Production*, 2009, **17**, S37-S45.
46. D. f. Transport, *Renewable Fuel Statistics 2019 Third Provisional Report*, D. f. Transport, 2020.
47. V. K. Mishra and R. Goswami, *Biofuels*, 2018, **9**, 273-289.
48. D. Y. C. Leung, X. Wu and M. K. H. Leung, *Applied Energy*, 2010, **87**, 1083-1095.

49. C. F. Hansen, A. Hernandez, B. P. Mullan, K. Moore, M. Trezona-Murray, R. H. King and J. R. Pluske, *Animal Production Science*, 2009, **49**, 154-161.
50. S. Hu, X. Luo, C. Wan and Y. Li, *Journal of Agricultural and Food Chemistry*, 2012, **60**, 5915-5921.
51. M. S. Ardi, M. K. Aroua and N. A. Hashim, *Renewable and Sustainable Energy Reviews*, 2015, **42**, 1164-1173.
52. M. Pagliaro, R. Ciriminna, H. Kimura, M. Rossi and C. Della Pina, *European Journal of Lipid Science and Technology*, 2009, **111**, 788-799.
53. R. Ciriminna, C. D. Pina, M. Rossi and M. Pagliaro, *European Journal of Lipid Science and Technology*, 2014, **116**, 1432-1439.
54. Z. Gholami, A. Z. Abdullah and K.-T. Lee, *Renewable and Sustainable Energy Reviews*, 2014, **39**, 327-341.
55. M. Rossi, C. Della Pina, M. Pagliaro, R. Ciriminna and P. Forni, *ChemSusChem*, 2008, **1**, 809-812.
56. S. S. Donkin, *Revista Brasileira de Zootecnia*, 2008, **37**, 280-286.
57. X. Luo, X. Ge, S. Cui and Y. Li, *Bioresource Technology*, 2016, **215**, 144-154.
58. G. Bagnato, A. Iulianelli, A. Sanna and A. Basile, *Membranes*, 2017, **7**, 17.
59. J. M. Naranjo, J. A. Posada, J. C. Higuita and C. A. Cardona, *Bioresource Technology*, 2013, **133**, 38-44.
60. S. S. Yazdani and R. Gonzalez, *Current Opinion in Biotechnology*, 2007, **18**, 213-219.
61. J. Kaur, A. K. Sarma, M. K. Jha and P. Gera, *Biotechnology Reports*, 2020, **27**, e00487.
62. F. Yang, M. A. Hanna and R. Sun, *Biotechnology for Biofuels*, 2012, **5**, 13.
63. P. S. Kong, M. K. Aroua and W. M. A. W. Daud, *Renewable and Sustainable Energy Reviews*, 2016, **63**, 533-555.
64. S. C. D'Angelo, A. Dall'Ara, C. Mondelli, J. Pérez-Ramírez and S. Papadokonstantakis, *ACS Sustainable Chemistry & Engineering*, 2018, **6**, 16563-16572.
65. M. R. Nanda, Z. Yuan, W. Qin and C. Xu, *Catalysis Reviews*, 2016, **58**, 309-336.
66. E. S. Vasiliadou and A. A. Lemonidou, *WIREs Energy and Environment*, 2015, **4**, 486-520.
67. D. Sun, Y. Yamada, S. Sato and W. Ueda, *Applied Catalysis B: Environmental*, 2016, **193**, 75-92.
68. M. R. Monteiro, C. L. Kugelmeier, R. S. Pinheiro, M. O. Batalha and A. da Silva César, *Renewable and Sustainable Energy Reviews*, 2018, **88**, 109-122.
69. U. I. Nda-Umar, I. Ramli, Y. H. Taufiq-Yap and E. N. Muhamad, *Catalysts*, 2018, **9**, 15.
70. I. Fatimah, I. Sahroni, G. Fadillah, M. M. Musawwa, T. M. I. Mahlia and O. Muraza, *Energies*, 2019, **12**, 2872.
71. A. Fasolini, D. Cespi, T. Tabanelli, R. Cucciniello and F. Cavani, *Catalysts*, 2019, **9**, 722.
72. S. Bagheri, N. M. Julkapli and W. A. Yehye, *Renewable and Sustainable Energy Reviews*, 2015, **41**, 113-127.
73. G. Dodekatos, S. Schünemann and H. Tüysüz, *ACS Catalysis*, 2018, **8**, 6301-6333.
74. C.-H. Zhou, J. N. Beltramini, Y.-X. Fan and G. Q. Lu, *Chemical Society Reviews*, 2008, **37**, 527-549.
75. B. Katryniok, H. Kimura, E. Skrzynska, J.-S. Girardon, P. Fongarland, M. Capron, R. Ducoulombier, N. Mimura, S. Paul and F. Dumeignil, *Green Chemistry*, 2011, **13**, 1960-1979.
76. B. Katryniok, S. Paul, V. Belliere-Baca, P. Rey and F. Dumeignil, *Green Chemistry*, 2010, **12**, 2079-2098.
77. B. Katryniok, S. Paul and F. Dumeignil, *ACS Catalysis*, 2013, **3**, 1819-1834.
78. C. H. Zhou, H. Zhao, D. S. Tong, L. M. Wu and W. H. Yu, *Catalysis Reviews*, 2013, **55**, 369-453.
79. J. Feng and B. Xu, *Progress in Reaction Kinetics and Mechanism*, 2014, **39**, 1-15.
80. P. D. Vaidya and A. E. Rodrigues, *Chemical Engineering & Technology*, 2009, **32**, 1463-1469.
81. N. H. Tran and G. S. K. Kannangara, *Chemical Society Reviews*, 2013, **42**, 9454-9479.
82. H. Atia, U. Armbruster and A. Martin, *Journal of Catalysis*, 2008, **258**, 71-82.

83. E. Tsukuda, S. Sato, R. Takahashi and T. Sodesawa, *Catalysis Communications*, 2007, **8**, 1349-1353.
84. A. Corma, G. W. Huber, L. Sauvanaud and P. O'Connor, *Journal of Catalysis*, 2008, **257**, 163-171.
85. G. v. B. Joost, H. V. Robertus and J. H. Hero, in *Biodiesel - Feedstocks, Production and Applications*, ed. Z. Fang, 2012, DOI: 10.5772/53691.
86. J. G. van Bennekom, R. H. Venderbosch, D. Assink, K. P. J. Lemmens and H. J. Heeres, *Chemical Engineering Journal*, 2012, **207-208**, 245-253.
87. A. Kostyniuk, D. Bajec and B. Likozar, *Green Chemistry*, 2020, **22**, 753-765.
88. G. G. P. Sabatier, *Compt. Rend.*, 1918, **166**.
89. *France Pat.,* 695,931, 1930.
90. *United States Pat.,* 2,042,224, 1936.
91. *United States Pat.,* 2,558,520, 1951.
92. *United States Pat.,* 5,387,720, 1995.
93. W. Bühler, E. Dinjus, H. J. Ederer, A. Kruse and C. Mas, *The Journal of Supercritical Fluids*, 2002, **22**, 37-53.
94. S.-H. Chai, H.-P. Wang, Y. Liang and B.-Q. Xu, *Green Chemistry*, 2007, **9**, 1130-1136.
95. A. Alhanash, E. F. Kozhevnikova and I. V. Kozhevnikov, *Applied Catalysis A: General*, 2010, **378**, 11-18.
96. I. Martinuzzi, Y. Azizi, J.-F. Devaux, S. Tretjak, O. Zahraa and J.-P. Leclerc, *Chemical Engineering Science*, 2014, **116**, 118-127.
97. A. K. Kinage, P. P. Upare, P. Kasinathan, Y. K. Hwang and J.-S. Chang, *Catalysis Communications*, 2010, **11**, 620-623.
98. D. Hernandez, M. Velasquez, P. Ayrault, D. Lopez, J. J. Fernandez, A. Santamaria and C. Batiot-Dupeyrat, *Applied Catalysis A: General*, 2013, **467**, 315-324.
99. J. Barrault, Y. Pouilloux, J. M. Clacens, C. Vanhove and S. Bancquart, *Catalysis Today*, 2002, **75**, 177-181.
100. C. L. Lima, S. J. S. Vasconcelos, J. M. Filho, B. C. Neto, M. G. C. Rocha, P. Bargiela and A. C. Oliveira, *Applied Catalysis A: General*, 2011, **399**, 50-62.
101. M. Velasquez, A. Santamaria and C. Batiot-Dupeyrat, *Applied Catalysis B: Environmental*, 2014, **160**, 606-613.
102. S. Sato, M. Akiyama, R. Takahashi, T. Hara, K. Inui and M. Yokota, *Applied Catalysis A: General*, 2008, **347**, 186-191.
103. S. Célerier, S. Morisset, I. Batonneau-Gener, T. Belin, K. Younes and C. Batiot-Dupeyrat, *Applied Catalysis A: General*, 2018, **557**, 135-144.
104. M. R. Nimlos, S. J. Blanksby, X. Qian, M. E. Himmel and D. K. Johnson, *The Journal of Physical Chemistry A*, 2006, **110**, 6145-6156.
105. W. Sun, J. Liu, X. Chu, C. Zhang and C. Liu, *Journal of Molecular Structure: THEOCHEM*, 2010, **942**, 38-42.
106. T. Laino, C. Tuma, A. Curioni, E. Jochnowitz and S. Stolz, *The Journal of Physical Chemistry A*, 2011, **115**, 3592-3595.
107. E. Yoda and A. Ootawa, *Applied Catalysis A: General*, 2009, **360**, 66-70.
108. K. Kongpatpanich, T. Nanok, B. Boekfa, M. Probst and J. Limtrakul, *Physical Chemistry Chemical Physics*, 2011, **13**, 6462-6470.
109. Y. Wang, J. Zhou and X. Guo, *RSC Advances*, 2015, **5**, 74611-74628.
110. J. ten Dam and U. Hanefeld, *ChemSusChem*, 2011, **4**, 1017-1034.
111. A. M. Ruppert, K. Weinberg and R. Palkovits, *Angewandte Chemie International Edition*, 2012, **51**, 2564-2601.
112. J. Chaminand, L. a. Djakovitch, P. Gallezot, P. Marion, C. Pinel and C. Rosier, *Green Chemistry*, 2004, **6**, 359-361.
113. M. Schlaf, *Dalton Transactions*, 2006, DOI: 10.1039/B608007C, 4645-4653.
114. C. S. Lee, M. K. Aroua, W. M. A. W. Daud, P. Cognet, Y. Pérès-Lucchese, P. L. Fabre, O. Reynes and L. Latapie, *Renewable and Sustainable Energy Reviews*, 2015, **42**, 963-972.
115. A. Martin, U. Armbruster, I. Gandarias and P. L. Arias, *European Journal of Lipid Science and Technology*, 2013, **115**, 9-27.

116. K. Tomishige, Y. Nakagawa and M. Tamura, *Green Chemistry*, 2017, **19**, 2876-2924.
117. H. Zhao, L. Zheng, X. Li, P. Chen and Z. Hou, *Catalysis Today*, 2019, DOI: https://doi.org/10.1016/j.cattod.2019.03.011.
118. D. Sun, Y. Yamada and S. Sato, *Applied Catalysis A: General*, 2014, **475**, 63-68.
119. M. Akiyama, S. Sato, R. Takahashi, K. Inui and M. Yokota, *Applied Catalysis A: General*, 2009, **371**, 60-66.
120. C.-W. Chiu, A. Tekeei, W. R. Sutterlin, J. M. Ronco and G. J. Suppes, *AIChE Journal*, 2008, **54**, 2456-2463.
121. D. G. C. Montassier, J. Barbier, J. P. Boitiaux, *Bull. Soc. Chim. Fr.*, 1989, **2**, 148-1585.
122. C. Montassier, J. C. Ménézo, J. Moukolo, J. Naja, L. C. Hoang, J. Barbier and J. P. Boitiaux, *Journal of Molecular Catalysis*, 1991, **70**, 65-84.
123. Y. Amada, Y. Shinmi, S. Koso, T. Kubota, Y. Nakagawa and K. Tomishige, *Applied Catalysis B: Environmental*, 2011, **105**, 117-127.
124. Y. Nakagawa, Y. Shinmi, S. Koso and K. Tomishige, *Journal of Catalysis*, 2010, **272**, 191-194.
125. C. Montassier, J. C. Ménézo, L. C. Hoang, C. Renaud and J. Barbier, *Journal of Molecular Catalysis*, 1991, **70**, 99-110.
126. S. Wang, K. Yin, Y. Zhang and H. Liu, *ACS Catalysis*, 2013, **3**, 2112-2121.
127. S. Zhu, X. Gao, Y. Zhu and Y. Li, *Green Chemistry*, 2016, **18**, 782-791.
128. S. Zhu, X. Gao, Y. Zhu, W. Fan, J. Wang and Y. Li, *Catalysis Science & Technology*, 2015, **5**, 1169-1180.
129. S. Zhu, X. Gao, Y. Zhu, Y. Zhu, H. Zheng and Y. Li, *Journal of Catalysis*, 2013, **303**, 70-79.
130. S. K. Tanielyan, N. Marin, G. Alvez, R. Bhagat, B. Miryala, R. L. Augustine and S. R. Schmidt, *Organic Process Research & Development*, 2014, **18**, 1419-1426.
131. J. Hu, Y. Fan, Y. Pei, M. Qiao, K. Fan, X. Zhang and B. Zong, *ACS Catalysis*, 2013, **3**, 2280-2287.
132. M. G. Musolino, L. A. Scarpino, F. Mauriello and R. Pietropaolo, *Green Chemistry*, 2009, **11**, 1511-1513.
133. M. G. Musolino, L. A. Scarpino, F. Mauriello and R. Pietropaolo, *ChemSusChem*, 2011, **4**, 1143-1150.
134. R. B. Mane and C. V. Rode, *Organic Process Research & Development*, 2012, **16**, 1043-1052.
135. I. Gandarias, P. L. Arias, J. Requies, M. El Doukkali and M. B. Güemez, *Journal of Catalysis*, 2011, **282**, 237-247.
136. I. Gandarias, P. L. Arias, S. G. Fernández, J. Requies, M. El Doukkali and M. B. Güemez, *Catalysis Today*, 2012, **195**, 22-31.
137. I. Furikado, T. Miyazawa, S. Koso, A. Shimao, K. Kunimori and K. Tomishige, *Green Chemistry*, 2007, **9**, 582-588.
138. T. Miyazawa, Y. Kusunoki, K. Kunimori and K. Tomishige, *Journal of Catalysis*, 2006, **240**, 213-221.
139. E. van Ryneveld, A. S. Mahomed, P. S. van Heerden, M. J. Green and H. B. Friedrich, *Green Chemistry*, 2011, **13**, 1819-1827.
140. M. L. Shozi, V. D. B. C. Dasireddy, S. Singh, P. Mohlala, D. J. Morgan and H. B. Friedrich, *ACS Sustainable Chemistry & Engineering*, 2016, **4**, 5752-5760.
141. 2009.
142. T. Montini, M. Melchionna, M. Monai and P. Fornasiero, *Chemical Reviews*, 2016, **116**, 5987-6041.
143. A. Trovarelli, *Catalysis Reviews*, 1996, **38**, 439-520.
144. L. Vivier and D. Duprez, *ChemSusChem*, 2010, **3**, 654-678.
145. W. Huang and Y. Gao, *Catalysis Science & Technology*, 2014, **4**, 3772-3784.
146. C. Sun, H. Li and L. Chen, *Energy & Environmental Science*, 2012, **5**, 8475-8505.
147. Z.-A. Qiao, Z. Wu and S. Dai, *ChemSusChem*, 2013, **6**, 1821-1833.
148. L. Fan, C. Wang, M. Chen and B. Zhu, *Journal of Power Sources*, 2013, **234**, 154-174.
149. M. Mogensen, N. M. Sammes and G. A. Tompsett, *Solid State Ionics*, 2000, **129**, 63-94.
150. J. Paier, C. Penschke and J. Sauer, *Chemical Reviews*, 2013, **113**, 3949-3985.

151. D. J. M. Bevan, *Journal of Inorganic and Nuclear Chemistry*, 1955, **1**, 49-59.
152. A. TROVARELLI, in *Catalysis by Ceria and Related Materials*, DOI: 10.1142/9781860949654_0002, pp. 15-50.
153. M. Yashima, D. Ishimura, Y. Yamaguchi, K. Ohoyama and K. Kawachi, *Chemical Physics Letters*, 2003, **372**, 784-787.
154. M. Zinkevich, D. Djurovic and F. Aldinger, *Solid State Ionics*, 2006, **177**, 989-1001.
155. J. Faber, M. A. Seitz and M. H. Mueller, *Journal of Physics and Chemistry of Solids*, 1976, **37**, 903-907.
156. R. J. Panlener, R. N. Blumenthal and J. E. Garnier, *Journal of Physics and Chemistry of Solids*, 1975, **36**, 1213-1222.
157. R. D. Shannon, *Acta Crystallographica Section A*, 1976, **32**, 751-767.
158. M. Yashima, in *Catalysis by Ceria and Related Materials*, DOI: 10.1142/9781848169647_0001, pp. 1-45.
159. L. Chen, P. Fleming, V. Morris, J. D. Holmes and M. A. Morris, *The Journal of Physical Chemistry C*, 2010, **114**, 12909-12919.
160. Q. Jiang, L. H. Liang and D. S. Zhao, *The Journal of Physical Chemistry B*, 2001, **105**, 6275-6277.
161. H. C. Yao and Y. F. Y. Yao, *Journal of Catalysis*, 1984, **86**, 254-265.
162. E. Aneggi, M. Boaro, C. d. Leitenburg, G. Dolcetti and A. Trovarelli, *Journal of Alloys and Compounds*, 2006, **408-412**, 1096-1102.
163. S. Bernal, J. J. Calvino, G. A. Cifredo and J. M. Rodriguez-Izquierdo, *The Journal of Physical Chemistry*, 1995, **99**, 11794-11796.
164. J. El Fallah, S. Boujana, H. Dexpert, A. Kiennemann, J. Majerus, O. Touret, F. Villain and F. Le Normand, *The Journal of Physical Chemistry*, 1994, **98**, 5522-5533.
165. F. Giordano, A. Trovarelli, C. de Leitenburg, G. Dolcetti and M. Giona, *Industrial & Engineering Chemistry Research*, 2001, **40**, 4828-4835.
166. F. Giordano, A. Trovarelli, C. de Leitenburg and M. Giona, *Journal of Catalysis*, 2000, **193**, 273-282.
167. Y. Sun, C. Li, I. Djerdj, O. Khalid, P. Cop, J. Sann, T. Weber, S. Werner, K. Turke, Y. Guo, B. M. Smarsly and H. Over, *Catalysis Science & Technology*, 2019, **9**, 2163-2172.
168. H. Li, G. Lu, Y. Wang, Y. Guo and Y. Guo, *Catalysis Communications*, 2010, **11**, 946-950.
169. S. Meiqing, W. Xinquan, A. Yuan, W. Duan, Z. Minwei and W. Jun, *Journal of Rare Earths*, 2007, **25**, 48-52.
170. R. Heinzmann, I. Issac, J.-P. Eufinger, G. Ulbrich, M. Lerch, J. Janek and S. Indris, *The Journal of Physical Chemistry C*, 2016, **120**, 8568-8577.
171. K. Yashiro, T. Suzuki, A. Kaimai, H. Matsumoto, Y. Nigara, T. Kawada, J. Mizusaki, J. Sfeir and J. Van herle, *Solid State Ionics*, 2004, **175**, 341-344.
172. L. Zhou, X. Li, Z. Yao, Z. Chen, M. Hong, R. Zhu, Y. Liang and J. Zhao, *Scientific Reports*, 2016, **6**, 23900.
173. F. Yang, J. Wei, W. Liu, J. Guo and Y. Yang, *Journal of Materials Chemistry A*, 2014, **2**, 5662-5667.
174. P. Venkataswamy, K. N. Rao, D. Jampaiah and B. M. Reddy, *Applied Catalysis B: Environmental*, 2015, **162**, 122-132.
175. D. Mukherjee, B. G. Rao and B. M. Reddy, *Applied Catalysis B: Environmental*, 2016, **197**, 105-115.
176. E. Sartoretti, C. Novara, F. Giorgis, M. Piumetti, S. Bensaid, N. Russo and D. Fino, *Scientific Reports*, 2019, **9**, 3875.
177. M. Konsolakis, M. Lykaki, S. Stefa, S. A. C. Carabineiro, G. Varvoutis, E. Papista and G. E. Marnellos, *Nanomaterials*, 2019, **9**, 1739.
178. C. Riley, A. De La Riva, S. Zhou, Q. Wan, E. Peterson, K. Artyushkova, M. D. Farahani, H. B. Friedrich, L. Burkemper, N.-V. Atudorei, S. Lin, H. Guo and A. Datye, *ChemCatChem*, 2019, **11**, 1526-1533.
179. C. Riley, S. Zhou, D. Kunwar, A. De La Riva, E. Peterson, R. Payne, L. Gao, S. Lin, H. Guo and A. Datye, *Journal of the American Chemical Society*, 2018, **140**, 12964-12973.
180. T. X. T. Sayle, S. C. Parker and C. R. A. Catlow, *Surface Science*, 1994, **316**, 329-336.

181. J. Conesa, *Surface Science*, 1995, **339**, 337-352.
182. C. Binet, M. Daturi and J.-C. Lavalley, *Catalysis Today*, 1999, **50**, 207-225.
183. H. A. Benesi and B. H. C. Winquist, in *Advances in Catalysis*, eds. D. D. Eley, H. Pines and P. B. Weisz, Academic Press, 1979, vol. 27, pp. 97-182.
184. *Catalysis Today*, 1989, **5**, 1-120.
185. H. Pines, in *The Chemistry of Catalytic Hydrocarbon Conversions*, ed. H. Pines, Academic Press, 1981, DOI: https://doi.org/10.1016/B978-0-12-557160-9.50006-X, pp. 1-122.
186. T. Kozo and H. Hideshi, *Chemistry Letters*, 1976, **5**, 625-626.
187. E. Selli and L. Forni, *Microporous and Mesoporous Materials*, 1999, **31**, 129-140.
188. A. Auroux and A. Gervasini, *The Journal of Physical Chemistry*, 1990, **94**, 6371-6379.
189. M. C. Kung and H. H. Kung, *Catalysis Reviews*, 1985, **27**, 425-460.
190. S. Carre, B. Tapin, N. S. Gnep, R. Revel and P. Magnoux, *Applied Catalysis A: General*, 2010, **372**, 26-33.
191. M. Guisnet, in *Studies in Surface Science and Catalysis*, eds. B. Imelik, C. Naccache, G. Coudurier, Y. B. Taarit and J. C. Vedrine, Elsevier, 1985, vol. 20, pp. 283-297.
192. T. Yamaguchi, N. Ikeda, H. Hattori and K. Tanabe, *Journal of Catalysis*, 1981, **67**, 324-330.
193. D. Martin and D. Duprez, *Journal of Molecular Catalysis A: Chemical*, 1997, **118**, 113-128.
194. J. C. Lavalley, *Catalysis Today*, 1996, **27**, 377-401.
195. M. Tamura, K.-i. Shimizu and A. Satsuma, *Applied Catalysis A: General*, 2012, **433-434**, 135-145.
196. H. Metiu, S. Chrétien, Z. Hu, B. Li and X. Sun, *The Journal of Physical Chemistry C*, 2012, **116**, 10439-10450.
197. P. W. Tasker, *Journal of Physics C: Solid State Physics*, 1979, **12**, 4977-4984.
198. H.-X. Mai, L.-D. Sun, Y.-W. Zhang, R. Si, W. Feng, H.-P. Zhang, H.-C. Liu and C.-H. Yan, *The Journal of Physical Chemistry B*, 2005, **109**, 24380-24385.
199. Tana, M. Zhang, J. Li, H. Li, Y. Li and W. Shen, *Catalysis Today*, 2009, **148**, 179-183.
200. L. Torrente-Murciano, A. Gilbank, B. Puertolas, T. Garcia, B. Solsona and D. Chadwick, *Applied Catalysis B: Environmental*, 2013, **132-133**, 116-122.
201. T. J. Fisher, Y. Zhou, T.-S. Wu, M. Wang, Y.-L. Soo and C. L. Cheung, *Nanoscale*, 2019, **11**, 4552-4561.
202. S. Agarwal, X. Zhu, E. J. M. Hensen, L. Lefferts and B. L. Mojet, *The Journal of Physical Chemistry C*, 2014, **118**, 4131-4142.
203. K. Zhou, X. Wang, X. Sun, Q. Peng and Y. Li, *Journal of Catalysis*, 2005, **229**, 206-212.
204. X. Liu, K. Zhou, L. Wang, B. Wang and Y. Li, *Journal of the American Chemical Society*, 2009, **131**, 3140-3141.
205. J. Lv, Y. Shen, L. Peng, X. Guo and W. Ding, *Chemical Communications*, 2010, **46**, 5909-5911.
206. Z. Yang, K. Zhou, X. Liu, Q. Tian, D. Lu and S. Yang, *Nanotechnology*, 2007, **18**, 185606.
207. W. Zhang, X. Niu, L. Chen, F. Yuan and Y. Zhu, *Scientific Reports*, 2016, **6**, 29062.
208. M. Baudin, M. Wójcik and K. Hermansson, *Surface Science*, 2000, **468**, 51-61.
209. T. Désaunay, A. Ringuedé, M. Cassir, F. Labat and C. Adamo, *Surface Science*, 2012, **606**, 305-311.
210. M. Molinari, S. C. Parker, D. C. Sayle and M. S. Islam, *The Journal of Physical Chemistry C*, 2012, **116**, 7073-7082.
211. M. Nolan, *Chemical Physics Letters*, 2010, **499**, 126-130.
212. M. Nolan, S. Grigoleit, D. C. Sayle, S. C. Parker and G. W. Watson, *Surface Science*, 2005, **576**, 217-229.
213. N. V. Skorodumova, M. Baudin and K. Hermansson, *Physical Review B*, 2004, **69**, 075401.
214. Z. Wu, M. Li, J. Howe, H. M. Meyer and S. H. Overbury, *Langmuir*, 2010, **26**, 16595-16606.
215. C. T. Nottbohm and C. Hess, *Catalysis Communications*, 2012, **22**, 39-42.

216. T. Taniguchi, T. Watanabe, N. Sugiyama, A. K. Subramani, H. Wagata, N. Matsushita and M. Yoshimura, *The Journal of Physical Chemistry C*, 2009, **113**, 19789-19793.
217. M. Guo, J. Lu, Y. Wu, Y. Wang and M. Luo, *Langmuir*, 2011, **27**, 3872-3877.
218. I. Kosacki, T. Suzuki, H. U. Anderson and P. Colomban, *Solid State Ionics*, 2002, **149**, 99-105.
219. J. E. Spanier, R. D. Robinson, F. Zhang, S.-W. Chan and I. P. Herman, *Physical Review B*, 2001, **64**, 245407.
220. T. Désaunay, G. Bonura, V. Chiodo, S. Freni, J. P. Couzinié, J. Bourgon, A. Ringuedé, F. Labat, C. Adamo and M. Cassir, *Journal of Catalysis*, 2013, **297**, 193-201.
221. Z. Wu, A. K. P. Mann, M. Li and S. H. Overbury, *The Journal of Physical Chemistry C*, 2015, **119**, 7340-7350.
222. R. Si and M. Flytzani-Stephanopoulos, *Angewandte Chemie International Edition*, 2008, **47**, 2884-2887.
223. H. Wang, L. Zhang, M. Li, Y. Liu and X. Bai, *Journal of Rare Earths*, 2013, **31**, 565-571.
224. V. M. Gonzalez-DelaCruz, J. P. Holgado, R. Pereñíguez and A. Caballero, *Journal of Catalysis*, 2008, **257**, 307-314.
225. I. I. Soykal, B. Bayram, H. Sohn, P. Gawade, J. T. Miller and U. S. Ozkan, *Applied Catalysis A: General*, 2012, **449**, 47-58.
226. T. Guo, J. Du and J. Li, *Journal of Materials Science*, 2016, **51**, 10917-10925.
227. B. Lin, Y. Liu, L. Heng, J. Ni, J. Lin and L. Jiang, *Catalysis Communications*, 2017, **101**, 15-19.
228. X.-S. Huang, H. Sun, L.-C. Wang, Y.-M. Liu, K.-N. Fan and Y. Cao, *Applied Catalysis B: Environmental*, 2009, **90**, 224-232.
229. Z. Wu, M. Li and S. H. Overbury, *Journal of Catalysis*, 2012, **285**, 61-73.
230. B. Liu, W. Li, W. Song and J. Liu, *Physical Chemistry Chemical Physics*, 2018, **20**, 16045-16059.
231. S. Liu, X. Wu, W. Liu, W. Chen, R. Ran, M. Li and D. Weng, *Journal of Catalysis*, 2016, **337**, 188-198.
232. E. Aneggi, D. Wiater, C. de Leitenburg, J. Llorca and A. Trovarelli, *ACS Catalysis*, 2014, **4**, 172-181.
233. L. Wang, Y. Wang, Y. Zhang, Y. Yu, H. He, X. Qin and B. Wang, *Catalysis Science & Technology*, 2016, **6**, 4840-4848.
234. J. M. López, A. L. Gilbank, T. García, B. Solsona, S. Agouram and L. Torrente-Murciano, *Applied Catalysis B: Environmental*, 2015, **174-175**, 403-412.
235. G. Vilé, S. Colussi, F. Krumeich, A. Trovarelli and J. Pérez-Ramírez, *Angewandte Chemie International Edition*, 2014, **53**, 12069-12072.
236. E. W. Zhao, Y. Xin, H. E. Hagelin-Weaver and C. R. Bowers, *ChemCatChem*, 2016, **8**, 2197-2201.
237. E. W. Zhao, H. Zheng, R. Zhou, H. E. Hagelin-Weaver and C. R. Bowers, *Angewandte Chemie International Edition*, 2015, **54**, 14270-14275.
238. A. K. P. Mann, Z. Wu, F. C. Calaza and S. H. Overbury, *ACS Catalysis*, 2014, **4**, 2437-2448.
239. R. W. Snell, S. H. Hakim, J. A. Dumesic and B. H. Shanks, *Applied Catalysis A: General*, 2013, **464-465**, 288-295.
240. L. Geng, J. Song, Y. Zhou, Y. Xie, J. Huang, W. Zhang, L. Peng and G. Liu, *Chemical Communications*, 2016, **52**, 13495-13498.
241. Y. Wang, F. Wang, Q. Song, Q. Xin, S. Xu and J. Xu, *Journal of the American Chemical Society*, 2013, **135**, 1506-1515.
242. Z. Zhang, Y. Wang, M. Wang, J. Lü, L. Li, Z. Zhang, M. Li, J. Jiang and F. Wang, *Chinese Journal of Catalysis*, 2015, **36**, 1623-1630.
243. Z. Wu, M. Li, D. R. Mullins and S. H. Overbury, *ACS Catalysis*, 2012, **2**, 2224-2234.
244. Y. Wang, F. Wang, C. Zhang, J. Zhang, M. Li and J. Xu, *Chemical Communications*, 2014, **50**, 2438-2441.
245. Z. Zhang, Y. Wang, M. Wang, J. Lu, C. Zhang, L. Li, J. Jiang and F. Wang, *Catalysis Science & Technology*, 2016, **6**, 1693-1700.

246. S. Laursen, D. Combita, A. B. Hungría, M. Boronat and A. Corma, *Angewandte Chemie International Edition*, 2012, **51**, 4190-4193.

Chapter 2

Experimental

This chapter details the experimental methods and procedures used throughout this thesis. A list of all chemicals used within this thesis is provided, followed by descriptions of the catalyst preparation methods utilised. Following on from this, explanations of the principles underpinning the characterisation techniques used are provided, alongside details of the experimental protocols. Finally, details surrounding the catalyst testing protocol are given and the relevant analytical techniques and calculations used to assess catalytic activity are presented.

2.1 Materials

The following chemicals, including their supplier and purity, were used throughout this work:

Table 1. The chemicals used throughout this thesis, with respective suppliers and purity levels.

Chemical	***Supplier***	***Purity***
Catalyst preparation		
Magnesium hydroxide	Sigma Aldrich	≥ 99 %
Cerium(III) nitrate hexahydrate	Sigma Aldrich	99.99 %
Ammonium hydroxide	Sigma Aldrich	28.0 - 30.0 % NH_3 basis
Sodium hydroxide	Fisher Scientific	99.7 %
Sodium carbonate	Sigma Aldrich	> 99
Citric acid	Sigma Aldrich	≥ 99.5 %
Copper(II) nitrate hemi(pentahydrate)	Sigma Aldrich	≥ 99.99 %
Cobalt(II) nitrate hexahydrate	Sigma Aldrich	99.999 %
Ethanol	Sigma Aldrich	99.8 %
Catalyst testing		
Silicon carbide	Sigma Aldrich	≥ 97.5 %
Acetaldehyde	Sigma Aldrich	> 99.5 %
Propionaldehyde	Sigma Aldrich	≥ 98 %
Acetone	Sigma Aldrich	≥ 99.9 %
Acrolein	Sigma Aldrich	≥ 99 %
Butyraldehyde	Sigma Aldrich	99 %
Methanol	Sigma Aldrich	≥ 99.9 %
2-propanol	Sigma Aldrich	> 99.5 %
Ethanol	Sigma Aldrich	≥99.5 %
2,3-butanedione	Sigma Aldrich	97 %
2-butanol	Sigma Aldrich	99.8 %
1-propanol	Sigma Aldrich	≥ 99.9 %
3-hexanone	Sigma Aldrich	98 %

2-hexanone	Sigma Aldrich	98 %
2-methyl-1-propanol	Sigma Aldrich	99.5 %
Allyl alcohol	Sigma Aldrich	≥ 99 %
Cyclopentanone	Sigma Aldrich	≥ 99 %
Hydroxyacetone	Sigma Aldrich	90 %
3-ethoxy-1-propanol	Sigma Aldrich	97 %
Acetic acid	Sigma Aldrich	≥ 99.7
Glycidol	Sigma Aldrich	96 %
Propionic acid	Sigma Aldrich	≥ 99.5 %
1,2-propanediol	Sigma Aldrich	≥ 99.5 %
Ethylene glycol	Sigma Aldrich	≥ 99 %
1,3-propanediol	Sigma Aldrich	≥ 99.6 %
Phenol	Sigma Aldrich	≥ 99.5 %
Glycerol	Sigma Aldrich	≥ 99.5 %
Acetaldehyde in helium (1000 ppm)	BOC	-
CO_2	BOC	> 99.99 %
CO	BOC	> 99.99 %
Argon	BOC	99.998 %

2.2 Catalyst preparation

2.2.1 MgO by reflux

The magnesium oxide catalyst used in Chapter 3 was prepared by a reflux method, in accordance with that previously reported by Haider *et al.*,[1] from commercially available magnesium hydroxide. Briefly, $Mg(OH)_2$ (*ca.* 2 g)was calcined under static air at 450 °C (10 °C min^{-1}) for 24 hours to generate magnesium oxide. This was then refluxed in deionised water (15 mL g^{-1}) at 110 °C for 3 hours to form a slurry which was dried at 110 °C for 24 hours. A second calcination step (600 °C, 10 °C min^{-1}, 3 hours, 100 mL min^{-1} N_2 flow) was then utilised to obtain the final oxide catalyst.

2.2.2 Ceria by co-precipitation

The ceria catalysts used in Chapter 3 were obtained by a precipitation method. $Ce(NO_3)_3{\cdot}6H_2O$ (20 mmol) was dissolved in D.I. water (200 mL) and held at a temperature of 80 °C. Ammonium hydroxide was slowly added to the Ce^{3+} solution until pH 9 was reached, at which point the solid was immediately recovered by vacuum filtration and thoroughly washed with warm D.I. water (500 mL) and ethanol (200 mL) before being dried at 110 °C for 16 hours. The final catalyst was obtained by calcination under static air at 400, 500, 600 or 700 °C (10 °C min^{-1}, 3 hours, static air).

2.2.3 Ceria nanostructures by hydrothermal

The ceria nanostructures used in Chapter 4 were prepared in accordance with the hydrothermal synthesis reported by Yan and co-workers.[2] Briefly, $Ce(NO_3)_3{\cdot}6H_2O$ (10 mmol) was dissolved in D.I. water (50 mL). A sodium hydroxide solution of appropriate concentration (150 mL) was rapidly added to the Ce^{3+} precursor solution giving a gel-like

precipitate which was vigorously stirred at room temperature for 10 minutes. The suspension (total volume 200 mL) was transferred to a PTFE-lined steel autoclave (total capacity of 300 mL) and heated under autogenous pressure at the appropriate temperature for the given morphology. Once fully cooled, the precipitates were collected by centrifugation, washed thoroughly three times with D.I. water (1500 mL) and once with ethanol (250 mL), dried *in vacuo* (80 °C; 15 hours) and finally calcined in static air at 400 °C (10 °C min^{-1}, 4 hours). The synthesis temperature and concentration of NaOH was varied dependant on desired morphology (rods: [NaOH] = 9 M, T = 100 °C; cubes: [NaOH] = 9 M, T = 180 °C; polyhedra: [NaOH] = 0.13 M, T = 100 °C).

2.2.4 Ceria and doped ceria by co-precipitation

Ceria and doped ceria catalysts used throughout Chapter 5 were prepared through a co-precipitation method. $Ce(NO_3)_3 \cdot 6H_2O$, $Cu(NO_3)_2 \cdot 2.5H_2O$, and $Co(NO_3)_2 \cdot 6H_2O$ solutions were prepared with D.I. water (0.25M). For ceria 250 mL of cerium nitrate solution was used; for the doped ceria, a total volume of 250 mL was used with volumetric ratios calculated to achieve a dopant concentration of 10 mol.%. The nitrate solutions were preheated to 60 °C before a sodium carbonate solution (1M) was added dropwise as a precipitating agent, until pH 9 was reached. The mixture was left aging at pH 9 for 1 hour at 60 °C. The precipitate was filtered under vacuum, washed with warm D.I. water (1500 mL) and left to dry for 16 hours in vacuo; after this time the solid was ground to a fine powder before being calcined at 500 °C for 4 hours under flowing air (10 °C min^{-1}).

2.3 Catalyst characterisation

2.3.1 X-Ray Diffraction (XRD)

X-ray diffraction (XRD) is a non-destructive technique, widely employed in the field of heterogeneous catalysis, which provides information on the crystallographic nature of a material. A crystalline material is a solid structure consisting of atoms, molecules or ions, with a regular geometrical arrangement, which is repeated indefinitely in the three dimensions (crystal or Bravais lattice). Lattice planes of a Bravais crystal can be described as planes whereby periodic intersections with the lattice occur and contain at least three noncollinear Bravais lattice points. All lattice planes can be described by Miller indices, given in the form (*hkl*). Interatomic distances in crystals are typically on the Ångstrom scale and X-rays possess wavelengths in the Ångstrom range. These X-rays are sufficiently energetic to probe internal crystal structures.[3] Since the wavelength of X-ray radiation is comparable to the periodic spacings in a lattice, diffraction occurs as the X-rays are reflected by the crystal planes producing a constructive interference pattern which provides structural information about the sample. XRD is the elastic (Thomson) scattering of X-ray photons by atoms or ions in a crystal lattice. Constructive interference relies on scattered X-rays which are in phase (Figure 1), and can only be achieved when the Bragg equation

(equation 1) is fulfilled. Since constructive interference only occurs when the conditions for the Bragg equation are satisfied, diffraction occurs only under these conditions.[4]

$$n\lambda = 2d_{hkl}sin\theta \quad \text{Eq. 1}$$

Where n = an integer representing reflection order; λ is the wavelength of electromagnetic radiation; d_{hkl} = lattice spacing and θ = diffraction angle.

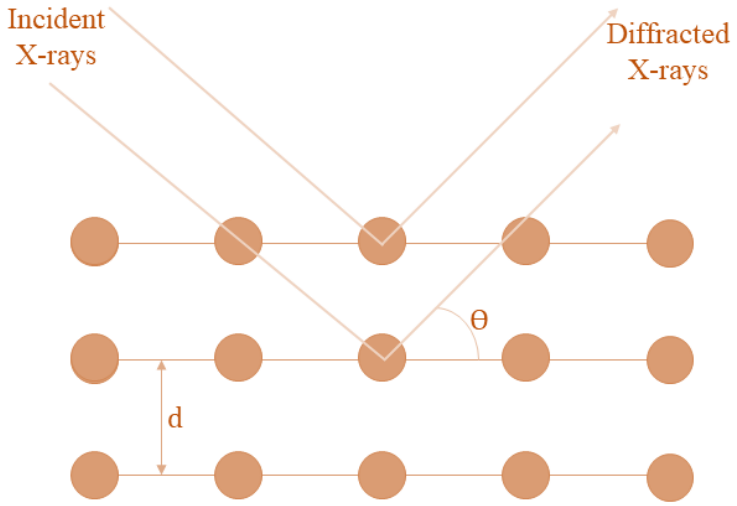

Figure 7. X-ray diffraction by a crystalline sample.[3]

Powder XRD (PXRD) is commonly used in the study of heterogeneous catalysts. In general, PXRD analysis is carried out by exposing the sample to a monochromatic X-ray source and detecting the resulting diffracted X-rays. Typically, the X-rays are produced by bombarding a metal target, such as copper, with high energy electrons generated from a hot tungsten filament and accelerated with a high voltage. When these electrons possess sufficient energy to eject the inner shell electrons of the copper metal, X-rays are produced. These X-rays pass through a monochromator where all wavelengths except Kα radiation are filtered out, resulting in the required monochromatic X-ray source. The X-rays then hit the sample and are scattered as previously described, with a peak in intensity observed when the Bragg equation is satisfied; constructive interference occurs. By maintaining a stationary X-ray source and using a movable detector to measure the angle at which constructive interference occurs (θ), the lattice spacing of the crystallite can be calculated in accordance with the Bragg relationship. For this, samples are typically rotated to increase the probability that the reflected X-rays are detected. PXRD patterns are collected over a range of 2θ angles. Each different crystalline solid has a unique diffraction pattern (diffractogram), which can be considered as a fingerprint for that material; phase identification can be performed by matching obtained diffraction patterns to International Centre for Diffraction Data (ICDD) database. As d_{hkl} (the lattice spacing) can be determined from PXRD, it is possible to obtain information about the lattice parameter of a material. The relationship

between lattice spacing and lattice parameter is dependent on crystal structure, but for a cubic structure such as CeO_2 it can be calculated with equation 2:

$$\frac{1}{d^2} = \frac{h^2 + k^2 + l^2}{a^2} \quad \text{Eq. 2}$$

Whereby d = lattice spacing; h,k and l = corresponding Miller indices for the given lattice spacing; a = lattice parameter.

The lattice parameter describes the dimensions of the unit cell in a solid material. Deviation of the lattice parameter from expected values can indicate the incorporation of an impurity or dopant material into the parent lattice. Additionally, variations in lattice parameter can indicate lattice contraction and expansion, which can provide further information into structural properties. The width of the diffraction peaks can provide information on the dimensions of the reflecting planes. As crystallite sizes decrease, the peaks broaden due to incomplete destructive interference in scattering directions where the X-rays are out of phase.[5] The Scherrer (equation 3) relates this line width to the crystallite size (equation 2):

$$L = \frac{K\lambda}{B cos\theta} \quad \text{Eq. 3}$$

Whereby L = is a measure of the crystallite size in the direction perpendicular to the reflecting plane; K = a constant based on crystallite shape (generally 0.9 - 1); λ = the X-ray wavelength; β = the peak width and θ = the angle between the beam and the normal on the reflecting plane.

The Scherrer equation can be employed for deriving crystallite sizes from XRD data. However, it should be noted that the error associated with the measurement significantly increases as the peaks become ill-defined. Particles generally < 5 nm cannot be detected and measured as the peaks are so broad, they merge into the background signal.

The strain and disorder in the sample and x-ray source need to be considered. By using an internal Si standard, the contribution from the x-ray source is noted and adjusted in the line broadening constant. The samples' lattice strain in the sample is calculated using equation 4:

$$Lattice\ strain = \frac{B}{4tan\theta} \quad \text{Eq. 4}$$

Where B = $\sqrt{\left(B_{obs}^2 - B_{std}^2\right)}$; B_{std} = peak broadening due to instrumental effects; B_{obs} = peak width and θ = peak position.

2.3.1.1 Experimental

Powder X-ray diffraction (XRD) analysis of the catalysts was carried out on a PANalytical X'pert Pro powder diffractometer (Malvern Panalytical, Malvern, UK) using a Cu source operated at 40 KeV and 40 mA with a Ge (111) monochromator to select $K_{\alpha 1}$ X-rays. Patterns were analysed from measurements taken over the 2θ angular range 05 – 80° (step size of 0.016°). Phase identification was performed by comparison of obtained diffractograms to entries in the International Centre for Diffraction Data (ICDD) database. Crystallite sizes and lattice strain were calculated with reference to a Si standard.

2.3.2 Thermogravimetric analysis – differential thermal analysis (TGA-DTA)

Thermogravimetric analysis (TGA) is a widely used characterisation tool that involves precisely measuring the mass of a sample as it is exposed to a specific environment. Typically, it involves the precise measurement of sample mass as a sample is heated at a well-controlled heating rate, under a given atmosphere. For example, the change in the physical or chemical state of a sample can be measured as temperature is increased under an inert, oxidising or reducing environment. This type of analysis can be used to model calcination procedures and establish when the decomposition of a sample has taken place. Generally, the data is represented as mass loss as a function of temperature, allowing identification of water desorption, complete decomposition or reduction temperatures to be identified. Furthermore, when the TGA analysis is carried out with an inert reference, the heat change can be measured in the sample relative to the reference. This is known as differential thermal analysis, DTA. DTA allows the determination of whether a process is exo- or endothermic and enables further insights to be made into the nature of the observed mass loss. In some applications, TGA can be coupled with IR spectroscopy and/or mass spectrometry to identify and quantify desorption products.

2.3.2.1 Experimental

TGA was performed using a Setaram Labsys 1600 in conjunction to DTA. 10-60 mg of the sample was loaded into alumina crucibles, heated to 800 °C (at 1 or 10 °C min^{-1}) in a flow of synthetic air or N_2 (50 mL min^{-1}) and held for 10 minutes before cooling. For each specified run, a blank run was first carried out and the results were subtracted from the relevant data to remove buoyancy effects. TGA profiles are expressed as the percentage of initial mass placed into the crucible remaining at a given temperature.

2.3.3 N_2 physisorption

N_2 physisorption is an essential tool when characterising solid materials used for catalytic applications. It can provide the user with information about the structural and textural properties of a material. Specific surface area (SSA) can be crucial to catalytic activity and is

typically determined in accordance with the Brunauer–Emmett–Teller (BET) method.[6] The technique is based on N_2 adsorption and is described below.

Physisorption is a slightly exothermic process, governed by Van der Waals' interactions and occurs over mono- and multi-layers of adsorbates. This is exploited in N_2 physisorption by generating an adsorption isotherm of N_2 at very low temperatures. Isotherms are recorded by measuring the quantity of N_2 adsorbed at different pressures; the shape of the resultant isotherm can reveal a great deal about some of the physicochemical properties of the solid sample.

Figure 2 shows the six adsorption isotherms exhibited by different types of materials.[7] Generally, Type I isotherms represent monolayer-only coverage. Type II shows that further adsorption takes place after monolayer coverage is achieved, leading to multi-layer formation, indicative of a large pore size distribution present in the material. Type III isotherms are indicative of multi-layer formation, without a well-defined monolayer; they are not often observed for N_2 adsorption on catalyst surfaces. Type IV isotherms are related to Type II isotherms but indicates a finite multi-layer formation is achieved. Type IV isotherms are characteristic of complete pore filling and are typically observed for mesoporous materials. Type V isotherms are similar to Type IV isotherms; they are indicative of capillary condensation, but without the monolayer formation. Lastly, a Type VI isotherm is characteristic of a nonporous material with a homogeneous surface. These isotherms are often exhibited when the temperature of the analysis is near the melting point of the adsorbed gas.

The point at which surface saturation occurs and multi-layer adsorption proceeds is an inflection point, typically referred to as point B. Application of the BET method to calculate surface area typically takes place at pressures below this inflection point. Equation 5 shows the BET[8] equation:

$$\frac{P}{V_a(P_0 - P)} = \frac{1}{V_m C} + \frac{C - 1}{V_m C}\left(\frac{P}{P_0}\right) \qquad \text{Eq. 5}$$

Where P = pressure; P_0 = saturation pressure; V_a = volume of gas adsorbed; V_m = volume of monolayer and C = multilayer adsorption parameter (equation 6).

$$C = e^{\frac{E_1 - E_{\geq 2}}{RT}} \qquad \text{Eq. 6}$$

Where E_1 = monolayer adsorption enthalpy, $E_{\geq 2}$ = adsorption enthalpy for second and higher layers, equal to enthalpy of vaporisation; R = ideal gas constant; T = temperature.

Specific surface area can then be calculated from the monolayer volume and the sample mass:

$$SSA = \frac{V_m \sigma N_a}{mv} \quad \text{Eq. 7}$$

Where V_m = monolayer volume; σ = area of N_2 molecule (0.162 nm^2); N_a = Avogadro's number, m = mass of sample, v = molar volume of gas.

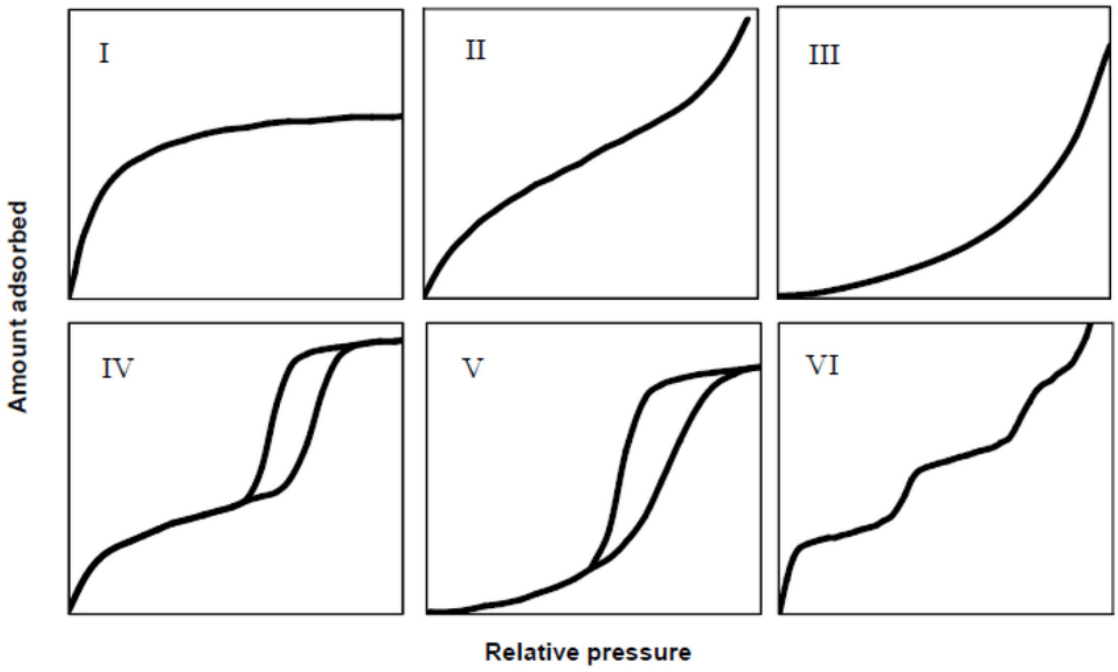

Figure 8. The six types of sorption isotherms identified by King.[7]

2.3.3.1 Experimental

Nitrogen adsorption isotherms were collected using a Quantachrome Quadrasorb evo™ surface area analyser at -196 °C. A 40-point analysis (20 adsorption points, 20 desorption points) was performed using N_2 as the adsorbate gas. Samples were degassed under vacuum at 200 °C for 3 hours prior to analysis. Surface areas were calculated in accordance with the BET method over the P/P_0 range of 0.05 – 0.3. Pore size distributions were calculated in accordance with the (Barrett-Joyner-Halenda) BJH method, using QuadraWin™ software.

2.3.4 Temperature programmed reduction/oxidation (TPR/O)

The reduction of a metal oxide can be described by equation 8:

$$MO_n + nH_2 \rightarrow M + nH_2O \quad \text{Eq. 8}$$

Temperature programmed reduction (TPR) is a chemisorption technique whereby a sample is heated with a linear heating rate (β) under a reductive atmosphere (typically H_2 diluted in an inert gas). The rate of reduction can be monitored by comparison of the gas composition at the inlet and outlet of the reactor. When H_2 is employed as the reductant, water is generated as a product and so the outlet stream is passed through a cold trap to condense any water prior to entering the thermal conductivity detector (TCD). This is important, as water can cause large shifts in the detector current and ultimately, influence the accuracy of the acquired data.[9] The gas composition at the reactor outlet is monitored

and as such, the temperatures at which H_2 is consumed, and hence the sample was reduced, can be detected. The area under a TPR curve is representative of hydrogen consumption and can be expressed as moles of H_2 consumed per mole or gram of metal oxide.

The free energy change for the reduction is given by equation 9:

$$\Delta G = \Delta G° + nRTln\left(\frac{p_{H2O}}{p_{H2}}\right) \quad \text{Eq. 9}$$

Where ΔG = change in Gibbs free energy for reduction, ΔG° = change in Gibbs free energy under standard conditions, n = stoichiometric coefficient of the reaction, R = ideal gas constant, T = temperature, p_{H2O} = partial pressure of water, p_{H2} = partial pressure of hydrogen.

For some metal oxides ΔG° is negative, indicating the thermodynamic feasibility of the reduction. However, even when ΔG° is positive, reduction can proceed provided that the term $\ln(p_{H2O}/p_{H2})$ is sufficiently negative to give a negative value of ΔG; this can be achieved by continuously sweeping any formed water vapour away out of the reaction zone.

H_2 consumption *via* reduction of a metal oxide can be quantified by calibration with a high purity metal oxide. Typically, copper oxide (CuO) is used to calibrate hydrogen consumption due to the large quantity of H_2 consumed through its reduction. To calibrate, experiments are performed with varying quantities of high purity CuO (> 99.995 %). The theoretical hydrogen consumption can be calculated from the sample masses of CuO used, using the reaction stoichiometry (equation 10). The peak area of H_2 consumed can then be related back to the amount of H_2 required for reduction of CuO, producing a calibration of peak area vs. H_2 consumption.

$$CuO_{(s)} + H_{2(g)} \rightarrow Cu_{(s)} + H_2O_{(g)} \quad \text{Eq. 10}$$

The kinetic parameters associated with the reduction process, *i.e.* activation energy, can be deduced from TPR data by considering the temperature at which the reduction rate is at a maximum.[10] The activation energy of reduction can be estimated using the Kissinger equation (equation 11). A series of TPR experiments are performed with varying heating rates (β), and the left-hand site of equation 9. ($\ln(\beta/T_{max})$ can be plotted against $1/T_{max}$ giving a straight line where the gradient is equal to $-E_a/R$.

$$ln\left(\frac{\beta}{T_{max}^2}\right) = K + \left(\frac{E_a}{R}\right)\frac{1}{T_{max}} \quad \text{Eq. 11}$$

Where β = heating rate (K min^{-1}); T_{max} = peak maximum; K = constant; E_a = activation energy; R = gas constant.

Temperature programmed oxidation (TPO) is based on identical principles to TPR only the sample is heated under an oxidative atmosphere (generally a dilute O_2 / inert gas mixture).

In such an experiment, it is oxygen consumption which is monitored as a function of temperature. For any TPO studies performed throughout this thesis, all analysis was performed on a non-quantitative basis only.

2.3.4.1 Experimental

TPR and TPO analyses were performed using a ChemBet chemisorption analyser (Quantachrome Instruments) equipped with a thermal conductivity detector (TCD). Samples (*ca.* 100 mg) were placed between 2 plugs of quartz wool in a U-shaped silica tube and pre-treated by heating to 130 (15 °C min^{-1}) for 1 hour under flowing He (80 mL min^{-1}). The samples were subsequently left to cool to room temperature before undergoing further heating to 900 °C (10 °C min^{-1} unless otherwise specified) under flowing 10 % H_2/Ar (30 mL min^{-1}) or 5 % O_2/He for TPR and TPO respectively. TPROR analyses were performed as above, but following the initial reduction step the sample was cooled to room temperature under He (80 mL min^{-1}). The procedure for TPO was then performed and the sample cooled to room temperature under He (80 mL min^{-1}), before a second TPR was completed.

H_2 consumption was quantified as described above, through calibration of the instrument with a highly pure CuO standard. For a given mass of CuO (> 99.999 %), the amount of hydrogen consumed to complete reduction was calculated; the peak area observed for a given mass was then plotted against H_2 consumption (Figure 3), to derive a response factor for hydrogen consumption.

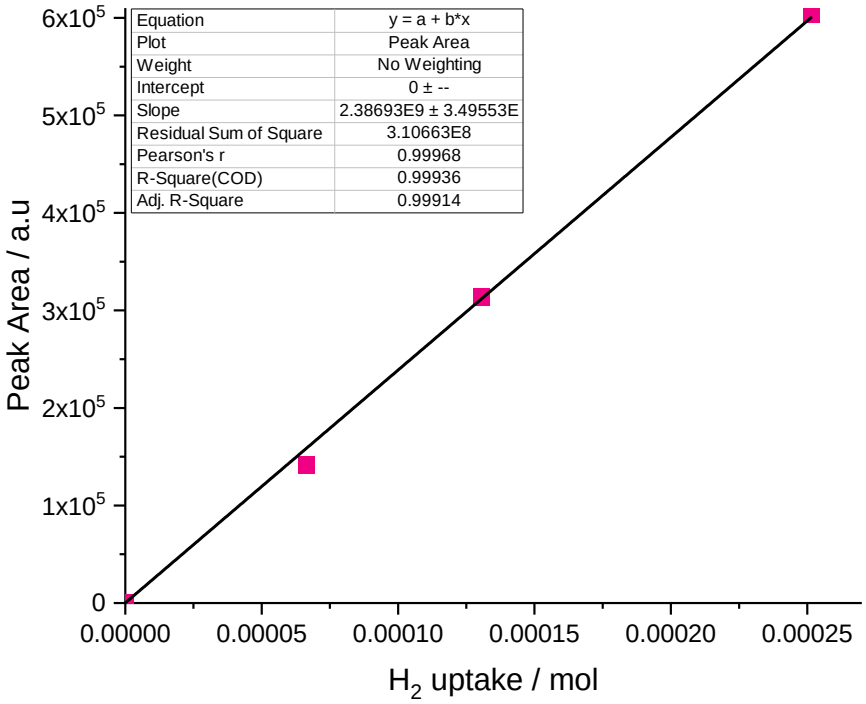

Figure 9. H_2 consumption calibration curve for TPR experiments. Peak areas obtained from precise masses of high purity CuO.

2.3.5 Temperature programmed desorption (TPD)

Temperature programmed desorption involves monitoring the rate of desorption of chemisorbed molecules as a function of temperature. Adsorption, which can be defined as the enrichment of a fluid (adsorbate) at the surface of a solid (adsorbent) or the increase in fluid density in the vicinity of an interface,[11] can be categorised as physisorption or chemisorption. Physisorption arises as the result of weak intermolecular forces and is non-specific, non-dissociative; it occurs only at reasonably low temperatures and is characterised by a low heat of adsorption (< 50 kJ mol^{-1}). Alternatively, chemisorption is characterised by a high heat of adsorption (> 50 kJ mol^{-1}) and can occur over a wide temperature range. Chemisorption is highly specific, monolayer forming and can take place associatively or dissociatively.[12]

TPD typically involves the saturation of a sample with a chemical species (adsorbate) and subsequently, heating the sample at a controlled ramp rate to monitor the temperature(s) at which desorption occurs. Following pre-treatment of the adsorbent, the sample is exposed to the adsorbate, generally at ambient temperatures. Any physisorbed species are subsequently removed by flowing an inert gas over the sample before desorption of remaining chemisorbed species is performed. The adsorbent is heated under an inert gas with a constant heating rate *($\beta = dT/dt = constant$)* with any desorbed species monitored by an appropriate detector (generally TCD, FID or QMS). The data generated from TPD experiments shows detector signal intensity as a function of time/temperature; since signal intensity is proportional to concentration of detected species as desorbed from the sample surface, it is proportional to the rate of desorption. Calibration of the detector by the direct admission of specific quantities of adsorbates, allows for quantitative measurements of desorbed species. Two primary pieces of information can be obtained from TPD profiles:

1) The area under the curve is proportional to the amount of desorbed species. This can allow for quantification of the adsorbed species (provided re-adsorption is negligible) and surface coverage to be determined.
2) The position of the peak maximum, T_{max}, can provide information on the strength of binding between adsorbate and adsorbent, which is related to the activation energy for desorption. Generally, higher desorption temperatures (*i.e.* higher values of T_{max}) represent stronger interactions between the surface and the adsorbed species, since more thermal energy is required to allow desorption.

Acidic probe molecules, such as CO_2 or SO_2, are used to investigate materials with basic sites; basic probe molecules, such as NH_3, pyridine or acetonitrile, are used to investigate materials containing acidic sites. CO_2 and NH_3 are the most widely probe molecules used for investigating the basic and acidic sites of materials, respectively. Some materials, such as ceria, are amphoteric, possessing both acidic and basic surface sites, thus TPD experiments

performed with acidic and basic probe molecules can provide useful information on the acid-base properties of a material.

2.3.5.1 Experimental

CO_2-TPD and NH_3-TPD were used in this work to analyse basic and acidic sites respectively using a Quantachrome ChemBET Chemisorption analyser equipped with a TCD. Calcined samples (*ca.* 100 mg) were heated to 130 °C for 1 hour under flowing He (40 mL min^{-1}). The sample was then cooled back down to room temperature; materials were then exposed to an excess quantity of adsorbate gas (40 mL min^{-1}) for 30 minutes. Physisorbed species were removed by heating to 110 °C for 1 hour under flowing He (40 mL min^{-1}). Desorption of chemisorbed species was performed by heating the catalysts from room temperature to 900 °C under flowing He (10 °C min^{-1}, 40 mL min^{-1}). Samples were also analysed under blank conditions (procedure as above but without the admission of adsorbate) to ensure pre-treatment conditions were sufficient to remove detectable surface contaminants.

Quantification was performed by direct injection of known quantities of the probe molecules *via* a titration loop. A given quantity of reactant gas was injected, with the change in thermal conductivity detected once the gas reaches the detector. Since the amount of analysis gas in moles can be calculated with the ideal gas equation, a plot of the detector peak area against amount of reactant gas in moles. This allowed for determination of the associated response factor to be calculated, which can subsequently be used to quantify the amount of analysis gas detected in a given experiment. This is shown in Figure 4.

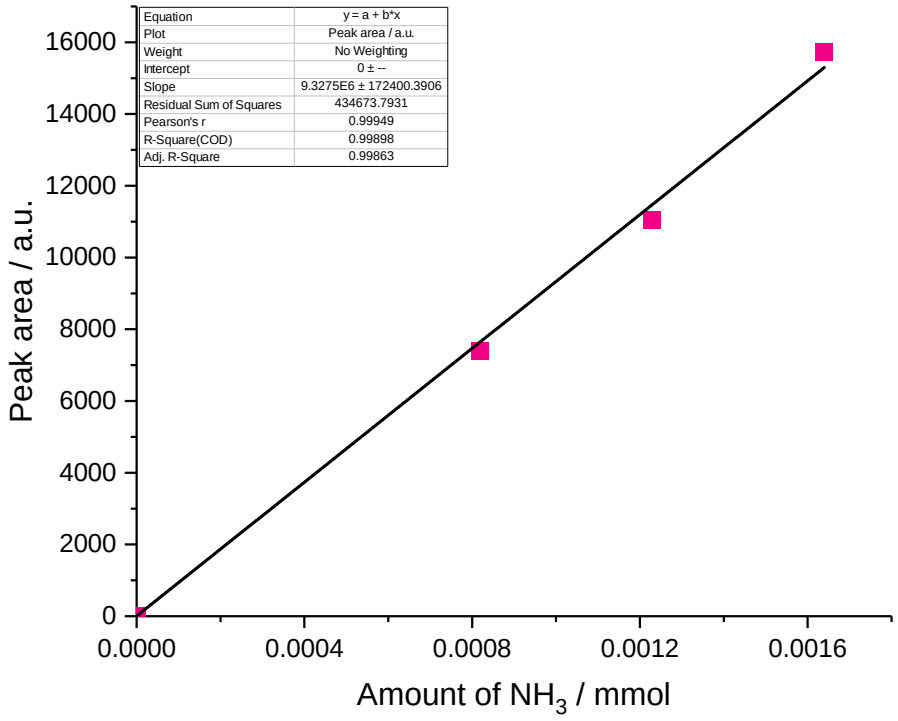

Figure 10. NH_3 calibration curve for TPD experiments. Peak areas obtained by injecting different quantities of reactant gas. A similar calibration was obtained for CO_2.

2.3.6 Transmission electron microscopy

Transmission Electron Microscopy (TEM) is a microscopy technique used to image samples on the nanometre scale, with atomic resolution possible. It is an incredibly important characterisation technique for the study of heterogeneous catalysts.[13] TEM can provide insight on the morphological, compositional and crystallographic properties of materials at the atomic scale.

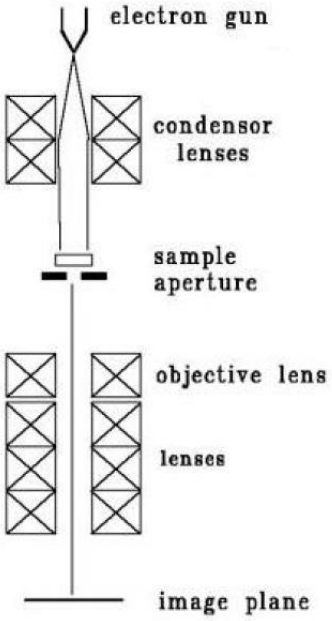

Figure 11. Schematic of an electron microscope in transmission mode (TEM).[5]

Typically, acquisition of a TEM image is as follows:[5] (i) A source of monochromatic electrons are emitted from an electron gun sitting at the top of the microscope and accelerated through the column under vacuum. The electron speed can be altered by varying the voltage of the gun, depending on the nature of the sample. (ii) Electrons are focused into a thin beam using electromagnetic lenses. High angle electrons are eliminated by a condenser, resulting in parallel rays which continue towards the samples. (iii) The electron beam then travels through the sample, which is required to be ultra-thin (< 200 nm) to allow for transmission of electrons. (iv) Depending on the density of the material, some electrons are scattered, whilst non-scattered electrons are detected by a fluorescent screen at the bottom of the microscope. This converts the electrons to light, creating an image of the sample. Differences in darkness correspond to differences in charge density, with lighter areas of an image representing a greater transmission of electrons through the sample. This is known as a bright field image. Alternatively, a dark field image can be produced from the diffracted electrons, which are detected slightly off-angle from the transmitted beam, when the electrons are diffracted by a crystalline sample. High angle annular dark field (HAADF) TEM involves the detection of electrons scattered at high angles. This method is highly sensitive to the atomic number, Z, of the scattering atom, with increased electron scattering observed

for heavy atoms. Consequently, heavier elements appear as bright regions in dark field images, in contrast to bright field images where they appear darker.

The use of a scanning transmission electron microscope (STEM) is required to acquire HAADF images. For this a focussed beam of high energy electrons is scanned over the surface of a thin sample specimen, resulting in transmitted and diffracted electrons. Backscattered and secondary electrons, and X-rays, measured by SEM and EDX (energy dispersive X-ray spectroscopy), respectively, can provide additional information about the surface and bulk structure of the material, respectively.

2.3.6.2 Experimental

Transmission electron microscopy (TEM) and scanning transmission electron microscopy (STEM) were performed on a JEOL JEM-2100 operating at 200 kV. Energy dispersive X-ray analysis (EDX) was done using an Oxford Instruments X-Max^N 80 detector and the data analysed using the Aztec software. Samples were prepared by a dry dispersion route and loaded on to 300 mesh copper grids coated with holey carbon film after grinding between glass slides. All samples were analysed with the assistance of Dr Thomas Davies. Particle size and lattice spacing measurements were made using ImageJ software.

2.3.8 Raman spectroscopy

Raman spectroscopy is a vibrational spectroscopy based on the principle of inelastic photon scattering.[14] The irradiation of a sample with monochromatic light of frequency ν_0, results in the photons being absorbed, transmitted or scattered. The vast majority of scattered photons are elastically scattered, that is, with the same energy as the incident photons. Elastic scattering, also known as Rayleigh scattering, occurs when an irradiated molecule is excited to a virtual energy level with an energy of $h\nu_0$ above the ground state, before decaying back down to the ground state with no energy exchanged between the sample and photon. A small percentage of the scattered photons are scattered with a different energy to that of the incident radiation. When a molecule is excited from the ground state to a virtual energy level, before decaying to the first excited vibrational level with a frequency of ν_{vib}, the photon is emitted with a lower energy than that of the incident photon. This is known as Stokes scattering, where the scattered photons have a frequency of $\nu_0 - \nu_{vib}$. Anti-Stokes scattering occurs when a molecule is excited from the first vibrational state to a virtual energy level before decaying down to the ground state. This results in energy being transferred to the scattered photons which have a higher frequency than the incident light ($\nu_0 - \nu_{vib}$). Rayleigh and Raman scattering are summarised in Figure 6. The relative intensities of Stokes and anti-Stokes scattering is dependent on the population of energy states. At room temperature Stokes scattering is usually of a much higher intensity, due to the proportion of molecules occupying the vibrational energy states being low. In addition to

Rayleigh and Raman scattering, fluorescence is also possible. This occurs when electrons are excited to an excited electronic state whereby decay to the ground state occurs with multiple transitions and is an undesirable process due to its ability to obscure the Raman spectrum.

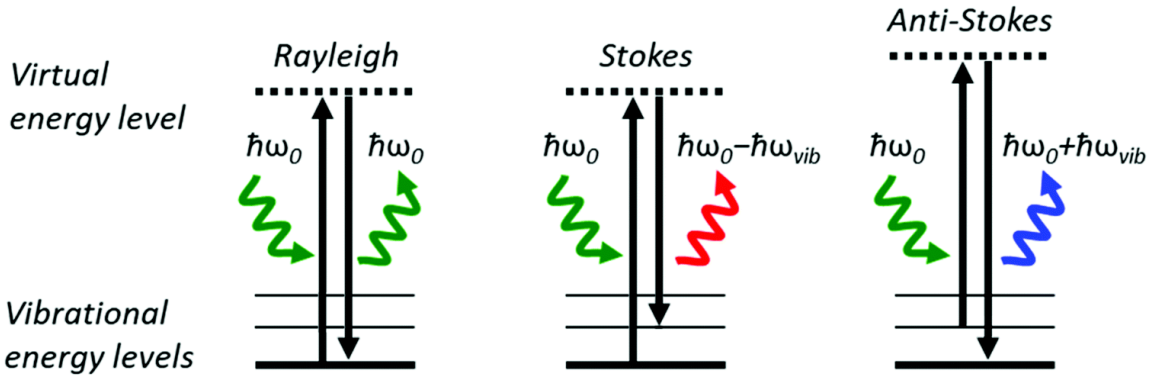

Figure 12. Energy levels during elastic (Rayleigh) and inelastic (Stokes and anti-Stokes) photon scattering. Image reproduced from Chem. Soc. Rev., 2020, 49, 554-592 - Reproduced by permission of The Royal Society of Chemistry

Not all vibrations can be observed by Raman spectroscopy. For a molecule to be Raman active, it must possess anisotropic molecular polarizability. This means that molecular polarizability must change during the vibration. Spherical molecules have isotropic polarizability and thus, are not Raman active. This selection rule means that highly symmetrical molecules, such as H_2 and O_2, can be observed by Raman spectroscopy.

Since Rayleigh scattering accounts for the vast majority of photons scattered, a highly sensitive detector is required to detect Raman scattering. This is typically achieved through the use of a charge coupled detector (CCD), a highly sensitive semiconductor-based device which transfers electronic charge. Intensity of charge is proportional to the detected photons thus quantitative Raman spectroscopy is possible.

2.3.8.1 Experimental

Raman spectroscopy was performed using a Renishaw inVia microscope with a green argon ion laser (λ = 514 nm). Samples were prepared by pressing onto a Raman inactive aluminium plate. Prior to sample analysis, the laser was calibrated using an internal Si reference and focused with an Olympus BH2-UMA microscope. Typically, 10 seconds of laser exposure and 10 accumulations were used in each scan, with the laser operated at a power of 1 %, although measurements with a laser power between 0.1 – 10 % were made. Cosmic ray removal was performed on all samples.

For CeO_2 samples, Raman spectra are typically dominated by an intense F_{2g} mode at a Raman shift of *ca.* 460 cm^{-1}, which is representative of the Ce-O_8 lattice. In addition to this, a much weaker peak at *ca.* 600 cm^{-1} is often observed, which has been attributed to the presence of defects within the lattice. The ratio of these two peak areas, conventionally

denoted as I_D/I_{F2g}, can be used to estimate the density of defects within the material. Throughout this thesis, this was achieved by integrating the observed peaks in a Raman spectrum using OriginLab software to obtain areas for the peaks observed at 460 cm^{-1} (I_{F2g}) and 600 cm^{-1} (I_D).

2.3.9 Infrared spectroscopy

Infrared spectroscopy (IR) is a spectroscopic technique which exploits the fact that vibrations can be excited by photons in the IR region of the electromagnetic spectrum.[14] Infrared radiation can be classified as far, mid and near, which are categorized as possessing energies of 1.2 – 25, 25 – 496 and 496 – 1240 meV, respectively. Molecules possess discrete levels of vibrational, rotational and electronic energy; these energies are quantised with transitions between energy levels only occurring when the amount of energy absorbed or emitted from the system is described by the Planck equation (equation 12).

$$\Delta E = h\nu \qquad \text{Eq. 12}$$

Where h = the Planck constant (6.63 x 10^{-34} m^2 kg s^{-1}) and ν = frequency of incident radiation

Vibrational energy levels are equidistant and can be estimated from the harmonic oscillator (equation 13):

$$E_n = \left(n + \frac{1}{2}\right) h\nu \qquad \text{Eq. 13}$$

Whereby E_n = energy of the n^{th} vibrational level; n = an integer; h = the Planck constant; and ν is described by equation 14:

$$\nu = \frac{1}{2\pi}\sqrt{\frac{k}{\mu}} \qquad \text{Eq. 14}$$

Where k = the force constant of the bond and μ = the reduced mass, as described by equation 15:

$$\mu = \frac{m_1 m_2}{m_1 + m_2} \qquad \text{Eq. 15}$$

Where m_i = mass of vibrating atoms

The absorption of photons from the mid-IR region, which corresponds to wavenumbers between 200 – 4000 cm^{-1}, can excite molecular vibrations such as stretching, bending, wagging *etc*. This in turn, allows for transition to a higher vibrational energy level. Alternatively, the absorption of photons from the near and far regions of IR result in lattice vibrations and vibrational overtones, respectively. As shown by equation 12, vibrational frequencies are related to both bond strength and atomic mass; a given vibrational frequency can therefore be correlated with a specific chemical bond. Similarly to Raman

spectroscopy, not all vibrations can be observed by IR spectroscopy. For a sample to be IR active, the vibration must result in a change in dipole moment. Consequently, highly symmetrical diatomic molecules such as H_2 and O_2 cannot be observed by IR.

Conventional IR spectroscopy, also known as dispersive spectroscopy, involves shining a monochromatic light at a sample and measuring the light absorption. This process is subsequently repeated for a range of wavelengths. Alternatively, a Fourier transform (FT) is a mathematic operation which has widely increased the capabilities of IR spectroscopy. FT-IR allows the measurement of multiple wavelengths to occur simultaneously. Through the use of a Michelson interferometer, a series of mirrors which allows the period transmission and blocking of each wavelength, IR spectra over a wide range can be obtained. FT-IR offers the advantage of a high signal-to-noise ratio due to the low susceptibility of interference occurring over multiple scans.

Diffuse reflectance infrared Fourier transform spectroscopy (DRIFTS) is an IR technique that does not require any sample preparation other than filling a sample holder with sample. The IR light is reflected and transmitted depending on the material. Ellipsoid mirrors concentrate the scattered light, which covers a wide range of angles due to the roughness of the samples surface, towards the detector. Spectra are typically shown as absorbance or reflectance as a function of wavenumber, although Kubelka-Munk units are sometimes used. Kubelka-Munk units involve the incorporation of a scaling factor, to directly correlate reflectance with concentration.

2.3.9.1 Experimental

DRIFTS measurements were taken on a Bruker Tensor 27 spectrometer fitted with a mercury cadmium telluride (MCT) detector. A sample was loaded into the Praying Mantis high temperature in situ cell (HVC-DRP-4) before pre-treatment under N_2 (20 mL min^{-1}) at 500 °C for 1 hour. The sample was then cooled to room temperature with background spectra obtained upon cooling.

2.3.10 Inductively coupled plasma mass spectrometry (ICP-MS)

ICP-MS is an elemental analysis technique which allows multiple elements to be measured simultaneously in a single procedure. Liquid samples are required for ICP-MS and thus, heterogeneous catalysts must be digested prior to analysis. For materials such as ceria, this is typically done through microwave heating of the sample in a strong acid matrix due to its low solubility. The liquid samples are initially nebulised, generating an aerosol that is transported into high temperature argon plasma. The plasma subsequently atomises and ionises the sample. The generated ions are then focussed into a beam through a set of electrostatic lenses, which guide the ion beam to a mass analyser. Here the ions are separated by mass-to-charge ratio, before being detected.

2.3.10.1 Experimental

The ICP-MS results presented within this thesis were obtained by Mr Simon Waller of the Analytical Services Department, School of Chemistry, Cardiff University. They were not obtained by the author.

2.4 Catalyst testing

2.4.1 Testing protocol

Catalytic reactions were performed using a gas-phase plug flow micro-reactor. Aqueous glycerol solutions (50 *wt*. %) were introduced into a preheater and vaporiser (305 °C) using an HPLC pump, at a flow rates of 0.016 mL min^{-1}. The glycerol feed was swept through the reactor using argon as carrier gas. All lines were heated to prevent any condensation taking place. Catalysts were pelleted, crushed and sieved to a uniform particle size (250-425 μm) prior to testing. The catalyst samples (typically 500 mg) were combined with silicon carbide to a uniform volume (0.5 mL) and packed into an 8 mm inner diameter stainless steel tube between two plugs of quartz wool. These conditions resulted in mass velocities and space velocities between 900 - 6000 L h^{-1}_{Ar} $kg^{-1}_{cat.}$ and 1800 – 9000 L h^{-1}_{Ar} $L^{-1}_{cat.}$, respectively. A thermocouple was placed in the catalyst bed and used to control reaction temperature; reactions were carried out between 320-480 °C. Liquid reaction products were collected using an ice-cold stainless-steel trap. A gas bag was attached at the exit line to collect the gaseous products.

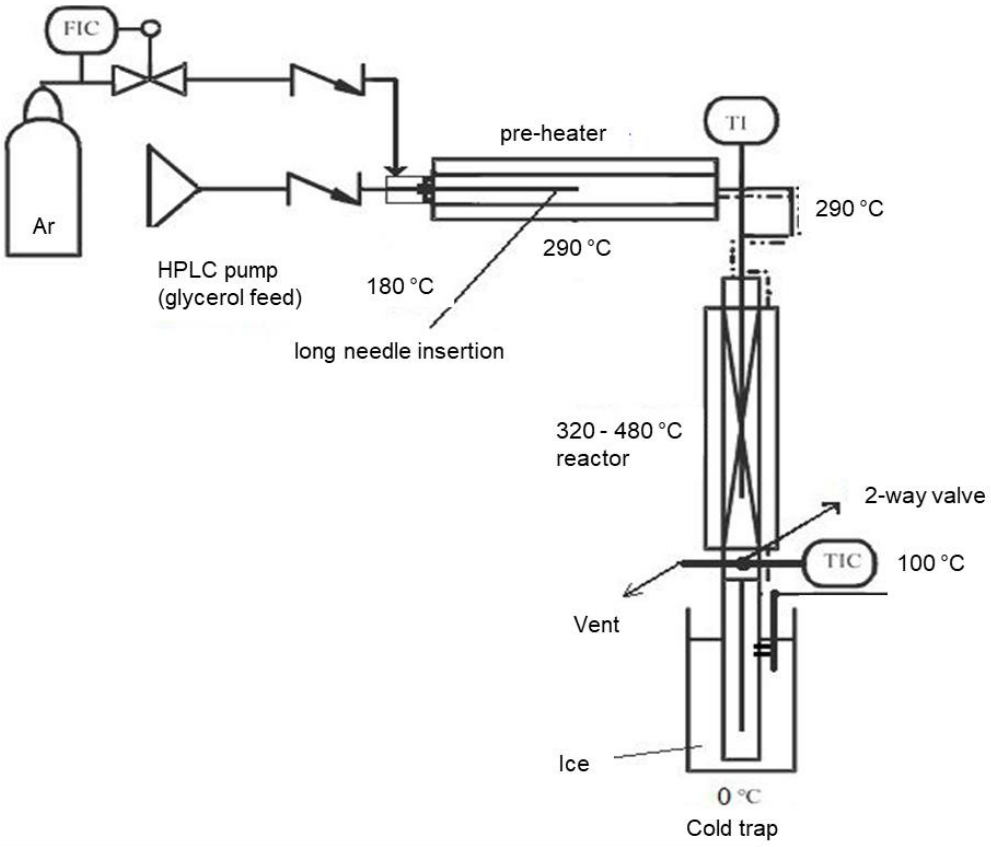

Figure 13. Reactor schematic for gas-phase glycerol conversions.

2.4.2 Product analysis

A full product list and retention times according to GC used is displayed in Table 2. GC, gas chromatography, is an analytical technique extensively used to separate and analyse mixtures of chemical compounds.[15, 16] Both liquid and gas phase samples can be analysed, with liquid samples initially vaporised at the sample injector; samples are then transported through the instrument *via* a carrier gas to a column where compounds are separated, before the analytes are subsequently detected. The column, may either be a capillary column, whereby a thin layer of non-volatile chemicals are coated onto the walls of a hollow column or a packed column, which contains an inert solid, coated with a thin layer of non-volatile chemicals, known as the stationary phase. The nature of the stationary phase will vary depending on the polarity of the analytes and the separation required. The different chemicals compounds present in a sample will interact with the stationary phase to differing extents, thus, leading to their elution from the column at different times (retention time). This allows for the separation and detection of the products formed. Separations can also be achieved through a temperature gradient whereby the temperature is increased to allow the elution of more strongly retained compounds. The carrier gas is known as the mobile phase and is an inert gas, usually He. It is important that the carrier gas has no interaction with the stationary phase.

Numerous types of detector are compatible with GC, with the most common including mass spectrometer (MS), flame ionization detector (FID) and thermal conductivity detector (TCD). GS-MS can be used to identify unknown products. Separated products are ionised and the *m/z* (mass-to-charge ratio) of resulting ions is continuously monitored. By analysing the relative intensity observed across a range of *m/z* values, known as the mass spectrum, it is possible to confirm, identify and quantify analytes.

Alternatively, FIDs and TCDs may be used to quantify known compounds. GC-FID is extensively used, particularly in the analysis of hydrocarbons. The effluent stream enters the detector where it is mixed with H_2/air and burnt, leading to the formation of ions and electrons, which flow between two electrodes present in the detector resulting in a current flow, which is amplified to generate a signal. FIDs typically provide high linearity over a wide concentration range, although low/no response is observed for several products including CO and CO_2. In order to overcome this limitation, a methanizer can be applied in conjunction with a FID. In such a case, the products are fully reduced to CH_4 over a Ni catalyst, prior to quantification by FID.

A TCD is a universal detector, suitable for analytes which cannot be detected using a FID. However, for most organic products, sensitivity is often much lower with a TCD than an FID. The temperature of a hot filament present in the detector and thus the electrical resistance, varies with the gas composition. With a constant flow of carrier gas, the temperature of the

filament is constant but as products are eluted, the composition and thermal conductivity of the gas stream is altered, resulting in changes in the temperature and resistance of the filament.

It should be noted that only products which can be successfully vaporised are suitable for GC analysis. The injection port where samples are initially vaporised typically has a maximum temperature of *ca.* 380 °C, therefore a compound must be sufficiently volatile as to undergo vaporisation at the temperatures. In order for products to be successfully separated and detected, they must not thermally degrade upon vaporisation and thus, the inlet temperature cannot be excessively high.

2.4.2.1 Liquid products by GC-FID

Liquid reaction products were analysed offline using a Varian CP 3800 gas chromatograph (GC1) equipped with a capillary column (ZB-Wax plus, 30 m x 0.53 mm x 1 µm). The injector port was maintained at 250 °C and a split-less injection was used. The initial column temperature (40 °C) was held for 2 mins, then ramped (20 °C min^{-1}) to 60 °C where it was held for 2 minutes before ramping to 220 °C (20 °C min^{-1}) and holding for 15 minutes. Products were analysed by an FID maintained at 300 °C. Cyclohexanol was used as an external standard. A glycerol calibration curve is shown in Figure 8; all liquid products were calibrated this way.

2.4.2.2 Carbon containing gases by GC-FID

Carbon based gas reaction products were analysed offline using a Varian 450-GC gas chromatograph (GC2) equipped with a capillary column (CP-Sil5CB, 50 m x 0.32 mm x 5 µm).The injector port was maintained at 200 °C and a 20:1 split ratio used. The initial column temperature (35 °C) was held for 15 mins and ramped (50 °C min^{-1}) to 100 °C where it was held for 3 minutes. Products were analysed by an FID with a methanizer, held at 200 °C and 350 °C respectively.

2.4.2.3 H_2 and O_2 by GC-TCD

H_2 and O_2 were analysed using a Varian CP3380 gas chromatograph (GC3) equipped with a Porapak Q column. The injector was held at 50 °C; the column was maintained at 30 °C for 15 minutes. Products were analysed by a TCD, with the filament maintained at 200 °C.

Table 2. Full product list with retention times and corresponding GC

Product	***Retention time***		
	GC1	GC2	GC3
Acetaldehyde	1.907		
Propionaldehyde	2.387		
Acetone	2.600		
Acrolein	2.840		
Butyraldehyde	3.133		

Methanol	3.480		
2-propanol	3.907		
Ethanol	4.013		
2,3-butanedione	4.547		
2-butanol	5.560		
1-propanol	5.800		
3-hexanone	5.907		
2-hexanone	6.360		
2-methyl-1-propanol	6.680		
Allyl alcohol	7.053		
Cyclopentanone	8.013		
Hydroxyacetone	9.373		
3-ethoxy-1-propanol	9.987		
Acetic acid	10.547		
Glycidol	10.790		
Propionic acid	11.240		
1,2-propanediol	11.747		
Ethylene glycol	12.013		
1,3-propanediol	13.080		
Phenol	14.760		
Glycerol	18.787		
CO		5.02	
CH_4		5.12	
CO_2		5.38	
H_2			2.222
O_2			2.902

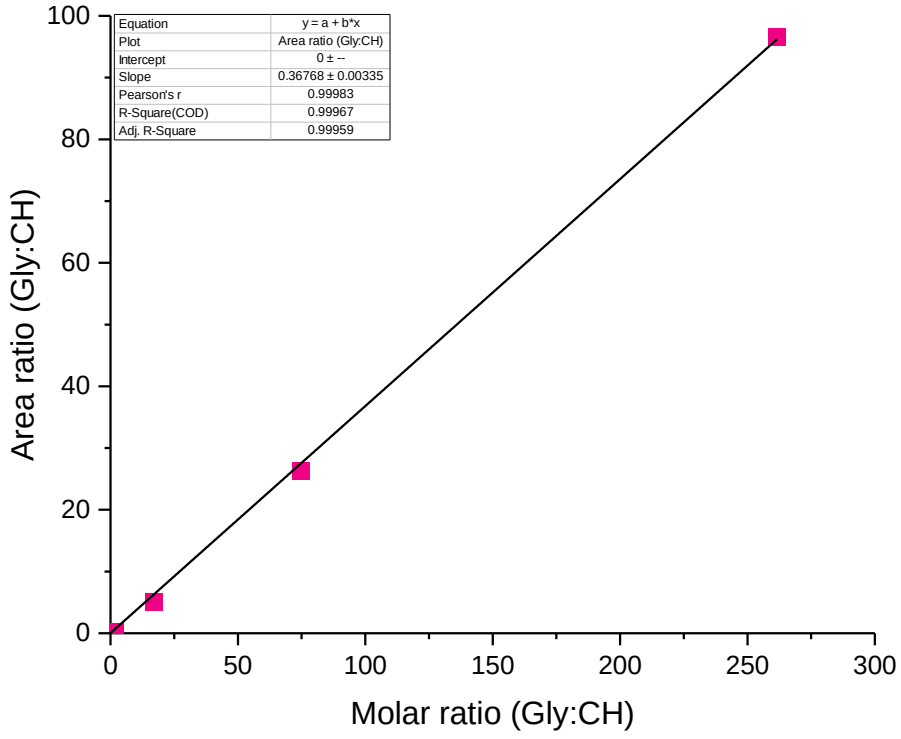

Figure 14. Glycerol (Gly) calibration using cyclohexanol (CH) as an internal standard.

2.4.2.4 Total carbon analysis

For certain experiments where the obtained carbon balance was low, total carbon analysis was performed. The liquid phase post-reaction sample was collected and sent to Exeter Analytical for CHN analysis; a sample of the feedstock prior to reaction was also sent for analysis to allow the % of C remaining in the liquid phase to be calculated. The % of carbon contained within gas phase products was analysed as described in section 2.4.2.2 and any carbon retained on the catalyst was quantified by TGA, with total carbon comprised of the sum of all liquid, gas and solid phase carbon after a catalytic reaction.

2.4.2.5 Qualitative LC-MS analysis

Some additional qualitative analysis of the post reaction effluent was conducted by liquid chromatography-mass spectrometry (LC-MS). This was conducted on a Bruker Amazon SL ion trap mass spectrometer which was operated in positive electrospray ion mode and coupled to a Thermo Ultimate HPLC system. The HPLC was equipped with a C-18 column (maintained at 40 °C) and utilized a gradient elution consisting of 0.1% formic acid in H_2O (A) and 0.1% formic acid in acetonitrile. 10 µL of sample was injected and the gradient elution was performed as illustrated in Table 3:

Table 3. The makeup of the mobile phase for the gradient elution used for LC-MS analysis

Time (min)	***A (%)***	***B (%)***
0.0	98	2
1.0	98	2
15.0	2	98
17.0	2	98
18.0	98	2
20.0	98	2
A = 0.1 % formic acid in H_2O and B = 0.1 % formic acid in acetonitrile.		

2.4.3 Calculations

Equation 16 was used to calculate the glycerol conversion (C_{GLY}) based on the molar difference between the carbon moles of glycerol fed into the reactor, g_{mi}, and that detected at the outlet, g_{mo}:

$$C_{GLY}\ (\%) = \left(\frac{g_{mi} - g_{mo}}{g_{mi}}\right) \times\ 100 \qquad \text{Eq. 16}$$

The product selectivity ($S_p(x)$, carbon *mol*. %) for any product, *x*, was calculated from the moles of carbon recovered of *x* (x_{Cm}) divided by the total moles of carbon in all products, y_{Cm} (equation 17).

$$S_p(x)(\%) = \left(\frac{x_{Cm}}{\sum_y y_{Cm}}\right) \times 100 \qquad \text{Eq. 17}$$

The carbon balance can be obtained by comparing the moles of carbon accounted for in unreacted glycerol and in the identified products to the moles of carbon in glycerol entering the reactor:

$$B_C(\%) = \left(\frac{g_{mo} + \Sigma_x x_{Cm}}{g_{mi}}\right) \times 100 \qquad \text{Eq. 18}$$

Functional group yield (Y, carbon mol. %) data were calculated by the sum of the selectivities for products containing that functional group S_G, multiplied by conversion C_{GLY}, multiplied by the carbon balance B_C, excluding coke (eq. 18).

$$Y\ (\%) = \left(\frac{(\Sigma\ S_G)\ x\ C_{GLY}}{100}\right) \times B_C\ (\%) \qquad \text{Eq. 19}$$

The overall carbon balance B_{Ctot} was calculated (eq. 20) by dividing the sum of the carbon moles of products x_{Cm}, coke x_{Ccoke} estimated from post reaction characterisation and unreacted glycerol g_{mo} by the carbon moles of glycerol injected into the reactor g_{mi}.

$$B_{Ctot} = \left(\frac{\Sigma_x x_{Cm} + x_{Ccoke} + g_{mo}}{g_{mi}}\right) \times 100 \qquad \text{Eq. 20}$$

The hydrogen balance B_H was calculated (eq. 21) by dividing the sum of the hydrogen moles of products x_H, hydrogen gas (GC3) x_{Hgas} and moles of hydrogen in unreacted glycerol g_{Hmo} by the moles of hydrogen in glycerol injected into the reactor g_{Hmi}.

$$B_H = \left(\frac{x_{Hp} + x_{Hgas} + g_{Hmo}}{g_{Hmi}}\right) \times 100 \qquad \text{Eq. 21}$$

The oxygen balance B_O was calculated (eq. 22) by dividing the sum of the oxygen moles of products x_O, oxygen gas (GC3) x_{Ogas} and moles of oxygen in unreacted glycerol g_{Omo} by the moles of oxygen in glycerol injected into the reactor g_{Omi}.

$$B_O = \left(\frac{x_O + x_{Ogas} + g_{Omo}}{g_{Omi}}\right) \times 100 \qquad \text{Eq. 22}$$

Carbon deposition (coke) on the catalyst was calculated dividing the mass loss as analysed by TGA of the used catalyst m_{LOST}, by the carbon moles of glycerol feed over the catalyst g_{mi} (eq.23).

$$Coke\ (\%) = \left(\frac{m_{LOST}}{g_{mi}}\right) \times 100 \qquad \text{Eq. 23}$$

The MeOH space-time-yield STY_{MEOH}, was calculated (eq. 24) from the mass of MeOH m_{MEOH}, produced per h (reaction time Rt), per mass of catalyst (m_{cat}, kg).

$$STY_{MEOH} = \left(\frac{m_{MEOH}\ (g)}{Rt\ (h) \times m_{cat}\ (kg)}\right) \qquad \text{Eq. 24}$$

2.5 References

1. M. H. Haider, N. F. Dummer, D. W. Knight, R. L. Jenkins, M. Howard, J. Moulijn, S. H. Taylor and G. J. Hutchings, *Nature Chemistry*, 2015, **7**, 1028.
2. H.-X. Mai, L.-D. Sun, Y.-W. Zhang, R. Si, W. Feng, H.-P. Zhang, H.-C. Liu and C.-H. Yan, *The Journal of Physical Chemistry B*, 2005, **109**, 24380-24385.
3. J. W. Niemantsverdriet, in *Spectroscopy in Catalysis*, ed. J. W. Niemantsverdriet, 2007, DOI: 10.1002/9783527611348.ch6, pp. 147-177.
4. M. Birkholz, in *Thin Film Analysis by X-Ray Scattering*, Wiley, 2005, DOI: 10.1002/3527607595.ch1, pp. 1-40.
5. I. Chorkendorff and J. W. Niemantsverdriet, in *Concepts of Modern Catalysis and Kinetics*, eds. I. Chorkendorff and J. W. Niemantsverdriet, 2005, DOI: 10.1002/3527602658.ch4, pp. 129-166.
6. F. Rouquerol, J. Rouquerol and K. Sing, in *Adsorption by Powders and Porous Solids*, eds. F. Rouquerol, J. Rouquerol and K. Sing, Academic Press, London, 1999, DOI: https://doi.org/10.1016/B978-012598920-6/50002-6, pp. 1-26.
7. K. S. W. Sing, *Journal*, 1985, **57**, 603.
8. S. Brunauer, P. H. Emmett and E. Teller, *Journal of the American Chemical Society*, 1938, **60**, 309-319.
9. A. Gervasini, in *Calorimetry and Thermal Methods in Catalysis*, ed. A. Auroux, Springer Berlin Heidelberg, Berlin, Heidelberg, 2013, DOI: 10.1007/978-3-642-11954-5_5, pp. 175-195.
10. J. W. Niemantsverdriet, in *Spectroscopy in Catalysis*, ed. J. W. Niemantsverdriet, 2007, DOI: 10.1002/9783527611348.ch2, ch. 2, pp. 11-38.
11. F. Rouquerol, J. Rouquerol and K. Sing, in *Adsorption by Powders and Porous Solids*, eds. F. Rouquerol, J. Rouquerol and K. Sing, Academic Press, London, 1999, DOI: https://doi.org/10.1016/B978-012598920-6/50002-6, ch. 1, pp. 1-26.
12. V. Rakić and L. Damjanović, in *Calorimetry and Thermal Methods in Catalysis*, ed. A. Auroux, Springer Berlin Heidelberg, Berlin, Heidelberg, 2013, DOI: 10.1007/978-3-642-11954-5_4, ch. 4, pp. 131-174.
13. J. W. Niemantsverdriet, in *Spectroscopy in Catalysis*, ed. J. W. Niemantsverdriet, 2007, DOI: 10.1002/9783527611348.ch7, pp. 179-216.
14. J. W. Niemantsverdriet, in *Spectroscopy in Catalysis*, ed. J. W. Niemantsverdriet, 2007, DOI: 10.1002/9783527611348.ch8, pp. 217-249.
15. O. D. Sparkman, Z. E. Penton and F. G. Kitson, in *Gas Chromatography and Mass Spectrometry (Second Edition)*, eds. O. D. Sparkman, Z. E. Penton and F. G. Kitson, Academic Press, Amsterdam, 2011, DOI: https://doi.org/10.1016/B978-0-12-373628-4.00002-2, pp. 15-83.
16. J. M. Miller, in *Chromatography*, ed. J. M. Miller, 2013, DOI: 10.1002/9780471980582.ch7, pp. 141-182.

Chapter 3

Glycerol to methanol over metal oxide catalysts

Some of the experimental results presented in this results chapter have been published in L. R. Smith *et al*., *Catalysis Science & Technology*, 2019, **9**, 1464-1475 and P. J. Smith et al. *Energies*, 2019, **12**, 1359-1372.

3.1 Introduction

As detailed in Chapter 1, the valorisation of GLY has been the focus of significant research efforts in recent years. It was recently shown that aqueous GLY feedstocks could be converted to MeOH, with a reasonably high selectivity, over simple metal oxide catalysts such as magnesium oxide (MgO) or ceria (CeO_2) under specific reaction conditions, without the need for an external reducatant.[1] Typically, reactions were performed between 175 – 400 °C, with space velocities in the range of 2000 – 24000 h^{-1}, with 0.25 – 5.0 g catalyst utilised. A reaction temperature of 300 °C resulted in the optimum MeOH yield over MgO, whereas the maximum yield over ceria was obtained at 340 °C. Very similar GLY conversions and product distributions were obtained from both highly pure GLY feedstocks and crude feedstocks, with a GLY purity of approximately 85%.

The proposed reaction scheme for the conversion of GLY to MeOH is shown in Figure 1. The dominant reaction pathway over both MgO and CeO_2 was through a monodehydration at the terminal position forming prop-2-ene-1,2-diol, an enol intermediate which tautomerises to yield hydroxyacetone (HA). As shown below, HA undergoes a radical fragmentation process, related to a Norrish type 1 reaction, generating MeOH and acetyl radicals. The MeOH radical is reduced to yield MeOH, whereas the acetyl radical is reduced to ACA, with further reduction to EtOH possible. Alternatively, the coupling of two acetyl radicals generates 2,3-BD, with the formation of 2,3-BD, a C_4 product from GLY, a C_3 product, providing good evidence for C-C bond formation and the radical nature of the acetyl species.

Alternatively, a second pathway to generate MeOH from GLY was proposed whereby GLY undergoes a radical C-C cleavage to yield MeOH and EG radicals. The former is reduced to generate a MeOH molecule whereas the latter loses a hydrogen radical to form hydroxyacetaldehyde. Similarly to HA, hydroxyacetaldehyde can undergo a radical fragmentation to produce MeOH and formaldehyde radicals, which reduce to MeOH and formaldehyde respectively. It was reported that formaldehyde was only detected in the parts per million range, suggesting that too is also further reduced to MeOH. A third route was also detected, although it was found to be minor over all the basic and redox materials tested. Typically an acid-catalysed process; GLY can undergo dehydration at the secondary

hydroxyl group, producing 3-hydroxypropanal, a highly reactive species which further dehydrates and yields ACR.

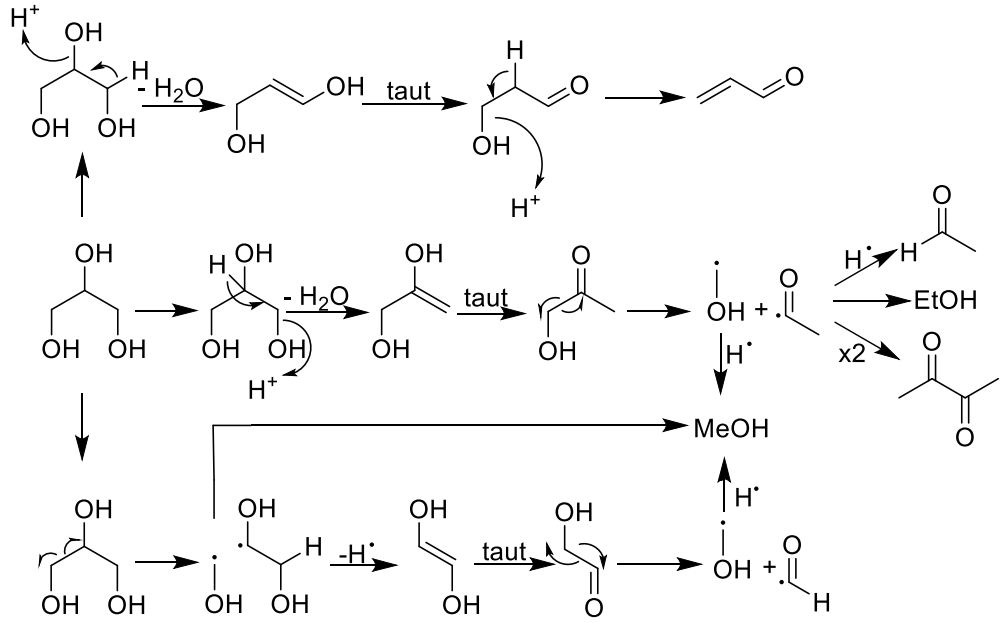

Figure 1. Proposed reaction scheme for the formation of MeOH from glycerol. Figure reproduced from Nature Chem, 2015, 7, 1028–1032. Copyright © 2015, Springer Nature.

The majority of studies were performed with aqueous GLY feedstocks in the concentration range of 0.5 – 10 wt.%, although feed concentrations up to 50 wt.% were briefly explored. Comparison of 0.5and 10 wt.% feedstocks over a MgO catalyst showed that the more concentrated GLY solution resulted in lower MeOH selectivity, as a consequence of increased by-products such as HA, ACA, ACR and EG. The MeOH space-time yield was not significantly increased with the more concentrated feedstock, despite the potential for a six-fold increase, given the increased catalyst mass used. Similar findings were observed over a ceria catalyst, with only minor increases in MeOH productivity detected as the GLY concentration was increased from 15 to 50 wt.%. These results were indicative of undesirable side-reactions occurring from more concentrated feedstocks which can occur simultaneously and reduce MeOH yields.

Throughout this chapter, the use of MgO and CeO_2 catalysts for the conversion of GLY to MeOH are further explored. The effect of temperature, GLY concentration and partial pressure are investigated over a basic MgO catalyst to better understand the complex reaction network and establish any additional side reactions which may occur with more concentrated feedstocks. Additional analysis protocols have been utilised in order to better study the complex reaction mixture and account for any unobserved carbon. The effect of calcination temperature on CeO_2 based catalysts has also been explored in order to study the effect of surface area, crystallite size and defect density on the obtained product distributions. Additionally, further analysis of the product mixture and total carbon content

is provided in an attempt to close the carbon balance and better understand the chemistry occurring over a redox catalyst throughout the conversion of GLY to MeOH.

3.2 Results

3.2.1 Blank reactions

Numerous investigations into gas phase GLY conversions over metal oxide catalysts have been performed, with temperatures typically ranging from 250 to 700 °C. Batiot-Dupeyrat and co-workers reported significant GLY conversions in the absence of any catalyst, with conversion reaching 80 % at 600 °C, for a 20 wt.% GLY feedstock in a N_2 at environment, although no details regarding product distribution were provided.[2] In this section, catalyst free reactions were performed across the temperature range 320 – 480 °C, with and without a 1 mL plug of silicon carbide (SiC), a common catalyst diluent. A 50 wt.% aqueous GLY solution was used as the GLY feed with a flow rate of 0.016 mL min^{-1} and was swept through the reactor with an argon carrier gas (50 mL min^{-1}).

GLY conversions and carbon balances achieved in the absence and presence of SiC are shown in Figure 2 with the corresponding product distributions displayed in Figure 3. In an empty reactor tube, no GLY conversion was observed to take place at a reaction temperature of 320 °C, but conversions of 6 and 11% were achieved at temperatures of 400 and 480 °C, respectively. The carbon balance was calculated to be 102, 95 and 98 % at temperatures of 320, 360 and 400 °C respectively. The lower carbon balance obtained at 360 °C was likely due to the presence of products below the detection limit; due to the diverse nature of products formed, accurate quantification of all products is challenging at low levels of GLY conversion. The full product distributions are shown in Table S.3.1a.

The major products detected over the empty tube were HA and allyl alcohol (AA), with carbon mole selectivities, herein referred to as selectivity/selectivities, of *ca.* 30 and 17 % respectively, contributing to ketone and alcohol yields of 3.1 and 2.5 % at 480 °C. Other recovered liquid phase products included ACA, ACR, MeOH, 1,2-PD and EG, with traces of propionaldehyde, ACE, 2,3-BD, 1-propanol, 3-hexanone, cyclopentanone, acetic acid, propionic acid, and 1,3-PD also detected. In addition to the aforementioned, products which are currently unidentified but observable by GC-FID (herein referred to as unknown products) were also detected. Small quantities of C_1 gases were also identified, primarily comprised of CO and CO_2 with traces of CH_4.

HA is a well-known GLY dehydration product, formed *via* thermally initiated loss of a primary hydroxyl group. Alternatively, AA was proposed to form through a radical mechanism, initiated at the C_2 position, as shown in Figure 4. AA has been widely reported from GLY, *via* selective ACR reduction, under catalysed conditions.[3-6] Additionally, AA production directly from GLY has been reported over iron based catalysts, through a

consecutive dehydration-hydrogen transfer mechanism.[6-9] The low selectivity to ACR, alongside the absence of a catalysts makes the production of AA through an ACR intermediate an unlikely process under the given conditions, and led to the proposal of an alternative, radical mechanism which is thermally initiated.

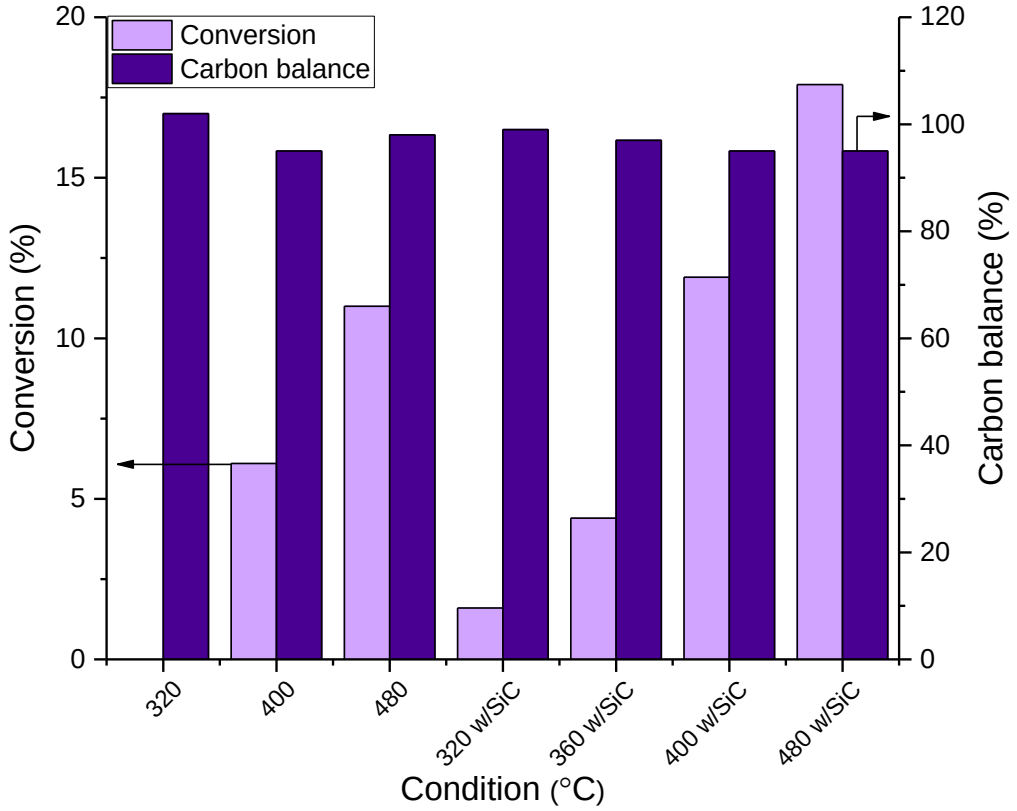

Figure 2. Glycerol conversion and carbon balance under catalyst free conditions between 320 – 480 °C, in the absence and presence of SiC. Reaction conditions; 50 wt. % glycerol (0.016 mL min^{-1}), 50 mL min^{-1} Ar, 3 hours.

To gain a greater understanding of the complex chemistry occurring under catalyst free conditions, SiC was employed to increase the contact between GLY and a hot surface. As SiC is used as a diluent in catalytic reactions to improve heat transfer, ideally its presence in the reaction should not influence the chemistry occurring. As shown in Figure 2, the presence of SiC resulted in increased GLY conversion compared with reactions performed with an empty reactor tube, with a conversion of 18 % observed at a reaction temperature of 480 °C, although at the lower temperature of 320 °C, this was less than 2 %. The modest levels of conversion achieved, particularly at higher reaction temperatures, suggest that SiC may not be completely inert in the reaction. However, it is considered that the role of SiC in increasing GLY conversion is to provide enhanced contact with a hot surface. In the absence of SiC, the majority of the vaporised feedstock stream will have no contact with a hot surface due to the increased reactor volume, whereas the reduced volume in the presence of a 1 mL SiC plug will greatly increase contact between vaporised GLY and a hot surface. The 1 mL

SiC plug reduced the volume from 1.00 to 0.49 mL, and subsequently reduced residence times from 1.20 to 0.59 seconds.

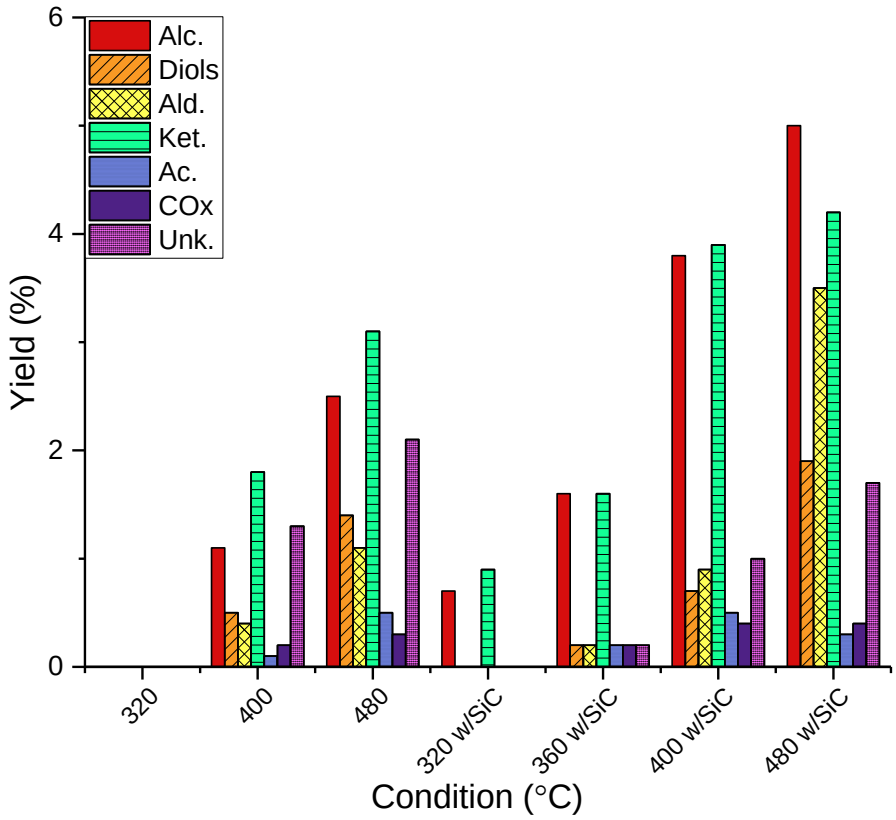

Figure 3. Product yields under catalyst free conditions between 320 – 480 °C, in the absence and presence of SiC. Reaction conditions; 50 wt. % glycerol (0.016 mL min^{-1}), 50 mL min^{-1} Ar, 3 hours.

In the presence of SiC, obtained product distributions were comparable with those observed from an empty reactor tube (full product selectivities are shown in Table A3.1b). At the lowest reaction temperature of 320 °C, the only detected products were HA and AA, which had selectivities of *ca.* 57 and 43 % respectively, although it is possible that other products were present at quantities below detectable limits. Interestingly, higher AA selectivity was observed at all reaction temperatures over SiC compared with a blank reactor tube indicating that the conversion of GLY to AA proceeds through a thermally initiated mechanism due to the increased AA observed with increased contact between GLY and a hot surface. A similar observation was made by Bühler *et al.* during their investigations into aqueous GLY conversions under near- and supercritical conditions (349 – 475 °C, 250 – 450 bar).[10] They found that at high reaction temperatures, AA was one of the dominant products formed. Analysis showed AA to be formed through a radical pathway, favoured by increasing reaction temperature and decreasing pressure. They proposed a mechanism whereby the initial loss of a hydroxyl group generates a radical species that can undergo a β-scission reaction, yielding AA, which is in agreement with the mechanism proposed in Figure 4.

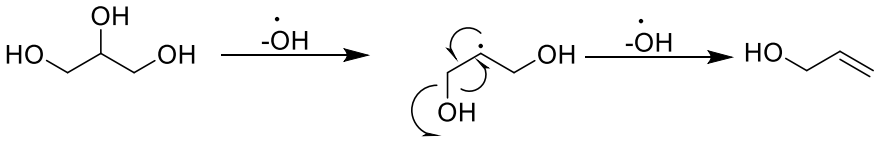

Figure 4. Proposed mechanism for the formation of allyl alcohol from glycerol *via* a radical mechanism

The selectivity to both HA and AA was found to decrease linearly with increasing GLY conversion, with selectivities of 23 and 22 % respectively at a reaction temperature of 480 °C. In contrast to this, the selectivity to unknown products increased as a function of temperature, suggesting that unidentified reaction pathways are taking place, and highlighting the complex nature of thermally initiated GLY conversions under catalyst free conditions. At higher reaction temperatures, significant quantities of ACA, ACR, 1,2-PD and EG were detected, with smaller quantities of MeOH, acetic acid, propanoic acid and 1,3-PD also observed. The inference of these results is that GLY can undergo thermal C-C and C-O cleavage under catalyst free conditions, potentially *via* a radical mechanism which is initiated through contact between GLY and a hot surface. Since similar products are observed under metal oxide catalysed conditions,[1] albeit with higher yields, the contribution of thermally formed products must be taken into consideration when assessing product distribution obtained over catalysts at high reaction temperatures.

3.2.2 Glycerol conversion over magnesium oxide

A magnesium oxide catalyst was prepared by a reflux method, from commercially available magnesium hydroxide. Briefly, $Mg(OH)_2$ was calcined under static air at 450 °C (10 °C min^{-1}) for 24 hours to generate magnesium oxide. This was then refluxed in deionised water (15 mL g^{-1}) for 3 hours to form a slurry which was dried at 110 °C for 24 hours. A final heat treatment step (600 °C, 10 °C min^{-1}, 3 hours, flowing N_2) was then utilised to obtain the final oxide catalyst; an overview of the catalyst preparation method is shown in Figure 5.

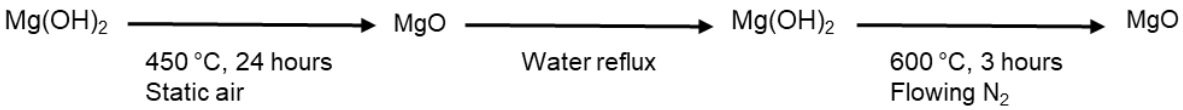

Figure 5. An overview of the MgO catalyst preparation method.

After the initial calcination of commercially available $Mg(OH)_2$, MgO with a surface area of 24 m^2 g^{-1} was obtained. Subsequent refluxing of the oxide in water regenerated $Mg(OH)_2$ with an enhanced surface area, which was then heat treated to generate MgO with a surface area of 129 m^2 g^{-1}. The corresponding XRD patterns of MgO after the initial calcination and after the final heat treatment are shown in Figure 6; prior to the reflux, MgO had a crystallite size of 27 nm whereas a crystallite size of 8 nm was obtained for the final catalyst. The rehydration of low surface area MgO induced significant physical changes with a dramatic

reduction in crystallinity and increase in surface area. This catalyst preparation method was used in the initial report of GLY to MeOH,[1] and so was utilised here for consistency.

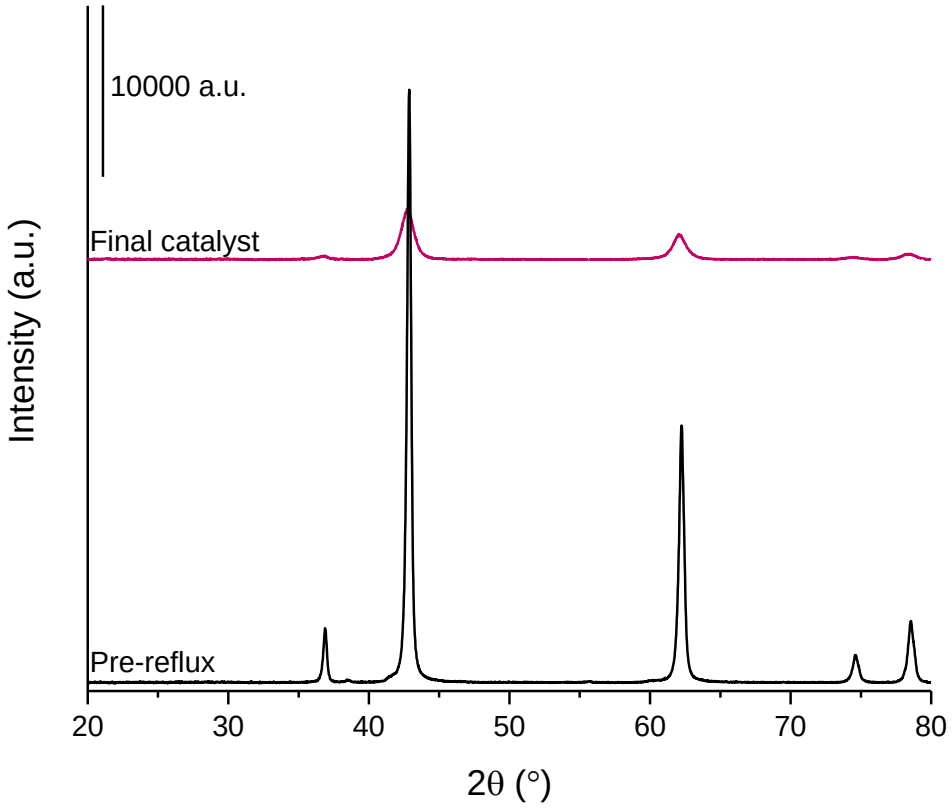

Figure 6. PXRD patterns of MgO after calcination and after a calcination, reflux, calcination cycle

The basicity of the final catalyst was investigated by CO_2-TPD (Figure 7), a well-established technique for probing the basic sites of MgO.[11, 12] The amount of desorbed CO_2 was calculated to be 457 μmol g^{-1} which corresponded to 3.5 μmol m^{-2}. This value is in good agreement with values previously reported in literature for similar catalyst preparation methods.[11, 13]

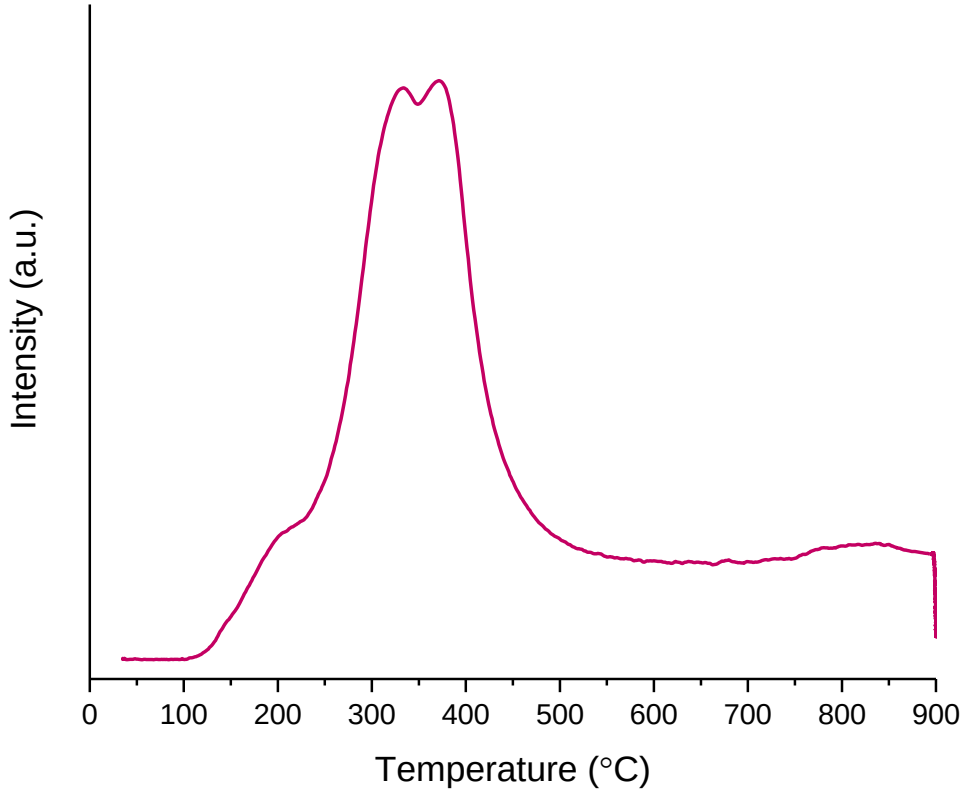

Figure 7. CO_2 TPD profile of MgO catalyst.

3.2.2.1 The effect of temperature

The effect of reaction temperature on GLY conversion is shown in Table 1, with selectivities to functional groups shown in Figure 8. A GLY conversion of 74 % was obtained at a reaction temperature of 360 °C, with full conversion reached above 440 °C. Across all temperatures investigated, the carbon mass balance was found to be in the range of 73 – 77 % and decreased with increasing reaction temperatures. More details surrounding the carbon balance are discussed in section 3.2.2.4. Liquid phase products accounted for more than 50 % of all carbon injected. The major products detected and their respective selectivites at a reaction temperature of 400 °C were MeOH (27.9 %), HA (17.9 %), ACA (13.3 %) and EG (5.8 %), with smaller quantities of propionaldehyde, ACR, EtOH, 2,3-BD, AA, acetic acid and 1,2-PD also detected. Numerous unidentified peaks were also observed in the chromatograms of the liquid product mixture; it was not possible to identify these additional products by comparison with commercial samples, so selectivity towards all unknown products is grouped and calculated based on an average response factor. Some additional liquid phase products were however detected and quantified, including ACE, butyraldehyde, propanol, butanol, hexanone, cyclopentanone, 3-ethoxy-1-propanol, propionic acid, 1,3-PD and phenol, although selectivity to these products was low at all reaction temperatures. Gaseous products detected included CO, CO_2 and traces of CH_4, no higher hydrocarbons were observed, despite the presence of numerous C_2-C_4 products in

the liquid phase. It is interesting to note that across the temperature range investigated, selectivity to AA remained low (< 2.5 %), in contrast to the catalyst free reactions performed over SiC. The significantly reduced AA selectivity and high HA selectivity observed over MgO indicate that the catalyst promotes the activation of a primary alcohol, inhibiting the radical mechanism for AA formation.

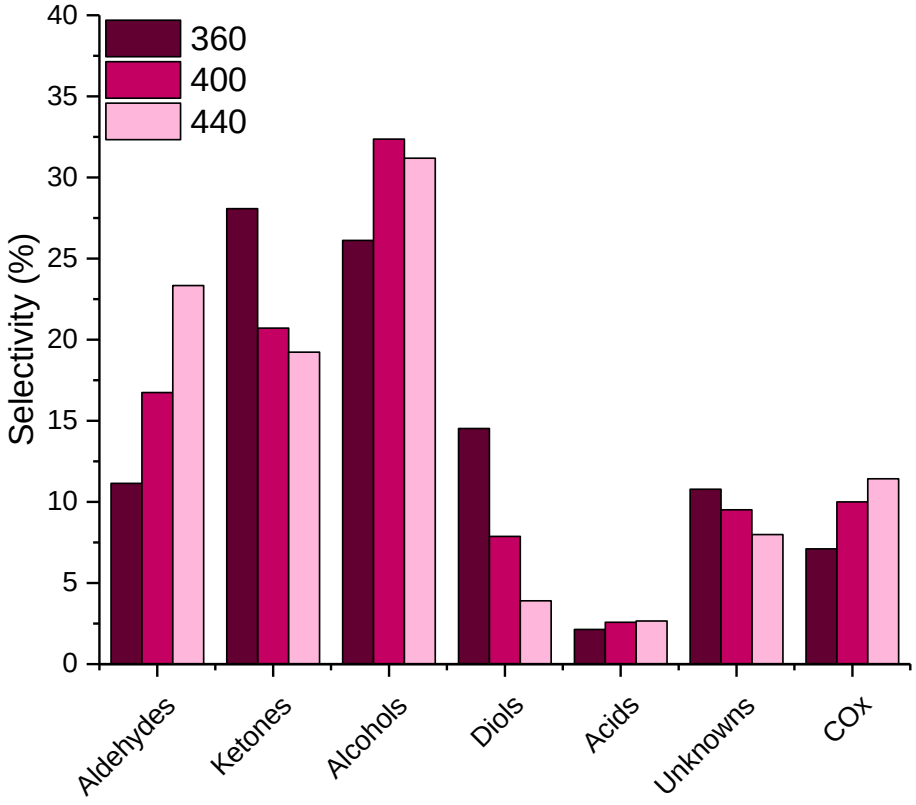

Figure 8. Collected product selectivies expressed as functional group selectivites following reaction over MgO at 360 (dark burgundy), 400 (pink) and 440 °C (pale pink). Reaction conditions; 50 wt. % glycerol (0.016 mL min^{-1}), 0.5 g MgO, 50 mL min^{-1} Ar, 3 hours, GHSV = 4615 h^{-1}.

A variation in product selectivity was observed with reaction temperature, the products are grouped into functional groups and summarised in Figure 8. The major product at lower temperatures was HA, accounting for the high ketone selectivity, which decreased with increasing reaction temperature, highlighting its role as an intermediate in the reaction. Similar trends were observed for diols, including 1,2-PD, 1,3-PD and EG, suggesting they too are further converted with increasing reaction temperature and GLY conversion.

In keeping with the catalyst free reactions, increasing reaction temperatures favoured selectivity to aldehydic products over MgO, with significant quantities of ACA produced (17 % at 440 °C) alongside smaller quantities of propionaldehyde and ACR (both *ca.* 3 %). In contrast to the aldehydes, alcohol selectivity reached a maximum at 400 °C, with a MeOH selectivity of 28 %, corresponding to a space-time-yield of 205 g h^{-1} $kg^{-1}_{cat.}$ Due to the

increased selectivity towards undesirable by-products such as ACA and CO_x at temperatures above 400 °C, higher reaction temperatures were not further explored.

Similar results were obtained when exploring the effect of carrier gas flow rates. The effect of reaction temperature was explored using a GHSV of 4615 h^{-1} so additional experiments were performed at 400 °C, with GHSVs of 2300 h^{-1} and 6920 h^{-1}. Due to technical issues with GC2, used to analyse carbon containing gases, it was not possible to obtain full product distributions and carbon balances. Comparable effects were observed with increasing reaction temperatures and decreasing GHSV and *vice versa*. Decreasing the GHSV from 4615 h^{-1} to 2300 h^{-1} resulted in full GLY conversion whilst increasing the GHSV to 6920 h^{-1} resulted in a decrease in conversion from 90 % to 78 %. A higher selectivity towards intermediate products, such as HA and 1,2-PD is observed with an increased GHSV with a reduced selectivity towards terminal products such as MeOH and ACA. Conversely, a decreased GHSV resulted in a higher selectivity towards terminal reaction products such as MeOH, ACA and ACE due to the increased conversion of intermediates such as HA.

Whilst the route to the main products was established in the initial report of GLY to MeOH,[1] the experiments discussed above, all performed with 50 wt.% GLY, and the use of more advanced analytical techniques allowed for the development of a reaction network, detailing the proposed routes for the proposed routes for numerous products. As shown in Figure 9, the route to the main terminal products, MeOH and ACA, is complex. Both are formed through the radical fragmentation of HA; additionally, the radical fragmentation of GLY produces a MeOH radical and an EG radical, the latter can form EG which can subsequently dehydrate to give ACA. The complexity of the reaction scheme and number of products formed make kinetic and thermodynamic analysis a significant challenge due to the number of competing reactions, and for this reason, it was not undertaken.

Product identification and quantification was performed by the collection of liquid and gas phase products and offline analysis by GC. Products were identified by GC-MS and then quantified with GC-FID using commercial standards. It should be noted that products **2** and **17**, 3-hydroxypropanal and ethenone, respectively, were neither confirmed or quantified by GC, due to their highly reactive nature and reasonably high reaction conditions used. Despite this, they have been well reported in literature,[14-18] and products obtained from these intermediates have been confirmed thus providing good support to their role as intermediates in the process. Radical intermediates were not detected due to their highly reactive, short lived nature; however, the presence of certain products provide good evidence for their presence. An example of this is 2,3-BD, a C_4 vicinal diketone, that seems unlikely to form from GLY, except through the coupling of two acetyl radicals.

Table 1. Glycerol conversion and product distribution over MgO at different temperatures.

Entry	***Condition (°C)***	X_{GLY} [a] ***(%)***	***Mass Balance (%)*** [b]			***Yield (%)***							***MeOH S.T.Y. (g^{1} h^{-1} kg^{-1})***	***Carbon deposition (mg g^{-1})***
			C	***H***	***O***	***Alc.***	***Diols***	***Ald.***	***Ket.***	***Ac.***	***COx***	***Unk.***		
1	360	74.0	74 (77)	72	67	19.5	10.7	8.2	20.8	1.6	5.3	8.0	131	81
2	400	89.9	73 (77)	71	61	29.2	7.1	15.0	18.6	2.3	6.9	8.5	205	122
3	440	100	68 (73)	61	55	31.5	3.9	23.3	19.2	2.7	11.1	8.0	204	125

[a] GLY conversion, [b] Carbon mass balance (± 3 %) values in parenthesis include catalyst carbon deposition, [c] Alc., alcohols; Ald., aldehydes; Ket., ketones; Ac., acids; Unk., unknowns (Full product list in Table A3.2). Reactions performed with 500 mg MgO; 50 mL/min Ar carrier gas; 3 hour reactions; 50 wt. % GLY; GHSV = 4615 h^{-1}.

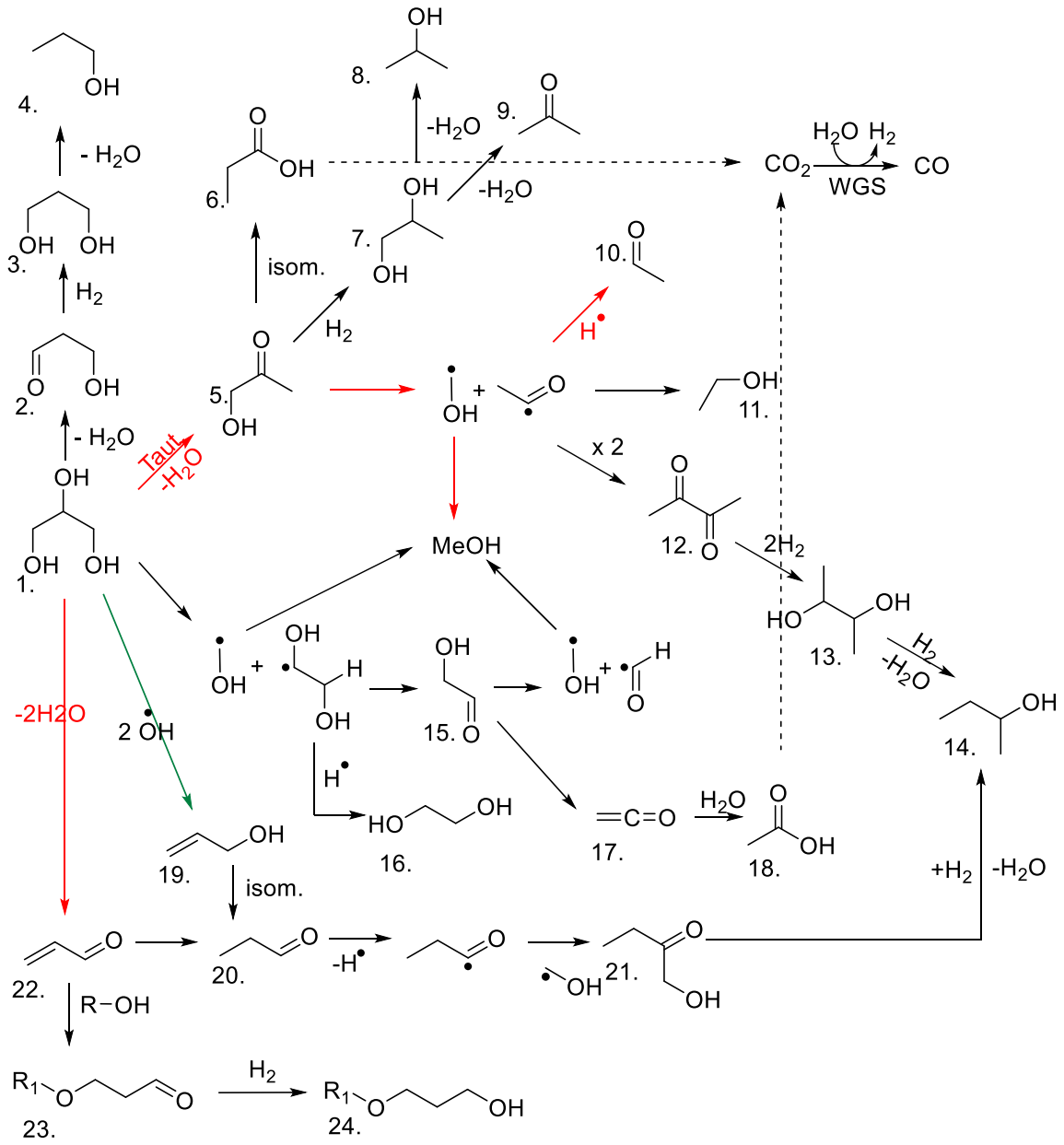

Figure 9. Proposed reaction network for the catalytic transformation of glycerol into a range of different products over MgO under argon. Red arrows correspond to dominant reaction pathways over MgO. The green arrow corresponds to a dominant pathway occurring in the absence of MgO. 1. glycerol; 2. *3-hydroxypropanal*; 3. 1,3-propanediol; 4. 1-propanol; 5. hydroxyacetone; 6. propanoic acid; 7. 1,2-propanediol; 8. 2-propanol; 9. acetone; 10. acetaldehyde; 11. ethanol; 12. 2,3-butanedione; 13. 2,3-butandiol; 14. 2-butanol; 15. glycolaldehyde; 16. ethylene glycol; 17. *ethenone*; 18. acetic acid; 19. allyl alcohol; 20. 1-propanal; 21. 1-hydroxyl-2-butanone; 22. acrolein; 23. 3-alkoxypropanal; 24. 3-alkoxy propanol. Figure reproduced from *Catal. Sci. Technol.*, 2019, 9, 1464-1475 - Reproduced by permission of The Royal Society of Chemistry.

3.2.2.2 The effect of feedstock concentration

Whilst all the reactions performed thus far have utilised 50 wt.% GLY feedstocks, catalytic GLY valorisations are typically performed with more dilute solutions, which along with varying carrier gas flow rates, makes direct comparison of space time yields difficult.[19, 20] The use of more concentrated feedstocks is highly desirable, due to the increased energy demands associated with vaporising larger quantities of water.[21] Despite this, the high

functionality of GLY can often lead to undesired side-products and reduced selectivity to the desired product.[22] Due to the high viscosity of GLY, feedstocks above 50 wt.% GLY were not explored, due to the potential to damage the HPLC pump responsible for introducing the GLY feed.

A series of reactions were performed whereby the feedstock was varied between 10 and 50 wt.%, whilst the mass of MgO catalyst was kept constant (500 mg), leading to varying catalyst to GLY ratios. An increase in GLY concentration from 10 to 50 wt.% resulted in an increase in GLY partial pressure from 0.026 mbar to 0.14 mbar, with an associated decrease in water partial pressure from 0.29 to 0.18 mbar. An additional reaction was also performed with 10 wt.% GLY and 100 mg of MgO to examine the effect of feedstock concentration with a constant catalyst to GLY ratio.

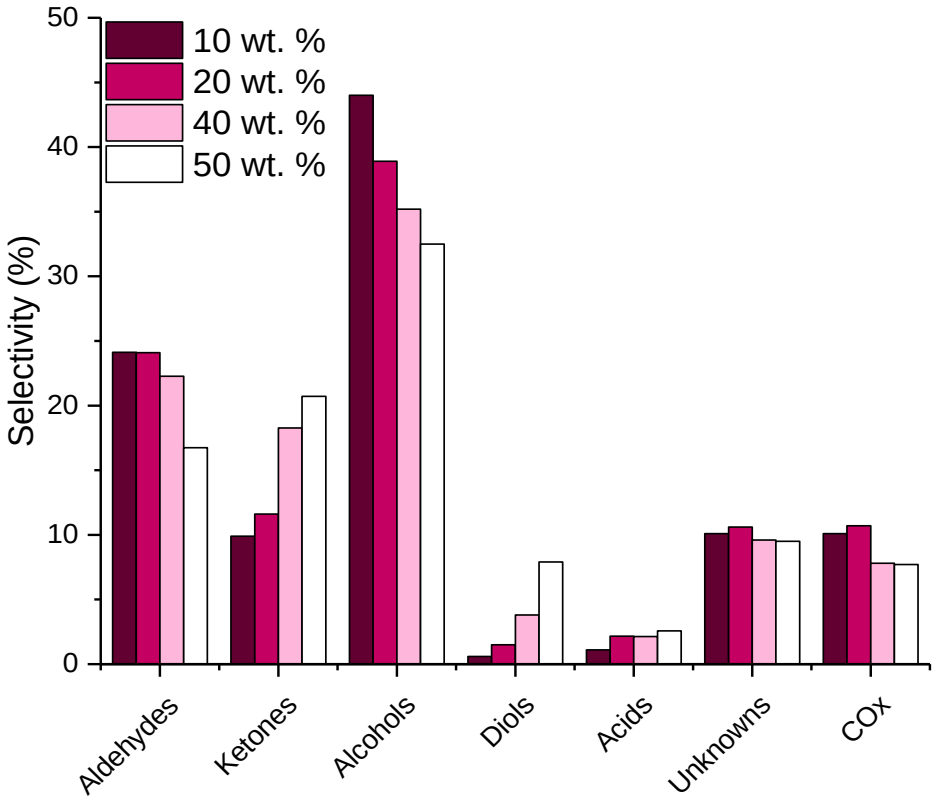

Figure10. Collected product selectivities expressed as carbon mole selectivity following reaction with 10 wt. % (dark burgundy; catalyst to glycerol (g/g) ratio of 1.8), 20 wt. % (pink, 0.8), 40 wt. % (pale pink, 0.4) and 50 wt. % (white, 0.3) over MgO. Reaction conditions; 400 °C, glycerol/water flow 0.016 mL min^{-1}, 0.5 g MgO, 50 mL min^{-1} Ar, 3 hours.

Product group selectivity as a function of GLY wt.% is shown in Figure 10, with the associated GLY conversions and products yields in Table 2. Only a trace of unconverted GLY was detected with a 40 wt.% GLY, whilst complete conversion was obtained from more dilute feedstocks. The carbon balance was shown to increase with decreasing GLY concentration. A potential explanation for this is the presence of additional products, likely with high molecular weights, which are undetectable through GC methods and thus are not

counted in the carbon balance. The formation of high molecular weight products has been reported to increase with increasing GLY concentration, and a higher GLY partial pressure would favour the formation of such products. Additionally, as water is known to help prevent condensation reactions, the higher partial pressure of water present through the use of more dilute GLY feedstocks could help prevent the formation of larger organic species.[23, 24]

Whilst similar products were obtained across all the reactions, the relative product selectivities varied as a function of GLY feedstock concentration and catalyst to GLY ratio. An increased ratio of catalyst : GLY, obtained with more dilute feedstocks, resulted in increased alcohol and aldehyde selectivities, comprised predominantly of MeOH and ACA, respectively. This was accompanied by a significant reduction in selectivity towards HA and EG. These results were not unexpected since it is sensible to suggest an increase in the ratio of catalyst to substrate would favour the production of terminal products at the expense of intermediates. The low diol selectivity observed with increasing catalyst to GLY ratio suggests that 1,2-PD and 1,3-PD can also be further converted. Similar findings were made by Montassier *et al*,[25] in a study into GLY hydrogenolysis whereby it was found that EG was readily converted to C_1 products at full GLY conversion.

MeOH selectivity increased with increasing proportions of catalyst, reaching a maximum of 34.9 % with 10 wt.% GLY and 500 mg MgO. In addition to MeOH, EtOH, 1-PrOH and 3-ethoxy-propanol were all found to increase with increasing catalyst to GLY ratios. For all the reactions performed over 500 mg of catalyst, the MeOH space time yield was highest for a 40 wt.% GLY feedstock, with a value of 219 g h^{-1} kg_{cat}^{-1}. A slightly lower value of 205 g h^{-1} kg_{cat}^{-1} was achieved with a 50 wt.% GLY feedstock, attributed to both the lower GLY conversion and carbon balance.

An additional reaction with 100 mg of catalyst and a 10 wt.% GLY feedstock was also performed and compared with a reaction; the 50 wt.% reaction described above. As the catalyst to GLY ratio was constant across these two reactions, the MeOH space time yield could be directly compared, and was found to be 255 and 205 g h^{-1} kg_{cat}^{-1} for the 10 and 50 wt.% reactions, respectively. This improvement was due to increases in carbon balance, GLY conversion, and MeOH selectivity. Whilst the MeOH selectivity was somewhat improved for the more dilute feedstock, at a constant GLY to catalyst ratio, a largely comparable product distribution is obtained. Due to the complex nature of the reaction scheme, deconvolution of the effects of catalyst to GLY ratio, GLY partial pressure, and catalyst contact time on MeOH yield are extremely challenging.

Table 2. Glycerol conversion and product distribution over MgO with differing feedstock concentration.

Entry	***Glycerol weight %***	***Cat : gly ratio (g/g)***	C_{GLY} [a] ***(%)***	***Mass Balance (%)*** [b]			***Yield (%)***							***MeOH S.T.Y. (g h^{-1} kg^{-1})***	***Carbon deposition (mg g^{-1})***
				C	***H***	***O***	***Alc.***	***Diols***	***Ald.***	***Ket.***	***Ac.***	***COx***	***Unk.***		
1	10	1.8	100	83 (84)	80	68	44.0	0.6	24.1	9.9	1.1	10.1	10.1	61	55
2	10	0.3[d]	96	83 (98)	84	67	37.5	8.4	16.7	19.6	1.2	3.3	9.4	255	75
3	20	0.8	100	80 (88)	76	67	38.9	1.5	24.1	11.6	2.2	10.7	10.6	105	80
4	40	0.4	99	78 (81)	74	62	34.8	3.8	22.1	18.1	2.1	7.7	9.5	219	87
5	50	0.3	90	73 (77)	71	61	29.3	7.1	15.0	18.6	2.3	6.9	8.6	205	122

[a] GLY conversion, [b] Carbon mass balance (± 3 %) – values in parenthesis include catalyst carbon deposition, [c] Alc., alcohols; Ald., aldehydes; Ket., ketones; Ac., acids; Unk., unknowns (Full product list in Table A3.3), [d] 100 mg catalyst used. Reactions performed with 500 mg MgO; 50 mL/min Ar carrier gas; 3 hour reactions; 400 °C; GHSV = 4615 h^{-1}.

3.2.2.3 Investigating catalyst stability

It is reasonable to anticipate a greater degree of catalyst deactivation with a more concentrated glycerol feedstock therefore the longer-term stability of the catalyst was investigated with a 50 wt.% GLY feed. All reactions, including the longer-term study, were performed with a "steady state" period of 2 hours 15 minutes, whereby the product mixture was diverted to a gas bubbler after the GLY flow is initiated. Collection and analysis of the product mixture during this 2-hour 15-minute period showed an extremely poor carbon balance, with an unstable product distribution. Following this period, products were periodically collected and analysed, as shown in Figure 11. A drop in GLY conversion of *ca.* 10 % was observed between hours 2 and 4, before stabilising at approximately 87 %. This was accompanied by an increase in carbon balance in the initial hours, before stabilising at *ca.* 65 % over the 48-hour period investigated.

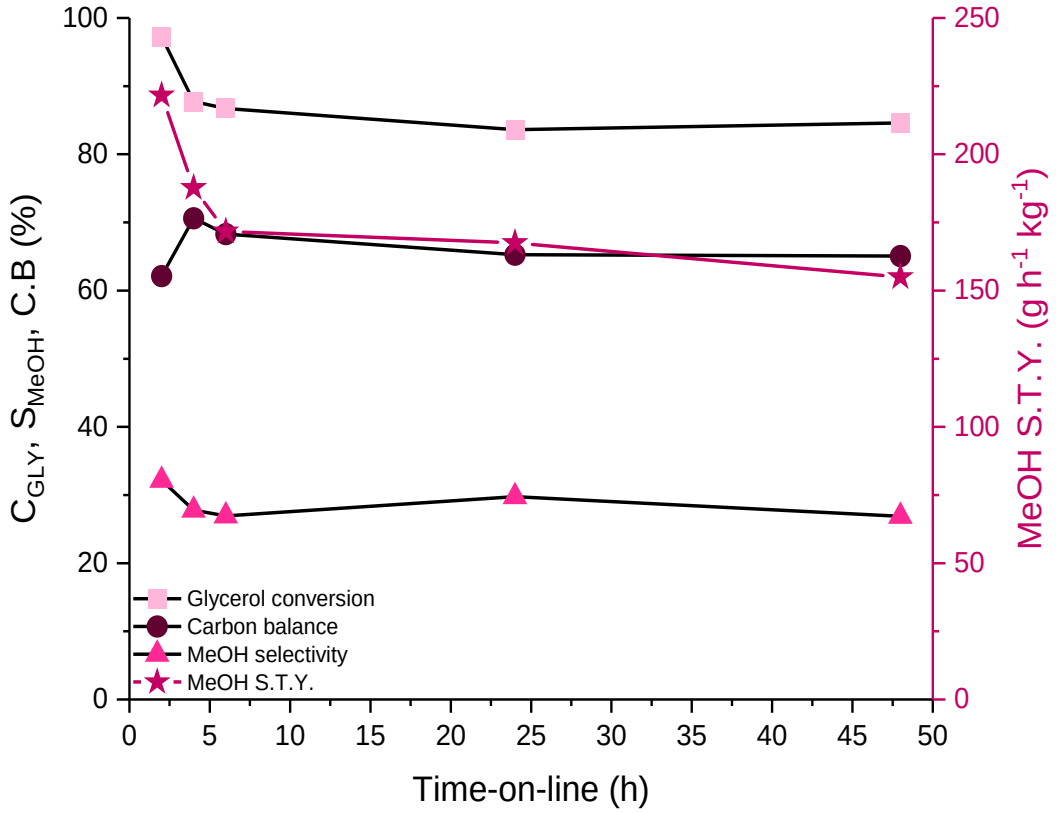

Figure11. Glycerol conversion (■), carbon balance (●), MeOH selectivity (▲), and MeOH space time yield (⋆) over MgO catalyst as a function of reaction time. Reaction conditions; 400 °C, glycerol flow (0.016 mL min^{-1}), 0.5 g MgO, 50 mL min^{-1} Ar.

Both MeOH selectivity and space time yield followed the same trend as GLY conversion, with a drop observed between hours 2 and 4, before stabilising. The constant levels of GLY conversion from between 4 and 48 hours on-line suggest that a period of 4 hours is required to achieve a steady-state system; after this time both conversion and product distribution (Table A3.4) were stable. The stability of the catalyst under these conditions is surprising given the poor carbon balance obtained but these results suggest that any carbon deposition

on the catalyst does not sufficiently block active sites to result in catalyst deactivation. Analysis of the catalyst after 48 hours on-stream by PXRD (Figure 12) showed no significant differences; the crystallite size, as estimated with the Scherrer equation applied to the (200) plane, was 94 Å pre-reaction and 90 Å, indicating no sintering or growth of the MgO catalyst during the reaction. Additionally, no sign of $Mg(OH)_2$ was observed; the transformation of MgO to $Mg(OH)_2$ upon exposure to liquid water is well known, but no such transformation was observed under the reaction conditions employed here, likely due to the relatively low contact time between water and the catalyst, and the high reaction temperature.

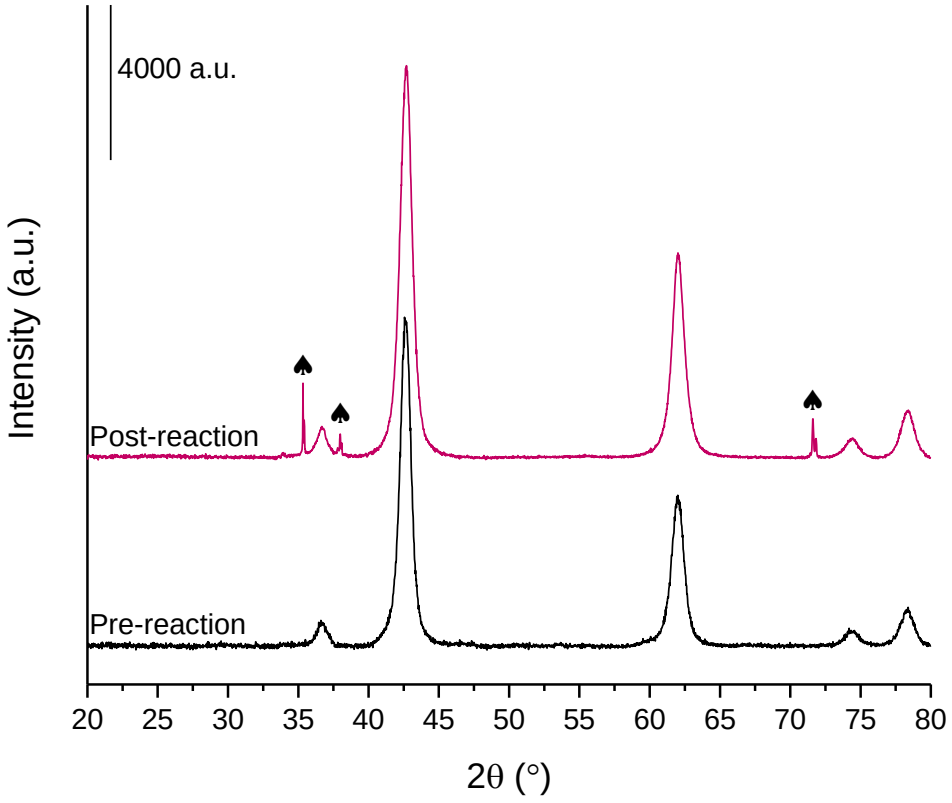

Figure 12. X-Ray diffraction patterns for the fresh, pelleted MgO catalyst and a used pelleted MgO catalyst after reaction with 50 wt.% glycerol in H_2O for 3 h at 400 °C. Residual SiC from the catalyst bed denoted with (♠).

3.2.2.4 Investigating the carbon balance

The stability of the catalyst over a longer time period despite the carbon balance prompted further investigations in an attempt to identify routes through which this carbon may be lost. Thermogravimetric analysis (TGA) was performed whereby a post-reaction sample was heated to 110 °C for a period of 30 minutes to remove any residual water prior to heating to 800 °C under a synthetic air environment. The pre-treatment step and absence of $Mg(OH)_2$ by XRD confirm that mass losses observed throughout the TGA experiments could be attributed to the presence of carbon based species on the catalyst surface. TGA experiments were performed on each post-reaction sample from the temperature and feedstock concentration studies, along with the sample retrieved after 48 hours of reaction.

All the used samples showed a significant mass loss which occurred at approximately 400 °C; the mass loss was accompanied by a significant exotherm, representative of the combustion of organic species from the catalyst surface, a representative example of the TGA-DTA heat flow measurement is shown in Figure 13.

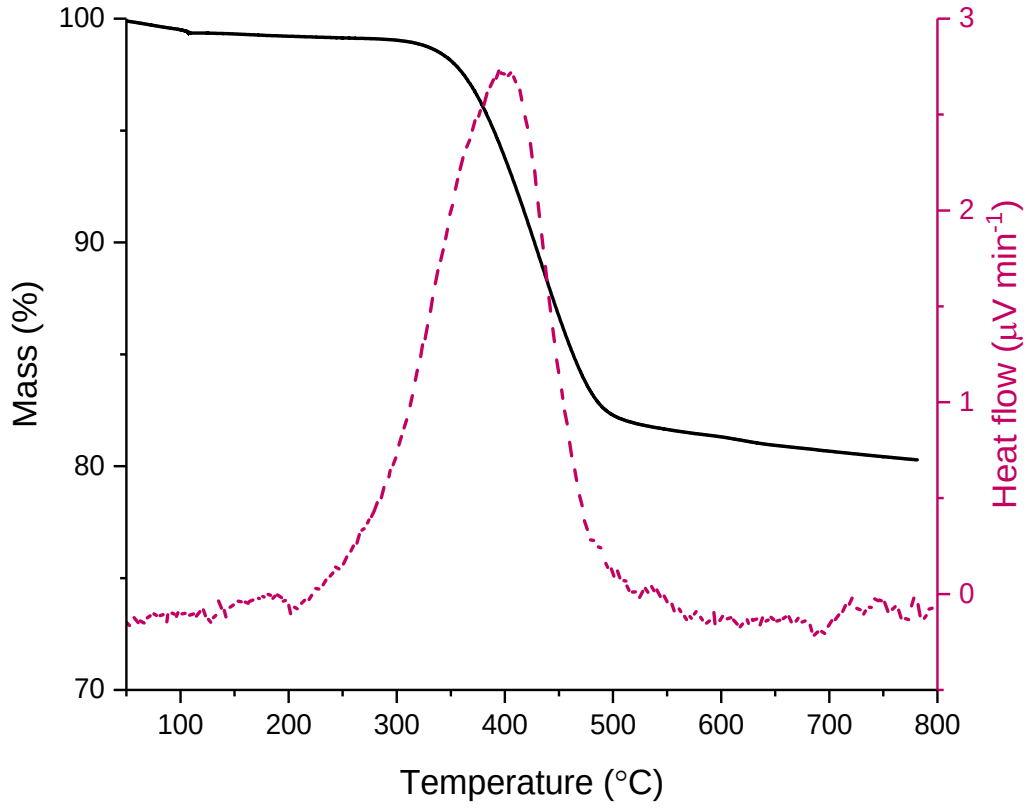

Figure 13. Thermogravimetric analysis of MgO showing mass loss (solid pink) and heat flow (black dashed line) after a 48 hour reaction at 400 C with 50 wt.% glycerol.

The mass losses obtained from the TGA experiments were used to estimate the quantity of carbon retained on the catalyst after a reaction, expressed as mg of carbon per gram of catalyst and are shown in Tables 1 and 2. Generally, an increasing reaction temperature and GLY concentration resulted in greater degrees of carbon deposition. As described above, the carbon balance is very poor during the 2-hour 15-minute (135 mins) period prior to product collection, thus an additional experiment was conducted whereby the catalyst was removed after this time. TGA showed the carbon deposition to be 80 mg g^{-1} compared with 122 mg g^{-1} after a typical 3 hour reaction (total time on-stream is 315 mins) representing a non-linear correlation between reaction time and carbon deposition, with a greater quantity of carbon deposited in the initial stages of the reaction. Coupled with the longer-term stability of the catalyst, these results suggest that the deposition of carbon on the catalyst surface at the start of the reaction could block a proportion of the catalytic sites responsible for catalyst coking and/or the production of undetected products.

Low carbon balances were also reported by Batiot-Dupeyrat and co-workers during investigations into GLY conversion over basic lanthanum-based catalysts.[2, 26] The findings of these studies suggested that high molecular weight organic species may also be produced under the reaction conditions. Additionally, GLY esterification and oligomerisation reactions have been reported over basic materials under comparable vapor phase reaction conditions.[27, 28] As the quantity of lost carbon increased with increasing GLY partial pressure (Table 2), it is reasonable to suggest the formation of high molecular weight products through intermolecular condensation reactions, that would be favoured through increased substrate concentration.

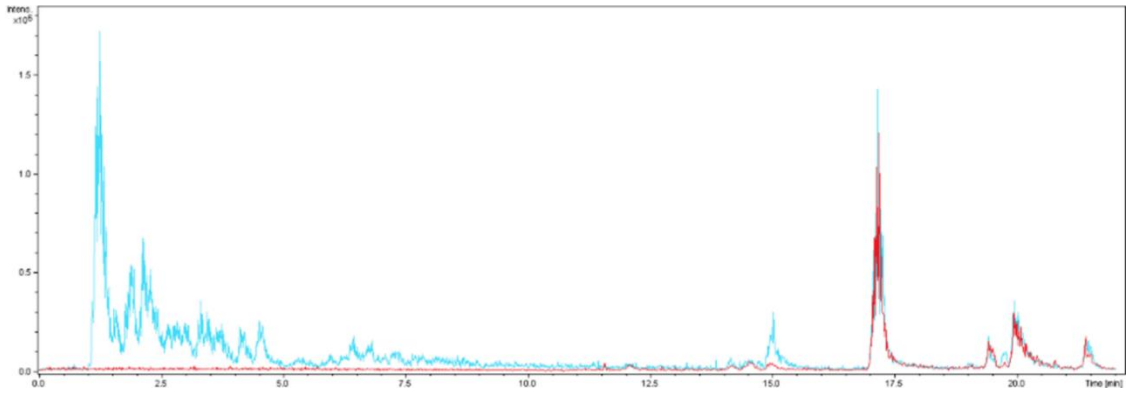

Figure 14. LC-MS chromatogram corresponding to the post reaction solution of a reaction run over MgO for 6 h. Detection parameters are fixed at 100 - 1000 m/z. Reaction conditions; 400 °C, glycerol flow (0.016 mL min^{-1}), 0.5 g MgO, 50 mL min^{-1} Ar, 3 hours. Blue line – chromatogram of the post reaction solution. Red line – chromatogram of a H_2O blank solution.

LC-MS analysis was performed in an attempt to identify the presence of any high molecular weight products, which would not have been observable through previous GC based analysis methods, due to their low volatility. A post reaction solution obtained after 6 hours at 400 °C with 50 wt.% GLY was first analysed by the usual GC methods prior to additional LC-MS analysis. Products and product fragments with *m/z* values between 100 and 1000 were screened. A blank sample of deionised water was also analysed to identify the presence of any contaminants. The obtained chromatogram (Figure 14) was extremely complex with numerous peaks present, preventing identification of any products. Despite this, the presence of numerous high molecular weight products was confirmed, providing evidence to the theory that the low carbon balance is a consequence of the presence of undetected products.

The carbon balance for this reaction as calculated from the liquid and gas phase products was 68 %. As it was only possible to perform qualitative LC-MS analysis, CHN analysis was also performed (analysis performed externally) on the liquid phase products to determine the total carbon content of the post-reaction sample. The sum of CHN analysis (76.8 %), gas phase products (11.7 %), and carbon deposition on the catalyst (5.5 %) provides a total

carbon balance and was 94 %. The remainder of missing carbon (6 %) has been attributed to reactor fouling due to experimental observations during post-reaction.

The above results highlight a key challenge surrounding the effective conversion of GLY to MeOH over MgO. Whilst reasonable MeOH selectivities were obtained, selectivity calculations do not account for missing carbon, and therefore, the poor carbon balances obtained must also be considered. As a basic material, it seems plausible that the basic properties of MgO are catalysing undesirable side-reactions such as the condensation reactions, with aldol condensations reported to occur readily over solid basic oxides.[29-31] The large organic molecules detected by LC-MS form through competitive reaction pathways, thus it is important to reduce these pathways without detrimental effect to the formation of desired products.

As described in the introductory chapter, the effective conversion of crude GLY is highly desirable. Due to the heterogeneous nature of crude GLY, the catalytic reactions discussed within this thesis were performed with high purity GLY, to exclude any influence from feedstock impurities from the obtained catalytic data. Nevertheless, crude GLY was obtained from Argent Energy (a large biodiesel producer) and used as a feedstock. Prior to the reaction, the crude sample was analysed and found to contain 67 wt. % GLY; small quantities of MeOH and 1,3-PD were also detected alongside longer carbon chain species. No significant difference in pH was measured between the pure (pH 6.8) and crude (pH 6.8) GLY samples. The reaction performed with a crude GLY feedstock over MgO showed comparable results to those achieved with high purity glycerol (Table A3.5). Difficulties were encountered with the use of a crude feedstock, due to the presence of inorganic contaminants (such as ash and catalyst residue) which could not be vaporised, leading to a build-up of solid material within the reactor. For this reason, no further reactions were performed with crude GLY. Whilst additional challenges were experienced through the use of crude GLY, these issues could be circumvented through improvements in the reactor design. The comparable catalytic activities observed with a high purity and crude GLY suggest that this process may provide an effective route for the valorisation of crude GLY feedstocks.

3.2.3 Glycerol conversion over ceria

3.2.3.1 The effect of reaction temperature

As described above, whilst good MeOH selectivities were achieved over a MgO catalyst, the observed carbon balance was often low, which was attributed to the formation of high molecular weight products, observed by LC-MS analysis. It was postulated that the high level of basicity of MgO was responsible for the formation of these high molecular weight products. Further experiments were performed with ceria, typically a less basic material

than MgO, in an attempt to improve upon the observable carbon balances whilst maintaining high selectivity to MeOH.

Commercially available ceria, obtained from Arcos Organics, was obtained and used as received (after pelleting) as a catalyst to investigate the effect of reaction temperature on GLY conversion. N_2 physisorption experiments showed the surface area to be low, with a value of 8 m^2 g^{-1} calculated in accordance with B.E.T. As shown in Figure 15 and Table 3, both GLY conversion and product distribution were significantly influenced by the reaction temperature. A low level of GLY conversion was achieved at 320 °C (21 %), which increased to 84 % at 360 °C. Almost complete conversion was observed at a reaction temperature of 400 °C (98 %), with full conversion reached at higher temperatures. At 320 °C the carbon balance was 100 %, reducing to 87 % at 360 °C, 80 % at 400 °C and 77 % at 440 °C. The excellent carbon balance achieved at the lowest reaction temperature was attributed to the modest level of GLY conversion, and the relatively low selectivity to more reactive species, such as ACA.

The main product detected at 320 °C was HA, with a selectivity of 49.1 %. HA selectivity steadily decreased with increasing reaction temperature, with only trace amounts detected at a reaction temperature of 440 °C. A similar trend was observed for EG and 1,2-PD, suggesting that both C_3 and C_2 oxygenates with more than one hydroxyl group and/or carbonyl group can be further converted to terminal reaction products.

The decreasing selectivity towards ketones (primarily HA) and diols with increasing reaction temperature was accompanied by increasing selectivity to alcohols, aldehydes and CO_x. MeOH selectivity increased steadily from 6.7 % at 320 °C to 15.7 % at 440 °C, whilst ACA increased from 4.6 to 17.0 % across the same temperature range. In addition to increasing ACA and MeOH selectivity with increasing reaction temperature, increases in ACE and 2,3-BD were also observed, which is reflected in the reasonable ketone yield even at the highest reaction temperature. This was to be anticipated since MeOH, ACA, ACE and 2,3-BD can all form through HA and so their increase correlates with reductions in HA yields.

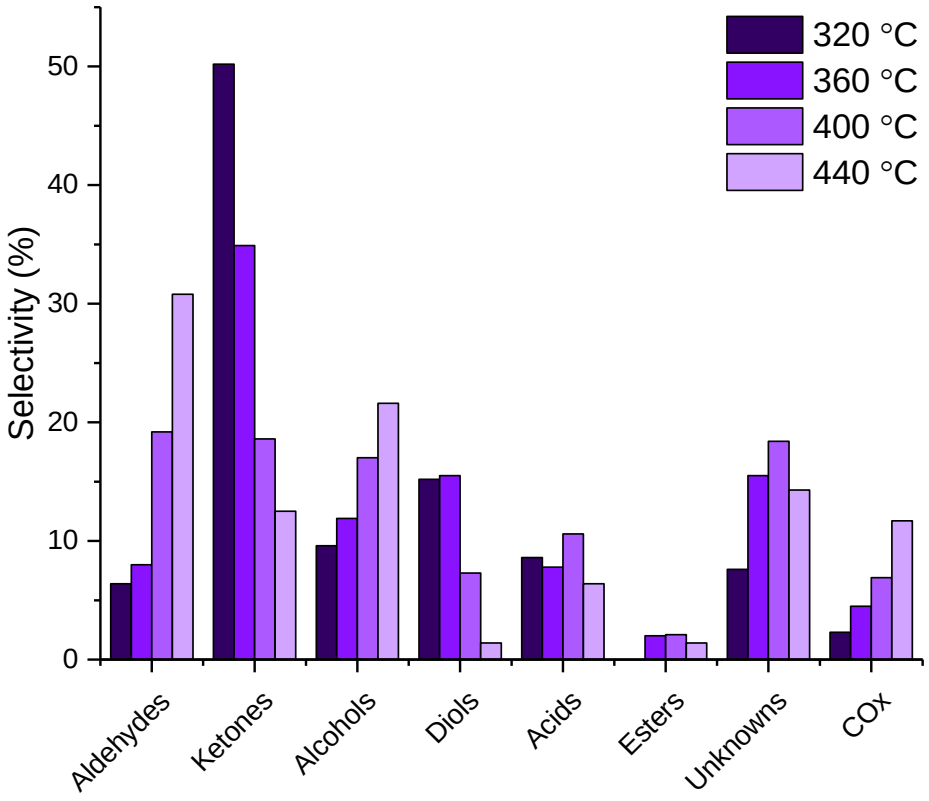

Figure 15. Influence of the reaction temperature on the product group selectivity at 320 °C (darkest purple bar), 360 °C (dark purple), 400 °C (light purple) and 440 °C (lightest purple bar). Reaction conditions; CeO_2 (8 m^2 g^{-1}) 1.5 g, 50 wt.% glycerol (0.016 mL min^{-1}) Ar 45 mL min^{-1}, GHSV 4154 h^{-1}.

The aldehyde yield increased with increasing reaction temperature and was comprised of ACA, ACR and propionaldehyde, all of which were favoured by higher temperatures. The MeOH space time yield also increased when the reaction temperature was increased, with values of 15.8, 59.8, 100.2 and 145.7 g_{MeOH} kg_{cat}^{-1} h^{-1} at 320, 360, 400 and 440 °C, respectively. Whilst MeOH productivity was favoured with increasing reaction temperature, at 440 °C the total aldehyde selectivity exceeded 30 %. Since aldehyde and CO_x production was favoured by increasing reaction temperature under both catalysed and catalyst free reactions, 400 °C was determined to be the maximum operating temperature for future experiments to try and minimise selectivity to these undesirable by-products.

Table 3. Glycerol conversion and product yield distribution for reactions over commercial CeO_2 performed at different temperatures.

Reaction temperature (°C)	X_{GLY} [a] ***(%)***	***Mass Balance (%)*** [b]			***Yield (%)*** [c]								***MeOH S.T.Y. (g h^{-1} kg^{-1})*** [d]
		C	***H***	***O***	***Alc.***	***Diols***	***Ald.***	***Ket.***	***Ac.***	***COx***	***Est.***	***Unk.***	
320	21	100	97	95	2.0	3.1	3.1	10.6	1.8	0.5	0.0	1.6	16
360	84	87	78	72	10.1	12.9	12.9	29.4	6.6	3.7	1.7	13.0	60
400	98	80	68	62	16.6	6.9	6.9	18.3	10.4	6.7	2.0	18.1	100
440	100	77	62	57	21.6	1.3	1.3	12.5	6.3	11.6	1.3	14.3	146

[a] GLY conversion; [b] Carbon mass balance (± 3 %) of products detected in GC1 and GC2, [c] yield of products detected in GC1 and GC2; Alc., alcohols; Ald., aldehydes; Ket., ketones; Ac., acids; Est., esters; Unk., unidentified products; [d] MeOH space time yield. Reaction conditions; 1.5 g CeO_2, 50 wt.% GLY (0.016 mL min^{-1}), Ar 45 mL min^{-1}, GHSV *ca*. 4154 h^{-1}.

3.2.3.2 The effect of calcination temperature

Whilst the previous section showed that commercially available low surface area ceria (8 $m^2\ g^{-1}$) could be effective catalyst for the conversion of GLY to MeOH but a high reaction temperature (> 400 °C) was required. At these temperatures, high levels of ACA and CO_x were also detected. Therefore, it was proposed that modifications to the catalyst surface area may result in increased MeOH yields at lower reaction temperatures. In order to investigate this, a series of catalysts were prepared by calcining a cerium hydroxide pre-cursor at various temperatures, to study the effect of ceria calcination temperature on surface area and crystallite size, and the subsequent effect on product distribution. Cerium hydroxide was prepared through the precipitation of a cerium(III) nitrate precursor with ammonium hydroxide at pH 9. The recovered solid was then dried at 120 °C for 16 hours before calcination under static air at 400, 500, 600 or 700 °C.

The PXRD patterns obtained for the ceria catalysts calcined at different temperatures is shown in Figure 16. All reflections were indexed to the cubic fluorite CeO_2 phase (JCPDS no. 34-0394, space group *Fm3m*) with no pre-cursor or impurity peaks detected. The intensity of diffraction peaks increased with higher calcination temperatures accompanied by decreasing peak widths, representing an increase in crystallinity with increasing calcination temperatures. The crystallite size was estimated using the Scherrer equation applied to the (111) reflection and was found to increase from 14 to 19 nm as the calcination temperature was increased from 400 to 700 °C. Similar findings were made by Mamontov *et al.*,[32] who found that any increases in crystallite size induced through an increase in calcination temperature remained, even once the sample was cooled back down to room temperature.

The effect of calcination temperature on the surface area of the materials was explored by N_2 sorption experiments. The isotherms are shown in Figure 17, with no significant differences observed across the materials.

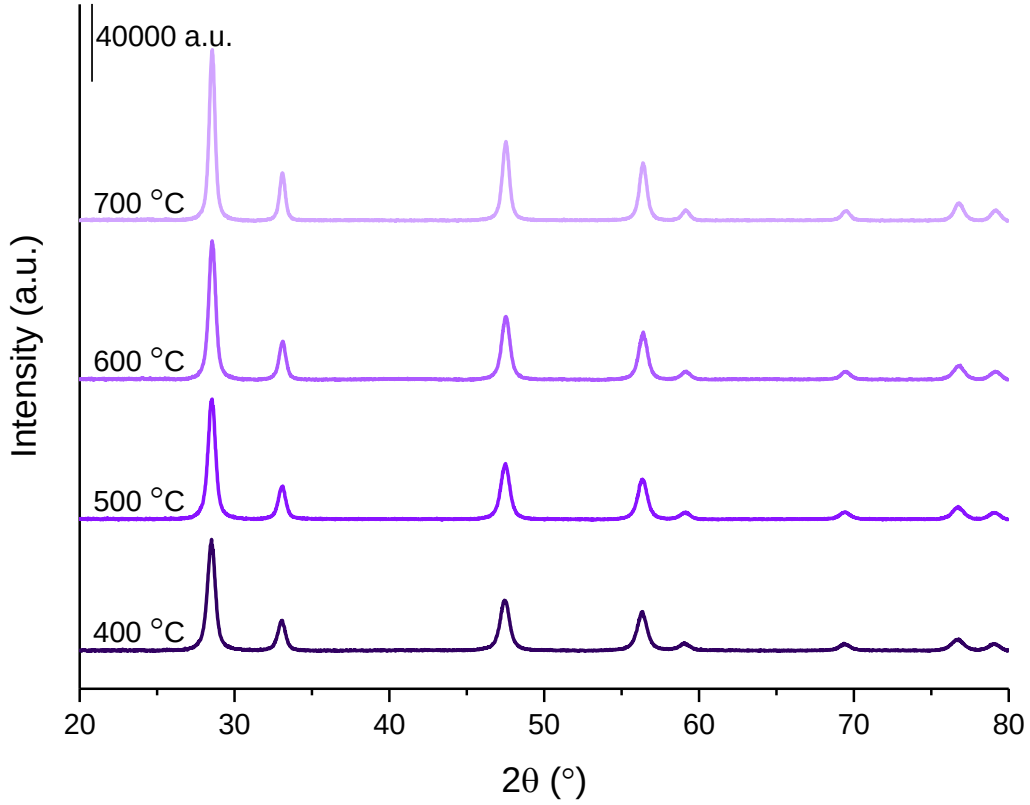

Figure 16. PXRD patterns of CeO_2 prepared by precipitation with ammonium hydroxide solution and calcined at different temperatures.

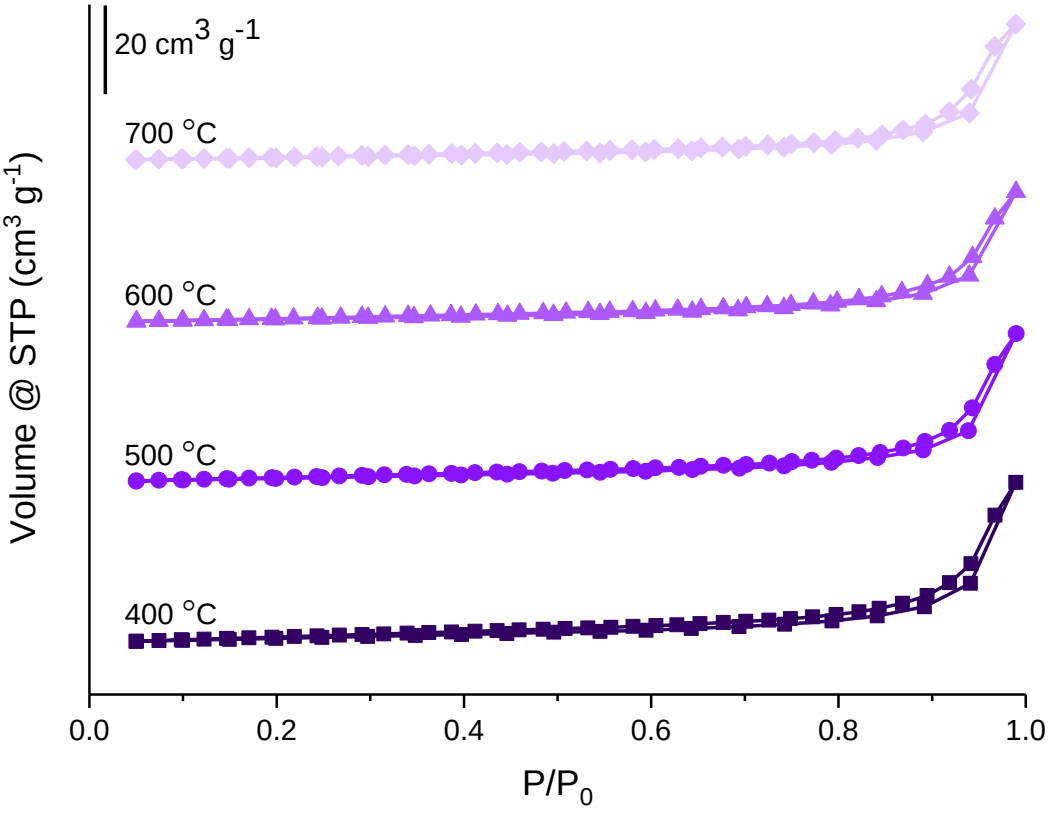

Figure 17. N_2 sorption isotherms for CeO_2 calcined at different temperatures.

As shown in Figure 18, the surface area of the obtained ceria decreased linearly with increasing calcination temperature. This loss of surface area was expected due to the

corresponding increase in crystallite size. A surface area of 38 m^2 g^{-1} was obtained by calcination at 400 °C, which reduced to 22 m^2 g^{-1} upon increasing the temperature to 700 °C

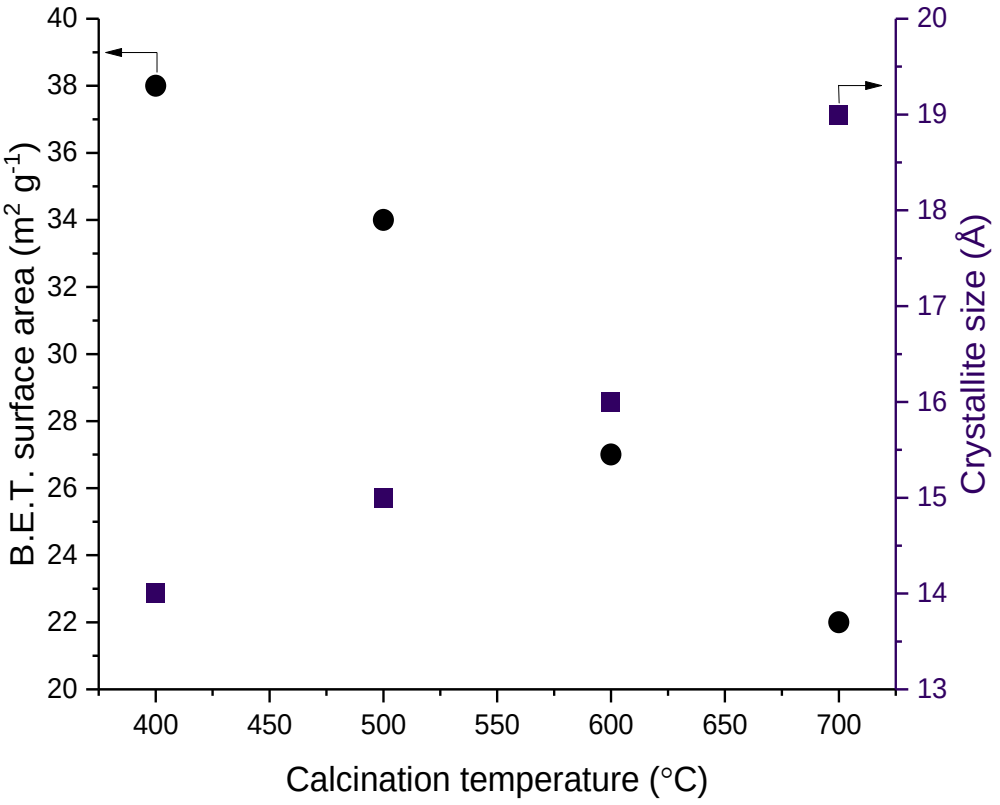

Figure 18. B.E.T. surface areas and crystallite sizes as a function of calcination temperature.

Additional analysis of the catalysts was also performed using Raman spectroscopy, a well-studied technique for the characterisation of ceria-based catalysts, particularly defect properties. The Raman spectra are shown in Figure 19 and were dominated by an intense F_{2g} mode at *ca.* 462 cm^{-1} which represents the symmetrical stretch of the Ce-O_8 lattice,[33, 34] where Ce and O are 8- and 4-coordinate, respectively. In addition to the dominant F_{2g} mode, an additional peak was observed at *ca.* 600 cm^{-1}. This much weaker band has been attributed to a defect mode, with the relative intensities of the defect band and F_{2g} band (I_D/I_{F2g}) used as an estimate of the defect density of ceria-based materials. Numerous investigations into the nature of this defect band have been undertaken. Whilst the defect band is widely acknowledged to represent oxygen defects, some authors ascribe it to Frenkel-type defects,[35] whilst others attribute it to oxygen vacancies which are required to maintain overall charge neutrality in the presence of Ce^{3+} cations.[36-38]

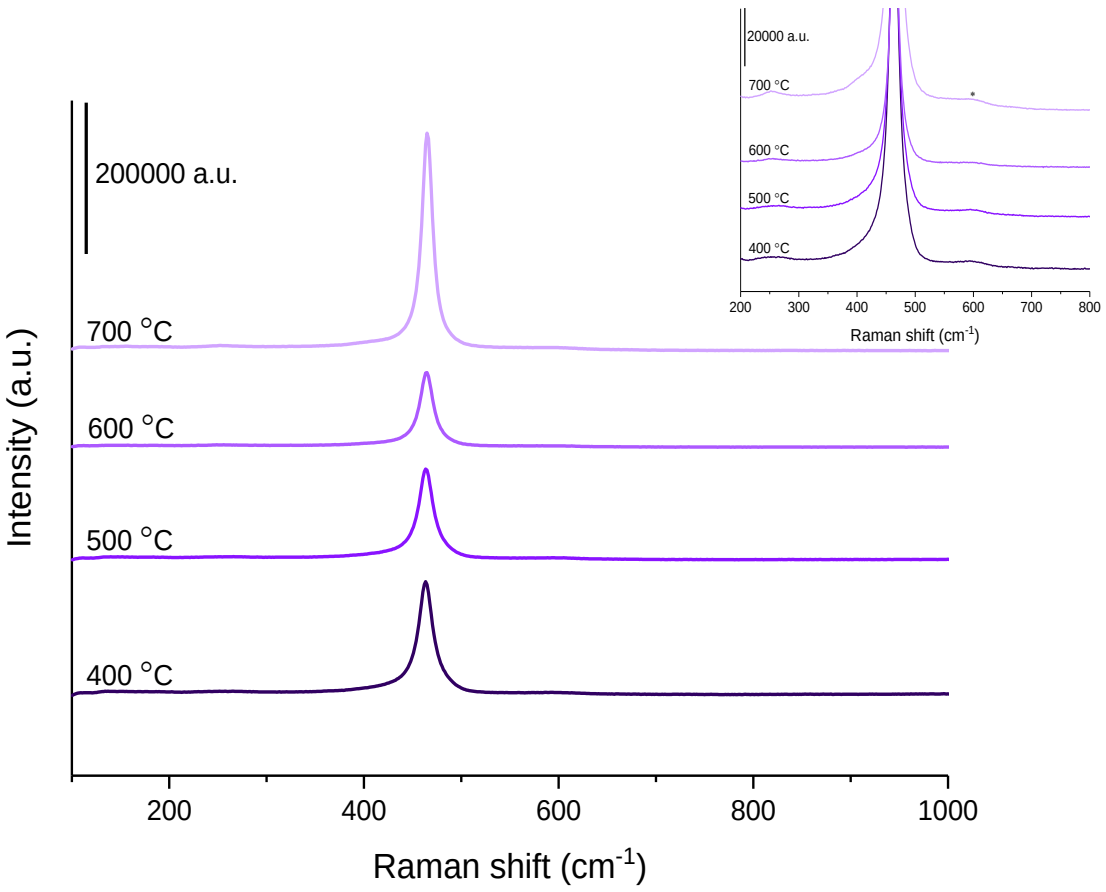

Figure 19. Raman spectra of CeO_2 calcined at different temperatures.

Ceria calcined at 400 °C had a defect density of 0.58 % which was found to increase to 0.83 % upon increasing the calcination to 500 °C. At higher calcination temperatures, the defect density was significantly reduced, with a value of 0.05 % from a calcination temperature of 700 °C. This was attributed to increase in crystallinity which occurs with higher calcination temperatures. The FWHM of the F_{2g} mode was in agreement with the defect densities calculated from the I_D/I_{F2g} ratio. The FWHM of the F_{2g} peak been reported as inversely proportional to crystallite size and can indicate the presence of defects.[39, 40] Since CeO_2 calcined at 500 °C has a larger crystallite size than CeO_2 calcined at 400 °C, one would expect a smaller FWHM for the material with the larger crystallite size. The slight increase in FWHM for ceria calcined at 500 °C, can therefore be attributed to an increase in oxygen defects present.

Table 4. Textural properties of CeO2 catalysts calcined at different temperatures.					
Calcination temperature (°C)	***BET surface area ($m^2 g^{-1}$)[a]***	***Crystallite size (nm)[b]***	***Defect density (%)[c]***	***Defect density per surface area ($\times 10^{-3}$ % m^{-2})[c]***	***FWHM of F_{2g} mode***
400	38	14	0.58	1.5	17.96
500	34	15	0.83	2.4	18.03
600	27	16	0.11	0.4	16.61
700	22	19	0.05	0.3	13.35
[a] calculated from N_2 adsorption measurements at -196 °C; [b] calculated from the Scherrer equation using the (111) reflection; [c] Calculated from Raman spectroscopy by I_D/I_{F2g} where I_D is the integrated area of the band at *ca.* 600 cm^{-1} and I_{F2g} is the integrated area of the F_{2g} band at 462 cm^{-1}					

GLY conversions obtained at a reaction temperature of 340 °C over the ceria catalysts calcined at different temperatures, and the corresponding product yields are shown in Table 4, whilst the product selectivities are illustrated in Figure 20 (the full product distribution is shown in Table A3.6). Catalyst masses were adjusted across the experiments in order to provide a constant total catalyst surface across the materials. Varying the catalyst mass resulted in differing catalyst bed volumes therefore the argon carrier gas flow rates were adjusted to maintain a constant GHSV across the experiments, at *ca.* 3450 h^{-1}. Increasing the argon flow rate to maintain the GHSV resulted in a decrease in partial pressure from 0.47 mbar over CeO_2 calcined at 400 °C to 0.29 mbar over CeO_2 calcined at 700 °C. Whilst the variation in GLY partial pressure introduces an additional variable across the experiments, the partial pressure of GLY is extremely low across all experiments, representing *ca.* 0.05 % of the total system pressure, and is therefore considered to have little influence on the results.

Based on the findings from the blank results discussed in section 3.2.1, the products obtained over the ceria catalysts can be attributed to the catalyst present in the reactor bed due to the negligible levels of GLY conversion which occurred over the SiC diluent at reaction temperatures < 360 °C. The experiments were performed in the manner described above to allow any changes in product distribution to be attributed to changes in the catalyst surface induced through varying the calcination temperature.

Table 5. Glycerol conversion and product yield distribution for reactions over CeO2 calcined at different temperatures (CT).

CT (°C)	***Catalyst mass (g)***	***Ar Flow rate (mL min^{-1})***	***X_{GLY} [a] (%)***	***Mass Balance (%)[b]***			***Yield (%)***								***MeOH S.T.Y. (g h^{-1} kg^{-1})***	***MeOH S.T.Y. (g h^{-1} m^{-2})***	***Carbon deposition (mg g^{-1})***
				C	***H***	***O***	***Alc.***	***Diol***	***Ald.***	***Ket.***	***Ac.***	***COx***	***Est.***	***Unk.***			
400	0.4998	15	83	82 (83)	75	67	7.9	6.0	8.5	24.7	5.2	2.9	0.7	11.3	84.3	2.22	17
500	0.5497	15	83	80 (81)	72	66	7.4	5.9	7.9	24.9	5.2	2.9	0.7	10.7	80.0	2.35	21
600	0.6995	20	80	84 (86)	76	70	8.1	5.3	8.4	25.2	6.4	3.4	0.6	11.7	59.3	2.19	19
700	0.8508	25	84	81 (84)	74	67	7.7	6.9	6.8	22.4	6.3	3.8	0.5	11.5	51.1	2.32	22

[a] GLY conversion; [b] Carbon mass balance (± 3 %) of products detected in GC1 and GC2, values in parenthesis include coke deposited on catalyst; [c] Carbon balance, values in parenthesis include coke from TGA measurements; [d] yield of products detected in GC1 and GC2; Alc., alcohols; Ald., aldehydes; Ket., ketones; Ac., acids; Est., esters; Unk., unidentified products; [e] MeOH space time yield. Reaction conditions; 340 °C, 50 wt.% Gly/H_2O, GHSV *ca*. 3450 h^{-1}.

With a constant total catalyst surface area and GHSV, GLY conversion was constant across the materials calcined at different temperatures, at approximately 83 %. The constant level of GLY conversion showed that any changes in crystallite size or defect density that occurred through varying the calcination temperature had no significant influence on the catalytic reactivity towards GLY.

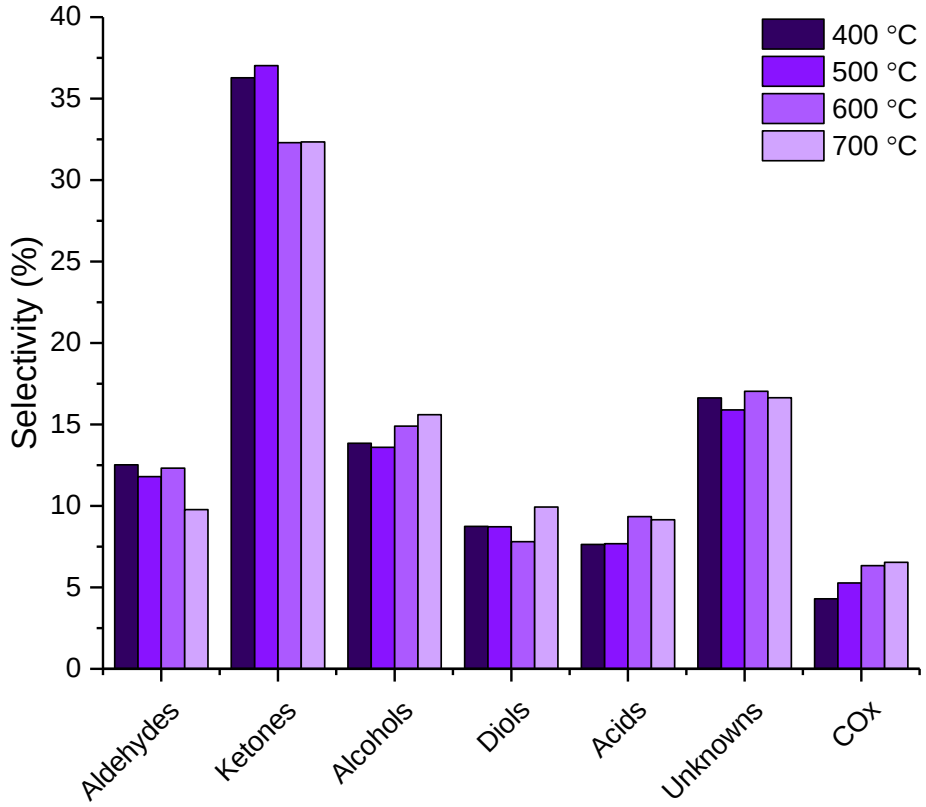

Figure 20. The product group selectivity over CeO2 calcined at different temperatures where the catalyst mass and Ar flow rate has been adjusted to maintain a consistent catalyst bed surface area. Reaction conditions; 340 °C, 50 wt.% glycerol (0.016 mL min^{-1}), 15 mL min^{-1} Ar, 3 hours, GHSV = 3450 h^{-1}.

The major product formed across all four catalysts was HA, with selectivities of 32.1, 33.0, 28.8 and 29.1 % for CeO_2 calcined from 400 to 700 °C, respectively, representing a standard deviation of 1.8 % across the materials. Other major products detected were ACA (*ca.* 9 %), MeOH (*ca.* 9 %), acetic acid (*ca.* 4 %), propionic acid (*ca.* 5 %), 1,2-PD (*ca.* 4 %) and EG (*ca.* 5 %). The deviation across these products was low (< 1 %), thus the product distributions are largely considered to be comparable. The MeOH space time yield decreased with increasing calcination temperature, due to the larger mass of catalyst required to maintain a constant surface area (Table 5). Normalisation of the MeOH space time yield to surface area shows a fairly constant value across the catalysts, varying only from 2.19 to 2.35 g h^{-1} m^{-2}_{cat}. No significant difference in carbon balance was achieved over the different catalysts, with an average value of 82 %. Similarly, all catalysts suffered from minimal carbon deposition (approximately 20 mg_{coke} g^{-1}_{cat}). These results imply that any differences in the

catalyst induced through varying the calcination temperature, such as crystallite size and defect density, have little influence on GLY conversion and product distribution with a constant catalyst bed surface area.

The estimation of carbon deposition through TGA experiments, showed the carbon lost through catalyst coking to be insignificant, accounting for < 3 % of the total carbon content in the reaction. As described in section 3.2.2.4, CHN analysis was also undertaken on a post-reaction mixture obtained over a ceria catalyst. Analysis of the reaction mixture obtained at 340 °C over CeO_2 calcined at 600 °C gave a total carbon balance of 94.6 %, comprised of CHN analysis (87.1 %), gas phase products (6.1 %) and carbon deposition (1.4 %). The remaining 5 % of carbon was attributed to reactor fouling. CHN analysis of all liquid phase products was found to be 87.1 %, in comparison, the sum of all liquid phase products as analysed by GC was 79 %, suggesting *ca.* 8 % of the carbon is contained in liquid phase products which cannot be analysed by GC.

Consequently, LC-MS analysis was employed to qualitatively assess the presence of any high molecular weight species (Figure 21). Products and fragments with *m/z* from 100 – 1000 were analysed. A blank sample of deionised water was also analysed to exclude any contaminants such as column bleed which was observed towards the end of the chromatogram. Similarly to the LC-MS analysis performed after a reaction with MgO (Figure 14), a very complex chromatogram was obtained, with numerous peaks detected, preventing successful product identification. Despite this, high molecular weight products were confirmed in the post reaction solution, indicating the presence of undesirable side reactions, which potentially form through base catalysed condensation reactions. As these high molecular weight products are undetectable by GC, discrepancies between the observed carbon balance and the total carbon balance are attributed to the presence of these heavy organic species.

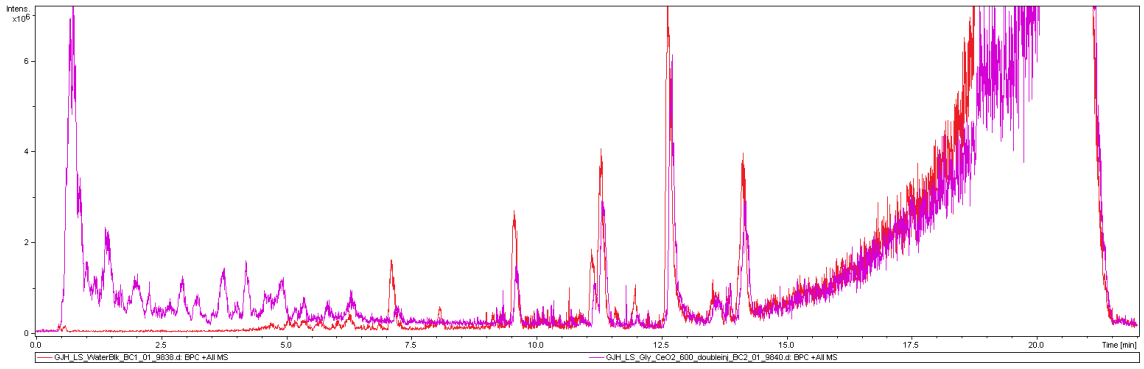

Figure 21. LC-MS chromatogram corresponding to the post reaction solution of a reaction run over CeO_2 for 6 h. Detection parameters are fixed at 100 - 1000 m/z. Reaction conditions; 340 °C, glycerol flow (0.016 mL min^{-1}), 0.7 g CeO_2, GHSV ca. 3450 h^{-1}. Pink line – chromatogram of the post reaction solution. Red line – chromatogram of a H_2O blank solution.

3.3 Conclusions

Throughout this chapter the gas phase conversion of GLY has been explored under both catalyst free and catalysed conditions, over magnesium oxide and ceria. All reactions were performed with an aqueous 50 wt.% GLY feedstock, unless otherwise specified, across a temperature range of 320 – 480 °C. Under catalyst free conditions, GLY conversion reached 18 % over SiC, a commonly used catalyst diluent, at a reaction temperature of 480 °C. The moderate levels of GLY conversion achieved in the absence of a catalyst highlighted the importance of optimising the catalyst to allow for the effective conversion of GLY to MeOH at lower reaction temperatures (< 400 °C), in order to minimise thermally initiated side reactions which may reduce MeOH yields.

Over MgO, a diverse product distribution was observed, with HA, 1,2-PD and EG dominating at a reaction temperature of 360 °C. At higher reaction temperatures, smaller quantities of these reaction products were observed, with larger amounts of MeOH, ACA, 2,3-BD and CO_x. A comprehensive reaction network was proposed based on the proportion of products observed with differing GLY conversion levels. For a 50 wt.% GLY solution, the MeOH space time yield was found to reach a maximum value of 205 g h^{-1} kg^{-1} at 400 °C, although this could be improved to 255 g h^{-1} kg^{-1} by reducing the GLY concentration and catalyst mass to 10 wt.% and 100 mg, respectively. This improvement in MeOH space time yield with a more dilute GLY feed was attributed to a reduction in the formation of high molecular weight products, thought to be formed through base catalysed condensation reactions, the presence of which are reflected in the lower carbon balance obtained with more concentrated GLY feedstocks.

The MgO catalyst was found to be stable over a 48-hour time period when a 50 wt.% GLY feedstock was used at a reaction temperature of 400 °C. Under these conditions the carbon balance was low, but stable, at *ca.* 65 %. Whilst moderate levels of carbon deposition were detected through post-reaction analysis of the catalyst, the longer-term stability of the catalyst suggested that no significant catalyst deactivation occurred. Additional analysis of the post-reaction solution showed that high molecular weight products were formed over MgO with a 50 wt.% GLY feedstock at 400 °C. The formation of these products was attributed to the basic nature of the catalyst, thus future efforts regarding the use of MgO for the conversion of GLY to MeOH should focus on tailoring the strength and density of basic sites to explore whether the formation of these high molecular weight products can be prevented.

Similar findings were made over a commercially available ceria catalyst. Increasing the reaction temperature led to a significant reduction in HA yield, as a consequence of its further conversion to ACA, MeOH, 2,3-BD, ACE and CO_x. Whilst MeOH selectivity was

increased by increasing the reaction temperature, this also resulted in significant increases towards aldehydic products and CO_x, with temperatures in excess of 400 °C considered to be unsuitable for the process, due to the dominance of ACA and CO_x under these conditions.

A subsequent investigation into the effect of calcination temperature on some of the physicochemical properties of ceria and how this may influence product distribution was undertaken. In order to investigate the influence of crystallite size and defect density, the catalyst mass was adjusted to maintain a constant catalyst surface area across experiments. At comparable GHSVs no significant differences in GLY conversion or product distribution were observed over the ceria catalysts calcined at different temperatures. Whilst these results suggested that the density of defect sites had no effect on the reactivity of GLY or intermediate products, it should be noted that any changes induced in the ceria catalysts through varying the calcination treatment were minimal, making it difficult to draw firm conclusions about the role of defects. Higher GLY conversions were obtained over ceria calcined at different temperatures in comparison with the commercial sample, due to the improved surface areas. However, the reaction temperature investigated (340 °C) was considered to be insufficient to maximise MeOH selectivity, due to the high levels of HA detected over all the catalysts. Consequently, the synthesis of ceria catalysts with altered chemical properties i.e. through varying the morphology or through the introduction of dopants, provides an opportunity to gain a greater understanding of the influence of properties such as defect density, reducibility and acid-base strength on the selectivity towards MeOH, to allow MeOH production to be maximised at reasonable temperatures (< 400 °C).

3.4 References

1. M. H. Haider, N. F. Dummer, D. W. Knight, R. L. Jenkins, M. Howard, J. Moulijn, S. H. Taylor and G. J. Hutchings, *Nature Chemistry*, 2015, **7**, 1028.
2. D. Hernandez, M. Velasquez, P. Ayrault, D. Lopez, J. J. Fernandez, A. Santamaria and C. Batiot-Dupeyrat, *Applied Catalysis A: General*, 2013, **467**, 315-324.
3. S. Tuokko, P. M. Pihko and K. Honkala, *Angewandte Chemie International Edition*, 2016, **55**, 1670-1674.
4. M. A. Aramendía, V. Borau, C. Jiménez, A. Marinas, J. M. Marinas, A. Porras and F. J. Urbano, *Catalysis Letters*, 1998, **50**, 173-177.
5. P. Claus, H. Hofmeister and C. Mohr, *Gold Bulletin*, 2004, **37**, 181-186.
6. W. Grünert, A. Brückner, H. Hofmeister and P. Claus, *The Journal of Physical Chemistry B*, 2004, **108**, 5709-5717.
7. T. Yoshikawa, T. Tago, A. Nakamura, A. Konaka, M. Mukaida and T. Masuda, *Research on Chemical Intermediates*, 2011, **37**, 1247.
8. H. Fujitsuka, K. Terai, M. Hayashi, T. Yoshikawa, Y. Nakasaka, T. Masuda and T. Tago, *Journal of the Japan Petroleum Institute*, 2019, **62**, 319-328.
9. G. Sánchez, B. Z. Dlugogorski, E. M. Kennedy and M. Stockenhuber, *Applied Catalysis A: General*, 2016, **509**, 130-142.
10. W. Bühler, E. Dinjus, H. J. Ederer, A. Kruse and C. Mas, *The Journal of Supercritical Fluids*, 2002, **22**, 37-53.

11. J. I. Di Cosimo, V. K. Díez, C. Ferretti and C. R. Apesteguía, in *Catalysis: Volume 26*, The Royal Society of Chemistry, 2014, vol. 26, pp. 1-28.
12. A. O. Menezes, P. S. Silva, E. Padrón Hernández, L. E. P. Borges and M. A. Fraga, *Langmuir*, 2010, **26**, 3382-3387.
13. S. Kuś, M. Otremba, A. Tórz and M. Taniewski, *Applied Catalysis A: General*, 2002, **230**, 263-270.
14. A. Corma, G. W. Huber, L. Sauvanaud and P. O'Connor, *Journal of Catalysis*, 2008, **257**, 163-171.
15. A. Alhanash, E. F. Kozhevnikova and I. V. Kozhevnikov, *Applied Catalysis A: General*, 2010, **378**, 11-18.
16. E. Tsukuda, S. Sato, R. Takahashi and T. Sodesawa, *Catalysis Communications*, 2007, **8**, 1349-1353.
17. M. T. Nguyen and G. Raspoet, *Canadian Journal of Chemistry*, 1999, **77**, 817-829.
18. T. F. Kahan, T. K. Ormond, G. B. Ellison and V. Vaida, *Chemical Physics Letters*, 2013, **565**, 1-4.
19. B. Katryniok, S. Paul, V. Bellière-Baca, P. Rey and F. Dumeignil, *Green Chemistry*, 2010, **12**, 2079-2098.
20. B. Katryniok, S. Paul, M. Capron and F. Dumeignil, *ChemSusChem*, 2009, **2**, 719-730.
21. W. Yan and G. J. Suppes, *Industrial & Engineering Chemistry Research*, 2009, **48**, 3279-3283.
22. R. B. Mane and C. V. Rode, *Organic Process Research & Development*, 2012, **16**, 1043-1052.
23. C. Liu, R. Liu and T. Wang, *The Canadian Journal of Chemical Engineering*, 2015, **93**, 2177-2183.
24. A. Talebian-Kiakalaieh and N. A. S. Amin, *Industrial & Engineering Chemistry Research*, 2015, **54**, 8113-8121.
25. C. Montassier, D. Giraud and J. Barbier, in *Studies in Surface Science and Catalysis*, eds. M. Guisnet, J. Barrault, C. Bouchoule, D. Duprez, C. Montassier and G. Pérot, Elsevier, 1988, vol. 41, pp. 165-170.
26. M. Velasquez, A. Santamaria and C. Batiot-Dupeyrat, *Applied Catalysis B: Environmental*, 2014, **160-161**, 606-613.
27. D. Kansy, K. Bosowska, K. Czaja and A. Poliwoda, *Polymers*, 2019, **11**, 144.
28. N. Zhong, L.-Z. Cheong and X. Xu, *European Journal of Lipid Science and Technology*, 2014, **116**, 97-107.
29. A. M. Hernández-Giménez, J. Ruiz-Martínez, B. Puértolas, J. Pérez-Ramírez, P. C. A. Bruijnincx and B. M. Weckhuysen, *Topics in Catalysis*, 2017, **60**, 1522-1536.
30. J. Quesada, L. Faba, E. Díaz and S. Ordóñez, *Applied Catalysis A: General*, 2017, **542**, 271-281.
31. A. Chieregato, J. Velasquez Ochoa, C. Bandinelli, G. Fornasari, F. Cavani and M. Mella, *ChemSusChem*, 2015, **8**, 377-388.
32. E. Mamontov, T. Egami, R. Brezny, M. Koranne and S. Tyagi, *The Journal of Physical Chemistry B*, 2000, **104**, 11110-11116.
33. J. R. McBride, K. C. Hass, B. D. Poindexter and W. H. Weber, *Journal of Applied Physics*, 1994, **76**, 2435-2441.
34. Y. Xu, F. Wang, X. Liu, Y. Liu, M. Luo, B. Teng, M. Fan and X. Liu, *The Journal of Physical Chemistry C*, 2019, **123**, 18889-18894.
35. Z. Wu, M. Li, J. Howe, H. M. Meyer and S. H. Overbury, *Langmuir*, 2010, **26**, 16595-16606.
36. A. Nakajima, A. Yoshihara and M. Ishigame, *Physical Review B*, 1994, **50**, 13297-13307.
37. M. Guo, J. Lu, Y. Wu, Y. Wang and M. Luo, *Langmuir*, 2011, **27**, 3872-3877.
38. T. Taniguchi, T. Watanabe, N. Sugiyama, A. K. Subramani, H. Wagata, N. Matsushita and M. Yoshimura, *The Journal of Physical Chemistry C*, 2009, **113**, 19789-19793.
39. I. Kosacki, T. Suzuki, H. U. Anderson and P. Colomban, *Solid State Ionics*, 2002, **149**, 99-105.

40. T. Hattori, K. Kobayashi and M. Ozawa, *Japanese Journal of Applied Physics*, 2016, **56**, 01AE06.

Chapter 4

The effect of ceria morphology on gas phase glycerol valorisations

4.1 Introduction

In chapter 3 the effect of the calcination temperature on the physical and chemical properties of ceria, and the subsequent influence on GLY reactivity was investigated. At comparable contact times, and with normalised catalyst surface area, no clear relationship between the calcination temperature and selectivity to MeOH was involved. It should, however, be noted that varying the calcination temperature did not induce significant differences in the physicochemical properties, and only minor differences in the acid-base and redox properties of the as-prepared ceria were observed.

Since the preparation of ceria nanostructures with well-defined morphologies was reported by Yan and co-workers in 2005, the effect of ceria morphology on its catalytic activity has been widely explored. It was shown that ceria nanocubes, nanorods, and nanopolyhedra can be synthesised through a simple hydrothermal preparation method, using cerium(III) nitrate as a cerium source and sodium hydroxide as a precipitating agent, with base concentration and synthesis temperature altered depending on the desired morphology.[1, 2] Analysis by HRTEM showed that the different morphologies predominantly expose different crystal planes: (100) for the cubes, (110) and (100) for the rods, and (111) and (100) for the polyhedra, thus providing a simple route to synthesise nanostructured ceria, with a variety of exposed crystal facets, without the use of surfactants or organic modifiers, which could influence reactivity.

As described thoroughly in the introduction (section 1.3.4), the effect of morphology and surface termination can significantly influence the physicochemical properties of ceria, and consequent catalytic activity. Yan and co-workers showed that the OSC (oxygen storage capacity) of the materials varied significantly depending on morphology;[2] on a μmol g^{-1} basis the OSC was found to follow the order rods > cubes ≈ polyhedra but when normalised for surface area, this switched to cubes > rods >> polyhedral. Cassir and co-workers investigated the surface dependency of H_2 reduction,[3] where the activation energy for surface reduction was found to be lowest for ceria cubes, followed by rods, attributed to the more reactive (100) and (110) surfaces, respectively. A Raman spectroscopy study undertaken by Wu *et al*. whereby the defects in ceria cubes, rods and octahdera were thoroughly investigated, under both reducing and oxidising conditions.[4] The intrinsic defects were found to be anionic Frenkel defects, which were found to be most abundant

over the rods, followed by the cubes and then octahdera. This trend followed the theoretical vacancy formation energy of (110) < (100) < (111), representative of the surfaces present in the samples.[5] An investigation into the effect of surface termination on the acid-base properties of ceria was also undertaken by Wu *et al.*, using a variety of acidic and basic probe molecules.[6] Lewis acid sites were found across all morphologies and surfaces, although these sites were found to be relatively weak and no surface dependence was observed. Alternatively, both the strength and quantity of basic sites were found to be: rods > cubes > octahdera, which was considered to be as a result of both the anionic coordination status and the presence of defect sites.

Opposite face sensitivity of ceria has been demonstrated for oxidation and hydrogenation reactions. The (100) surface was found to be optimal for CO oxidation, attributed to the enhanced OSC, whereas the (111) surface was shown to be beneficial for acetylene hydrogenation reactions.[7] The enhanced activity of the (111) surface was attributed to the ability of less coordinatively unsaturated oxygen anions to more effectively stabilise reactive intermediates.

For more complex reactions, both the catalytic activity and product selectivity can be influenced by the effect of the ceria morphology.[8, 9] A recent study was undertaken by Mann *et al.*,[8] whereby the adsorption and reactivity of ACA was investigated over morphologically controlled ceria samples. When sample masses were normalised to provide the same total surface area, initial rates of ACA consumption followed the order: wires > cubes > octahedra, although the wires and cubes both displayed more rapid deactivation than the octahedra. Numerous products were detected for all morphologies, with significant differences in product distribution observed across the materials. EtOH was formed through a Cannizzaro disproportionation reaction *via* an acetate intermediate; the selectivity to EtOH followed the trend for theoretical basicity of the exposed surfaces, and was of the order wires ≈ cubes >> octahedra. Since C_1 products such as CO, CO_2 and CH_4 were formed via C-C cleavage of an acetate intermediate, the trend for these products was in full agreement with the EtOH trend. Crotonaldehyde was formed over all morphologies, through an aldol condensation coupling mechanism, with the selectivity to crotonaldehyde following the trend octahedra > wires > cubes. The higher selectivity observed over the octahedra was attributed to the increased rate of crotonaldehyde desorption from the (111) surface compared with the (100) and (110) surfaces. Crotonaldehyde was found to be one of the major intermediates in the formation of coke, thus the lower levels of catalyst deactivation observed for the octahedra was attributed to the lower conversion of crotonaldehyde.

A recent study into GLY oxidation over ceria nanocubes, nanorods and commercial samples showed that the surface area normalised catalytic activity followed the trend: cubes > rods

> commercial samples.[9] Interestingly, significant differences in product distribution were observed, with glyceric acid, a C_3 oxidation product observed as the major product over the rods and commercial samples. Alternatively, glycolic acid and formic acid, C_2 and C_1 oxidation products, respectively, were the dominant products observed over the cubes. The formation of C_1 and C_2 products occurred as a consequence of C-C cleavage. Subsequent analysis showed there was a strong correlation between the amount of H_2O_2 produced *in-situ* and the selectivity towards C-C cleavage products. The authors noted no correlation between the redox or defect properties of the ceria samples and the observed catalytic activity, leading them to ascribe the differences in reactivity to the presence of different crystallographic facets.

Throughout this chapter, the effect of ceria morphology on gas-phase reactions of GLY are fully explored. Since the physicochemical properties of ceria can vary significantly depending on morphology, comprehensive discussion of catalyst characterisation precedes any catalyst testing. As established in the previous chapter, product distribution is strongly linked to GLY conversion and can vary significantly with temperature and contact time. Consequently, materials have been compared under identical reaction conditions, maintaining a constant GHSV across a range of temperatures. Additional reactions have been performed whereby catalyst masses (and subsequent volumes) were altered to achieve comparable levels of GLY conversion, known as *iso*-conversion, to allow for direct comparison of product distributions over the three morphologies. Any differences in product distribution were discussed with respect to the reaction mechanism and competing pathways, and the subsequent influence on MeOH productivity.

4.2 Results

4.2.1 Effect of morphology on structural and textural properties of ceria

Ceria nanostructures with cubic, rod-like, and polyhedral morphologies, here-in referred to as Ce-C, Ce-R and Ce-P, respectively, were prepared in accordance with a hydrothermal synthesis, initially reported by Yan and co-workers.[2] Experimental details of the preparation are given in section 2.2.3. The PXRD patterns for the as-prepared materials are shown in Figure 1. All samples were indexed to the cubic fluorite ceria structure (space group *Fm3m*, JCPDS 01-089-8436), with no impurity or pre-cursor peaks observed. Crystallinity of the samples was of the order Ce-C > Ce-P > Ce-R, as evidenced by the FWHM of the diffraction peaks, with the crystallite sizes displayed in Table 1. The sharper reflections observed for Ce-C are representative of a larger crystallite size, likely due to the harsher synthesis conditions, requiring both concentrated base and a high synthesis temperature. The peak positions for the (111) and (200) diffraction peaks are also shown in Table 1. The (111) peak, the most intense for all samples, was at positions of 28.436, 28.491 and 28.498 ° for Ce-C, Ce-R and Ce-P, respectively. An inverse relationship exists

between peak position and lattice parameter, with a lower 2θ value resulting in higher lattice parameters.

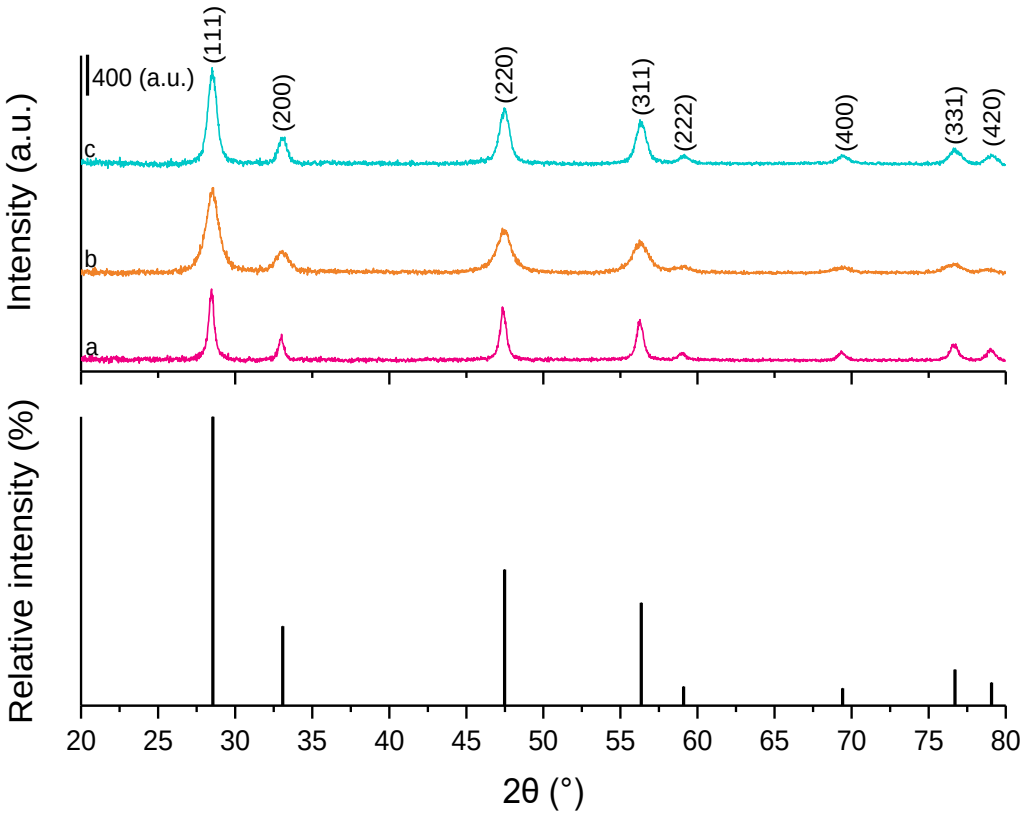

Figure 1. PXRD patterns of morphologically controlled ceria (stick pattern from JCPDS 01-089-8436 also shown for reference).

The lattice parameter for stoichiometric, bulk ceria is 0.5411 nm (JCPDS 01-089-8436); lattice parameters were increased for all three materials (Table 1), with the largest lattice parameter calculated for Ce-C (0.5432 nm). The substitution of Ce^{4+} cations with Ce^{3+} results in an increased lattice parameter due to their larger ionic radius ($r_{Ce^{4+}}$ = 0.94 Å; $r_{Ce^{3+}}$ = 1.14 Å). However, lattice parameters need to be carefully considered since opposing effects can offset one another. As shown by Morris and co-workers, lattice expansion can be counteracted by lattice contraction which occurs as a consequence of additional pressure arising from surface tension between the crystallite and the ambient atmosphere.[10, 11] It was found that the smaller the crystallite, the larger the lattice contraction is, due to increasing surface tension. Whilst the lattice parameters may suggest that the Ce^{3+} concentration is of the order Ce-C > Ce-R and Ce-P, crystallite sizes are of the order Ce-R > Ce-P > Ce-C, indicating competing lattice expansion and contraction. Lattice strain was highest for Ce-R, followed by Ce-P, with the lowest level of strain observed for Ce-C, this was in agreement with previously published works,[12] and mirrored the trend of crystallite size.

Interestingly, slight differences in the intensity of the diffraction peaks were observed for the different morphologies (Table A4.1 in the Appendix). Ce-C showed a higher ratio of

relative intensities for the (200) and (111) reflections compared with both the reference and the other samples, indicative of growth in the [200] direction. The lower intensity ratio of (111) to (111), (200) and (220) reflections calculated for Ce-C was also in agreement with this result.[13-15]

An inverse relationship was observed between crystallinity and surface area; surface areas calculated in accordance with the BET method were 23, 85 and 65 m^2 g^{-1} for Ce-C, Ce-R and Ce-P, respectively. The nitrogen sorption isotherms are shown in Figure 2; full pore size distributions and pore volumes are shown in the appendix (Figure A4.1a-c). In agreement with the surface areas, Ce-R had the highest pore volume with a cumulative value of 0.689 mL g^{-1}, although Ce-P had the lowest cumulative pore volume, at 0.099 mL g^{-1}, with an intermediate pore volume of 0.159 mL g^{-1} measured for Ce-C. Analysis of the pore size distribution with the BJH method showed a mesoporous distribution for Ce-C, with a broad peak centred at 17.1 nm. Similar results were found for Ce-R, where a broad maximum was observed at 30.1 nm, although a sharper, less intense peak was also observed at 3.1 nm, indicating a bimodal pore distribution. Significant differences were calculated for Ce-P, with a much narrower pore size distribution, centred at 5.1 nm.

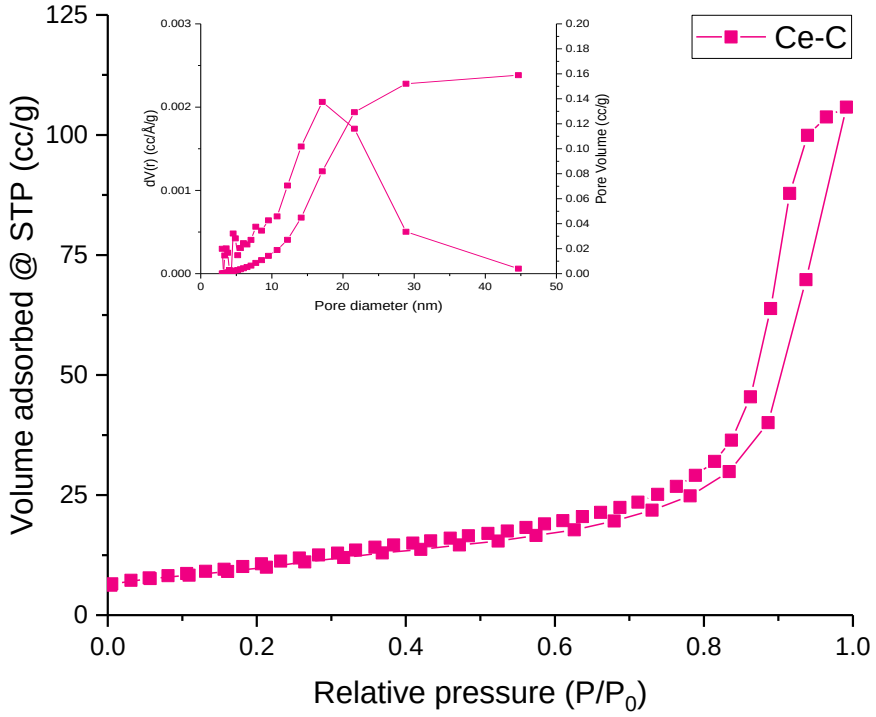

Figure 2a. N2 adsorption-desorption isotherm of Ce-C. Inset shows the pore size distribution and cumulative pore volume calculated in accordance with the BJH method.

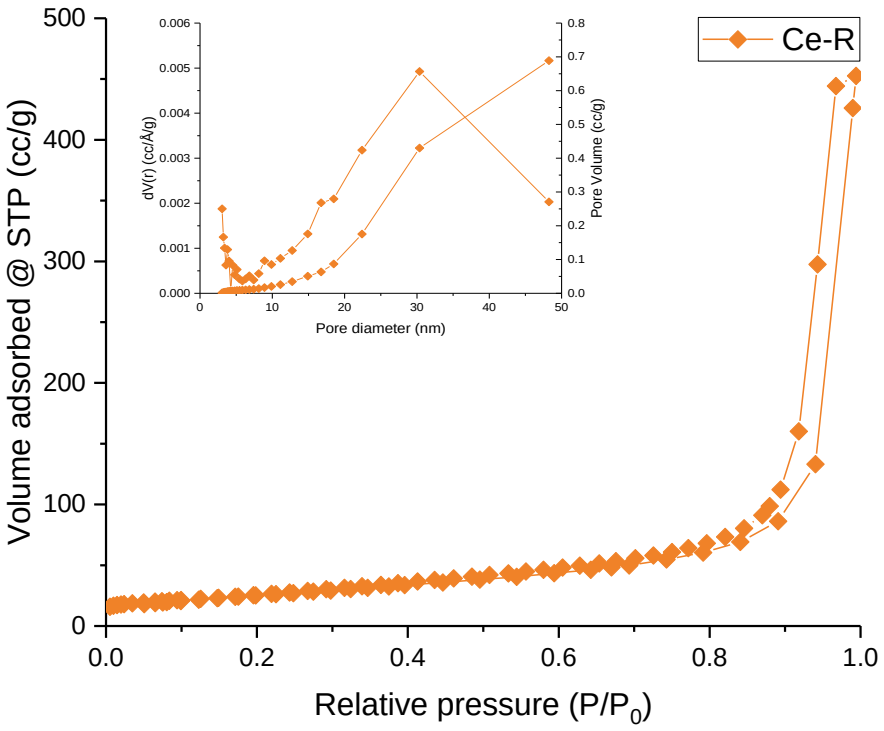

Figure 2b. N2 adsorption-desorption isotherm of Ce-R. Inset shows the pore size distribution and cumulative pore volume calculated in accordance with the BJH method.

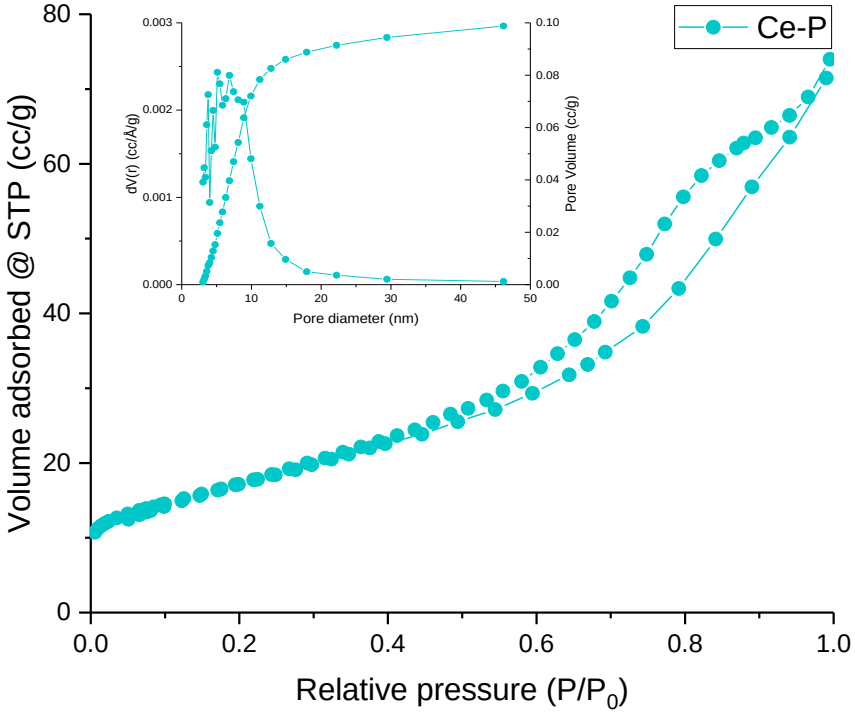

Figure 2c. N2 adsorption-desorption isotherm of Ce-P. Inset shows the pore size distribution and cumulative pore volume calculated in accordance with the BJH method.

Table 1. Structural and textural properties of morphologically controlled ceria										
Morphology	***Peak position (°)[a]***	***Miller indices[a]***	***FWHM[a]***	***Crystallite size (nm)[a]***	***Lattice parameter (Å)[a]***	***Lattice strain (%)[a]***	***TEM particle size (nm)[b]***	***Exposed crystal planes[b]***	***Specific surface area ($m^2 g^{-1}$)[c]***	***Cumulative pore volume ($mL g^{-1}$)[c]***
Ce-C	28.436	111	0.401	20.4	5.4322	0.691	19.3 ± 2.2	(100)	23	0.159
	32.960	200	0.392	21.1	5.4306	0.578				
Ce-R	28.491	111	1.000	7.6	5.4218	1.719	7.1 ± 0.7 x (50 – 200)	(110) & (100)	85	0.689
	33.015	200	1.083	7.7	5.4221	1.595				
Ce-P	28.498	111	0.697	11.8	5.4206	1.198	10.7 ± 0.9	(111) & (100)	65	0.099
	33.044	200	0.697	12.0	5.4173	1.018				
a. Determined from PXRD; b. measured by TEM; c. calculated from N_2 sorption isotherms										

The morphology of the prepared ceria materials was investigated by TEM, as shown in Figure 3. A very regular cubic morphology was observed for Ce-C, with well-defined edges, although slight rounding at the corners of the cubes could be seen. Similarly, Ce-R displayed a regular rod-like structure, although it should be noted that the edges were less-well defined than in Ce-C, suggesting some degree of surface roughness in Ce-R. Whilst the images of Ce-P showed the particles to be fairly regular in size, a more irregular geometry was observed for Ce-P, with their morphology most closely resembling that of a truncated octahedron, a previously reported morphology for CeO_2 nanocrystals.[2, 16-18]

Interplanar spacings were measured in order to determine the exposed surface terminations present in each material. For Ce-C, the dominant measurement was found to be 0.26 nm, which represents the (200) lattice fringe. Some additional measurements with a value of 0.31 nm were also made, indicating that (111) facets are also present in Ce-C. Ce-R displayed interplanar spacing of 0.27 nm down the length of the rod (along the x axis), indicative of (100) planes; measurements of 0.19 nm were identified across the width of the rod (along the y axis), which were representative of (110) planes. This was indicative of nanorod growth in the [110] direction, with the exposure of (110) and (100) surfaces, in agreement with previously published works.[2, 19-21] For Ce-P, the dominant lattice spacing was measured to be 0.32 nm, indicating the dominant surface for the polyhedral morphology was the most stable (111) surface; additional measurements were made at 0.26 nm, revealing the presence of some (100) facets. Similar findings were made by Trovarelli and co-workers,[13] who demonstrated the exposure of (100) surfaces when octahedral particles transitioned to truncated octahedra under thermal treatments. Additionally, thermal treatments above 700 °C of samples with a cubic morphology led to the formation of a truncated cubes and the exposure of (111) surfaces.

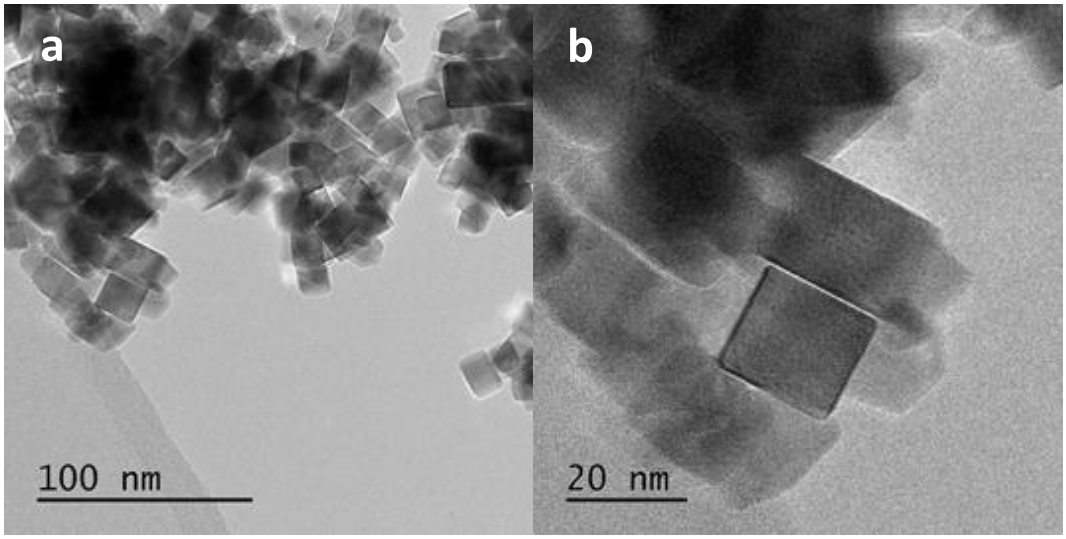

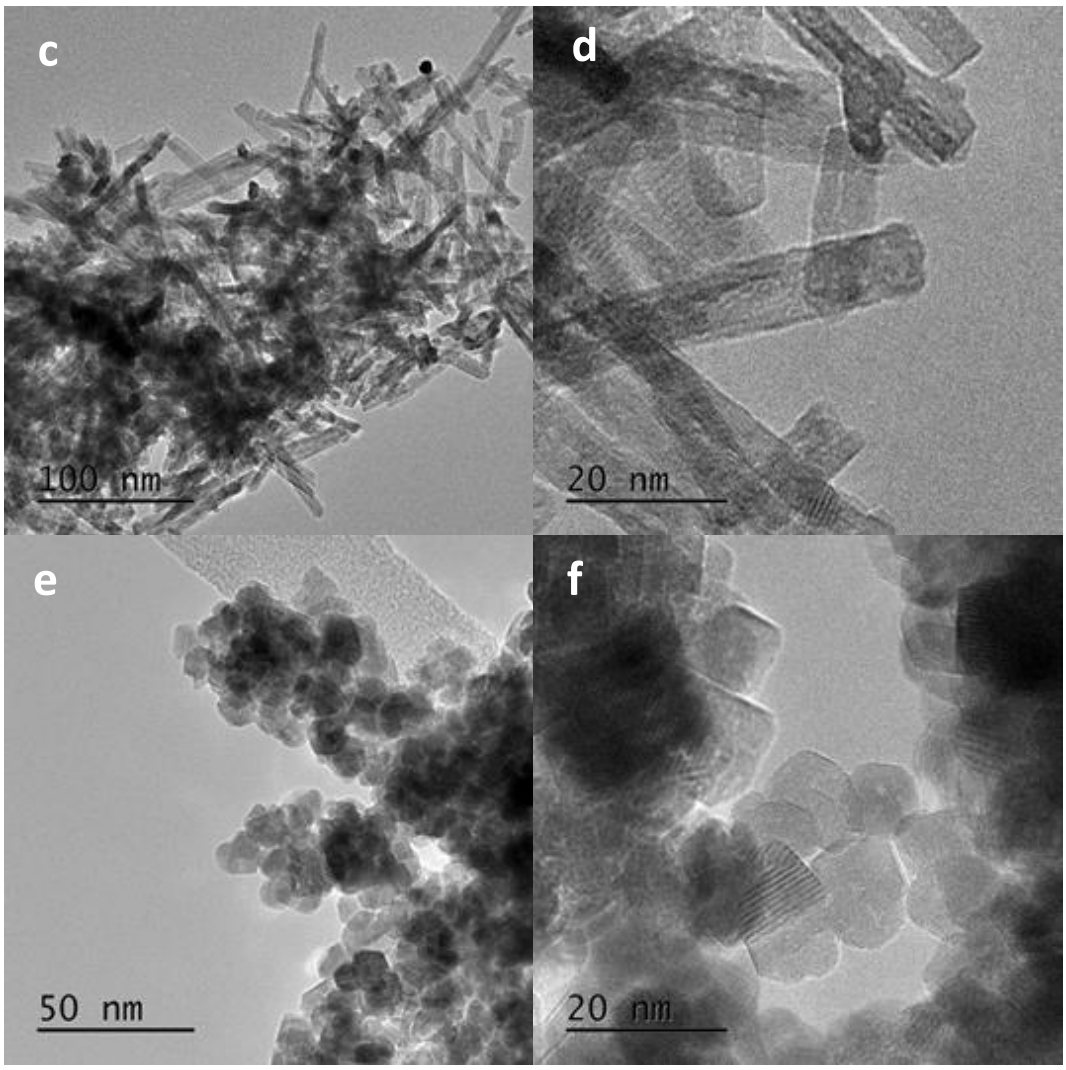

Figure 3. TEM images of ceria Ce-C (a & b), Ce-R (c & d), and Ce-P (e & f).

The particle size distributions are shown in Figure 4, with a minimum of 250 particles counted; generally, well-defined particle size distributions were obtained. Ce-C exhibited a well-defined cubic morphology; the length of the cube edges varied between 12 – 25 nm, but a size of 19 nm was most common. The rod-based morphology of Ce-R means that width and length measurements were required in order to obtain full particle size distributions. The width of Ce-R was fairly uniform, with a range of 5 – 10 nm, centred at 7 nm. It was not possible to measure the length of enough particles to obtain a statistically significant length distribution. That said, an average length of 90 nm was measured, with a range of 50 – 200 nm, which was in good agreement with the sizes reported by Yan and co-workers.[2] Ce-P, with an approximate truncated octahedral geometry, was measured across the widest points, and had an approximate particle size of 11 nm, ranging from 8 – 14 nm.

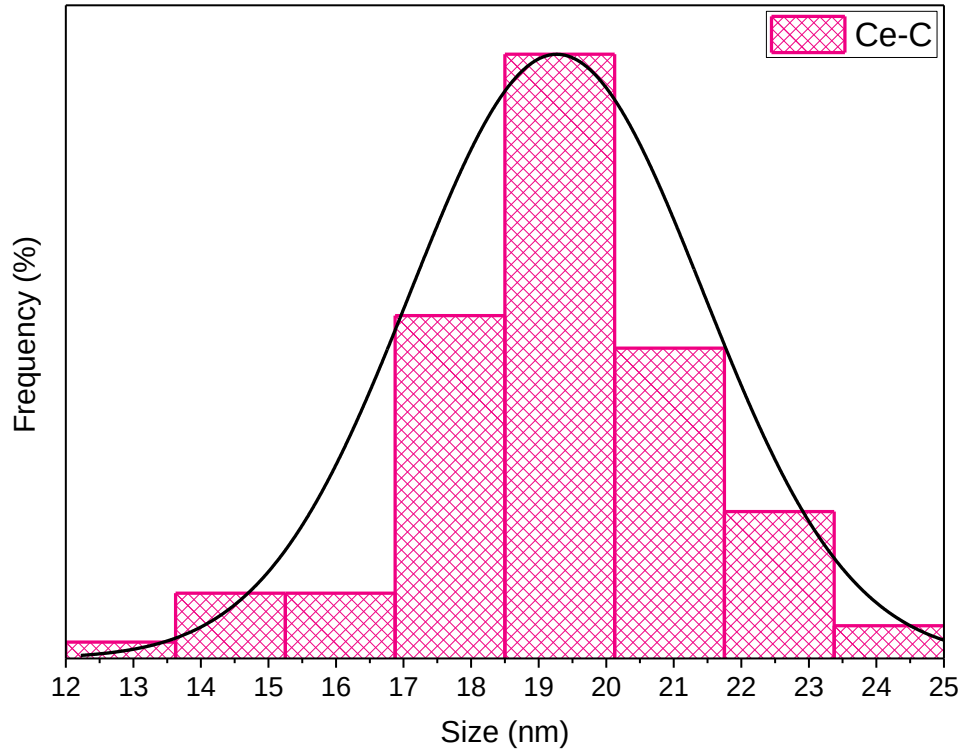

Figure 4a. Particle size distribution of Ce-C.

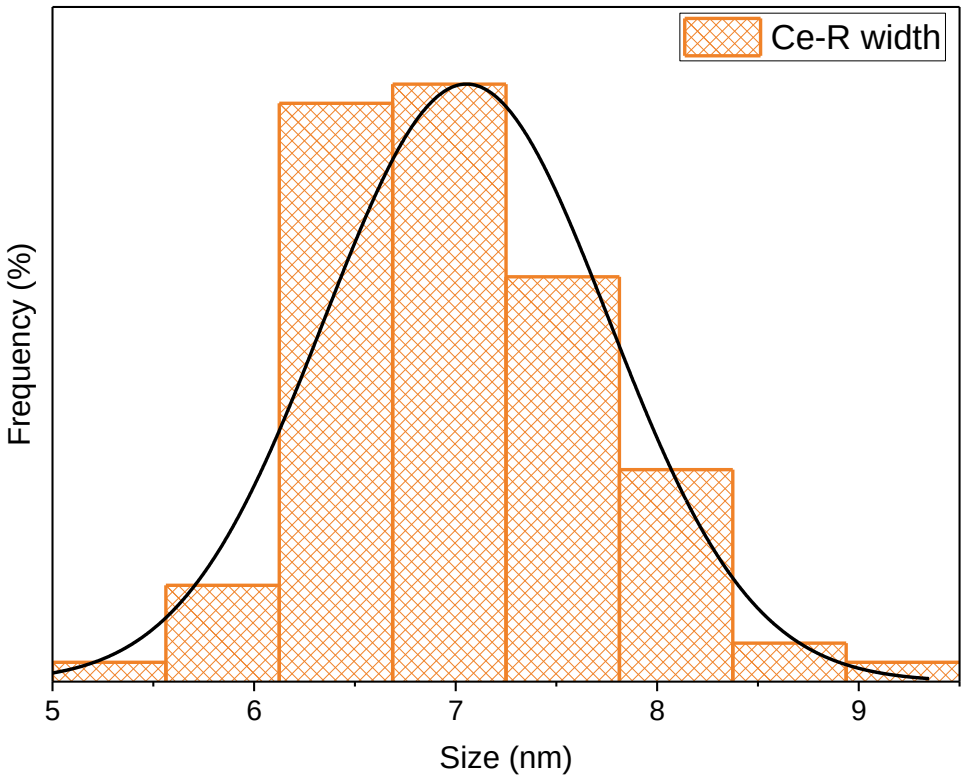

Figure 4b. Particle width distribution of Ce-R

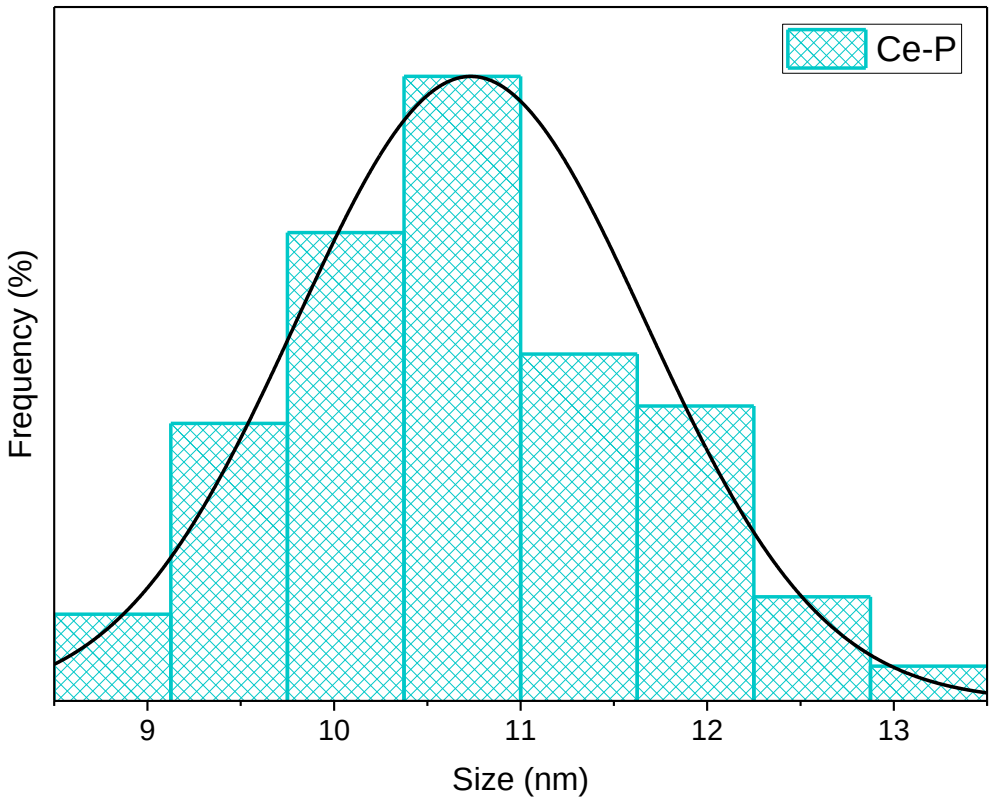

Figure 4c. Particle size distribution of Ce-P

4.2.2 Effect of morphology on the redox and defect properties of ceria

Defects in the materials were probed using visible Raman spectroscopy, a technique widely established for the study of ceria based materials.[4, 22, 23] The spectra were dominated by a triply degenerate F_{2g} mode at a Raman shift of 462 cm^{-1}, representative of symmetrical breathing of the Ce-O_8 lattice, where Ce and O have coordination numbers of 8 and 4 respectively.[24, 25] Also present are much weaker bands at wavenumbers of *ca.* 250 cm^{-1} and 600 cm^{-1}. The latter has been assigned to a defect induced mode (D), with the relative ratios of the defect band to the F_{2g} band (I_D/I_{F2g}) used to estimate the density of defects in ceria based materials, although the precise origin of this mode has been the focus of much discussion.[22, 25-29] A weak band was also observed at 1180 cm^{-1} for all three samples which is representative of a second order longitudinal optical mode (2LO). No differences were observed between the three samples, so this was not investigated any further.

Studies by Taniguchi *et al.* and Luo and co-workers used visible and UV Raman spectroscopy to probe the defect sites in doped ceria.[22, 26] The band centred around 600 cm^{-1} was ascribed to defects with O_h symmetry whereby the cation is octacoordinated and forms an MO_8 type complex by Taniguichi. Similar findings were made by Luo and co-workers who attributed the band at 600 cm^{-1} to the intrinsic oxygen vacancies required to maintain charge neutrality in the presence of Ce^{3+}cations. Wu *et al.* probed the defect sites on un-doped ceria nanostructures with well-defined crystal planes, and proposed an alternative assignment to the defect band at *ca.* 600 cm^{-1}.[4] XPS studies showed very similar levels of Ce^{3+} across all

morphologies, but with nanorods showing the most intense band at 600 cm^{-1} followed by nanocubes with nanopolyhedra showing the least intense defect band. The rods exposed the (110) and (100) surfaces, cubes expose the (100) surface and the polyhedra expose the (111) and (100) surfaces, thus the intensity of the defect band in the Raman spectra is in agreement with the theoretical energy of defect formation which is of the order (110) < (100) < (111). As Raman is not a surface technique and also probes the bulk of a sample, these results suggest that the surface termination influences the defect sites in bulk ceria. Consequently, the authors suggest that the band at 600 cm^{-1} is due to Frenkel-type oxygen defects which form on the surface and develop into the bulk.

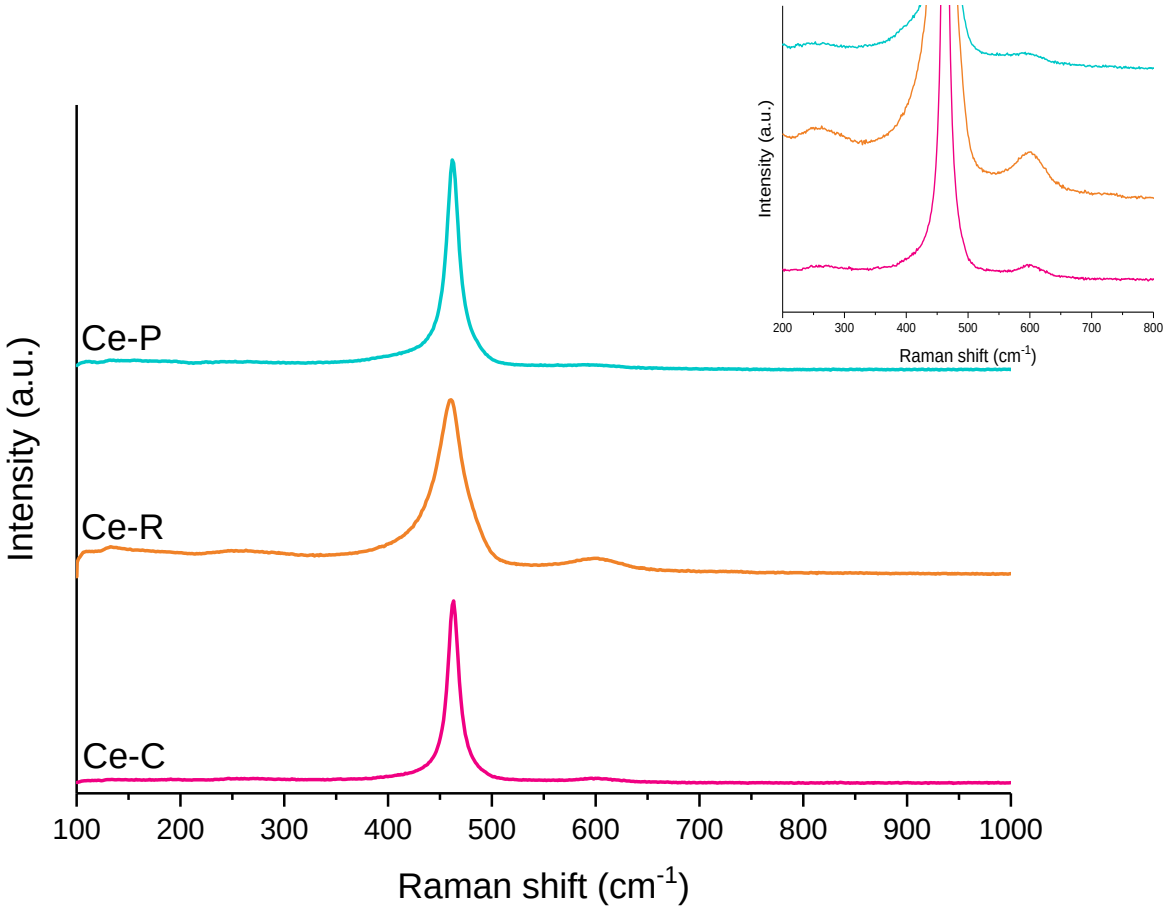

Figure 5. Visible Raman spectra of Ce-C (pink line), Ce-R (orange line) and polyhedra (blue line). Obtained at λ = 514 nm with a laser power of 1 %. Inset shows 200 – 700 cm-1 spectral region.

In full agreement with the findings of Wu *et al.*, Raman spectra of the as prepared ceria nanostructures (Figure 5) showed the I_D/I_{F2g} ratio (Table 2) to be of the order Ce-R > Ce-C >> Ce-P, indicating that defect densities followed the same trend. This is attributed to the lower energy of defect formation on the (110) and (100) surfaces and the subsequent effects on the bulk structure. Additionally, the F_{2g} band observed for the rods was much broader than for the other morphologies which is consistent with an increased defect density and smaller crystallite size as observed by XRD and TEM.

The band at 250 cm^{-1} has recently been attributed to Ce-O longitudinal stretching in the outermost layers.[30] It was suggested that an increase in surface-to-bulk ratio, and thus a greater proportion of outermost layers, results in a greater intensity at a Raman shift of 250 cm^{-1}. This would correlate well with the observed Raman spectra, whereby Ce-R, possessing the highest surface-to-bulk ratio, showed the highest intensity at 250 cm^{-1}. Alternatively, this band has previously been assigned to a Ce-OH vibration,[24] with a higher intensity representative of a higher hydroxyl density. Again, this explanation would be consistent with the obtained spectra, since Ce-R, which is formed through a $Ce(OH)_3$ intermediate, likely possesses the highest hydroxyl density.

Table 2. Defect properties as measured by Raman spectroscopy

Morphology	***F_{2g} band position (cm^{-1})***	***F_{2g} FWHM***	***I_D/I_{F2g}***
Ce-C	461	14.3	0.03
Ce-R	462	37.7	0.07
Ce-P	463	16.3	0.002

H_2-TPR was employed investigate the reducibility of the materials, as shown in Figure 6. It is widely accepted that the high temperature peak observed during CeO_2 H_2-TPR is due to the reduction of bulk species, whilst lower temperature peaks are attributed to the reduction of surface oxygen species.[31] For all materials, a high temperature reduction peak with a maximum at *ca.* 800 °C was observed, although it should be noted that for Ce-R, the bulk reduction peak was shifted by *ca.* 40 °C, down to 765 °C. This suggests, similarly to the Raman data, that the surface termination may influence properties within the bulk structure.

At first glance, Ce-C displayed a bimodal peak distribution with a single, broad low temperature reduction peak with a maximum at 520 °C, in addition to the higher temperature bulk reduction peak. Closer inspection revealed the presence of multiple low temperature reduction peaks, with additional low intensity peaks observed at 320 and 625 °C. A similar profile was observed for Ce-R, although the main surface reduction peak was shifted to a lower temperature of 478 °C. Additional peaks were detected at 312 and 378 °C, although they were obscured by the main surface reduction peak and appeared as shoulders, preventing peak deconvolution. In comparison, two well-defined and distinct low temperature reduction peaks were observed for Ce-P, with temperatures centred at 416 and 523 °C. The peak at 416 °C was noticeably sharper than typically observed, with the lower temperature of reduction suggesting increased reducibility of Ce-P.

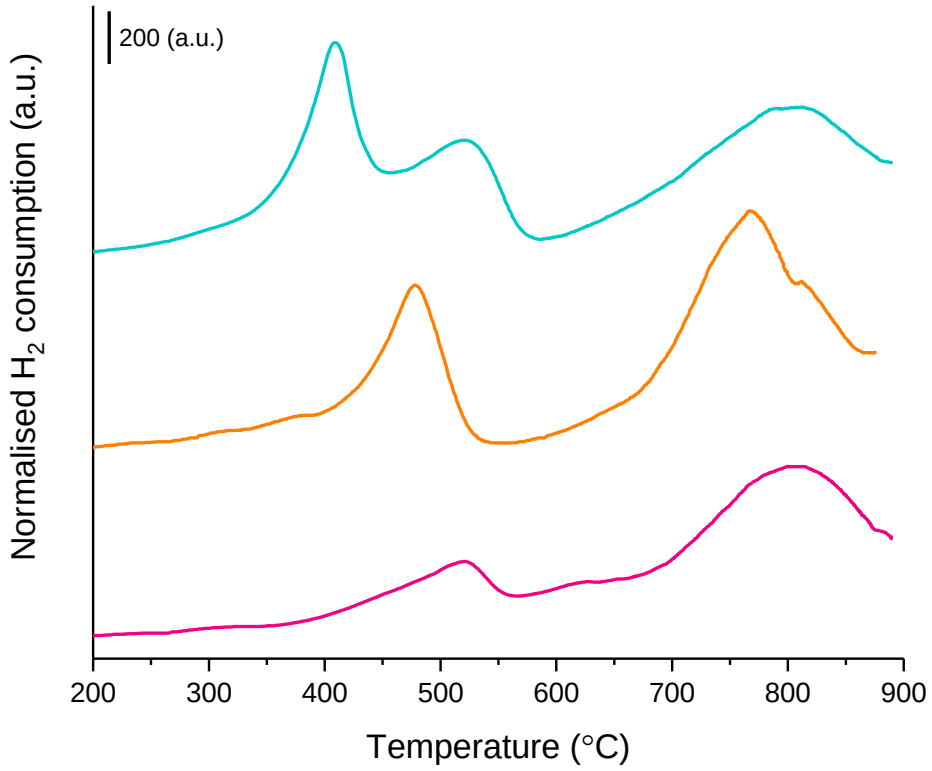

Figure 6. H_2-TPR profiles. Ce-C is represented by the bottom pink line, Ce-R by the orange middle line and Ce-P by the blue top line. All samples were heated at a rate of 10 K min^{-1} under 30 mL min^{-1} 10 % H2/Ar.

H_2 consumption was quantified in accordance with the procedure detailed in Chapter 2. It was found to be highest over Ce-R at 685 $\mu mol_{H2}\, g^{-1}$, followed by Ce-P (572 $\mu mol_{H2}\, g^{-1}$) and then Ce-C (81 $\mu mol_{H2}\, g^{-1}$). However, once normalized to surface area, Ce-P showed the highest H_2 consumption (9.9 $\mu mol_{H2}\, m^{-2}$) followed by Ce-R (8.1 $\mu mol_{H2}\, m^{-2}$) and Ce-C (2.3 $\mu mol_{H2}\, m^{-2}$). The correlation between surface area and low temperature hydrogen consumption has been well-demonstrated for CeO_2 catalysts,[32-35] so the order of hydrogen consumption per gram was fully expected. However, it is not clear why, when normalized to surface area, hydrogen consumption is significantly lower over Ce-C than the other morphologies.

Temperature programmed reduction-oxidation-reduction (TPR-O-R) cycles were also performed to further investigate the redox properties of ceria, since a study by Dolcetti and co-workers suggested the "real" redox properties of ceria can be studied by high temperature redox cycling.[36] To achieve this, the sample was reduced up to 900 °C under H_2/Ar before the gas was switched to He and the sample left to fully cool to room temperature. Once cool, the gas was switched to O_2/He and the temperature was ramped to 900 °C; again the gas was switched to He whilst the sample was allowed to cool back to room temperature. Prior to any TP analyses, the colour of the ceria was a pale yellow, after the initial TPR this changed to a purple colour for all samples, indicating the reduction of Ce^{4+}

to Ce^{3+}. The oxidation step was accompanied by a colour change from purple back to yellow, indicating the occurrence of re-oxidation. Due to difficulties obtaining a stable baseline, TPO analyses were performed non-quantitatively, although oxygen consumption was clearly observed.

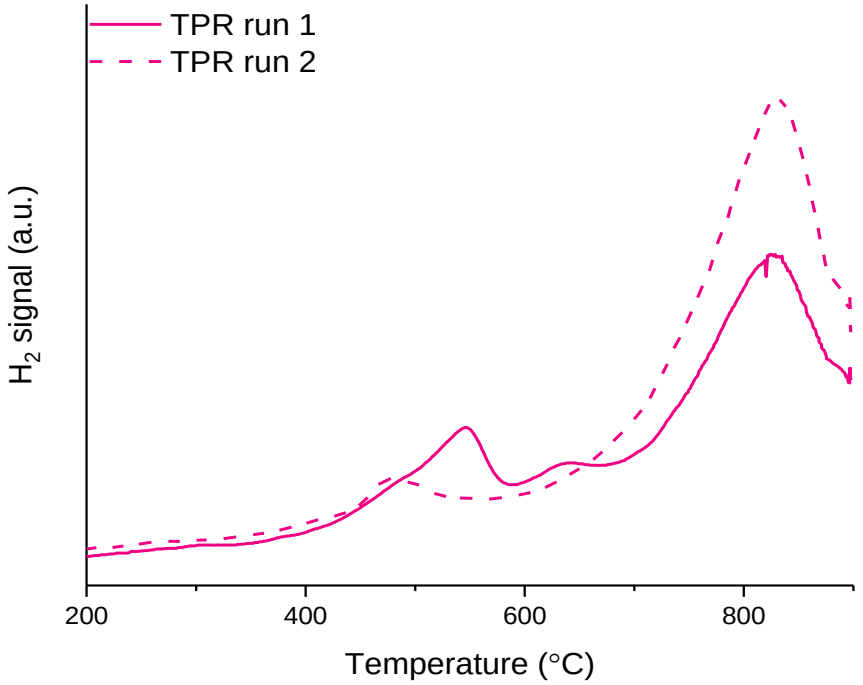

Figure 7a. First and second TPR profiles for CeC. The first reduction profile is represented by a solid line, the second profile is shown with the dashed line.

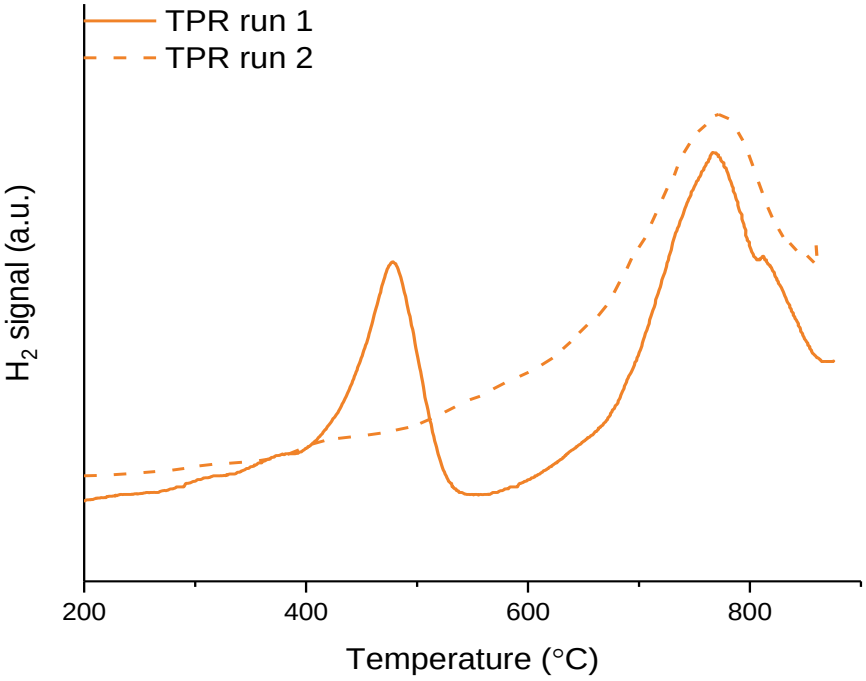

Figure 7b. First and second TPR profiles for Ce-R. The first reduction profile is represented by a solid line, the second profile is shown with the dashed line.

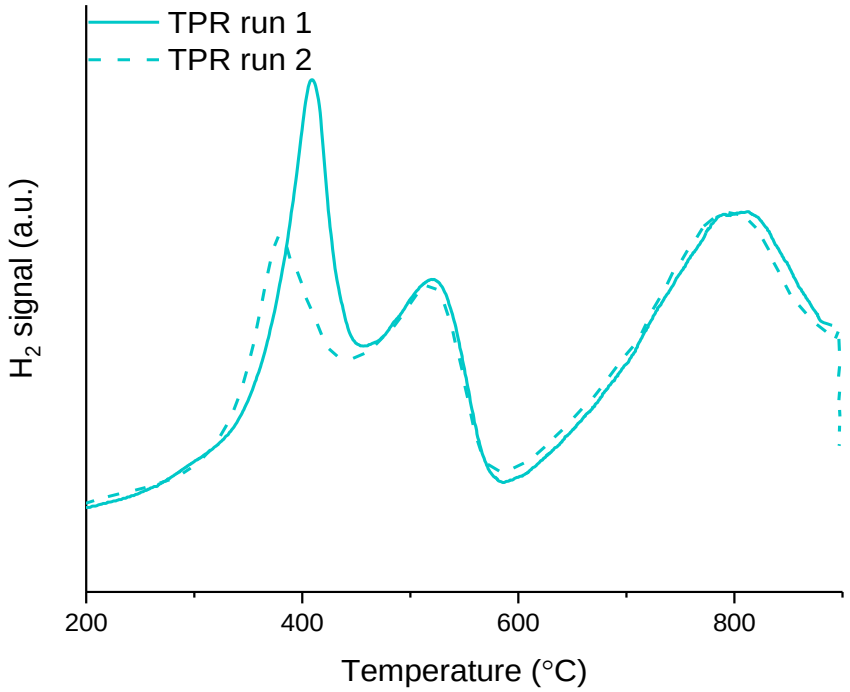

Figure 7c. First and second TPR profiles for Ce-P. The first reduction profile is represented by a solid line, the second profile is shown with the dashed line.

The second TPR profile for Ce-C (Figure 7a) showed a significant reduction in hydrogen consumption below 600 °C, suggesting a significant loss of surface area, with the peak at 625 °C disappearing completely. Interesting, whilst the surface reduction peak was reduced in intensity, a shift to a lower temperature by *ca.* 70 °C was also observed. The loss of surface reduction was even greater for Ce-R (Figure 7b), with no well-defined surface reduction peak observed at all, although it should be noted that significant peak broadening of the higher temperature peak occurred, which may have obscured low intensity peaks. For both Ce-C and Ce-R, a significant increase in intensity was observed for the higher temperature bulk reduction process, indicated significant and loss of surface area occurred for both materials. Interestingly, whilst a slight decrease in the intensity of lowest temperature reduction peak was observed for Ce-P (Figure 7c), with a shift to a lower temperature of *ca.* 30 °C to 385 °C, the second reduction profile was otherwise identical to the initial profile, suggesting a minimal loss of surface area, and highly stable redox properties, even with high temperature redox cycling up to 900 °C. These results, coupled with the initial TPR profiles and hydrogen consumption values ($\mu mol_{H2}\ m^{-2}$), suggest that Ce-P possesses enhanced reducibility, compared with Ce-C and Ce-R.

4.2.3 Effect of morphology on the acid-base properties of ceria

The acid-base properties of ceria can vary according to morphology, due to the different coordination states of the cations and anions;[6] in the bulk structure, the coordination numbers of Ce^{4+} and O^{2-} are 8 and 4 respectively, whereas for the (111), (110) and (100) surfaces, the coordination number of Ce^{4+} is 7, 6 and 6, respectively, whilst the coordination

number of O^{2-} is 3, 3 and 2, respectively. Based on the differing degrees of coordinative unsaturation, the theoretical acidity is (100) ≈ (110) > (111) which would result in the trend of Ce-C ≈ Ce-R > Ce-P whilst the basicity is (100) > (110) ≈ (111) resulting in theoretical basicity of Ce-C > Ce-R ≈ Ce-P.

Temperature programmed desorption (TPD) of acidic and basic probe molecules is a well-established technique to probe basic and acidic sites respectively, and can provide information about the strength and density of sites present.[37] The basic sites were probed by CO_2 desorption. A blank run was performed without admitting CO_2 to the sample, which resulted in no CO_2 being detected, indicating the pre-treatment conditions were sufficient to remove any adsorbed atmospheric CO_2. Of the materials, Ce-R showed the highest levels of CO_2 desorption per gram which is expected since they possess the highest surface area. Both Ce-C and Ce-P showed very similar quantities of CO_2 desorbed (Table 3), but with very different desorption profiles (Figure 8a).

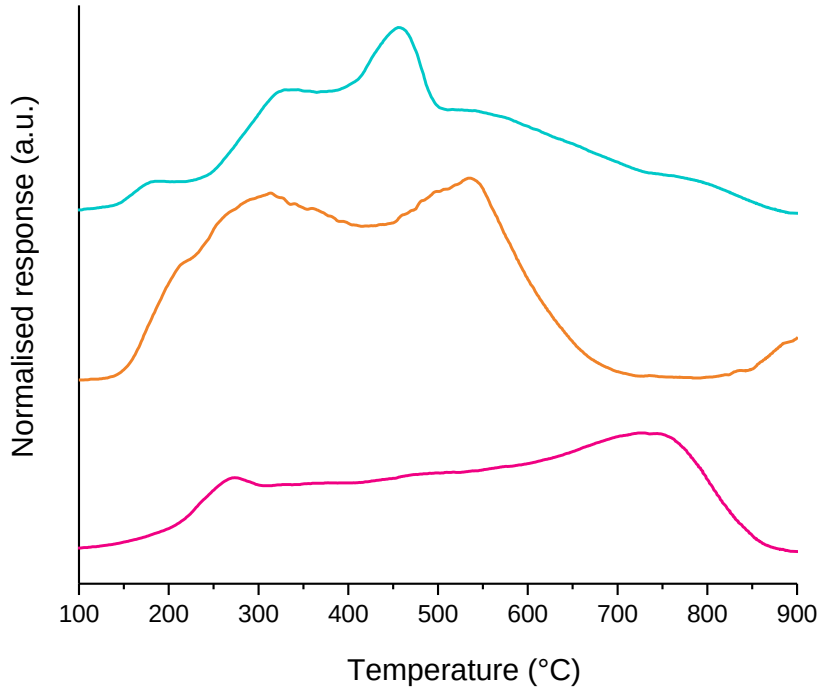

Figure 8a. CO_2 temperature programmed desorption profiles. Ce-C is represented by the pink line, Ce-R by the orange line and Ce-P by the blue line. All samples were heated at a rate of 10 K min^{-1} under 30 mL min^{-1} He.

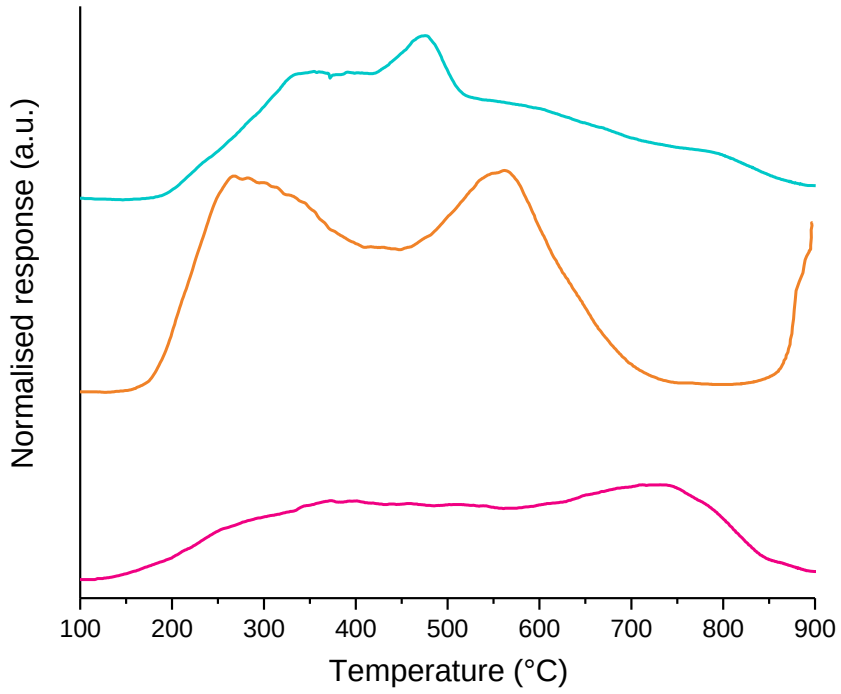

Figure 8b. NH_3 temperature programmed desorption profiles. Ce-C is represented by the pink line, Ce-R by the orange line and Ce-P by the blue line. All samples were heated at a rate of 10 K min^{-1} under 30 mL min^{-1} He.

Ce-P showed the most complex distribution of basic sites, with peaks observed at 180, 336, 452, 546 and 786 °C, suggesting a wide range of basic strength sites. The peak at *ca.* 450 °C was the most intense, suggesting mainly medium strength basic sites present with polyhedral morphology. On the other hand, Ce-C showed a wide desorption profile across the range 125 – 880 °C, with clear maxima observed at 268 and 736 °C whilst deconvolution showed an additional peak at 488 °C. In contrast to the desorption profile of Ce-P, the highest quantity of CO_2 was desorbed at high temperatures, indicating a high proportion of strongly basic sites present in Ce-C. A higher quantity of desorbed CO_2 was observed for Ce-R, with a simpler desorption pattern, consisting of 2 well defined peaks at 315 and 536 °C. Additionally, the start of a peak can be observed from 850 – 900 °C, indicative of very strongly basic sites, although the temperature of 900 °C was insufficient to complete desorption so this could not be quantified.

Table 3. Acid-base properties of morphologically controlled ceria					
Morphology	***CO_2 desorbed ($\mu mol\ g^{-1}$)[a]***	***CO_2 desorbed ($\mu mol\ m^{-2}$)***	***NH_3 desorbed ($\mu mol\ g^{-1}$) [b]***	***NH_3 desorbed ($\mu mol\ m^{-2}$)***	***Basicity / acidity ratio***
Ce-C	95	2.7	13	0.37	7.3
Ce-R	138	1.6	23	0.27	6.0
Ce-P	100	1.7	15	0.26	6.5
[a] calculated from CO_2 TPD; [b] calculated from NH_3 TPD					

The presence and strength of any acid sites present were probed by NH_3-TPD. The desorption profiles observed (Figure 8b) were very similar to those obtained with a CO_2 adsorbate, although some minor features were lost. As with the basicity measurements, similar quantities of NH_3 per gram of catalyst were desorbed for Ce-C and Ce-P, with a higher amount over Ce-R, however, when normalised for surface area, very comparable quantities were desorbed over Ce-R and Ce-P. As described above, the different coordination number of cerium cations and oxygen anions at the surface is dependent on the surface present. From the different degrees of surface coordinative unsaturation (*cus*) of cations and anions present in the different surfaces, the theoretical basicity of surface O^{2-} is (100) > (110) ≈ (111) whilst the theoretical acidity of surface Ce^{4+} is (100) ≈ (110) > (111).[6] TPD analysis showed that the basicity followed the theoretical trend based on *cus*, with Ce-C, containing mainly the (100) surface, showing higher levels of basicity than Ce-R and Ce-P, which possessed mainly (110) and (111) surfaces respectively. In contrast, acidity measurements deviated from the predicted trend, with Ce-R, containing (110) surfaces, exhibiting lower acidity that theoretically predicted. This was attributed to the increased defect density of Ce-R, as measured by Raman, which can reduce the acidity of cerium cations, resulting in lower Lewis acidity.[6]

4.2.4 Effect of morphology on glycerol conversions at a GHSV of 3600 h^{-1}

Initially the prepared materials were tested under identical reaction conditions, to investigate the effect of morphology on catalytic activity. Catalyst mass, volume and space velocity were kept constant, at reaction temperatures of 320, 360 and 400 °C. GLY conversion as a function of temperature is shown in Figure 9 with obtained product yields grouped into functional groups given in Table 4. At all reaction temperatures, significantly lower GLY conversions were obtained over Ce-C compared with Ce-R and Ce-P. At 320 °C, GLY conversions of 17, 65 and 58 % were obtained over Ce-C, Ce-R and Ce-P, respectively with carbon balances of 93, 81 and 91 %. As shown in chapter 3 (section 3.2.1), at a reaction

temperature of 320 °C, negligible GLY conversion takes place in the absence of a catalyst. Normalisation of GLY conversion to catalyst surface area as a function of time showed GLY conversion to be constant across the three materials, with a value of *ca.* 0.28 μmol h^{-1} m^{-2}. This indicated that catalytic activity was determined by surface area, although, at higher reaction temperatures, thermal effects are more dominant and so GLY conversion is not solely determined by catalyst surface area.

Increasing the reaction temperature to 360 °C resulted in significant increases in GLY conversion over Ce-R and Ce-P, with almost all GLY converted. In contrast, a modest increase in GLY conversion was observed over Ce-C, with a conversion of 29 % achieved. The carbon balance remained high over Ce-P (> 90 %) but dropped to 83 and 76 % over Ce-C and Ce-R, respectively.

At 400 °C, only traces of unconverted GLY were observed over Ce-R and Ce-P whilst conversion reached 91% over Ce-C. Under these conditions, a significant decrease in carbon balance was achieved, at 61, 62 and 67 % over Ce-C, Ce-R and Ce-P respectively. Thermogravimetric analysis (TGA) was utilised to estimate the coke content of the catalysts after reaction at 400 °C; carbon deposition was highest over Ce-R at 65 mg g^{-1}, followed by Ce-C (47 mg g^{-1}) and Ce-P (16 mg g^{-1}). As shown in Table 1, only a small proportion of carbon lost is in the form of carbon deposition on the catalyst, accounting for < 2 % of the carbon balance over all materials. Whilst only a small quantity of carbon injected was retained on the catalyst surface as coke, the significantly reduced carbon balances obtained at 400 °C are indicative of the presence of additional chemical species were cannot be identified by our analysis methods, using GC-FID. Further details are given below (section 4.2.6).

At 320 °C, similar functional group product yields were similar between Ce-R and Ce-P (Table 4) with significantly lower yields obtained over Ce-C, predominantly due to the lower GLY conversion observed. In particular, the MeOH space time yield (STY) was very similar over Ce-R and Ce-P, at 39 and 40 g_{MeOH} h^{-1} kg_{cat}^{-1}, respectively, and a factor of ten lower over Ce-C at 4 g_{MeOH} h^{-1} kg_{cat}^{-1}.

As the temperature was increased to 360 °C, significant increases in product yields were observed for Ce-R and Ce-P, with more minor increases observed for Ce-C due to the modest increase in GLY conversion over this catalyst. Ce-P resulted in the highest yields of all functional groups except ketones, due to the increased carbon balance when compared with Ce-R, despite the similar conversion levels and product selectivity. A similar trend was observed for the MeOH STY, whereby a significantly higher productivity was reported for Ce-P compared with Ce-R, despite the comparable MeOH selectivities. Due to the significantly lower conversion achieved over Ce-C, it was not possible to directly compare product distributions.

At the highest reaction temperature of 400 °C, the yield of alcohol and ketones was highest over Ce-P, predominantly due to the high MeOH and ACE selectivies, respectively, followed by Ce-R and then Ce-C. The same trends were observed for the yield of CO_x, comprised of CO and CO_2 with traces of CH_4, considered to be undesirable by-products in the reaction. The highest yield of aldehydes was obtained over Ce-R, followed by Ce-C, comprised mainly of ACA, with smaller amounts of propionaldehyde and ACR. The lower aldehyde yield observed over Ce-P was attributed to increased conversion of ACA to ACE, which will be discussed below in more detail. Interestingly, a significantly higher yield of unknown products was formed over Ce-C suggesting that the HA pathway, which typically dominates over ceria catalysts, was not the major reaction pathway over Ce-C. This will be discussed in greater detail in the following sections. The MeOH STY followed the trend Ce-P > Ce-R >> Ce-C; MeOH selectivities of 24.5 and 22.6 % were reported for Ce-P, with a much lower selectivity of 10.0 % reported over Ce-C.

Table 4. Glycerol conversion and product distribution over CeO_2 with different morphologies

Entry	*Catalyst morphology*	*Reaction T (°C)*	*C_{GLY} [a] (%)*	*Mass Balance (%)[b]*			*Yield[c] (%)*							*MeOH S.T.Y. ($g\ h^{-1} kg_{cat}^{-1}$)*	*Carbon deposition ($mg\ g^{-1}$) [d]*
				C	*H*	*O*	*Alc.*	*Diols*	*Ald.*	*Ket.*	*Ac.*	*Cox*	*Unk.*		
1	Ce-C	320	17	93	91	91	1.1	1.9	3.0	2.4	0.7	1.0	5.8	4.0	-
2		360	29	83	81	81	2.7	3.5	5.2	5.9	1.1	1.6	4.4	8.9	-
3		400	91	61 (62)	53	54	15.6	6.5	5.9	6.4	4.3	7.7	15.5	60.4	47
4	Ce-R	320	65	82	75	73	5.7	8.2	4.1	17.5	5.6	3.3	8.1	39.4	-
5		360	98	76	66	63	10.4	9.3	7.8	19.8	8.9	6.3	11.8	90.9	-
6		400	> 99	62 (64)	48	56	20.2	0.8	7.8	10.8	1.4	15.1	6.5	164.3	66
7	Ce-P	320	58	91	84	82	4.9	7.3	4.3	17.6	4.1	2.9	11.3	40.2	-
8		360	96	91	80	76	14.6	12.4	12.4	11.3	11.9	8.9	15.3	121.5	-
9		400	> 99	67 (67)	51	63	23.5	0.3	3.2	15.0	2.1	18.8	4.3	201.3	16

[a] GLY conversion; [b] Carbon mass balance (± 3 %) of products detected in GC1 and GC2 (values in parenthesis include coke deposited on catalyst); [c] yield of products detected in GC1 and GC2; Alc., alcohols; Ald., aldehydes; Ket., ketones; Ac., acids; Unk., unknowns; [d] Calculated from TGA analysis. Reaction conditions; 50 wt.% GLY/water flow 0.016 mL min^{-1}, 0.5 g CeO_2, 15 mL min^{-1} Ar, GHSV = 3600 h^{-1}; 3 hours. Full product distribution is shown in the appendix (Table A4.2)

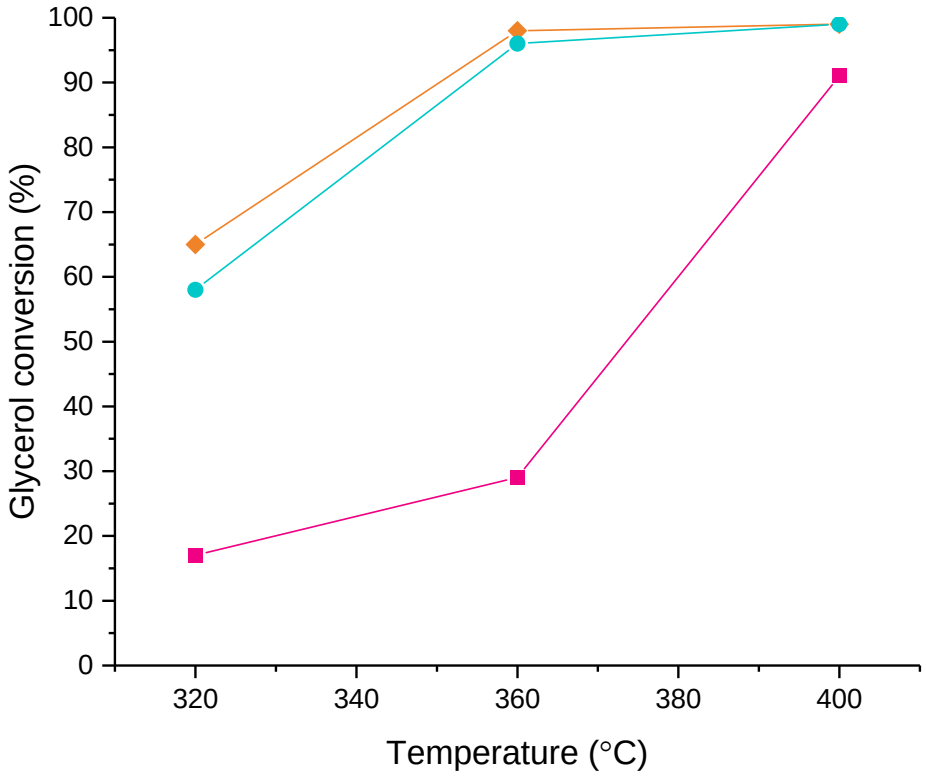

Figure 9. Glycerol conversion at different temperatures at a space velocity of 3600 h^{-1} over Ce-C (pink symbols), Ce-R (orange symbols) and Ce-P (blue symbols). Reaction conditions; 50 wt. % glycerol (0.016 mL min^{-1}), 0.5 g CeO_2, 15 mL min^{-1} Ar, 3 hours, GHSV = 3600 h^{-1}.

4.2.5 Effect of ceria morphology on product distributions under *iso*-conversion

4.2.5.1 Low conversion

As shown in Chapter 3, a strong relationship between product distribution and GLY conversion exists. [38, 39] Since significantly lower GLY conversions were achieved over Ce-C compared with Ce-R and Ce-P at all temperatures tested, the product distributions could not be directly compared across the three catalysts. In order to overcome this limitation, catalyst masses and subsequent space velocities were altered to achieve comparable levels of GLY conversion across all materials. A GLY conversion of 17 % was attained over Ce-C at 320 °C with a GHSV of 3600 h^{-1}. GHSVs were adjusted to 11250 and 9000 h^{-1}, over Ce-R and Ce-P respectively, resulting in conversions of 14 and 16 %. Similarly to experiments performed at a constant GHSV, normalisation of GLY conversion to the total catalyst surface was constant across all three catalysts, giving a value of *ca.* 0.28 $mmol_{gly}$ h^{-1} $m^{-2}{}_{cat}$. The carbon balance was high (*ca.* 95 %) across all morphologies, with any lost carbon attributed to reactor fouling and/or uncollected products.

Due to the diverse range of products formed, products are grouped into their functional groups; product distributions by functional groups at a GLY conversion of *ca.* 15 % are shown in Figure 10. Product distributions were similar over Ce-R and Ce-P, with HA as the main product detected, at selectivities of 37.4 and 43.3 % respectively, contributing to the

high ketone selectivity observed. The other major products observed over Ce-R and Ce-P were 1,2-PD (*ca.* 6 %), EG (*ca.* 7 %), MeOH (*ca.* 8 %) and ACA (*ca.* 5 %); smaller quantities of numerous other products were found including ACR, 2,3-BD, AA, acetic acid, propanoic acid, CO and CO_2 with trace amounts of propionaldehyde, ACE, EtOH, PrOH and 1,3-PD. Unidentified products were also observed over Ce-R and Ce-P. These products were observed with GC1 but it was not possible to determine their identity, despite numerous attempts, thus selectivity to these unknown compounds was calculated using average response factors from known products with similar retention times.

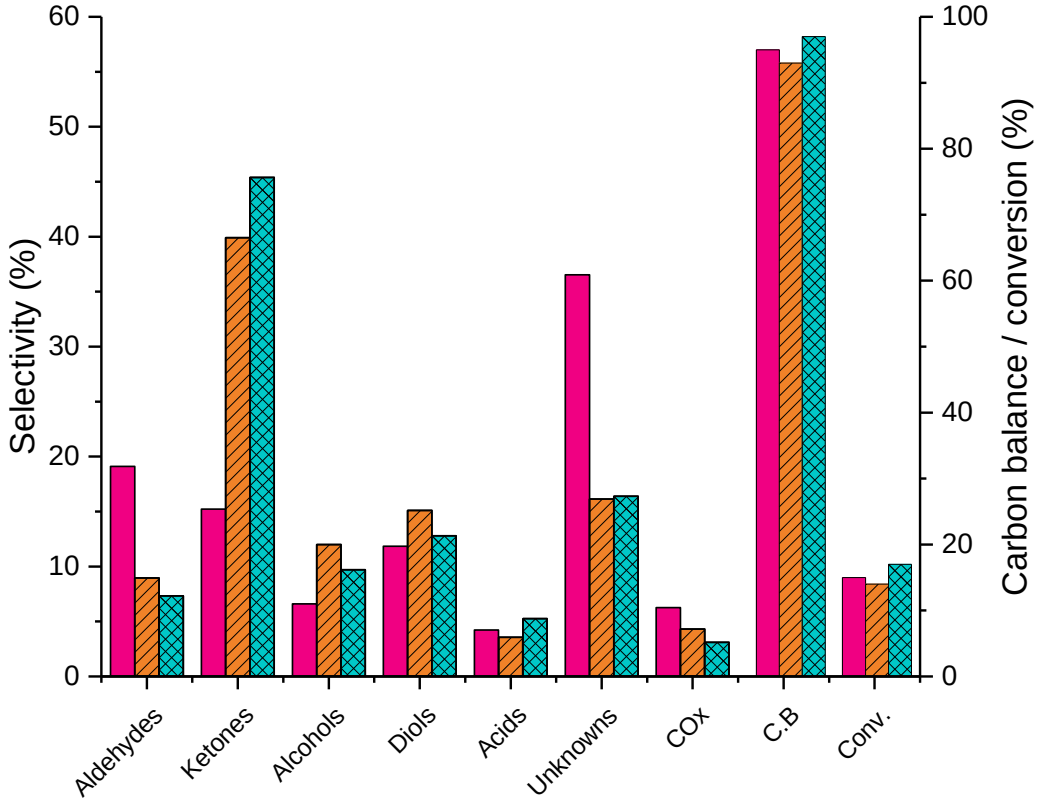

Figure 10. Product distributions at a glycerol conversion of ca. 15 % over Ce-C (pink bars), Ce-R (orange bars) and Ce-P (blue bars). Reaction conditions; 320 °C, 50 wt. % glycerol (0.016 mL min^{-1}), 15 mL min^{-1} Ar, 3 hours, GHSV = 3600 h^{-1} (Ce-C), 11250 h^{-1} (Ce-R), and 9000 h^{-1} (Ce-P)

Significant differences in product distribution were achieved over Ce-C when compared with Ce-R and Ce-P; HA selectivity was significantly reduced (14.1 %) with larger quantities of ACR detected (14.5 % selectivity). Additionally, a high selectivity towards unknown products was observed (*ca.* 37 %), suggesting the dehydration of GLY via the loss of a primary hydroxyl group to yield HA is not the dominant reaction pathway over Ce-C. Other detected products were similar to those obtained over Ce-R and Ce-P and included EG (6.8 %), ACA (4.2 %), MeOH (3.5 %) and CO_2 (5.0 %), with propionaldehyde, ACE, EtOH, 2,3-BD, AA, acetic acid, propanoic acid, 1,2-PD, 1,3-PD and CO observed in smaller quantities.

4.2.5.2 High conversion

As we have previously shown that MeOH is a terminal product,[38, 40] high MeOH selectivity is typically only observed at very high GLY conversions. To compare MeOH selectivity at full GLY conversion, an increased catalyst mass (and subsequent volume) of Ce-C was used to decrease the space velocity. Since full GLY conversion was achieved at a space velocity of 3600 h^{-1} over Ce-R and Ce-P at 400 °C, the space velocity was reduced to 1800 h^{-1} over Ce-C to achieve the same level of conversion. Product distributions under these conditions are shown in Figure 11.

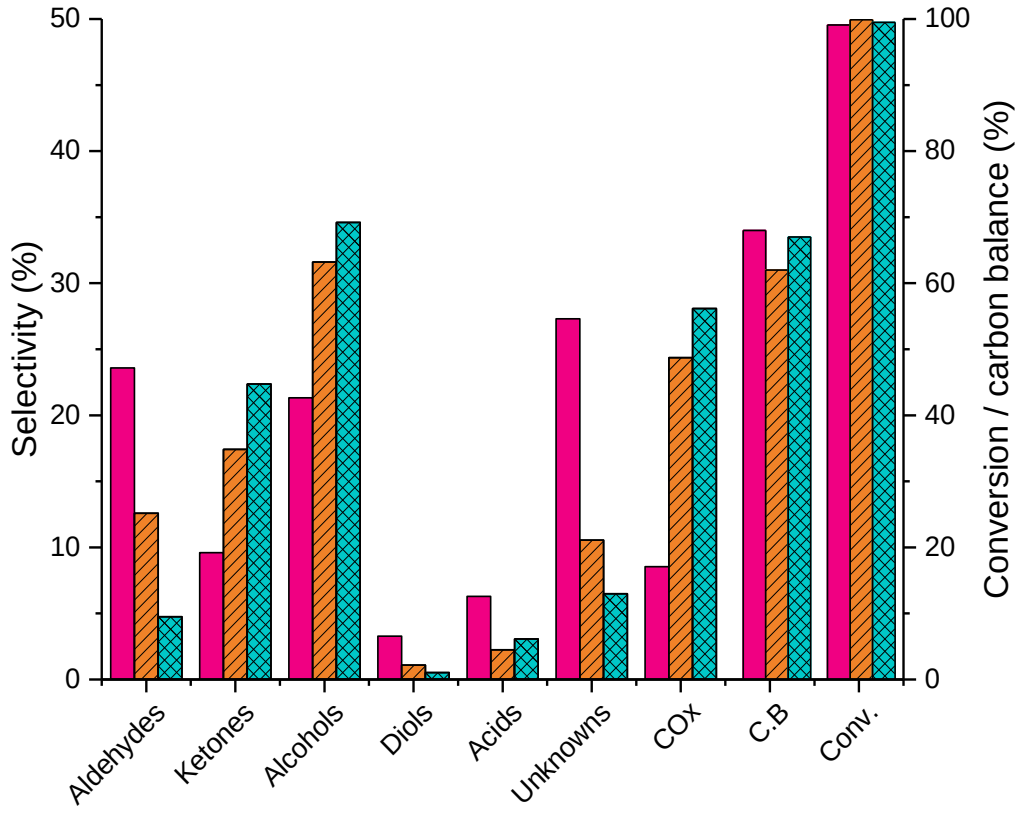

Figure 11. Product distributions at a glycerol conversion of > 95 % over Ce-C (pink bars), Ce-R (orange bars) and Ce-P (blue bars). Reaction conditions; 400 °C, 50 wt. % glycerol (0.016 mL min^{-1}), 15 mL min^{-1} Ar, 3 hours, GHSV = 1800 h^{-1} (Ce-C), 3600 h^{-1} (Ce-R), and 3600 h^{-1} (Ce-P).

Product distribution by functional group appears to vary somewhat over all three morphologies, although fairly similar product distributions are observed for Ce-R and Ce-P. Alcohol selectivity was of the order Ce-P > Ce-R >> Ce-C, with MeOH selectivities of 24.5, 22.6 and 13.1 % respectively. Other alcohols included EtOH, 2-PrOH, 1-PrOH and AA; EtOH and PrOH selectivities followed the same order as MeOH selectivity, whereas AA showed the opposite trend.

Under these reaction conditions, only small quantities of HA were observed over all materials. Low selectivity to diol products, EG, 1,2-PD and 1,3-PD, was also observed. These results suggest that these products are intermediates in the process, and can be further converted, which is consistent with previous findings.

Reasonably high aldehyde selectivity was observed over Ce-C (*ca.* 24 %), comprised predominantly of ACA (16.5 %) with smaller quantities of propionaldehyde (4.1 %) and ACR (2.7 %) also detected. The selectivity to ACR over Ce-C was significantly lower than was observed at low GLY conversions, likely due to the higher reaction temperature used, as previously reported by other authours.[41] A total aldehyde selectivity of 13 % was observed over Ce-R, composed of ACA (5.8 %), propionaldehyde (5.6 %) along with small quantities of ACR and butyraldehyde. Less than 5 % of the total product distribution over Ce-P consisted of aldehydes, primarily due to the low ACA selectivity observed. The low aldehyde selectivity observed over Ce-P, and to a lesser extent Ce-R, was attributed to the presence of ketonization reactions, which have been widely reported over CeO_2 and CeO_2-containing catalysts,[42-44] whereby 2 ACA molecules and a water react to give ACE, CO_2 and 2 equivalents of H_2. No H_2 gas was detected throughout these experiments, but hydrogen is required to form several products, including MeOH, suggesting it was consumed *in-situ*. ACE and CO_2 selectivities followed the trend Ce-P > Ce-R >> Ce-C, the opposite order to ACA selectivity, suggesting ACA was more effectively converted to ACE *via* ketonization reactions over Ce-P.

A reasonable selectivity towards ketones was observed over Ce-R and Ce-P, despite the high levels of HA conversion. This was attributed mainly to ACE and 2,3-BD, with small quantities of HA, cyclopentatone and hexanone also detected. As shown in Figure 10, at complete GLY conversion, high ketone selectivity is typically accompanied by low aldehyde selectivity, and high CO_x selectivity. Both CO and CO_2 were observed over all materials; these are undesirable by-products which are typically produced under conditions yielding high levels of MeOH. Future works will focus on reducing CO_x levels without reducing MeOH selectivity. For all three catalysts, a low (< 70 %) carbon balance was achieved at full GLY conversion. Excluding catalyst coking, the carbon balances were found to be 68, 62 and 67 % over Ce-C, Ce-R and Ce-P, respectively. When accounting for any carbon deposited on the catalyst surface in the form of coke, the carbon balances were calculated to be 69, 64 and 68 % over Ce-C, Ce-R and Ce-P, respectively, suggesting that the loss of carbon through catalytic coking was minimal. To further investigate the carbon balance, CHN analysis was performed on post-reaction samples obtained over all three materials, under full GLY conversion conditions. The total carbon content of the reaction was calculated as the sum of catalyst coking, gaseous products and CHN analysis, as shown in Table 5, and was found to be approximately 95 % for all three materials. The missing *ca.* 5 % was attributed to reactor fouling, observed when cleaning the reactor following a catalytic test. fouling. The discrepancies between observed carbon balances as calculated from GC analysis, and total organic carbon analysis was attributed to the formation of insoluble humin-type products,

which were visibly present; similar findings were made by Hernandez *et al.* over lanthanum based materials.[45]

Table 5. Full product distribution at iso-conversion at C_{gly} > 99% and a reaction temperature of 400 °C. Space velocities: Ce-C = 1800 h^{-1}, Ce-R = 3600 h^{-1}, Ce-P = 3600 h^{-1}.			
	Ce-C	***Ce-R***	***Ce-P***
Coking	1.8	2.4	0.8
Gaseous products	7.9	17.2	19.5
CHN analysis	84.8	75.7	76.1
Total Carbon Content	94.5	95.3	96.4
Reaction conditions; 400 °C, 50 wt. % GLY (0.016 mL min^{-1}), 15 mL min^{-1} Ar, 3 hours, GHSV = 1800 h^{-1} (Ce-C), 3600 h^{-1} (Ce-R), and 3600 h^{-1} (Ce-P).			

The total carbon content was similar across all three materials, although the proportion of gaseous products was significantly lower for Ce-C compared with Ce-R and Ce-P. The proportion of gaseous products followed the trend Ce-P > Ce-R >> Ce-C, which was in agreement with the trend of MeOH selectivity, suggesting a correlation between high MeOH and CO_x selectivities. Catalyst coking was of the order Ce-R > Ce-C > Ce-P. Whilst there was no direct correlation between the total acidity or basicity of the materials, it is possible that the level of catalyst coking was determined by the relative proportion of strong acid sites, as estimated by NH_3-TPD. Due to the complexity of the desorption profiles it was not possible to deconvolute the peaks, but it can be seen that Ce-R had the strongest acid sites (Figure 8b), with Ce-P possessing the lowest amount of strong acid sites suggesting catalyst acidity may influence carbon deposition over ceria catalysts.

4.2.6 Contact time effects

As shown earlier (section 4.2.4), with catalyst mass and GHSVs kept constant, GLY conversion followed the trend Ce-R > Ce-P >> Ce-C, in agreement with the trend of catalyst surface area. Due to the inherent differences in surface area and consequent catalytic activity, it was not possible to compare product distributions at constant GLY conversions and GHSVs. To achieve comparable GLY conversion levels over three materials with different surface areas, different catalyst masses were required. Since all the morphologies had similar densities, altering the catalyst mass resulted in significant differences in GHSV and contact time.

At a reaction temperature of 320 °C and a GHSV of 3600 h^{-1}, ACR selectivity was 15 % over Ce-C, and 2 % over both Ce-R and Ce-P, respectively, with GLY conversions of 15, 65 and 58 %. Due to differences in GLY conversion, it was difficult to attribute the increased ACR

observed over Ce-C solely to morphological differences, due to possible relationships between GLY conversion and ACR selectivity. Altering the GHSVs to achieve a constant GLY conversion of *ca.* 15 % over all three materials resulted in ACR selectivities of 14.5, 3.2 and 1.5 % over Ce-C, Ce-R and Ce-P, respectively. This showed that the differences in ACR selectivity obtained over Ce-C *vs.* Ce-R and Ce-P was not due to differences in GLY conversion.

To achieve comparable GLY conversion over the three materials, an increased contact time was required over Ce-C, therefore it was considered important to investigate the effect of increased contact time for Ce-R and Ce-P to determine whether the increased ACR observed for Ce-C was a result of the increased contact time.

Numerous reactions were performed between 320 and 400 °C, with a variety of GHSVs explored, as shown in Table 5. As explained above, due to the inherent differences in surface area and consequent catalytic activity, it was not possible to compare product distributions at constant GLY conversions and GHSVs. Typically, at a given reaction temperature, an increase in contact time resulted in a decrease in ACR selectivity. This is illustrated by entries 2, 4 and 6 in Table 5. At a reaction temperature of 320 °C, ACR selectivities of 3.2, 2.4, and 1.3 % were obtained at GHSVs of 11250, 3600, and 1500 h^{-1}, respectively over Ce-R. These results provide good confirmation that the increased ACR selectivity observed over Ce-C at *iso*-conversion was not a result of the increased contact time required to achieve comparable GLY conversions. Coupled with the experiments performed at *iso*-conversion, the experiments performed with increased contact times over Ce-R and Ce-P provide good evidence that the increased ACR selectivity observed over Ce-C was related to morphological differences between the catalysts, and was not merely a consequence of GLY conversion or catalyst contact time.

The highest MeOH productivity was observed over Ce-P at a reaction temperature of 400 °C and a GHSV of 3600 h^{-1}, with a STY of 201 g h^{-1} kg^{-1}_{cat}. Reactions performed at 320 and 360 °C over Ce-P showed that MeOH selectivity was not positively influenced by an increased contact time. Entries 3, 5, and 7 in Table 5 show reactions over Ce-P at 320 °C, at GHSVs of 9000, 3600, and 1800 h^{-1}, respectively; as the GHSV was reduced, MeOH selectivity decreased from 8.3 to 7.0 to 6.5 %. A similar trend was observed at 360 °C (entries 10 and 12, Table 5), whereby reducing the SV from 3600 to 1800 h^{-1} resulted in MeOH selectivity decreasing from 12.0 to 9.4 %. These results suggest that MeOH itself may be further converted with increased catalyst contact, thus no attempts to improve the STY over Ce-P at 400 °C by increased contact time were made.

Entries 15 and 17 in Table 5 compares reactions at 400 °C over Ce-R at GHSVs of 3600 and 11250 h^{-1}, respectively. It was hypothesised that a reduction in contact time may lead to an

increase in MeOH productivity due to a decrease in any sequential reactions which may lead to lower MeOH selectivities. However, the associated decrease in contact time from 1 to 0.3 sec resulted in a significant decrease in MeOH selectivity, from 22.6 to 12.8 %. In contrast to the reaction performed at 3600 h^{-1}, a significant quantity of HA was detected with a shorter contact time. This highlighted the importance of the conversion of intermediate products in order to maximise MeOH selectivity.

Table 5. Glycerol conversion and main product selectivities as a function of contact time at various temperatures								
Entry	***Catalyst***	***Reaction T (°C)***	***GHSV (h^{-1})***	***Contact time (s)***	***C_{GLY}[a] (%)***	***ACR (%)***	***MeOH (%)***	***HA (%)***
1	***Ce-C***	320	3600	1.0	15	14.2	3.5	14.1
2	***Ce-R***	320	11250	0.3	15	3.2	7.7	37.4
3	***Ce-P***	320	9000	0.4	15	1.5	8.3	43.3
4	***Ce-R***	320	3600	1.0	65	2.4	7.2	29.8
5	***Ce-P***	320	3600	1.0	58	1.8	7.0	30.2
6	***Ce-R***	320	1500	2.4	99	1.3	7.3	15.0
7	***Ce-P***	320	1800	2.0	91	1.5	6.5	15.5
8	***Ce-C***	360	3600	1.0	29	12.7	6.0	21.8
9	***Ce-R***	360	3600	1.0	98	1.9	10.5	21.1
10	***Ce-P***	360	3600	1.0	96	1.5	12.0	7.3
11	***Ce-R***	360	1500	2.4	100	0.3	13.1	2.3
12	***Ce-P***	360	1800	2.0	>99	0.5	9.4	2.0
13	***Ce-C***	400	1800	2.0	>99	2.7	13.1	2.8
14	***Ce-C***	400	3600	1.0	91	1.1	10.0	8.0
15	***Ce-R***	400	3600	1.0	>99	0.8	22.6	0.4
16	***Ce-P***	400	3600	1.0	>99	0.3	24.5	0.3
17	***Ce-R***	400	11250	0.3	86	2.1	12.8	21.9

[a] GLY conversion; Reaction conditions; 50 wt.% GLY/water flow 0.016 mL min^{-1}, variable catalyst mass, 15 mL min^{-1} Ar, GHSV as reported; 3 hours.

4.2.7 Mechanistic discussion

The results discussed above, both at a constant GHSV and at *iso*-conversion, suggest that ceria morphology does not affect catalyst activity, which appears to be dictated by surface area, but can significantly influence product distribution. At complete GLY conversion, MeOH space time yields (STY) followed the order of MeOH selectivity, with the highest STY obtained over Ce-P (201 g h^{-1} kg^{-1}), followed by Ce-R (164 g h^{-1}) and then Ce-C (47 g^{-1} kg^{-1}). The MeOH STY trend at full conversion, mirrored the HA STY at low conversion, with values of 155 g h^{-1} kg^{-1}, 105 g h^{-1} kg^{-1}, and 12 g h^{-1} kg^{-1} for Ce-P, Ce-R and Ce-P, respectively. As shown in Figure 12, there appears to be a strong correlation between HA STY at low GLY conversion and MeOH STY at high conversion.

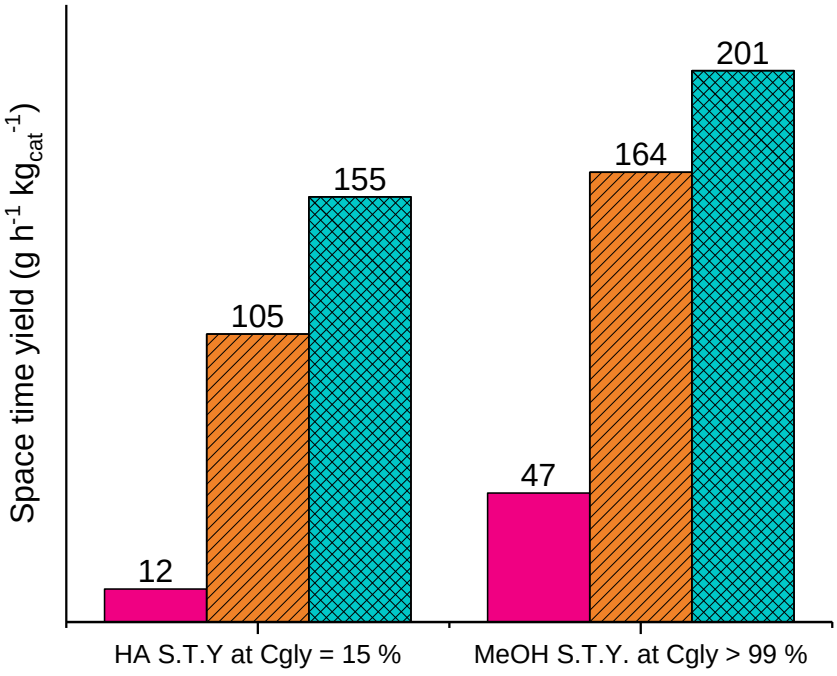

Figure 12. Hydroxyacetone and methanol space time yields over Ce-C (pink), Ce-R (orange) and Ce-P (blue) where catalyst mass and carrier flow rates were altered to achieve glycerol conversions of > 99 %. Low conversion reactions performed at 320 °C; high conversion reactions performed at 400 °C. GHSVs between 1800 h^{-1} and 11250 h^{-1}.

As discussed in Chapter 3, HA is an intermediate product in the conversion of GLY to MeOH, formed by mono-dehydration at the terminal position. The high HA selectivity observed over Ce-P and Ce-R at *ca.* 15 % conversion, suggested that this was the dominant reaction pathway over these catalysts. As shown in Scheme 1, HA can undergo a radical fragmentation process, in a process closely related to a photochemical Norrish type 1 mechanism (see appendix section 1), leading to the production of MeOH and acetyl radicals, which are reduced to MeOH and ACA respectively. Alternatively, 2,3-BD can form through the coupling of 2 acetyl radicals, whereas EtOH is the result of further ACA reduction.

At low GLY conversion, moderate levels of 1,2-propandiol and propanoic acid were detected over Ce-P and Ce-R. The former was attributed to HA reduction and was not detected in any

significant quantity at high conversion, suggesting that 1,2-PD can be further converted throughout the process. It isn't immediately clear how propanoic acid is formed, although it seems likely to be through HA isomerisation, as previously reported under similar reaction conditions.[41] As discussed above, ACE was attributed to ACA ketonisation, due to the corresponding increase in CO_2 and drop in ACA selectivity observed, although, it is also possible that ACE form through HA hydrogenolysis, or 1,2-PD dehydration. The number of observed products adds a level of complexity to the reaction, and makes it difficult to definitively ascertain the route for certain products. Given the reaction conditions, particularly those used for high conversion experiments, it seems likely that certain products, such as ACE, can be formed *via* more than one route.

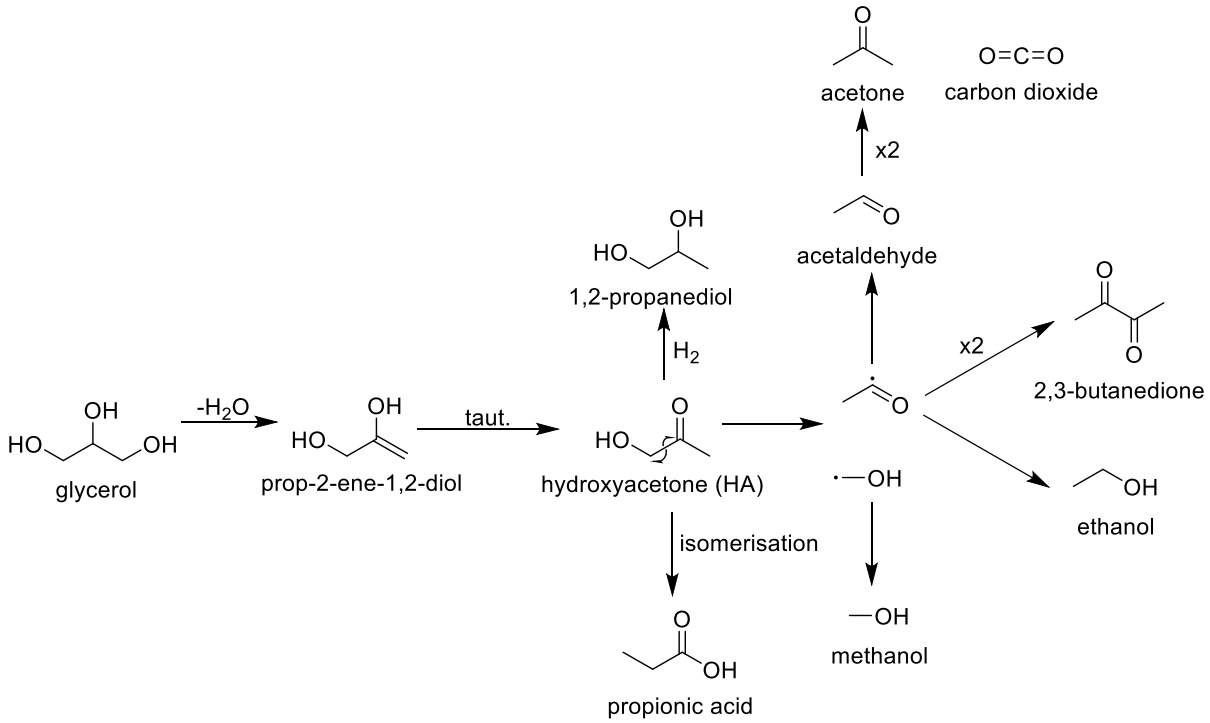

Scheme 1. The major reaction pathway observed over Ce-R and Ce-P.

The significantly lower HA selectivity observed for Ce-C at *ca.* 15 % conversion indicated that the HA route was not the dominant reaction pathway. The ACR selectivity (15 %) was unexpected, since previous investigations over basic materials including ceria have typically shown much lower ACR selectivity.[46] Whereas HA is formed *via* dehydration at the terminal position, ACR, a double-dehydration product, is well known to form through a 3-hydroxypropanal (3-HPA) intermediate, initiated by dehydration at the secondary position.[41, 47, 48] 3-HPA is reported to be a highly reactive species, which is not available commercially, thus its identity was not confirmed. Nevertheless, the increased selectivity to 1,3-PD and AA, formed through 3-HPA and ACR reduction, respectively, suggest an alternative reaction pathway takes place over Ce-C, as shown in Scheme 2. In addition to 3-HPA reduction and dehydration, a retro-aldol reaction is also possible, which would yield formaldehyde and ACA. Formaldehyde quantification was not performed, due to the

inability to analyse it by GC-FID, due to the low response factor. Additionally, formaldehyde is a highly reactive species, thus it seems likely that, if formed, it may go on to react further. GC-MS analysis, performed on a non-quantitative basis only, showed the presence of 1,3,5-trioxane in the post-reaction feed, confirming that formaldehyde was formed. The high ACA selectivity observed for Ce-C was in agreement with this theory, since 3-HPA degradation becomes increasingly favourable over dehydration with increasing reaction temperature.[49, 50]

Since MeOH cannot be produced through the pathway shown in Scheme 2, the reduced MeOH production observed over Ce-C is attributed to an increase in this reaction pathway. These results indicate that a high selectivity to HA at low GLY conversion is crucial to obtaining a high MeOH selectivity at full conversion, over ceria catalysts.

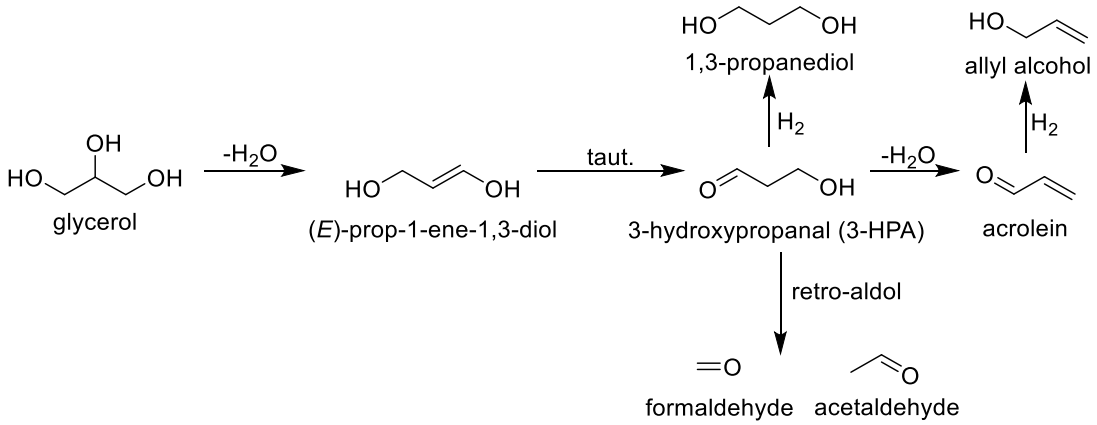

Scheme 2. The alternative reaction pathway observed over Ce-C.

With the aim of gaining a further understanding of the mechanistic differences observed for Ce-C, *in-situ* DRIFTS experiments were attempted. The experimental set-up involved passing a stream of N_2 gas through a heated bubbler containing an aqueous GLY solution. Unfortunately, the experiments were unsuccessful. Due to the high viscosity and low volatility of GLY, it was not possible to effectively introduce GLY into the system; any attempt to increase GLY in the gas stream resulted in significant increases in water vapour, which saturated any obtained spectra. As such, it was not possible to study the interactions of aqueous GLY feeds in the gas phase with the different ceria catalysts with the available equipment.

The adsorption of water on the low index surfaces of ceria has been investigated using DFT techniques by Islam and co-workers.[51] Dissociative water adsorption was found to be thermodynamically favourable over the (100) and (110) surfaces whereas associative and dissociative water adsorption was equally favourable for the (111) surface. The temperatures of desorption showed that water desorption occurred much more readily over the (111) surface, likely due to the higher degree of coordination of the cerium cations. In contrast, the highest desorption temperature was calculated for the (100) surface, with

temperatures of *ca.* 550 – 575 °C required for desorption of dissociatively adsorbed water. Similar findings were made by Kropp *et al.*, who found that dissociative water adsorption was strongly favoured over the (100) surface, leading to a fully hydroxylated surface.[52] It is possible that the more strongly bound dissociative water present over the Ce(100) surface contributes to the divergence in reaction mechanism observed over Ce-C. Alternatively, it is possible that there are variations in the interactions between GLY and the different surfaces leading to differences in product distribution. Whilst these interactions are difficult to study experimentally due to the nature of GLY, this topic provides an interesting avenue to further explore through collaborations with computational chemists.

4.3 Conclusions

Ceria catalysts with well-defined cubic (Ce-C), rod-like (Ce-R), and polyhedral (Ce-P) morphologies were prepared by a hydrothermal synthesis method. TEM imaging showed that the (100) surface was exposed in Ce-C, with Ce-R possessing (110) and (100) surfaces, and Ce-P exposing the more stable (111) surface although additional (100) planes were also observed. The materials were thoroughly characterised and surface areas were found to follow the trend Ce-R > Ce-P >> Ce-C, which was an inverse trend to crystallite and particle size. Analysis by Raman spectroscopy allowed the density of defects to be estimated in the order Ce-R > Ce-C >> Ce-P. Further characterisation by H_2-TPR, CO_2 and NH_3 showed there to be significant differences in reducibility, basicity, and acidity, respectively, across the materials.

Initially, catalyst testing was performed over the materials at a GHSV of 3600 h^{-1} at reaction temperatures of 320, 360 and 400 °C. At all temperatures, GLY conversion was of the order Ce-R > Ce-P >> Ce-C, which was in agreement with the trend of surface area. At a reaction temperature of 320 °C, GLY conversion was 17, 65 and 58 % over Ce-C, Ce-R and Ce-P, respectively. Interestingly, once normalised to catalyst surface area, this corresponded to a value of *ca.* 0.28 μmol h^{-1} m^{-2} for all three materials. As the reaction temperature was increased to 360 °C, the level of GLY conversion increased to 29, 98 and 96 % for Ce-C, Ce-R and Ce-P, respectively. A further increase in reaction temperature to 400 °C resulted in GLY conversions > 99 % for Ce-R and Ce-P, whilst a conversion of 91 % was obtained over Ce-C. Due to the significant differences in GLY conversion between Ce-R and Ce-P, and Ce-C at a given temperature, it was not possible to directly compared product distributions across the three materials under these conditions. As shown in Chapter 3, product distribution is heavily dependent on GLY conversion, thus it was considered to investigate the effect of ceria morphology at comparable GLY conversions.

Subsequent reactions were performed whereby the catalyst mass was adjusted to achieve *iso*-conversion over the three morphologies. At a reaction temperature of 320 °C, GLY

conversions of *ca.* 15 % were achieved over Ce-C, Ce-R, and Ce-P at GHSVs of 3600, 11250 and 9000 h^{-1}, respectively. Under these conditions, significant quantities of HA were detected over all three materials, with selectivities of 43.3, 37.4, and 14.1 % over Ce-P, Ce-R and Ce-C, respectively. The decreased HA selectivity observed over Ce-C was also accompanied by an increase in ACR selectivity (14.5 %) compared with Ce-R (3.2 %) and Ce-P (1.5 %). HA and ACR are formed *via* different reaction pathways, with HA involving dehydration at the terminal position. Alternatively, ACR is formed *via* a 3-HPA intermediate, initiated by the loss of the secondary hydroxyl group. Thus, the increased ACR selectivity observed over Ce-C is indicative of a divergence in reaction mechanism.

Additional experiments were also performed with an increased mass of Ce-C at a reaction temperature of 400 °C, to achieve *iso*-conversion at high GLY levels (> 99 %). Under these conditions, MeOH was the major product formed over Ce-P and Ce-R, with selectivities of 24.5 and 22.6 %. MeOH was also observed over Ce-C but with a significantly lower selectivity of 13.1 %. This corresponded to MeOH STYs of 201, 164 and 47 g h^{-1} kg^{-1}_{cat} over Ce-P, Ce-R and Ce-C, respectively. A strong correlation was shown to exist between HA STY at low conversion, and high MeOH STY at high GLY conversion. Since MeOH is predominantly produced *via* HA fragmentation, the lower MeOH productivity obtained over Ce-C was attributed to the divergence in reaction mechanism described above. Products such as AA and 1,3-PD, also produced *via* the same reaction pathway as ACR, were observed in higher selectivities over Ce-C providing further support to this theory.

Due to the inherently lower activity of Ce-C, a significantly higher contact time was required to achieve comparable GLY conversions. Numerous reactions were performed with increased contact times over Ce-R and Ce-P to identify whether any relationship existed between increased contact time and the increased ACR selectivity observed over Ce-C. Whilst the effect of contact time was not probed in depth over Ce-R and Ce-P, typically ACR selectivity was found to decrease with increasing contact time. Consequently, the increased ACR selectivity observed over Ce-C can be attributed to differences within the catalysts and not to the reaction conditions used. Future work should focus on gaining a greater understanding of the interactions of aqueous GLY feedstocks with the low index surface present within the ceria catalysts in order to further explore differences in reaction mechanisms.

The highest MeOH selectivity and STY were obtained over Ce-P at 400 °C and 3600 h^{-1}, with values of 24.5 % and 201 g h^{-1} kg^{-1}_{cat}, respectively. This suggests that the (111) surface, predominantly exposed in Ce-P, is preferential for the conversion of GLY to MeOH. The lower defect density and smaller pore volume present in Ce-P were found to be beneficial for MeOH selectivity, potentially due to a reduction in sequential reactions which reduce

MeOH yields. The dependency of MeOH selectivity on the exposed ceria surface provides a basis to inform rational catalyst design moving forward. Additionally, the strong correlation between high HA STYs at low GLY conversions, and high MeOH STYs at high GLY conversions highlights the mechanistic requirements to achieve high MeOH productivity.

4.4 References

1. Q. Wu, F. Zhang, P. Xiao, H. Tao, X. Wang, Z. Hu and Y. Lü, *The Journal of Physical Chemistry C*, 2008, **112**, 17076-17080.
2. H.-X. Mai, L.-D. Sun, Y.-W. Zhang, R. Si, W. Feng, H.-P. Zhang, H.-C. Liu and C.-H. Yan, *The Journal of Physical Chemistry B*, 2005, **109**, 24380-24385.
3. T. Désaunay, G. Bonura, V. Chiodo, S. Freni, J. P. Couzinié, J. Bourgon, A. Ringuedé, F. Labat, C. Adamo and M. Cassir, *Journal of Catalysis*, 2013, **297**, 193-201.
4. Z. Wu, M. Li, J. Howe, H. M. Meyer and S. H. Overbury, *Langmuir*, 2010, **26**, 16595-16606.
5. M. Nolan, S. C. Parker and G. W. Watson, *Surface Science*, 2005, **595**, 223-232.
6. Z. Wu, A. K. P. Mann, M. Li and S. H. Overbury, *The Journal of Physical Chemistry C*, 2015, **119**, 7340-7350.
7. G. Vilé, S. Colussi, F. Krumeich, A. Trovarelli and J. Pérez-Ramírez, *Angewandte Chemie International Edition*, 2014, **53**, 12069-12072.
8. A. K. P. Mann, Z. Wu, F. C. Calaza and S. H. Overbury, *ACS Catalysis*, 2014, **4**, 2437-2448.
9. M. Tinoco, S. Fernandez-Garcia, A. Villa, J. M. Gonzalez, G. Blanco, A. B. Hungria, L. Jiang, L. Prati, J. J. Calvino and X. Chen, *Catalysis Science & Technology*, 2019, **9**, 2328-2334.
10. L. Chen, P. Fleming, V. Morris, J. D. Holmes and M. A. Morris, *The Journal of Physical Chemistry C*, 2010, **114**, 12909-12919.
11. Q. Jiang, L. H. Liang and D. S. Zhao, *The Journal of Physical Chemistry B*, 2001, **105**, 6275-6277.
12. R. Si and M. Flytzani-Stephanopoulos, *Angewandte Chemie International Edition*, 2008, **47**, 2884-2887.
13. E. Aneggi, D. Wiater, C. de Leitenburg, J. Llorca and A. Trovarelli, *ACS Catalysis*, 2014, **4**, 172-181.
14. S. Chowdhury and K.-S. Lin, *Materials Chemistry and Physics*, 2012, **133**, 163-169.
15. C. Pan, D. Zhang, L. Shi and J. Fang, *European Journal of Inorganic Chemistry*, 2008, **2008**, 2429-2436.
16. Y. Zhang, S. Bals and G. Van Tendeloo, *Particle & Particle Systems Characterization*, 2019, **36**, 1800287.
17. X. Wang, Z. Jiang, B. Zheng, Z. Xie and L. Zheng, *CrystEngComm*, 2012, **14**, 7579-7582.
18. J. P. Y. Tan, H. R. Tan, C. Boothroyd, Y. L. Foo, C. B. He and M. Lin, *The Journal of Physical Chemistry C*, 2011, **115**, 3544-3551.
19. K. Zhou, X. Wang, X. Sun, Q. Peng and Y. Li, *Journal of Catalysis*, 2005, **229**, 206-212.
20. Z. Liu, X. Li, M. Mayyas, P. Koshy, J. N. Hart and C. C. Sorrell, *CrystEngComm*, 2017, **19**, 4766-4776.
21. J. M. López, A. L. Gilbank, T. García, B. Solsona, S. Agouram and L. Torrente-Murciano, *Applied Catalysis B: Environmental*, 2015, **174-175**, 403-412.
22. T. Taniguchi, T. Watanabe, N. Sugiyama, A. K. Subramani, H. Wagata, N. Matsushita and M. Yoshimura, *The Journal of Physical Chemistry C*, 2009, **113**, 19789-19793.
23. A. Nakajima, A. Yoshihara and M. Ishigame, *Physical Review B*, 1994, **50**, 13297-13307.
24. A. Filtschew, K. Hofmann and C. Hess, *The Journal of Physical Chemistry C*, 2016, **120**, 6694-6703.
25. W. H. Weber, K. C. Hass and J. R. McBride, *Physical Review B*, 1993, **48**, 178-185.
26. M. Guo, J. Lu, Y. Wu, Y. Wang and M. Luo, *Langmuir*, 2011, **27**, 3872-3877.

27. B. M. Reddy, A. Khan, Y. Yamada, T. Kobayashi, S. Loridant and J.-C. Volta, *The Journal of Physical Chemistry B*, 2003, **107**, 5162-5167.
28. A. S., D. M. Z. D., R. M., Š. M. and P. Z. V., *Journal of Raman Spectroscopy*, 2009, **40**, 650-655.
29. J. R. McBride, K. C. Hass, B. D. Poindexter and W. H. Weber, *Journal of Applied Physics*, 1994, **76**, 2435-2441.
30. C. Schilling, A. Hofmann, C. Hess and M. V. Ganduglia-Pirovano, *The Journal of Physical Chemistry C*, 2017, **121**, 20834-20849.
31. A. Trovarelli, *Catalysis Reviews*, 1996, **38**, 439-520.
32. S. Bernal, J. J. Calvino, G. A. Cifredo, J. M. Gatica, J. A. P. Omil and J. M. Pintado, *Journal of the Chemical Society, Faraday Transactions*, 1993, **89**, 3499-3505.
33. F. Giordano, A. Trovarelli, C. de Leitenburg and M. Giona, *Journal of Catalysis*, 2000, **193**, 273-282.
34. V. Perrichon, A. Laachir, G. Bergeret, R. Fréty, L. Tournayan and O. Touret, *Journal of the Chemical Society, Faraday Transactions*, 1994, **90**, 773-781.
35. L. A. Bruce, M. Hoang, A. E. Hughes and T. W. Turney, *Applied Catalysis A: General*, 1996, **134**, 351-362.
36. D. Terribile, A. Trovarelli, C. de Leitenburg, G. Dolcetti and J. Llorca, *Chemistry of Materials*, 1997, **9**, 2676-2678.
37. R. J. Cvetanović and Y. Amenomiya, *Catalysis Reviews*, 1972, **6**, 21-48.
38. L. R. Smith, P. J. Smith, K. S. Mugford, M. Douthwaite, N. F. Dummer, D. J. Willock, M. Howard, D. W. Knight, S. H. Taylor and G. J. Hutchings, *Catalysis Science & Technology*, 2019, **9**, 1464-1475.
39. P. J. Smith, L. Smith, N. F. Dummer, M. Douthwaite, D. J. Willock, M. Howard, D. W. Knight, S. H. Taylor and G. J. Hutchings, *Energies*, 2019, **12**, 1359.
40. M. H. Haider, N. F. Dummer, D. W. Knight, R. L. Jenkins, M. Howard, J. Moulijn, S. H. Taylor and G. J. Hutchings, *Nature Chemistry*, 2015, **7**, 1028.
41. A. Corma, G. W. Huber, L. Sauvanaud and P. O'Connor, *Journal of Catalysis*, 2008, **257**, 163-171.
42. A. Gangadharan, M. Shen, T. Sooknoi, D. E. Resasco and R. G. Mallinson, *Applied Catalysis A: General*, 2010, **385**, 80-91.
43. L. M. Orozco, M. Renz and A. Corma, *Green Chemistry*, 2017, **19**, 1555-1569.
44. L. Vivier and D. Duprez, *ChemSusChem*, 2010, **3**, 654-678.
45. D. Hernandez, M. Velasquez, P. Ayrault, D. Lopez, J. J. Fernandez, A. Santamaria and C. Batiot-Dupeyrat, *Applied Catalysis A: General*, 2013, **467**, 315-324.
46. S.-H. Chai, H.-P. Wang, Y. Liang and B.-Q. Xu, *Green Chemistry*, 2007, **9**, 1130-1136.
47. E. Tsukuda, S. Sato, R. Takahashi and T. Sodesawa, *Catalysis Communications*, 2007, **8**, 1349-1353.
48. B. Katryniok, S. Paul, M. Capron and F. Dumeignil, *ChemSusChem*, 2009, **2**, 719-730.
49. P. Lauriol-Garbey, J. M. M. Millet, S. Loridant, V. Bellière-Baca and P. Rey, *Journal of Catalysis*, 2011, **281**, 362-370.
50. F. Wang, J.-L. Dubois and W. Ueda, *Journal of Catalysis*, 2009, **268**, 260-267.
51. M. Molinari, S. C. Parker, D. C. Sayle and M. S. Islam, *The Journal of Physical Chemistry C*, 2012, **116**, 7073-7082.
52. T. Kropp, J. Paier and J. Sauer, *The Journal of Physical Chemistry C*, 2017, **121**, 21571-21578.

Chapter 5

Transition metal doped ceria for the conversion of glycerol to methanol

5.1 Introduction

As shown in the previous results chapters, HA is the major intermediate in the conversion of GLY to MeOH over ceria-based catalysts, and is the dominant product detected at low conversion. The results presented in Chapter 4, whereby a strong correlation between HA space time yields at low GLY conversion and MeOH space time yields at high GLY conversion was demonstrated, suggesting that a high selectivity towards the HA pathway is crucial in obtaining high MeOH selectivity over ceria-based catalysts.

Whilst GLY dehydration has mainly been focussed on the production of ACR, there have been a number of studies which report the conversion of GLY to HA in good yields over copper based catalysts. HA was reported with a selectivity as high as 97 % by Chiu *et al.*, over copper-chromite catalysts, at a reaction temperature of 230 °C with a 2.5 wt,% aqueous GLY feedstock.[1] A low partial pressure of GLY was required in order to achieve high HA selectivity; decomposition products were found to form with second-order reaction mechanisms, thus by-product formation was reduced at lower GLY partial pressures. Sato *et al.* identified binary Cu-Zn-Zr-Al oxide materials as active catalysts for GLY dehydration to HA.[2] The highest HA selectivity of 90 mol.% was reported over a 60 mol.% Cu/Al_2O_3 catalyst at a reaction temperature of 250 °C with a 30 wt.% aqueous GLY feed diluted with N_2 carrier gas. The authors found that pre-treatment of the catalyst under H_2 at reaction temperature (250 °C) was crucial to achieve high activity and catalyst stability. The unreduced Cu/Al_2O_3 catalyst showed significant deactivation over the 5-hour reaction period, attributed to coke formation, whereas the reduced catalyst maintained high activity and HA selectivity over the same time-on-stream. This led the authors to conclude that Cu^0 was the active site for the dehydration of GLY to HA.

Batiot-Dupeyrat and co-workers reported a HA yield of 76 % over a La_2CuO_4 catalyst at a reaction temperature of 280 °C with a feedstock of 20 % v/v pure GLY in N_2.[3] In contrast to the findings of Sato *et al.*, the reduction of La_2CuO_4 with H_2 prior to reaction was detrimental to GLY conversion and HA selectivity, with low HA yields reported over Cu^0 catalysts. Results suggested that whilst Cu^+ was active for the conversion of GLY to HA, but the lower activity of Cu_2O *vs.* La_2CuO_4 suggests that interaction between lanthanum and copper is beneficial for HA production. Significantly higher activity was observed over La_2CuO_4

compared with Cu^0/La_2O_3, with 80 mg of the former required to achieve the same activity as 1 g of the latter, highlighting the beneficial role of Cu and La species.

Concentrated aqueous GLY feedstocks (80 wt.%) were also investigated by Batiot-Dupeyrat and co-workers.[4] In the presence of water, 5 wt.% Cu-MgF_2 was found to be significantly more active than La_2CuO_4, resulting in HA yields of 45.5 and 26.7 %, respectively, at a reaction temperature of 260 °C. The superior activity of Cu-MgF_2 compared with Cu-MgO, Mg(OH)F, and La_2CuO_4 was attributed to its Lewis acidity, and the ability of the catalyst to stabilise copper in the +1 state.

Recent work within the group showed that MeOH productivity could be enhanced by incorporating praseodymium into a ceria catalyst.[5] The surface area normalised MeOH STY was found to be 0.052, 0.029 and 0.076 $mmol_{MeOH}\ m^{-2}\ h^{-1}$ over CeO_2, $CeZrO_x$ and $CePrO_x$ respectively. In contrast to zirconium, which led to a decrease in MeOH productivity as a consequence of increased ACR selectivity, the incorporation of Pr was beneficial for MeOH production. Whilst the inclusion of Pr led to a decrease in catalyst surface area from 56 to 28 $m^2\ g^{-1}$, resulting in a decrease in GLY conversion, the MeOH selectivity remained high, leading to an increase in intrinsic activity. It was considered that the presence of a Ce-Pr solid solution, and the enhanced reducibility, were advantageous for the conversion of GLY to MeOH.

The aim of this chapter was to explore the effects of copper and cobalt dopants on the performance of ceria catalysts for MeOH production. Copper has been shown to be beneficial for the conversion of GLY to HA, the main intermediate to MeOH, thus it was hypothesised that a copper doped ceria catalyst may provide superior activity. Additionally, the incorporation of both copper and cobalt dopants has been shown to significantly enhance the reducibility of ceria catalysts, which was considered to be a factor in the relatively high activity of $CePrO_x$ compared with CeO_2, as described above. Throughout this chapter, the effect of copper and cobalt dopants on MeOH are investigated *via* the synthesis, characterisation, and testing of CeO_2, $CuCeO_x$ and $CoCeO_x$ catalysts.

5.2 Results

5.2.1 The preparation of ceria and doped ceria through co-precipitation routes

Ceria (CeO_2), copper doped ceria ($CuCeO_x$), and cobalt doped ceria ($CoCeO_x$) were prepared from their respective nitrate precursors using sodium carbonate as a precipitation agent. Experimental details for the preparations are described fully in section 2.2.4. TG-DTA analysis (Figure 1) was performed on the precipitated materials prior to calcination but after thorough drying (110 °C, 16 hours). The CeO_2 precursor exhibited a total mass loss of 20.2 % by 800 °C, with a mass loss of 17.7 % occurring between 205 – 265 °C. The total mass

loss is close to the theoretical mass loss for the following decomposition reaction of basic cerium carbonate:

$$4Ce(OH)CO_3 + O_2 \rightarrow 4CeO_2 + 4CO_2 + 2H_2O$$

Similar mass loss profiles were observed for the CuCe and CoCe precursors, although the major mass loss event occurred over a wider temperature range, particularly for the CuCe precursor. For all three materials, the major mass loss event was accompanied by an endotherm, occurring at 245, 266, and 261 °C for Ce, CuCe, and CoCe precursors, respectively. The endothermic behaviour observed has been previously attributed to the dehydration and decarbonisation of $Ce(OH)CO_3$ during the decomposition-oxidation transformation to CeO_2.[6-8]

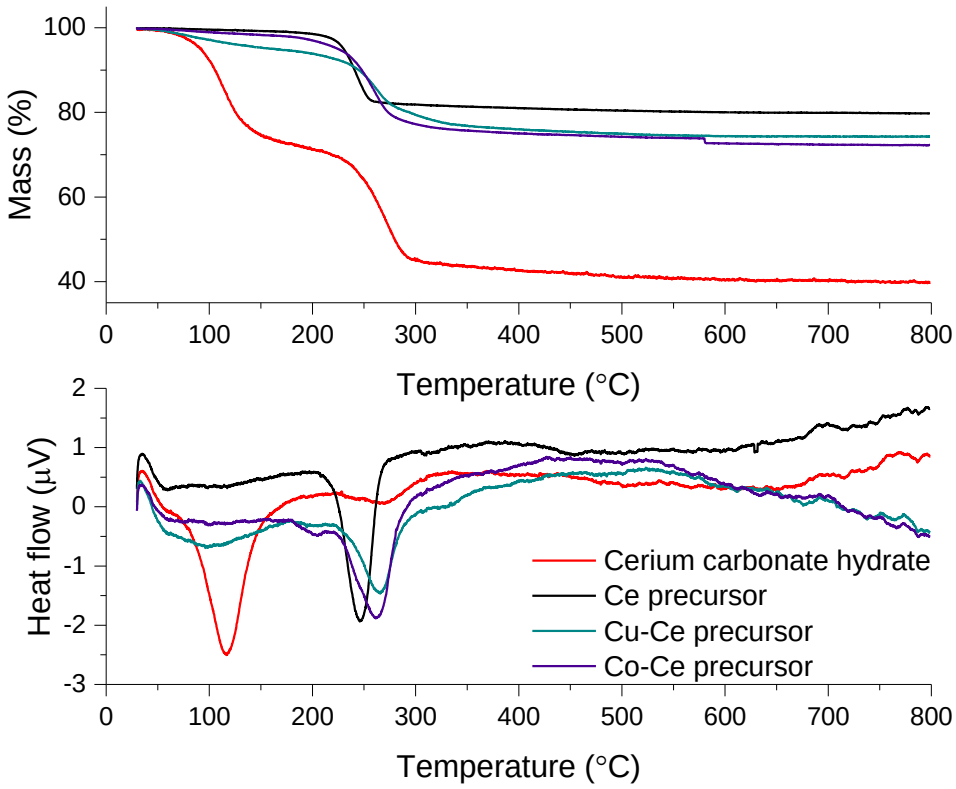

Figure 1. TGA (upper panel) and DTA (lower panel) profiles of the Ce, CuCe and CoCe precursors prior to calcination. The profile of commercially available cerium carbonate hydrate is also shown for comparison. Analysis conditions: 20 – 50 mg of sample, 5 °C min^{-1} ramp rate, synthetic air atmosphere.

Based on the TG-DTA profiles, a calcination temperature of 500 °C was used. All results and characterisation henceforth referred to the calcined materials, denoted as CeO_2, $CuCeO_x$ and $CoCeO_x$. Precursor ratios were calculated to give a dopant ratio of 10 mol.%. ICP-MS analysis was performed to determine the dopant concentrations within the bulk structures (Table 1). The dopant molar ratios were found to be 9.2 and 11.2 % for copper and cobalt, respectively, close to the nominal values expected from the ratio of precursors used within the preparation.

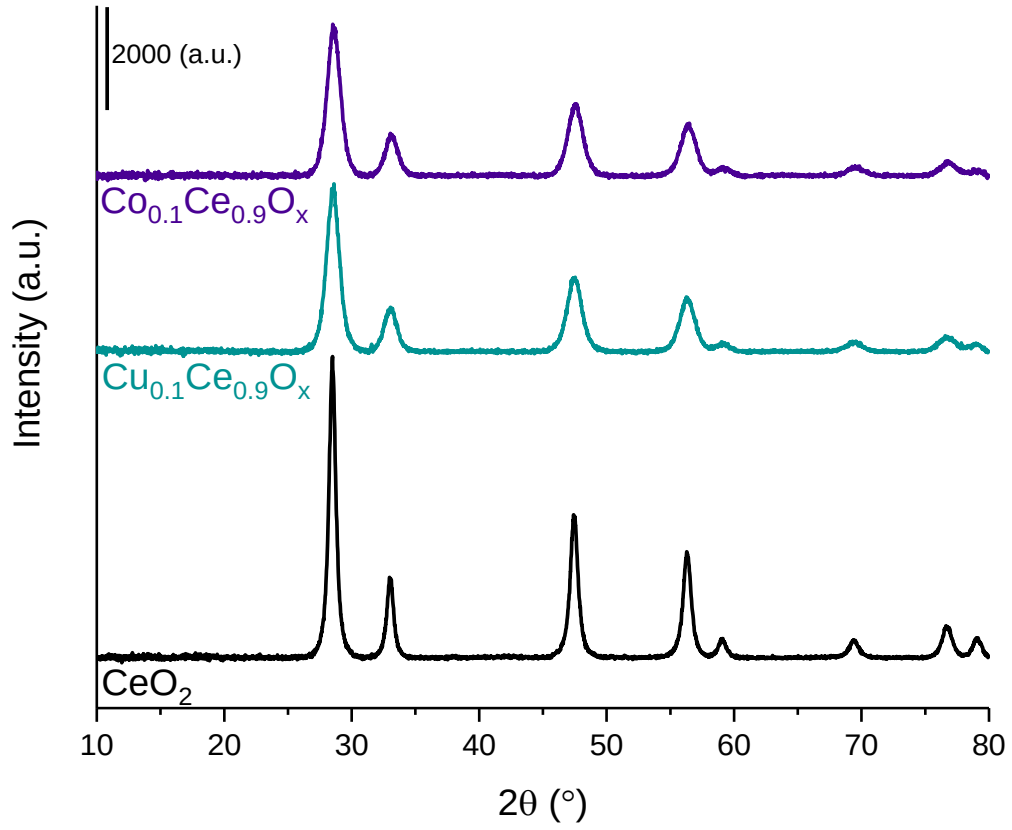

Figure 2. PXRD patterns of CeO_2, $Cu_{0.1}Ce_{0.9}O_x$, $Co_{0.1}Ce_{0.9}O_x$.

Figure 2 shows the PXRD patterns for the as-prepared samples, with further details provided in Table 1. All observed diffraction peaks observed were indexed to the cubic fluorite structure of ceria (space group *Fm3m*, JCPDS 01-089-8436). No diffraction peaks associated with copper or cobalt oxides were present, suggesting a homogeneous distribution of dopant ions within the ceria lattice. Whilst no dopant diffraction peaks were observed, this does not provide definitive confirmation that all the dopant ions were incorporated into the ceria lattice. The absence of diffraction peaks for the dopant phase confirmed the absence of a separate crystalline dopant phase although it is possible for the dopants to be present as amorphous oxide phases, or as small crystallites below the detection limit of XRD.[9-11]

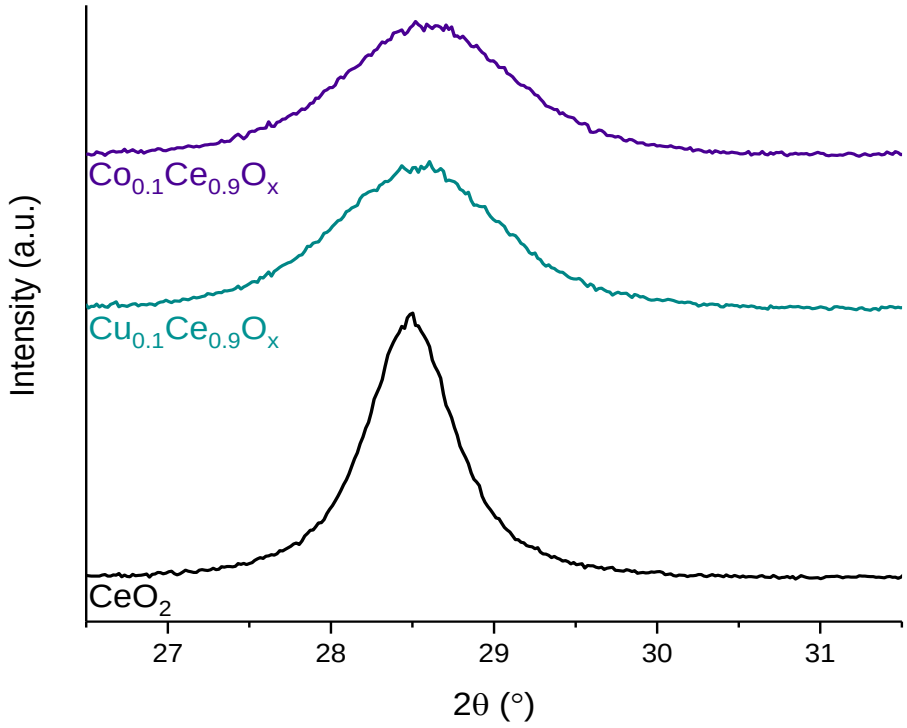

Figure 3. Inset of PXRD patterns of CeO_2, $Cu_{0.1}Ce_{0.9}O_x$, $Co_{0.1}Ce_{0.9}O_x$ showing the CeO_2(111) diffraction peak

As shown in figure 3, the addition of copper and cobalt dopants resulted in a slight shift of diffraction peaks to higher values of 2θ. Since higher values of 2θ are representative of a smaller lattice parameter, the shift in diffraction peaks is representative of lattice contraction. This was evidenced by the decrease in the lattice parameter (5.416 and 5.410Å for $CuCeO_x$ and $CoCeO_x$, respectively) when compared with the undoped sample (5.423 Å). The ionic radii of Cu ions (Cu^{2+} = 0.73 Å; Cu^{+} = 0.77 Å) and Co ions (Co^{3+} = 0.61 Å; Co^{2+} = 0.75Å) are significantly smaller than that of Ce^{4+} (0.97 Å) so the decrease in lattice parameter is indicative of the inclusion of smaller dopant ions into the ceria lattice.[12-14] However, the effect of dopants on the lattice parameter of ceria is not trivial and complicated by several competing effects. The inclusion of aliovalent dopants such as Cu^{2+} or Co^{2+} results in an increase in oxygen vacancy defect, as shown in equation 1:

$$CuO = Cu''_{Ce} + V_O^{\cdot\cdot} + O_O \qquad \text{Eq. 1}$$

Whereby Cu_{ce}'' represents Cu^{2+} in the place of a Ce^{4+} ion within the ceria lattice with double negative charge, $V_ö$ represents an oxygen vacancy with a double positive charge and O_O represents an oxygen anion occupying a lattice site with neutral charge. Oxygen vacancies have been found to have a significantly smaller ionic radius (1.16 Å) than oxygen anions (1.38 Å).[15, 16] Whilst the presence of smaller dopant ions and oxygen vacancies may lead one to expect a significant decrease in lattice parameter, the presence of oxygen vacancies is accompanied by the reduction of nearby Ce^{4+} ions to Ce^{3+} to compensate for the difference in charge between Ce^{4+} and Cu^{2+} ions and maintain overall charge neutrality.[14] Since the

ionic radius of Ce^{3+} is noticeably larger than that of Ce^{4+} (Ce^{3+} = 1.14 Å; Ce^{4+} = 0.97 Å), its presence can lead to expansion of the ceria lattice, resulting in a larger lattice parameter.[12, 17, 18] Thus, it is considered that the variation in lattice parameter observed with the addition of copper and cobalt dopants provides good evidence for incorporation of these elements into the ceria lattice.

The diffraction pattern for pure CeO_2 displayed significantly sharper peaks than the doped samples, indicative of increased crystallinity. The Scherrer equation was used to estimate crystallite sizes based on the (111) diffraction peak; calculations performed on the (200) peak were also agreement. As shown in Table 1, crystallite sizes were 15, 7 and 6 nm, for CeO_2, $CuCeO_x$ and $CoCeO_x$, respectively. The inclusion of dopant elements resulted in an increased lattice strain, due to the resulting defects induced within the lattice. This increase in strain within the lattice can disrupt crystallite growth, hence resulting in smaller crystallite sizes.[19] An inverse relationship between crystallite size and surface area was observed. Surface area was found to follow the trend $CoCeO_x$ > $CuCeO_x$ > CeO_2 with both doped materials showing similarly enhanced surface areas compared to the undoped ceria.

Table 1. Structural properties of ceria and doped ceria

Sample	***Dopant molar ratio (%)***	***111 peak position (°)***	***Crystallite size (nm)[b]***	***Lattice parameter (Å)[b]***	***Lattice strain (%)[b]***	***Surface area ($m^2 g^{-1}$)[c]***
CeO_2		28.485	15	5.423	0.93	46
$CuCeO_x$	9.2	28.519	7	5.416	1.97	61
$CoCeO_x$	11.2	28.553	6	5.410	2.21	63

a. Determined by ICP-MS; b. Determined from PXRD; c. Calculated from N_2 sorption isotherms

5.2.2 The effect of Cu and Co dopants on the physicochemical properties of ceria

Raman spectroscopy was used to gain a further understanding into the effects of dopants on the structure of the ceria-based catalysts, particularly with regards to defect properties. As shown in Figure 4, all spectra were dominated by an intense peak at *ca.* 464 cm^{-1} which is attributed to the F_{2g} vibrational mode of ceria, representative of the symmetrical stretching of the Ce-O_8 unit cell. The F_{2g} peak was shifted by *ca.* 2 cm^{-1} for both $CuCeO_x$ and $CoCeO_x$. This red shift is indicative of inhomogeneous strain and phonon confinement, which is observed with smaller crystallites.[20] In addition to the peak shift, significant broadening of the F_{2g} mode was observed following the substitution of copper and cobalt into the ceria

lattice. An inverse relationship exists between the full-width-half-maximum (FWHM) of the F_{2g} mode and CeO_2 crystallite size,[21, 22] which is consistent with the smaller crystallite sizes for the doped materials, as derived by XRD. The intensity of the F_{2g} mode in the undoped sample was significantly higher (*ca.* x25) than in the doped samples, indicative of disorder within the anionic sublattice of the doped materials.[23]

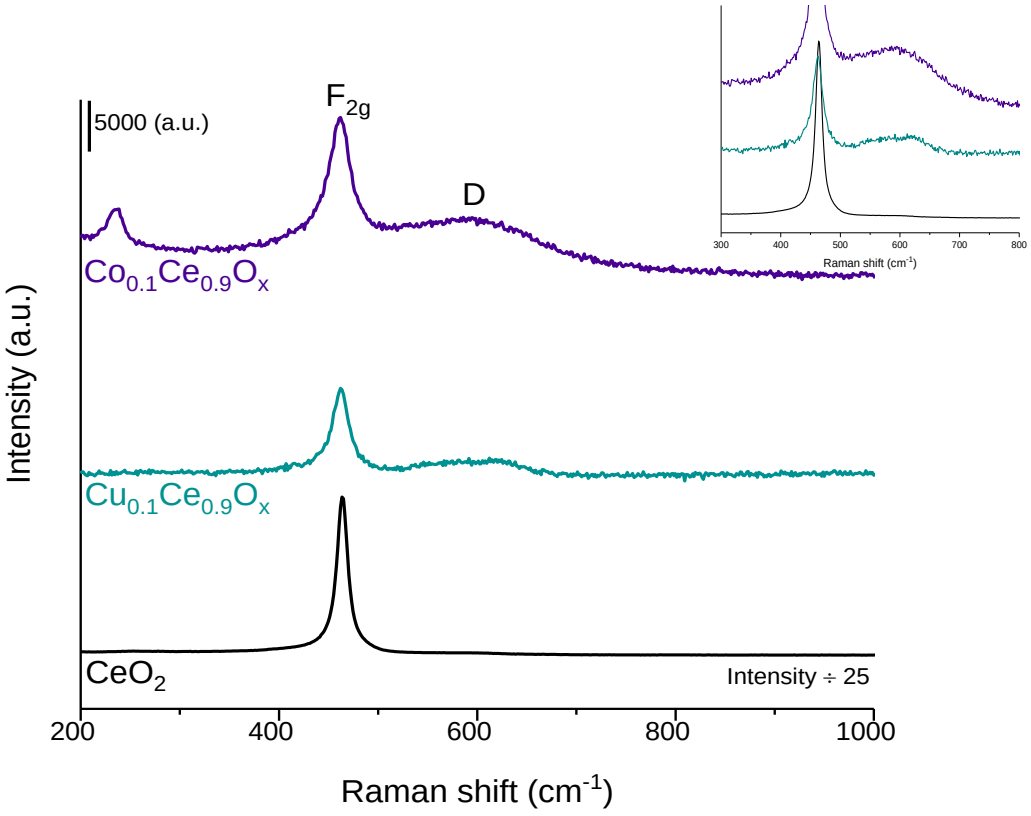

Figure 4. Visible Raman spectra of CeO_2, $Cu_{0.1}Ce_{0.9}O_x$, $Co_{0.1}Ce_{0.9}O_x$. Obtained at λ = 514 nm with a laser power of 5 %. Inset shows 300 – 800 cm^{-1} spectral region

In addition to the F_{2g} mode, a broad peak at a Raman shift of *ca.* 600 cm^{-1} was also observed. Whilst the intensity was very weak for the undoped sample, this peak was significant for both the doped materials. The mode at *ca.* 600 cm^{-1} is attributed to the presence of intrinsic anionic Frenkel defects, whereby oxygen anions are vacant from their lattice sites and are instead present in interstitial sites.[24-27] Closer inspection of the spectra for $CuCeO_x$ showed that the band at *ca.* 600 cm^{-1} was comprised of three peaks with maxima at *ca.* 560, 595 and 626 cm^{-1}; due to the overlap and broad nature of the peaks, deconvolution was not possible. The peak centred at *ca.* 560 cm^{-1} has been attributed to the presence of oxygen vacancies coupled with Ce^{3+} or aliovalent dopant cations.[27-29] On the other hand, the band centred at 626 cm^{-1} has been associated with extrinsic defects, induced through the addition of dopant elements.[25, 30] Whilst these additional defect bands were not observed for $CoCeO_x$, full peak deconvolution was not performed, therefore, it is possible that these modes were obscured by the band centred at 595 cm^{-1}.

The spectrum obtained for $CoCeO_x$ displayed an additional mode, at a Raman shift of 236 cm^{-1}, that was absent for both of the other samples. It was not possible to unambiguously assign this mode. A peak at *ca.* 250 cm^{-1} has previously been reported for ceria nanostructures, and has been attributed to the longitudinal stretching of surface Ce-O layers[31] and to surface Ce-OH vibrations.[32] Since this mode has been associated with increasing surface-to-volume ratio, it is possible that the peak observed in the $CoCeO_x$ spectrum could be assigned to a surface species. Whilst the cobalt doped sample exhibited the smallest crystallite size, the difference in crystallite size between the Cu and Co samples was minimal, so if this mode were representative of a Ce-O or Ce-OH stretch, it would likely be present in the $CuCeO_x$ spectra, albeit with a weaker intensity. Additionally, the shift between expected peak position of 250 cm^{-1} and observed peak position of 236 cm^{-1} is likely too large to be explained by the addition of Co as a dopant. Furthermore, the position of this peak could not be assigned to any Raman active cobalt oxide modes.[12, 33]

Since all the Raman modes from 560 – 630 cm^{-1} have been attributed to the presence of defects within ceria based materials, the relative peak areas of the defect band mode(s) and F_{2g} mode (I_D/I_{F2g}) can provide information of the relative concentration of defects within the materials.[27, 29, 30] The ratios of the defect band and F_{2g} mode are presented in Table 2, and follow the trend $CoCeO_x > CuCeO_x >> CeO_2$. This indicates that the quantity of defects within the doped materials is significantly higher than in the undoped materials. The concentration of defects was calculated to be slightly higher in the cobalt doped sample, although the precise nature of the defects may differ between the Co and Cu samples in a way that was not resolvable from the obtained spectra.

Table 2. Defect properties as measured by Raman spectroscopy

Material	***F_{2g} band position (cm^{-1})***	***F_{2g} FWHM (cm^{-1})***	***D band position (cm^{-1})***	***I_D/I_{F2g}***
CeO_2	464	13.9	598	1.59×10^{-3}
$CuCeO_x$	462	70.2	560, 595, 626	0.468
$CoCeO_x$	462	59.4	595	0.609

H_2-TPR was used not only to analyse the reducibility of the materials, but also as a means of further studying the surface species following the addition of dopants. As shown in Figure 5, a bimodal peak distribution was obtained for CeO_2. A broad low intensity peak was observed with a maximum at 510 °C with a second peak centred at 810 °C, attributed to the reduction of surface and bulk species, respectively. Numerous studies have correlated the

area of the low temperature (< 600 °C) reduction peak with the surface area of ceria, although quantitative surface area measurements are not reliable through this method.[34-36]

The high temperature, bulk reduction peak (centred at *ca.* 810 °C) was unaffected by the incorporation of copper and cobalt. Alternatively, the reduction profiles of CeO_2, $CuCeO_x$ and $CoCeO_x$ exhibited significant differences below 650 °C. An intense peak with a maximum of 178 °C was observed for $CuCeO_x$, whilst a weak shoulder at 152 °C could also be detected. This was indicative of the presence of Cu-O-Ce species and small highly dispersed CuO_x surface species, respectively.[36-38] The absence of a reduction peak between 200 – 250 °C was in agreement with XRD analysis, confirming the absence of crystalline copper oxide. These results suggest that the $CuCeO_x$ catalyst is indeed copper doped ceria, although small well-disperse copper oxide species may exist on the surface.

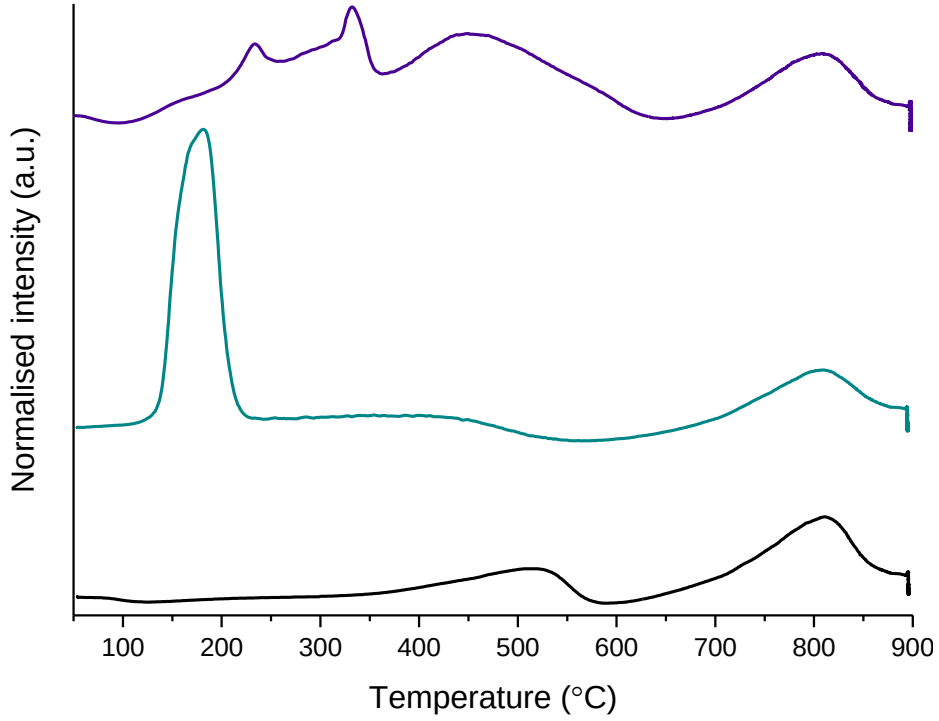

Figure 5. H_2-TPR profiles of CeO_2, $Cu_{0.1}Ce_{0.9}O_x$, $Co_{0.1}Ce_{0.9}O_x$ where CeO_2 is represented by the bottom black line, $Cu_{0.1}Ce_{0.9}O_x$ by the green middle line and $Co_{0.1}Ce_{0.9}O_x$ by the purple top line. All samples were heated at a rate of 10 K min^{-1} under 30 mL min^{-1} 10 % H_2/Ar.

A more complex reduction profile was observed for $CoCeO_x$ with peak maxima present at 234, 332 and 452 °C. The peak at 452 °C is attributed to the reduction of surface ceria species, which occurs at a lower temperature due to the promotional effect of CoO_x and CeO_2 on each other's reducibility.[39, 40] The peaks at lower temperatures have been attributed to the reduction of Co_3O_4 and CoO.[41, 42] As shown in Table 3, significant differences in H_2 consumption values were observed amongst the three catalysts; overall H_2 consumption followed the order $CoCeO_x$ > $CuCeO_x$ > CeO_2.

Significant differences in the CO_2 desorption profiles were also observed (Figure 6). As an acidic molecule, CO_2 TPD is a well-established technique for investigating the basicity of materials. All samples were first analysed under blank conditions, whereby no CO_2 was admitted into the system, in order to confirm that no catalyst decomposition occurred and that the pre-treatment conditions were adequate for the removal of any atmospheric adsorbates. All the catalysts showed complex desorption profiles, which presented challenges with effective peak deconvolution. Nevertheless, it is clear that the strength and quantity of basic sites varies with the addition of Cu and Co dopants.

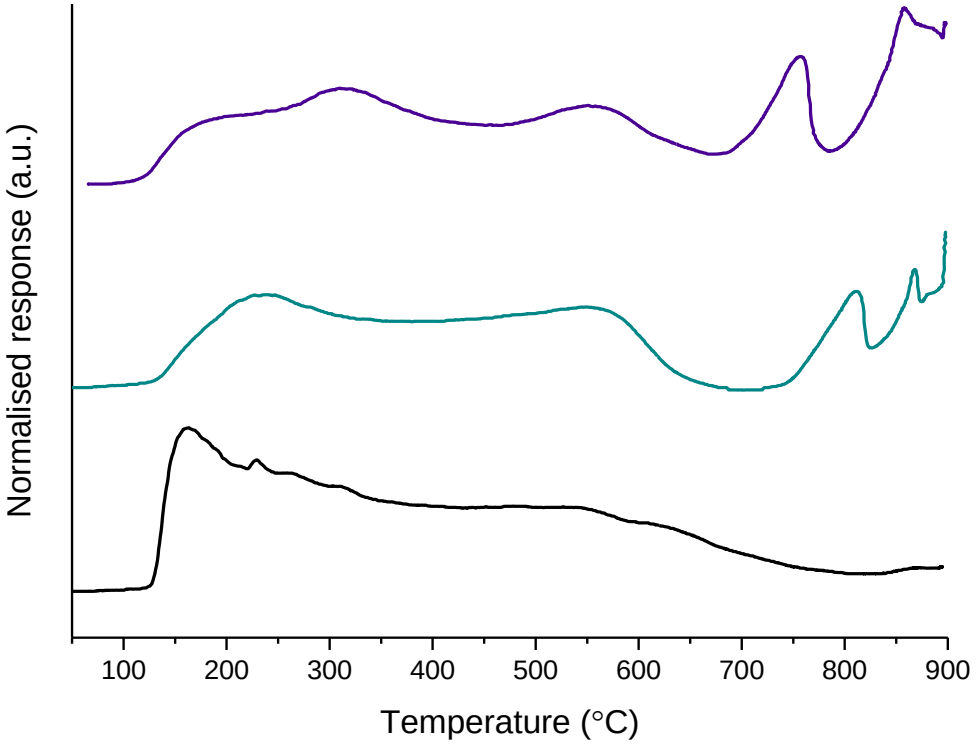

Figure 6. CO_2-TPD profiles of CeO_2, $Cu_{0.1}Ce_{0.9}O_x$, $Co_{0.1}Ce_{0.9}O_x$ where CeO_2 is represented by the bottom black line, $Cu_{0.1}Ce_{0.9}O_x$ by the green middle line and $Co_{0.1}Ce_{0.9}O_x$ by the purple top line. All samples were heated at a rate of 10 K min^{-1} under 30 mL min^{-1} He.

Whilst very similar quantities of CO_2 were desorbed from CeO_2 and $CoCeO_x$ on a μmol g^{-1}, once normalised for the differences in surface area, the quantity of CO_2 desorbed followed the trend CeO_2 > $CoCeO_x$ > $CuCeO_x$. As shown in Figure 6, the major CO_2 desorption peak for CeO_2 occurred at *ca.* 165 °C; additional weaker peaks could also be observed as broad overlapping peaks with maxima at 230, 545 and 635 °C. For $CuCeO_x$, the majority of CO_2 was desorbed between 120 – 700 °C, with two broad overlapping peaks centred at 235 and 560 °C. In addition to this, additional sharper peaks were observed at temperatures > 800 °C, indicating the presence of more strongly basic sites. Below 675 °C, $CoCeO_x$ showed a broad desorption profile, with peak maxima at 190, 312, and 550 °C. Similarly to $CuCeO_x$, additional shaper peaks were observed at temperatures of 755 and 860 °C, suggesting the presence of strongly basic sites. These results suggest that there may be a greater quantity of basic sites present in CeO_2, due to the greater quantity of CO_2 desorbed, although the

strength of basic sites appears higher in the doped samples, as indicated by the higher desorption temperatures observed.

Table 3. H_2 consumption and CO_2 desorption as measured by H_2-TPR and CO_2-TPD, respectively

Material	*H_2 consumption ($\mu mol\ g^{-1}$)*	*H_2 consumption ($\mu mol\ m^{-2}$)*	*CO_2 desorbed ($\mu mol\ g^{-1}$)*	*CO_2 desorbed ($\mu mol\ m^{-2}$)*
CeO_2	153	3.32	79.8	1.73
$CuCeO_x$	779	12.77	61.7	1.01
$CoCeO_x$	1150	18.25	80.7	1.28

5.2.3 Glycerol conversions

Initially, the catalysts were tested with 500 mg of catalyst (diluted with SiC) and a 50 wt.% GLY feedstock at 320 °C. This corresponded to a GHSV of 3600 h^{-1} for CeO_2 and 3000 h^{-1} for $CuCeO_x$ and $CoCeO_x$, due to the slightly higher density of the undoped material. The obtained product distributions, GLY conversions and carbon balances are shown in figure 7. GLY conversion of 58, 44, and 48 % were obtained over CeO_2, $CuCeO_x$ and $CoCeO_x$, respectively, despite the significantly lower surface area of CeO_2 (46 $m^2\ g^{-1}$) compared with $CuCeO_x$ (61 $m^2\ g^{-1}$) and $CoCeO_x$ (63 $m^2\ g^{-1}$). Normalisation of GLY conversion to surface area showed the activity to be of the order $CeO_2 > CoCeO_x \approx CuCeO_x$. As shown in previous chapters, there is a significant relationship between GLY conversion and product distribution, with intermediate products such as HA favoured at low GLY conversion. Thus, an additional experiment was also performed with a reduced mass of CeO_2 catalyst (300 mg) in order to achieve a GLY conversion (45 %) comparable with that obtained over the doped materials. No significant difference in carbon balance was observed across the materials, with values ranging between 87-91 %.

As shown below, ketone selectivity was highest for $CuCeO_x$ followed by $CoCeO_x$, predominantly due to the high selectivity towards HA, at 42.4 and 39.6 %, respectively, which was in agreement with the theory that dopant ions may increase HA selectivity at lower conversions. Noticeable lower diol selectivity was observed over the doped materials, with reduced amounts of 1,2-PD and EG when compared with CeO_2, despite higher levels of H_2 production also being observed. MeOH selectivity was fairly low (< 10 %) over all catalysts, likely due to the relatively low reaction temperature and GLY conversion, which were not sufficient to effectively convert intermediate products to MeOH.

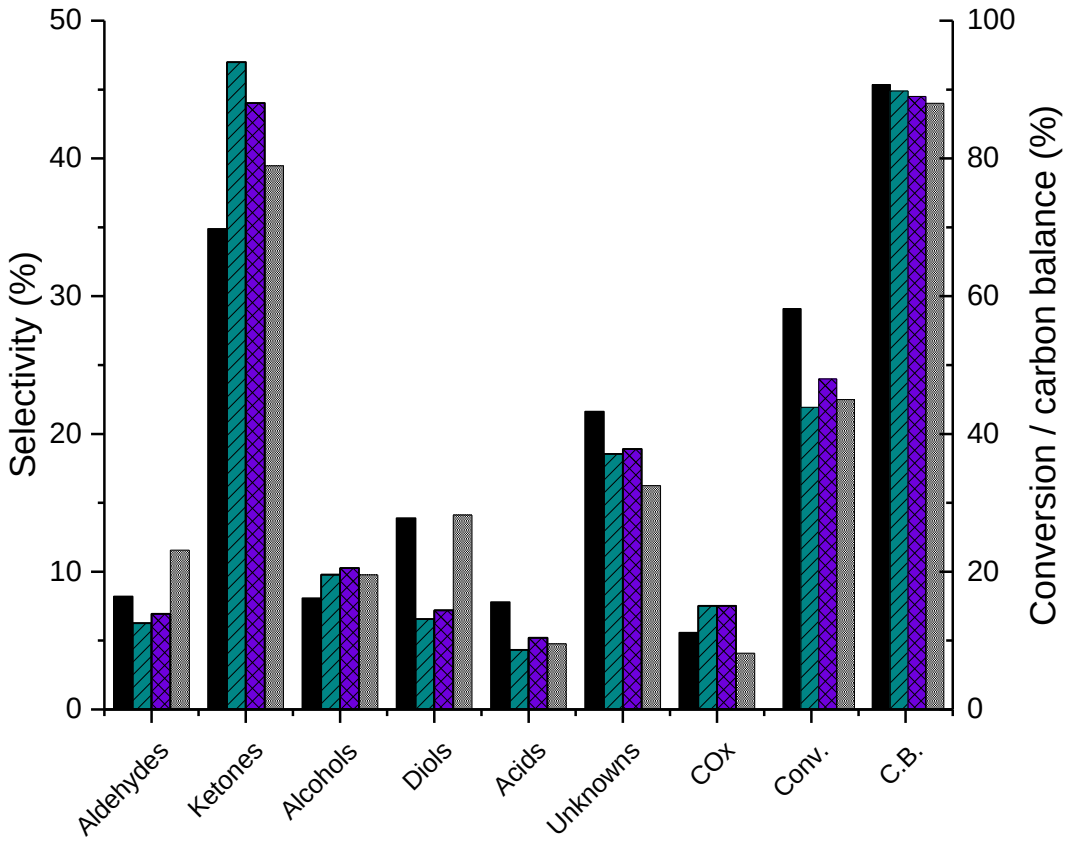

Figure 7. Product distributions etc. over CeO_2 (black bars), $CuCeO_x$ (green striped bars), $CoCeO_x$ (purple hatched bars) and CeO_2 (300 mg) (white checkerboard bars). Reaction conditions; 320 °C, 50 wt. % glycerol (0.016 mL min^{-1}), 15 mL min^{-1} Ar, 3 hours, GHSV = 3600 h^{-1} (5000 h^{-1} for CeO_2 (300 mg)).

As the reaction temperature was increased to 360 °C, a significant increase in GLY conversion was observed over CeO_2 (98 %), whilst conversions of *ca.* 80 % were obtained over $CuCeO_x$, $CoCeO_x$ and CeO_2 (300 mg) (Figure 8). Whilst noticeably higher GLY conversion was observed, HA was the major product detected over all catalysts, although with lower selectivities than observed at 320 °C. Moderate increases in ACA and MeOH selectivity were also observed suggesting HA conversion did occur at these conditions. No significant differences in product distribution were observed between CeO_2 (300 mg), $CuCeO_x$ and $CoCeO_x$, with HA selectivities of 31.1, 27.8, and 29.8 %, respectively, calculated. Very similar selectivities to ACA and MeOH were also obtained over the three materials. ACA selectivities were found to be 8.9, 9.8, and 9.6 % respectively, over $CuCeO_x$, $CoCeO_x$ and CeO_2 (300 mg), while the corresponding MeOH selectivities were 8.9, 9.4, and 10.7 %.

The moderate (typically < 10 %) ACA and MeOHs selectivities observed under these reaction conditions, along with the moderate (*ca.* 30 %) HA selectivity, suggest that HA is not effectively converted to MeOH under these conditions. As shown in previous chapters, a significant increase in MeOH selectivity and STY is often observed as the reaction temperature is increased to 400 °C, thus additional experiments at a higher reaction temperature were performed.

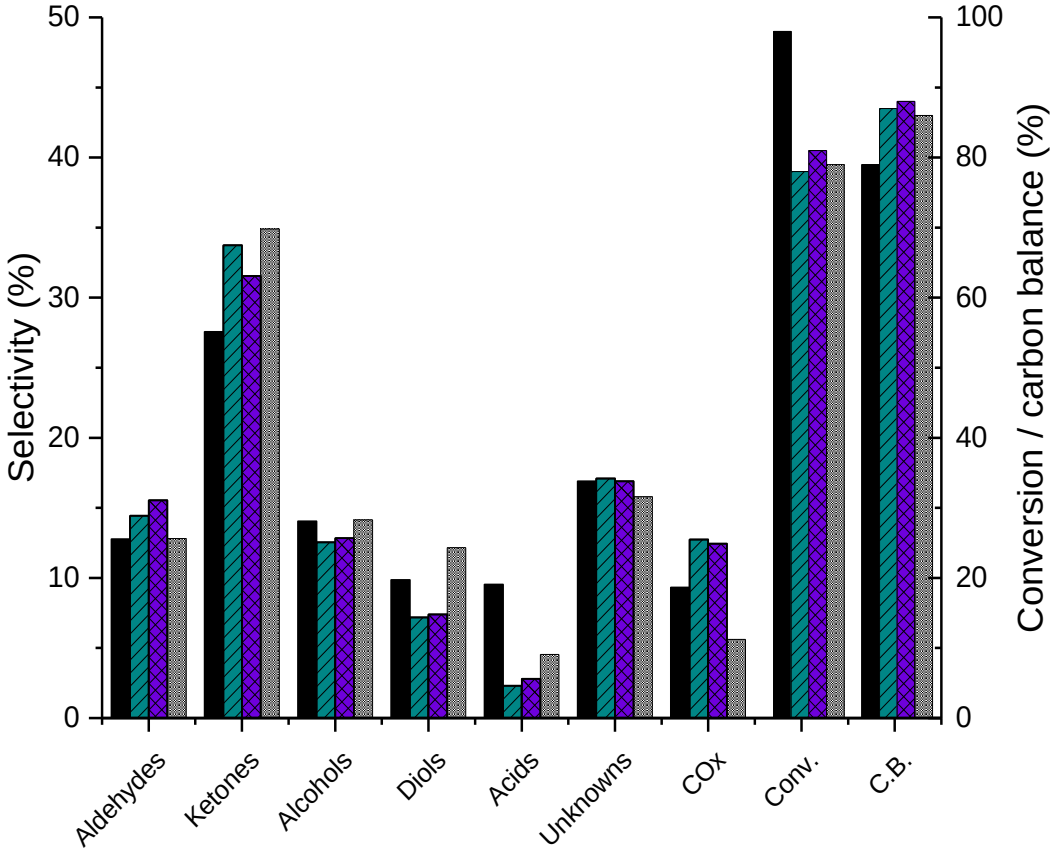

Figure 8. Product distributions etc. over CeO_2 (black bars), $CuCeO_x$ (green striped bars), $CoCeO_x$ (purple hatched bars) and CeO_2 (300 mg) (white checkerboard bars). Reaction conditions; 360 °C, 50 wt. % glycerol (0.016 mL min^{-1}), 15 mL min^{-1} Ar, 3 hours, GHSV = 3600 h^{-1} (5000 h^{-1} for CeO_2 (300 mg)).

Increasing the reaction temperature to 400 °C resulted in completed GLY conversion over CeO_2, with conversions of 94, 95, and 95 % over $CuCeO_x$, $CoCeO_x$, and CeO_2 (300 mg), respectively (Figure 9; full product distributions are shown in Table A5.3). Significantly higher MeOH and CO_x selectivies were obtained over CeO_2 along with reduced selectivities towards diols, ketones, and unknown products. Only traces of HA were detected, with the ketone selectivity comprised predominantly of ACE and 2,3-BD. Both of these products are considered to be terminal products which do not react further under the given conditions, as discussed in previous chapters. MeOH selectivity followed the trend CeO_2 > CeO_2 (300 mg) > $CoCeO_x$ > $CuCeO_x$. MeOH selectivity was significantly higher for CeO_2 (21.3 %) compared with CeO_2 (300 mg) (12.9 %) which was attributed to the increased conversion of HA with a higher catalyst mass and GLY conversion. Once again, this highlights the importance of effectively converting intermediate products, to maximise MeOH selectivity.

Significant differences in product distribution were observed across $CuCeO_x$, $CoCeO_x$ and CeO_2 (300 mg). Whilst the addition of dopants resulted in a moderate increase in carbon balance (*ca.* 5 %), they were not beneficial for MeOH selectivity. Whilst higher levels of HA were observed at low conversion over the doped materials, this did not translate to high MeOH selectivity at high conversion. Lower HA selectivity was detected over the doped

materials, which along with the increased ACA selectivity, suggests that HA was converted to some extent under these conditions, although this wasn't an effective route to MeOH. The lower alcohol selectivity observed for the doped materials compared with CeO_2 (300 mg) was accompanied by an increase in CO_x; CO_x selectivity was calculated to be 15.0, 14.1, and 6.9 % for $CuCeO_x$, $CoCeO_x$, and CeO_2 (300 mg). These results, discussed in more detail below, suggest that produced MeOH may not be stable over the doped catalysts. Thus, it would be beneficial to investigate the stability of the MeOH, under reaction conditions and through spectroscopic techniques (*e.g.* DRIFTS) to assess how any interactions between the catalyst and MeOH may reduce MeOH selectivity.

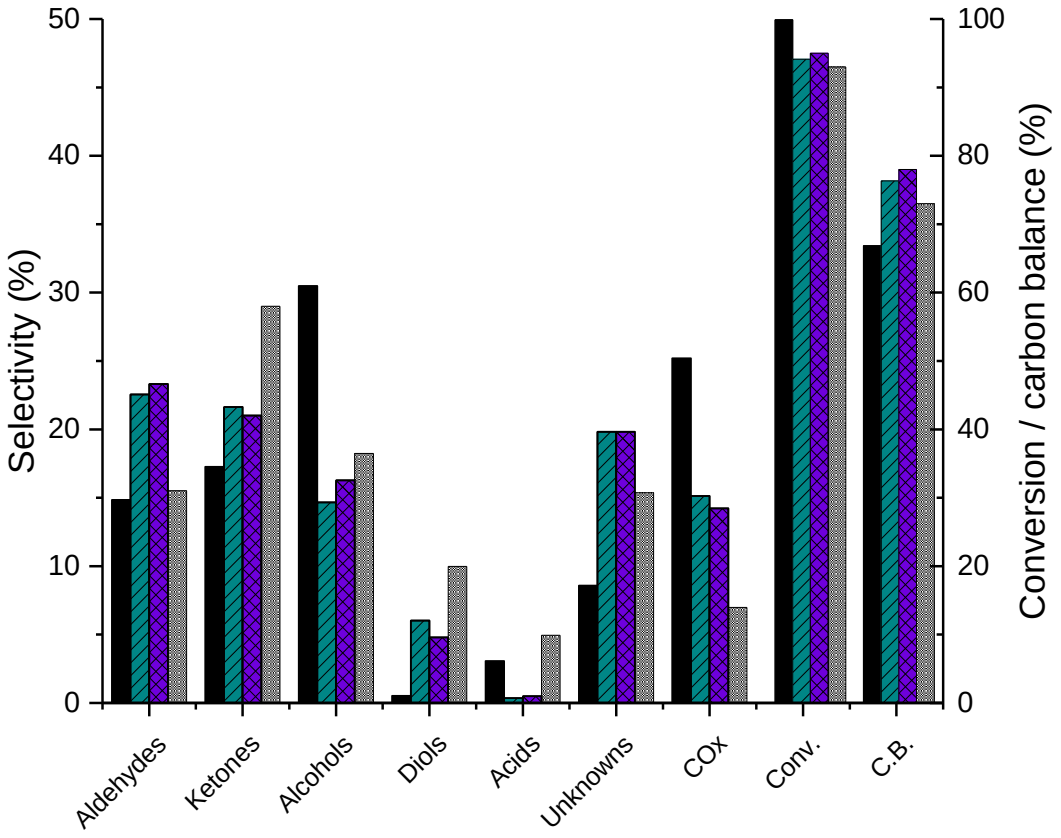

Figure 9. Product distributions etc. over CeO_2 (black bars), $CuCeO_x$ (green striped bars), $CoCeO_x$ (purple hatched bars) and CeO_2 (300 mg) (white checkerboard bars). Reaction conditions; 400 °C, 50 wt. % glycerol (0.016 mL min^{-1}), 15 mL min^{-1} Ar, 3 hours, GHSV = 3600 h^{-1} (5000 h^{-1} for CeO_2 (300 mg)).

All product selectivies are calculated on a carbon mole basis, to account for the different number of carbon atoms in several products (e.g. MeOH is C_1, ACA is C_2, HA is C_3). Whilst this effectively represents the selectivity to all carbon containing products, what is not shown is any hydrogen produced. As shown below (Figure 10), significantly more H_2 was produced over the doped materials than undoped ceria. Comparing the product distributions over $CuCeO_x$, $CoCeO_x$ and CeO_2 (300 mg) at 400 °C showed that significantly higher CO_x selectivities were observed over $CuCeO_x$, $CoCeO_x$ compared with CeO_2. The reactions performed with CeO_2 (500 mg) cannot be directly compared in terms of CO_x

selectivity due to the differences in GLY conversion. Whilst the difference between 95 and 100 % GLY conversion may not seem particularly significant, noticeable differences in product distribution are observed between these conversion levels. As shown in previous chapters, at GLY conversions > 99 % a significant increase in terminal products, such as MeOH and CO_x, are observed due to the increased conversion of intermediate products.

The increased CO_x observed over $CuCeO_x$ and $CoCeO_x$ compared with CeO_2 (300 mg) was comprised predominantly of CO. With CeO_2 (300 mg) the CO/CO_2 ratio was approximately 0.85 whereas it was *ca.* 2.27 over the doped catalysts. The increased selectivity towards CO and H_2 obtained over $CuCeO_x$ and $CoCeO_x$, alongside the reduced MeOH productivity, suggest that MeOH may be further converted over these catalysts. The ratio of CO/CO_2 is indicative of MeOH decomposition ($CH_3OH \rightarrow CO + 2H_2$) as opposed to MeOH steam reforming ($CH_3OH + H_2O \rightarrow CO_2 + 3H_2$).[43] MeOH STYs were calculated to be 161.2, 83.3, 91.4, and 158.1 g h^{-1} kg^{-1}_{cat} for CeO_2, $CuCeO_x$, $CoCeO_x$, and CeO_2 (300 mg), respectively. Whilst MeOH productivity was significantly lower over the doped catalysts, the moderate ACA and HA selectivities are in agreement with the theory that MeOH was produced and then further converted. MeOH STY followed the order $CeO_2 >> CoCeO_x > CuCeO_x$, whereas H_2 production followed the inverse order of $CuCeO_x > CoCeO_x >> CeO_2$.

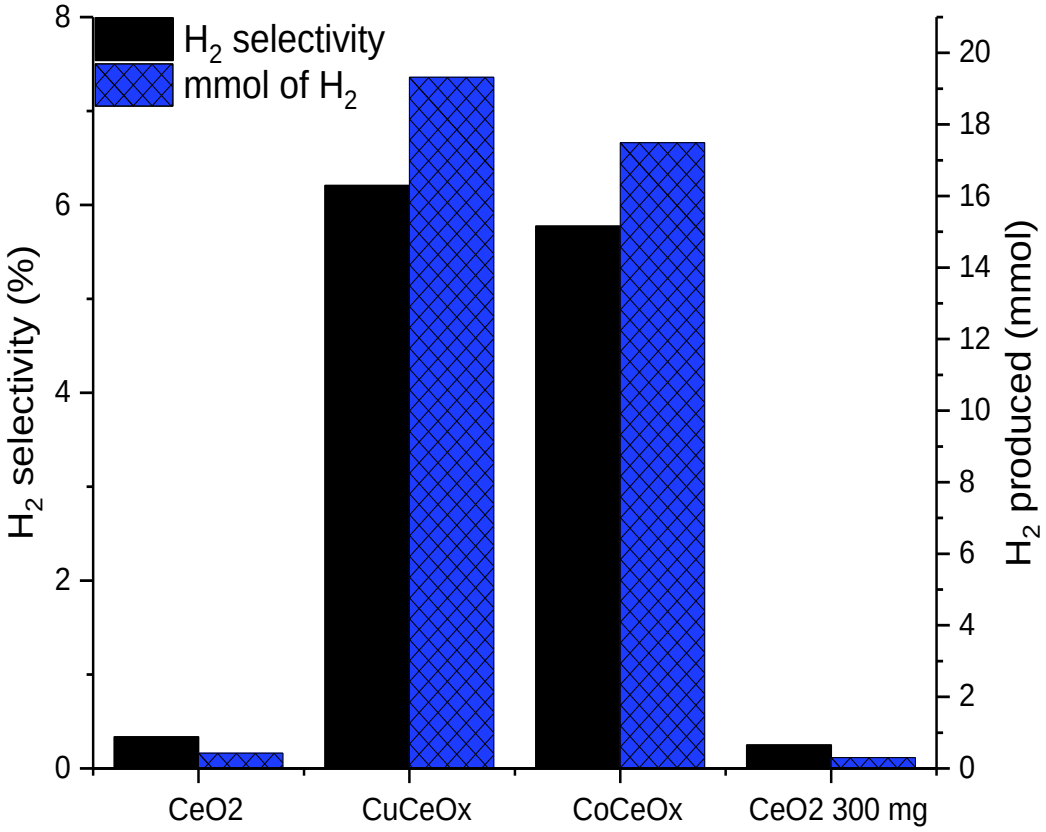

Figure 10. H_2 selectivity and production in mmol over CeO_2, $CuCeO_x$, $CoCeO_x$ and CeO_2 (300 mg) at 400 °C. Reaction conditions; 400 °C, 50 wt. % glycerol (0.016 mL min^{-1}), 15 mL min^{-1} Ar, 3 hours, GHSV = 3600 h^{-1} (5000 h^{-1} for CeO_2 (300 mg)).

5.2.4 *In-situ* H_2 consumption

As described above, moderate H_2 yields were obtained over $CuCeO_x$ and $CoCeO_x$. In addition to this, a reasonably high selectivity to aldehydic products was also observed, with ACA comprising *ca.* 15 % of the product selectivity. Whilst H_2 was produced under the conditions described above, species such as aldehydes and ketones were not significantly reduced to their corresponding alcohols under those conditions. This is not particularly unexpected given the absence of a hydrogenation catalyst. The hydrogenation of aldehydic species with H_2 produced *in-situ* is an interesting scenario which may provide a route to increased alcohol yields, despite a reduction in MeOH productivity.

Due to the complexity of the reaction scheme, model reactions were performed whereby the concentrations of ACA and H_2 produced over $CuCeO_x$ at 400 °C were replicated by co-feeding a dilute ACA stream with H_2 to investigate the feasibility of using a hydrogenation catalyst in a second catalyst bed to reduce aldehydic species at low partial pressures of H_2. Reactions were carried out at atmospheric pressure, with a H_2 partial pressure of 0.15 bar. The catalysts investigated were Pt/Al_2O_3, Pt/C and Ru/C; all catalysts had a metal loading of 5 wt.% and were commercial catalysts. Catalyst testing was performed at 80, 100 and 120 °C (Figure 11), and catalysts were pre-reduced prior to use.

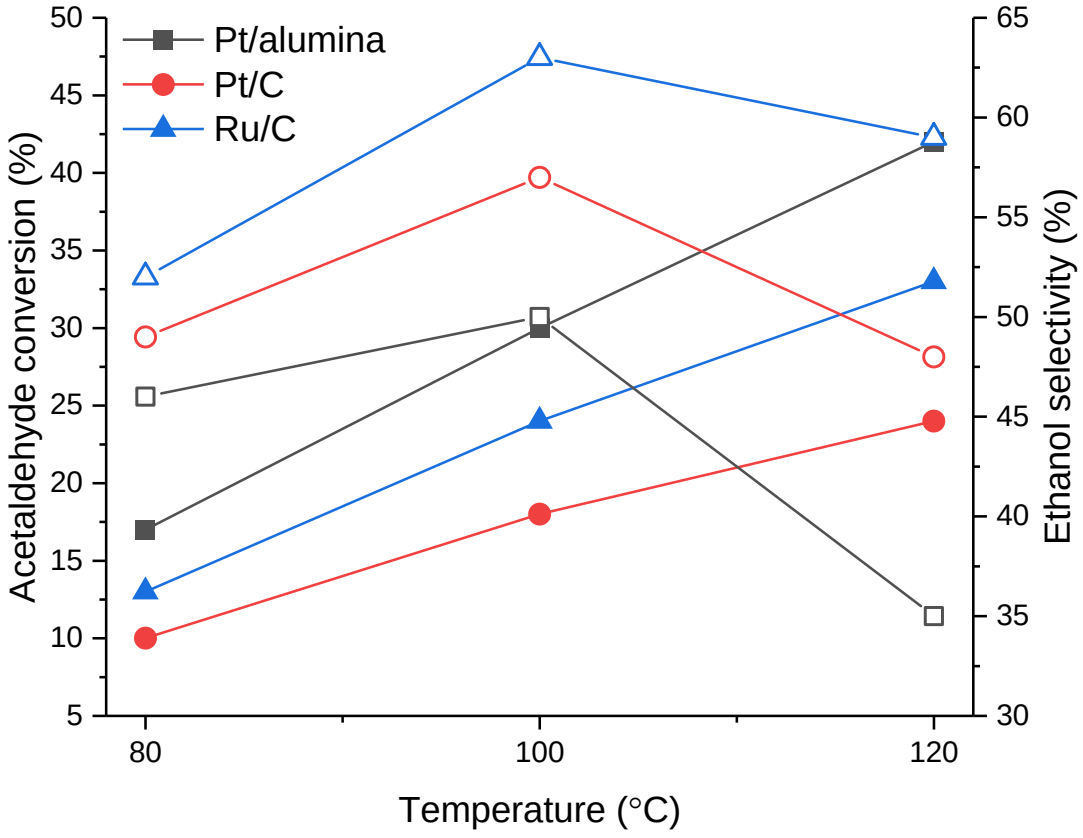

Figure 11. Acetaldehyde conversion (filled symbols) and ethanol selectivity (hollow symbols) over Pt/alumina (black squares), Pt/C (red circles), and Ru/C (blue triangles) at 400 °C. Reaction conditions; 80 – 120 °C, 100 mg 5 wt.% catalyst, GHSV *ca.* 15000 h^{-1}, 3 hours on line.

Due to the presence of unidentified gas phase products, EtOH selectivity was calculated as the % of EtOH formed (mmol) compared with the theoretical maximum quantity of EtOH formed at that level of ACA conversion. ACA conversion followed the order Pt/Al_2O_3 > Ru/C > Pt/C, and increased for all catalysts with increasing temperature. Despite the higher activity of Pt/Al_2O_3, the highest EtOH yield of 19.1 % was obtained over Ru/C. Selectivity to EtOH was lowest for Pt/Al_2O_3, despite it showing the highest ACA conversion. This is likely due to the acidic nature of the support, which has been shown to catalyse ACA dehydration to ethylene.[44, 45] The unidentified gas phase products were confirmed not to be CO, CO_2, CH_4 or MeOH, with ethylene and ethene likely formed by ACA dehydration and subsequent reduction. The higher selectivity to EtOH observed over the C supported catalysts was likely due to a suppression in ACA dehydration with reduced acidity.[45]

It should be noted that these experiments were preliminary studies with no optimisation of reaction parameters, thus the yields achieved over Ru/C suggest that it may be worth further exploring this catalyst for the reduction of ACA to EtOH, under optimised reaction conditions, before using more realistic operating conditions, i.e. with multiple substrates present.

5.3 Conclusions

The addition of copper and cobalt to cerium oxide catalysts has been explored for the conversion of GLY to MeOH. Characterisation of the materials showed the dopant ions (10 mol.%) were well incorporated into the ceria lattice, with no phase segregation detected; the doped materials had an increased surface area compared with the undoped ceria, with smaller crystallite sizes also observed. Raman spectroscopy showed the defect density followed the trend $CoCeO_x$ > $CuCeO_x$ >> CeO_2, which was the same trend as H_2 consumption, although the Cu catalyst showed significantly higher H_2 consumption at low temperatures. The basicity of the materials was probed by CO_2 TPD. Overall CO_2 desorption was highest for CeO_2 followed by $CoCeO_x$, although the doped materials showed high temperature (> 800 °C) desorption peaks, indicating the presence of more strongly basic sites.

At all reaction temperatures tested, GLY conversion was of the order CeO_2 > $CoCeO_x$ ≈ $CuCeO_x$. When one considers the increased surface area of the doped materials, it is clear that the undoped ceria is significantly more active more the conversion of GLY under these conditions. Due to the higher activity of CeO_2, additional experiments were performed with a reduced mass of CeO_2, to achieve comparable levels of GLY conversion across the materials. This allowed the effect of dopants on product distribution to be assessed without potentially competing effects of GLY conversion levels.

At the lower reaction temperature of 320 °C, HA was the major product formed over all catalysts, with the highest selectivity observed over $CuCeO_x$ (42.4 %) followed by $CoCeO_x$.

This was in agreement with previous literature reports, whereby copper based catalysts have shown to be effective for HA production from GLY.

Despite the fact that increased HA production was observed over the doped ceria catalysts at reasonably low conversion, this did not translate to an increase in MeOH selectivity at higher conversion. At a reaction temperature of 400 °C, MeOH STYs were found to be 161.2, 83.3, 91.4, and 158.1 g h^{-1} kg^{-1} for CeO_2, $CuCeO_x$, $CoCeO_x$ and CeO_2 (300 mg), respectively, corresponding to MeOH selectivities of 21.3, 10.2, 11.0 and 12.9 %. Interestingly, despite the significantly lower MeOH selectivity obtained over a reduced mass of CeO_2, the MeOH STY was maintained. This is partly because STY is a function of catalyst mass, and partly due to the improved carbon balance, once again highlighting the importance in achieving high MeOH selectivities with high carbon balances to maximise MeOH productivity. Significantly lower MeOH STYs were obtained over $CuCeO_x$ and $CoCeO_x$ vs. undoped ceria, which was also accompanied by lower HA and higher ACA selectivities than were observed over CeO_2 (300 mg), suggesting that HA had been further converted under the conditions. A moderate CO_x selectivity (*ca.* 15 %) was also observed, predominantly comprised of CO. In addition to this, reasonably high H_2 selectivity was observed over the doped materials with with a CO/H2 ratio of *ca*. 5:1 detected over CuCeOx. The low MeOH productivity, despite the moderate HA conversion and ACA selectivity, coupled with the relatively high levels of CO and H_2, are indicative that MeOH itself may be further converted over the doped ceria catalysts. An interesting are of future work in this area would be to further explore the reactivity of MeOH over CeO_2, $CuCeO_x$ and $CoCeO_x$, to determine whether MeOH conversion is the cause of the lower MeOH productivity observed over the doped materials.

Since moderate amounts of H_2 and ACA were produced over $CuCeO_x$ at 400 °C, it was hypothesised that the H_2 produced in-situ could be used to reduce the presence of aldehydic species, thus model reactions were performed with a mix of pure ACA (diluted in He) co-fed with H_2. The reaction conditions were modelled on those used in the GLY conversion reactions with the mix of ACA and H_2 replicated using dilute ACA gas. Temperatures between 80 and 120 °C were investigated using commercially available 5 wt.% Pt/Al_2O_3, Pt/C, and Ru/C catalysts, all of which were pre-reduced under H_2 prior to use.

The order of activity for ACA conversion was found to be Pt/Al_2O_3 > Ru/C > Pt/C with ACA conversion steadily increasing with increasing reaction temperature for all catalysts. All three catalysts also showed a volcano-type plot when it came to EtOH selectivity, with maximum EtOH selectivities achieved at a reaction temperature of 100 °C. That said, the maximum EtOH yield of 19.1 % was achieved over Ru/C at 120 ° C, despite a slight reduction in selectivity, due to the increase in conversion. EtOH selectivity followed the trend Ru/C > Pt/C > Pt/Al_2O_3, which could be due to the reduced acidity of the carbon supported catalysts

compared with alumina. Alumina supports have been reported to catalyse the dehydration of ACA to ethylene, which would reduce observed EtOH yields.[44, 45] These experiments were preliminary experiments, performed without optimising reaction conditions, thus the EtOH yield of 19.1 % achieved over Ru/C was fairly promising, and suggests it may be possible to increase the total alcohol yield through the addition of a second catalyst bad. An interesting area for future work would be to optimise the conditions over Ru/C to determine whether EtOH productivity can be improved.

5.4 References

1. C.-W. Chiu, A. Tekeei, W. R. Sutterlin, J. M. Ronco and G. J. Suppes, *AIChE Journal*, 2008, **54**, 2456-2463.
2. S. Sato, M. Akiyama, R. Takahashi, T. Hara, K. Inui and M. Yokota, *Applied Catalysis A: General*, 2008, **347**, 186-191.
3. M. Velasquez, A. Santamaria and C. Batiot-Dupeyrat, *Applied Catalysis B: Environmental*, 2014, **160**, 606-613.
4. S. Célerier, S. Morisset, I. Batonneau-Gener, T. Belin, K. Younes and C. Batiot-Dupeyrat, *Applied Catalysis A: General*, 2018, **557**, 135-144.
5. J. Devlia, L. Smith, M. Douthwaite, S. H. Taylor, D. J. Willock, G. J. Hutchings and N. F. Dummer, *Philosophical Transactions of the Royal Society A: Mathematical, Physical and Engineering Sciences*, 2020, **378**, 20200059.
6. Z. Guo, F. Du, G. Li and Z. Cui, *Inorganic Chemistry*, 2006, **45**, 4167-4169.
7. J.-G. Li, T. Ikegami, Y. Wang and T. Mori, *Journal of the American Ceramic Society*, 2002, **85**, 2376-2378.
8. P. Janoš, J. Henych, J. Pfeifer, N. Zemanová, V. Pilařová, D. Milde, T. Opletal, J. Tolasz, M. Malý and V. Štengl, *Environmental Science: Nano*, 2017, **4**, 1283-1293.
9. X. Zheng, X. Zhang, X. Wang, S. Wang and S. Wu, *Applied Catalysis A: General*, 2005, **295**, 142-149.
10. C. Lamonier, A. Bennani, A. D'Huysser, A. Aboukaïs and G. Wrobel, *Journal of the Chemical Society, Faraday Transactions*, 1996, **92**, 131-136.
11. P. Bera, S. T. Aruna, K. C. Patil and M. S. Hegde, *Journal of Catalysis*, 1999, **186**, 36-44.
12. P. Sudarsanam, B. Hillary, D. K. Deepa, M. H. Amin, B. Mallesham, B. M. Reddy and S. K. Bhargava, *Catalysis Science & Technology*, 2015, **5**, 3496-3500.
13. S. Li, N. Wang, Y. Yue, G. Wang, Z. Zu and Y. Zhang, *Chemical Science*, 2015, **6**, 2495-2500.
14. S. T. Hossain, E. Azeeva, K. Zhang, E. T. Zell, D. T. Bernard, S. Balaz and R. Wang, *Applied Surface Science*, 2018, **455**, 132-143.
15. P. Bera, K. R. Priolkar, P. R. Sarode, M. S. Hegde, S. Emura, R. Kumashiro and N. P. Lalla, *Chemistry of Materials*, 2002, **14**, 3591-3601.
16. S. Hočevar, U. O. Krašovec, B. Orel, A. S. Aricó and H. Kim, *Applied Catalysis B: Environmental*, 2000, **28**, 113-125.
17. C. Sun and D. Xue, *Physical Chemistry Chemical Physics*, 2013, **15**, 14414-14419.
18. S. Y. Yao, W. Q. Xu, A. C. Johnston-Peck, F. Z. Zhao, Z. Y. Liu, S. Luo, S. D. Senanayake, A. Martínez-Arias, W. J. Liu and J. A. Rodriguez, *Physical Chemistry Chemical Physics*, 2014, **16**, 17183-17195.
19. D. Jampaiah, K. M. Tur, S. J. Ippolito, Y. M. Sabri, J. Tardio, S. K. Bhargava and B. M. Reddy, *RSC Advances*, 2013, **3**, 12963-12974.
20. M. Fernández-García, A. Martínez-Arias, J. C. Hanson and J. A. Rodriguez, *Chemical Reviews*, 2004, **104**, 4063-4104.
21. I. Kosacki, T. Suzuki, H. U. Anderson and P. Colomban, *Solid State Ionics*, 2002, **149**, 99-105.
22. W. H. Weber, K. C. Hass and J. R. McBride, *Physical Review B*, 1993, **48**, 178-185.

23. M. Kang, X. Wu, J. Zhang, N. Zhao, W. Wei and Y. Sun, *RSC Advances*, 2014, **4**, 5583-5590.
24. Y. Lee, G. He, A. J. Akey, R. Si, M. Flytzani-Stephanopoulos and I. P. Herman, *Journal of the American Chemical Society*, 2011, **133**, 12952-12955.
25. M. Dosa, M. Piumetti, S. Bensaid, T. Andana, C. Novara, F. Giorgis, D. Fino and N. Russo, *Catalysis Letters*, 2018, **148**, 298-311.
26. S. Agarwal, X. Zhu, E. J. M. Hensen, L. Lefferts and B. L. Mojet, *The Journal of Physical Chemistry C*, 2014, **118**, 4131-4142.
27. Z. Wu, M. Li, J. Howe, H. M. Meyer and S. H. Overbury, *Langmuir*, 2010, **26**, 16595-16606.
28. J. E. Spanier, R. D. Robinson, F. Zhang, S.-W. Chan and I. P. Herman, *Physical Review B*, 2001, **64**, 245407.
29. L. Li, F. Chen, J.-Q. Lu and M.-F. Luo, *The Journal of Physical Chemistry A*, 2011, **115**, 7972-7977.
30. E. Sartoretti, C. Novara, F. Giorgis, M. Piumetti, S. Bensaid, N. Russo and D. Fino, *Scientific Reports*, 2019, **9**, 3875.
31. C. Schilling, A. Hofmann, C. Hess and M. V. Ganduglia-Pirovano, *The Journal of Physical Chemistry C*, 2017, **121**, 20834-20849.
32. A. Filtschew, K. Hofmann and C. Hess, *The Journal of Physical Chemistry C*, 2016, **120**, 6694-6703.
33. L. E. Gómez, E. E. Miró and A. V. Boix, *International Journal of Hydrogen Energy*, 2013, **38**, 5645-5654.
34. M. F. L. Johnson and J. Mooi, *Journal of Catalysis*, 1987, **103**, 502-505.
35. F. Giordano, A. Trovarelli, C. de Leitenburg and M. Giona, *Journal of Catalysis*, 2000, **193**, 273-282.
36. J. Beckers and G. Rothenberg, *Dalton Transactions*, 2008, DOI: 10.1039/B809769K, 6573-6578.
37. W. Zhu, K. Tang, J. Li, W. Liu, X. Niu, G. Zhao, X. Ma, Z. Liu, H. Wei and Y. Yang, *RSC Advances*, 2016, **6**, 46966-46971.
38. M.-F. Luo, Y.-J. Zhong, X.-X. Yuan and X.-M. Zheng, *Applied Catalysis A: General*, 1997, **162**, 121-131.
39. D. Jampaiah, P. Venkataswamy, V. E. Coyle, B. M. Reddy and S. K. Bhargava, *RSC Advances*, 2016, **6**, 80541-80548.
40. B. Govinda Rao, D. Jampaiah, P. Venkataswamy and B. M. Reddy, *ChemistrySelect*, 2016, **1**, 6681-6691.
41. Q. Tang, Q. Zhang, H. Wu and Y. Wang, *Journal of Catalysis*, 2005, **230**, 384-397.
42. S. Hassan, R. Kumar, A. Tiwari, W. Song, L. van Haandel, J. K. Pandey, E. Hensen and B. Chowdhury, *Molecular Catalysis*, 2018, **451**, 238-246.
43. M. A. Díaz-Pérez, J. Moya, J. C. Serrano-Ruiz and J. Faria, *Industrial & Engineering Chemistry Research*, 2018, **57**, 15268-15279.
44. J. F. DeWilde, C. J. Czopinski and A. Bhan, *ACS Catalysis*, 2014, **4**, 4425-4433.
45. J. Ob-eye, P. Praserthdam and B. Jongsomjit, *Catalysts*, 2019, **9**, 66.

Chapter 6

Conclusions and future work

6.1 Conclusions

The overall objective of this thesis was to further explore the gas phase conversion of GLY to MeOH over ceria-based catalysts. Over recent years, there has been a steady increase in the production of biofuels, due to rising concerns regarding the dependency of society on fossil fuels, and the associated negative environmental consequences. One of the most widely used biofuels is biodiesel. Fatty acid methyl esters, known as biodiesel, are produced *via* a transesterification reaction between triglycerides and MeOH, typically in a base-catalysed process. GLY is the major by-product of the transesterification reaction and accounts for approximately 10 wt.% of the product yield. An excess of 40 billion kg of biodiesel was produced in 2019, corresponding to approximately 4 billion kg of GLY.[1] Whereas GLY was once produced predominantly through fatty acids production and saponification, biodiesel production is now the main supply driver for GLY.

As a reagent in the synthesis of biodiesel and an incredibly valuable chemical intermediate, the production of MeOH from renewable sources is highly desirable, providing significant environmental benefits. Industrial MeOH synthesis involves the reaction of fossil fuel derived syngas, typically over a $Cu/Zn/Al_2O_3$ catalyst, with production now in excess of 20 billion kg per annum.[2] Whilst MeOH synthesis is a well-established industrial reaction, there are serious associated environmental concerns. Particularly, the rising CO_2 levels, and the subsequent effects on global temperature and climate, necessitates a route to MeOH synthesis that does not involve the use of fossil fuels. The direct hydrogenation of CO_2 provides a renewable carbon source for MeOH production. However, in order for MeOH synthesis to be truly renewable, the hydrogen must also be derived from non-fossil fuel-based sources.

As a result of the significant increase in biodiesel production, the supply of GLY now exceeds the demand from traditional markets. The conversion of GLY to MeOH offers a route to the sustainable production of MeOH. Additionally, since MeOH is a reagent in biodiesel production and GLY is the main by-product of the biodiesel process, the conversion of GLY to MeOH provides an opportunity to close the sustainability loop of biodiesel production. In addition to the environmental advantages this would bring, the conversion of a waste product to a valuable chemical intermediate provides economic advantages.

The conversion of vaporised aqueous GLY feedstocks to MeOH was discovered by the Hutchings group in 2015.[3] This was a one-step process, performed at atmospheric pressure and without the requirement of an external reductant. In addition to MeOH, a number of other products such as ACA, EtOH, HA, ACR, EG, ACE and CO_2 were also observed. Whilst the initial report showed CeO_2 to be an effective catalyst for the reaction, the majority of studies were performed with a 10 wt.% GLY feed and difficulties maintaining high MeOH selectivity were observed as the concentration of the aqueous GLY feedstock was increased. As the GLY feedstock concentration was increased from 15 to 50 wt.% (in water), a decrease in MeOH selectivity from 56 to 34 % was observed, corresponding to STYs of 18 and 25 g_{MeOH} kg^{-1}_{cat} h^{-1}, respectively. The moderate increase in STY, despite the potential for a much larger increase, highlights the challenging nature of working with more concentrated GLY feedstocks, due to its highly functionalised, reactive nature. Nevertheless, the scale of GLY production and the associated low costs of GLY mean that high levels of catalyst productivity and the ability to selectively convert more concentrated feedstocks are of the utmost importance.

Chapter 3: Glycerol to methanol over metal oxide catalysts

The aim of chapter 3 was to explore the gas phase conversion of more concentrated GLY feedstocks to MeOH over magnesium oxide and cerium oxide catalysts, in order to gain a greater understanding of the complicated chemistry taking place. Initially, blank reactions were performed in the absence of any catalyst, both with an empty reactor tube and with a plug of inert SiC, which is used as a diluent under catalysed conditions. In an empty reactor tube, minimal GLY conversion was observed, reaching a maximum of *ca.* 10 % at a reaction temperature of 480 °C. The addition of a SiC plug led to an enhancement in GLY conversion at all temperatures; low levels (< 5 %) were observed at 320 and 360 °C but a moderate GLY conversion of 18 % was achieved at the highest reaction temperature of 480 °C. This corresponded to alcohol and ketone yields of *ca*. 5 %, composed predominantly of AA and HA, respectively. Whilst these results may suggest that SiC is not inert in the reaction, it is more likely that GLY conversion is increased in the presence of SiC due to increased contact between GLY and a hot surface. In an empty reactor tube, the majority of vaporised GLY will likely have no contact with the hot surface of the reactor. The addition of SiC led to a significant reduction in reactor volume thus leading to an increase in contact between GLY and a hot surface, which resulted in an increase in GLY conversion. These results highlighted the importance of optimising catalyst activity to achieve effective MeOH productivity at lower reaction temperatures (< 400 °C), in order to minimise side-reactions which could reduce the yield of MeOH.

A diverse product distribution was obtained with a 50 wt.% GLY feedstock over a magnesium oxide catalyst. At a lower reaction temperature of 360 °C, products such as HA,

1,2-PD and EG were predominantly observed. As the reaction temperature was increased, selectivity towards these products significantly decreased, as a consequence of increased MeOH, ACA, 2,3-BD and CO_x selectivities. MeOH productivity was found to reach a maximum at 400 °C, with a STY of 205 g h^{-1} kg_{cat}^{-1}. An investigation into the effect of GLY feedstock concentration showed that this could be improved to 255 g h^{-1} kg^{-1}_{cat} by reducing the GLY feedstock concentration from 50 to 10 wt.% and reducing the catalyst mass proportionally. The improvement in MeOH productivity observed with more dilute GLY feedstocks was attributed to a reduction in the formation of high molecular weight products *via* condensation reactions, which reduce the observed carbon balance and subsequent MeOH yields.

At a reaction temperature of 400 °C and with a 50 wt.% GLY feedstock, the MgO catalyst was shown to be stable over a period of 48 hours. Whilst the carbon balance was fairly low (*ca.* 65 %), it was stable under these conditions. Post-reaction analysis of the catalyst showed moderate levels of carbon deposition, although the stability of the catalyst over time suggested no significant catalyst deactivation occurred. Additional analysis of the post-reaction solution was performed in order to gain a further understanding of the carbon balance. LC-MS showed the presence of high molecular weight products. These products cannot be detected using routine GC analysis due to their low volatility, so are not included in carbon balance calculations. CHN analysis was utilised to determine the total carbon balance post-reaction, which was found to be 94 %, with the remaining carbon attributed to reactor fouling.

The effect of reaction temperature was also explored over a commercially available CeO_2 catalyst. Similarly to MgO, HA was the major product at the lowest reaction temperature of 320 °C, with a selectivity of 49 %, alongside EG and 1,2-PD. As the reaction temperature was increased, selectivity to these products decreased significantly as the selectivity to MeOH, ACA, ACE, and CO_x increased. In agreement with the results obtained over MgO, this highlighted the role of HA, 1,2-PD and EG as intermediate products which are further converted during the process.

An investigation into the effect of calcination temperature on the physicochemical properties of ceria and the subsequent effects on product distribution was undertaken. A series of catalysts were prepared by treating cerium(III) nitrate salts with ammonium hydroxide solution whereby the subsequent precursor was calcined at 400, 500, 600 and 700 °C to yield the final ceria catalysts. The catalysts were tested at comparable GHSVs with the catalyst mass adjusted to normalise the differences in surface area. The resultant product distributions suggested that there was no clear relationship between the crystallinity and defect density of the catalysts, as estimated by PXRD and Raman,

respectively, and the reactivity of GLY and intermediate products. With a constant surface area and GHSV, no significant distances in GLY conversion and product distribution were observed across the series of catalysts. That said, the differences in defect density were fairly minimal, suggesting that further varying the physicochemical properties of ceria are crucial to gaining further understanding of the chemistry taking place during the conversion of GLY to MeOH.

Chapter 4: The effect of ceria morphology on gas phase glycerol valorisations

Chapter 4 focussed on the use of morphologically controlled ceria nanostructures as catalysts for the reaction. Ceria nanorods (Ce-R), nanocubes (Ce-C), and nanopolyhedra (Ce-P) which preferentially exposed the (110), (100), and (111) surfaces, respectively, were prepared in accordance with the procedure reported by Yan and co-workers in 2005.[4] In addition to the TEM imaging, used to confirm the surface planes present, characterisation by XRD, N_2-physisorption and Raman spectroscopy was also performed to gain further insight into the structure of the materials. Surface area was found to follow the order Ce-R > Ce-P >> Ce-C, which was the opposite trend to crystallinity and particle size, although a higher cumulative pore volume was observed for Ce-C *vs.* Ce-P, due to the larger pore size. Raman analysis showed there was a significantly lower density of defects present in Ce-P compared with the other morphologies. Interestingly, the obtained TPR profiles and associated analyses suggested Ce-P possessed enhanced reducibility. It was difficult to fully correlate the acid/base properties of the materials with the exposed surfaces, but significant differences were observed across the catalysts.

Initial catalytic testing was performed under identical reaction conditions, with 0.5 g catalyst, corresponding to a GHSV of 3600 h^{-1}, at reaction temperatures of 320, 360 and 400 °C. At all given temperatures, GLY conversion followed the order Ce-R > Ce-P >> Ce-C, which was in agreement with the calculated surface areas of the catalysts. Whilst significant differences in product distribution were observed across the materials, the differing levels of GLY conversion meant that it was not possible to fully assess the role of morphology under these conditions.

Subsequent reactions were performed whereby the catalyst mass, and corresponding GHSVs, were altered in order to achieve comparable levels of GLY conversion. Reactions were performed with a GLY conversion of *ca.* 15 % at a reaction temperature of 320 °C, and > 99 % at a temperature of 400 °C, by decreasing the mass of Ce-R and Ce-P, and increasing the mass of Ce-C, respectively. At low GLY conversions, significant amounts of HA were detected over all three materials, albeit with a significantly lower selectivity over Ce-C; HA selectivities were 43.3, 37.4, and 14.1 % over Ce-P, Ce-R and Ce-C, respectively. The decrease in HA observed over Ce-C was attributed to the increased selectivity towards ACR (14.5 %) compared with Ce-R (3.2 %) and Ce-P (1.5 %). In contrast to HA, which is formed

through GLY dehydration at the terminal position, ACR is formed *via* a double dehydration, initiated through the loss of the secondary hydroxyl group. The increased selectivity towards ACR observed over Ce-C suggest a divergence in reaction mechanism over this catalyst.

At high (> 99 %) conversions, MeOH selectivities of 24.5, 22.6 and 13.1 % were obtained over Ce-P, Ce-R and Ce-C, respectively. Small quantities of EtOH and PrOH were observed, with selectivities following the same trend as MeOH. Alternatively, products such as ACA, ACR and AA followed the order Ce-C > Ce-R > Ce-P. This was in agreement with the product distribution at low conversion, highlighting the divergence in reaction mechanism over Ce-C. MeOH space time yields (STY) followed the trend of MeOH selectivity, with values of 201, 164, 47 g^{-1} kg^{-1}, for Ce-P, Ce-R and Ce-C, respectively. This mirrored the trend of HA STYs at low conversion, with values of 155 g h^{-1} kg^{-1}, 105 g h^{-1} kg^{-1}, and 12 g h^{-1} kg^{-1} for Ce-P, Ce-R and Ce-C, respectively. The strong correlation between HA productivity at low conversion and high MeOH productivity at high conversion is indicative of the role as HA as an intermediate in the process.

Additional experiments were used to confirm that the increased catalyst contact time required to achieve comparable GLY conversions over Ce-C. Generally, an increased contact time over Ce-R and Ce-P resulted in a decreased selectivity towards ACR. Thus, it was considered that the differences in product distribution observed over Ce-C could be attributed to differences associated with the catalyst and not the reaction conditions. An important area for future work would be to gain a greater insight into the differences in reaction mechanism by probing the interactions of vaporised aqueous GLY feedstocks with the CeO_2 (100), (110), and (111) surfaces. The (111) surface, predominantly exposed by Ce-P, appeared to be beneficial for MeOH productivity, as did the associated lower defect density and pore volume. The dependency of product distribution on surface plane should be considered during future work, in the context of rational catalyst design.

Chapter 5: Transition metal doped ceria for the conversion of glycerol to methanol

The use of morphologically controlled ceria nanostructures in chapter 4 showed there was a strong correlation between HA productivity at low GLY conversion and MeOH productivity at high GLY conversion. Numerous literature reports detail the use of copper-based catalysts for the conversion of GLY to HA,[5-8] thus it was hypothesised that the addition of copper as a dopant into the ceria catalyst may increase MeOH production, due to the role of HA as an intermediate in the process. The use of cobalt was also investigated for comparison, and to gain greater insights into the process.

Characterisation showed that the dopant ions were well incorporated into the materials, and their inclusion resulted in significantly reduced crystallinity and an increased surface area. The doped ceria catalysts showed significantly higher defect densities and reducibility compared with the undoped sample. The total quantity of CO_2 desorbed from the materials decreased with the addition of Cu and Co, suggesting a decrease in the quantity of basic sites, although higher temperature desorption peaks were observed, suggesting the strength of basic sites may have increased with the incorporation of dopants.

Despite the lower surface area of CeO_2, it was found to be the most active with GLY conversions following the order CeO_2 > $CoCeO_x$ ≈ $CuCeO_x$. Consequently, additional experiments were performed with a reduced mass of CeO_2 to achieve comparable levels of GLY conversion and allow the role of the dopants to be assessed with the effect of GLY conversion. HA selectivity was highest for $CuCeO_x$ (42.4 %), which was in agreement with the theory that the inclusion of a Cu dopant may increase HA selectivity at lower levels of GLY conversion.

At a reaction temperature of 400 °C, MeOH STYs were found to be 161.2, 83.3, 91.4, and 158.1 g h^{-1} kg^{-1} for CeO_2, $CoCeO_x$, $CuCeO_x$ and CeO_2 (300 mg), respectively. Full GLY conversion was achieved over CeO_2 at 400 °C, which reduced to 95 % over 300 mg of catalyst; this corresponded to MeOH selectivities of 21.3 and 12.9 % respectively. However, despite the significant differences in MeOH selectivity, there was little difference in STY. Since STY is a function of catalyst mass, this was partly expected due to the reduced mass, however, the increased carbon balance was partly responsible for the reasonably high MeOH STY over CeO_2 (300 mg) despite the moderate (12.9 %) selectivity. Once again, this highlights the importance in improving the observed carbon balance in order to maximise MeOH production.

Significantly lower MeOH STYs were obtained over $CuCeO_x$ and $CoCeO_x$ *vs*. undoped ceria, despite slightly higher carbon balances being achieved over the doped materials. Additionally, lower HA and higher ACA selectivities were observed over the doped catalysts compared with CeO_2 (300 mg), suggesting that HA had been further converted. In addition to the reasonably high ACA selectivity (*ca.* 15 %), a moderate CO_x selectivity was observed (also *ca.* 15 %) comprised predominantly of CO. The presence of CO in the gas stream was also accompanied by H_2, with a CO/H_2 ratio of *ca.* 5:1 over $CuCeO_x$. The low MeOH productivity, despite the reasonable HA conversion and ACA selectivity, alongside the relatively high CO and H_2 selectivities, indicate that MeOH itself may be further converted. Reaction performed with undoped CeO_2 showed that no significant MeOH conversion occurred under reaction conditions but due to time constraints, these experiments were not possible with the doped catalysts. Future work in this area should focus on understanding

the stability of MeOH over the doped materials to establish whether this is the reason for the lower MeOH STYs, particularly given the enhanced HA selectivity, the major intermediate for MeOH, at low GLY conversion. *In-situ* MeOH DRIFTS experiments may be beneficial to elucidate any differences in reactivity between CeO_2, $CuCeO_x$ and $CoCeO_x$.

Due to the fact that moderate amounts of H_2 and ACA were produced over $CuCeO_x$ at 400 °C, model reactions were performed with a mix of pure ACA (diluted in He) co-fed with H_2, in order to simply study the feasibility of using H_2 produced *in-situ* to reduced aldehydic species to their corresponding alcohols. The reaction conditions were modelled on those used in the GLY conversion reactions only with a dilute ACA/H_2/He gas mix as the reaction feed, a lower operating temperature (80 – 120 °C) and a hydrogenation catalyst instead of a ceria-based material. The catalysts investigated were commercially available 5 wt.% Pt/Al_2O_3, Pt/C, and Ru/C; all were pre-reduced at 400 °C prior to use.

Whilst EtOH was detected over Pt/Al_2O_3, a maximum yield of 15 % was achieved at a reaction temperature of 100 °C. Whilst ACA conversion increased as the temperature decreased, this was accompanied by a significant decrease in EtOH selectivity (EtOH selectivity is based on theoretical EtOH production at that level of conversion, due to the presence of unidentified by-products). Whilst EtOH was the only liquid phase product detected, two additional gas phase products were observed. These products were confirmed not to be CO, CO_2, CH_4 or MeOH, and were most likely ethylene and ethene, formed through ACA dehydration and subsequent reduction, due to the acidity of the alumina support.[9, 10]

Pt/C and Ru/C were then investigated as catalysts for the conversion of ACA to EtOH. The order of activity for ACA conversion was found to be Pt/Al_2O_3 > Ru/C > Pt/C with ACA steadily increasing with reaction temperature for all catalysts. All three catalysts also showed a volcano-type plot when it came to EtOH selectivity, with maximum EtOH selectivities achieved at a reaction temperature of 100 °C. That said, the maximum EtOH yield of 19.1 % was achieved over Ru/C at 120 ° C. EtOH selectivity followed the trend Ru/C > Pt/C > Pt/Al_2O_3, which could be due to the reduced acidity of the carbon supported catalysts compared with alumina. Whilst the EtOH yields achieved were generally fairly low, these studies were preliminary with no optimisation of the reaction conditions, thus the yields achieved over Ru/C suggest it may warrant further investigation, under optimised conditions.

6.2 Outlook and future work

The gas conversion of aqueous GLY feedstocks to MeOH over magnesium oxide and cerium oxide catalysts is a complex reaction, involving multiple steps and accompanied by a variety of side reactions resulting in numerous by-products. As shown by the blank reactions in

Chapter 3, thermally initiated non-catalysed reactions can take place, particularly at reaction temperatures in excess of 400 °C. As described earlier, the aim of this thesis was to explore the conversion of more concentrated feedstocks, which is particularly important due to the GLY surplus and its associated low value. Whilst the majority of this thesis was performed using CeO_2 catalysts, preliminary studies in Chapter 3 were performed over MgO as a catalyst. These results showed that MeOH productivity could be improved by reducing the concentration of the aqueous GLY feedstock with a respective reduction in catalyst mass. These results, and MgO as a catalyst, were not further explored within this thesis but are being further investigated within the research group. Nevertheless, these results do highlight the challenges of working with more concentrated GLY feedstocks, particularly at elevated temperatures.

Throughout Chapter 3, carbon balances and additional product analysis was thoroughly discussed. Generally, as GLY conversion and MeOH selectivity increased, an associated decrease in carbon balance was observed. CHN analysis of post reaction solutions, obtained over MgO and CeO_2 catalysts, showed that the total overall carbon balance was *ca*. 95 %, with the missing 5 % attributed to reactor fouling and/or uncollected products. Analysis by HPLC showed the presence of high molecular weight products, although it was not possible to identify their identity. Since these products are formed through undesirable side-reactions, an important aspect of future work should be to minimise the formation of these high molecular weight products, whilst maintaining high GLY conversion and MeOH selectivity.

Of all the ceria catalysts tested throughout this thesis, the highest MeOH selectivity was reported for Ce-P, a polyhedral shaped nanostructure prepared *via* hydrothermal techniques, discussed fully in Chapter 4. Whilst it was difficult to fully correlate physicochemical properties with product distribution, the exposure of the CeO_2(111) surface and lower pore volume, along, were shown to be beneficial for MeOH productivity. A low defect density was observed for Ce-P by Raman spectroscopy, although analysis by H_2-TPR showed Ce-P possessed higher reducibility *vs*. Ce-R and Ce-C. An interesting aspect of future work would be to further investigate the role of reducibility in undoped ceria catalysts. In addition to the exposure of the (111) surface, TEM also showed Ce-P to be composed of small particles (*ca*. 11 nm). Numerous reports have detailed the enhanced low temperature reducibility of ceria with decreasing particle size and increasing surface area, thus it may be beneficial to explore the synthesis parameters for Ce-P to see whether MeOH selectivity could further be enhanced.

The highest MeOH STY was obtained over Ce-P and was 201 g h^{-1} kg^{-1}, which was significantly higher than the STYs obtained over other CeO_2 catalysts tested throughout this

thesis and other works[3, 11] Whilst the MeOH STY and selectivity was high, this was accompanied by high levels of CO_x (predominantly CO_2) and a low observed carbon balance of 67 %. A good avenue for future work would be to further optimise reaction conditions (GLY wt.%, GHSV etc.) to assess whether the high STY observed for Ce-P could be further improved.

The use of copper and cobalt as dopants for ceria catalysts did not lead to an increase in GLY conversion or MeOH selectivity, despite resulted in increased catalyst surface areas, with undoped ceria shown to display significantly higher MeOH STYs. The use of $CuCeO_x$ and $CoCeO_x$ resulted in an increased selectivity to CO and H_2, suggesting that MeOH decomposition ($CH_3OH \rightarrow CO + H_2$) may be responsible for the lower MeOH productivity observed. These results highlight the importance of assessing the stability of MeOH over the catalyst, in order to ensure that MeOH produced doesn't undergo further transformations.

The results within this thesis highlight the complexity of the reactions involved in the conversion of GLY to MeOH. It was shown that GLY conversion was determined by predominantly by surface area of undoped ceria catalysts. The exposure of different ceria surfaces resulted in significant differences in product distributions due to divergences in reaction mechanisms. Outside of the conversion of GLY to MeOH, these results may provide wider insights into to the interaction of polyols with different surface terminations and the subsequent effect on product distribution.

6.3 References

1. REN21, *Renewables 2020 Global Status Report*, Report ISBN 978-3-948393-00-7, 2020.
2. M. Bowker, *ChemCatChem*, 2019, **11**, 4238-4246.
3. M. H. Haider, N. F. Dummer, D. W. Knight, R. L. Jenkins, M. Howard, J. Moulijn, S. H. Taylor and G. J. Hutchings, *Nature Chemistry*, 2015, **7**, 1028.
4. H.-X. Mai, L.-D. Sun, Y.-W. Zhang, R. Si, W. Feng, H.-P. Zhang, H.-C. Liu and C.-H. Yan, *The Journal of Physical Chemistry B*, 2005, **109**, 24380-24385.
5. C.-W. Chiu, A. Tekeei, W. R. Sutterlin, J. M. Ronco and G. J. Suppes, *AIChE Journal*, 2008, **54**, 2456-2463.
6. S. Sato, M. Akiyama, R. Takahashi, T. Hara, K. Inui and M. Yokota, *Applied Catalysis A: General*, 2008, **347**, 186-191.
7. M. Velasquez, A. Santamaria and C. Batiot-Dupeyrat, *Applied Catalysis B: Environmental*, 2014, **160**, 606-613.
8. S. Célerier, S. Morisset, I. Batonneau-Gener, T. Belin, K. Younes and C. Batiot-Dupeyrat, *Applied Catalysis A: General*, 2018, **557**, 135-144.
9. J. F. DeWilde, C. J. Czopinski and A. Bhan, *ACS Catalysis*, 2014, **4**, 4425-4433.
10. J. Ob-eye, P. Praserthdam and B. Jongsomjit, *Catalysts*, 2019, **9**, 66.
11. J. Devlia, L. Smith, M. Douthwaite, S. H. Taylor, D. J. Willock, G. J. Hutchings and N. F. Dummer, *Philosophical Transactions of the Royal Society A: Mathematical, Physical and Engineering Sciences*, 2020, **378**, 20200059.

Chapter 7

Appendix

Reaction mechanisms: Norrish type 1 like radical fragmentation

The radical fragmentation of hydroxyacetone has been referred to as a Norrish type 1 like reaction. The Norrish type 1 reaction is a photochemical process whereby C-C bond cleavage occurs between the α carbon and the carbonyl group of aldehydes and ketones.[1, 2]

Hydroxyacetone

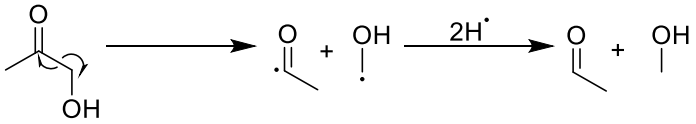

Hydroxyacetaldehyde

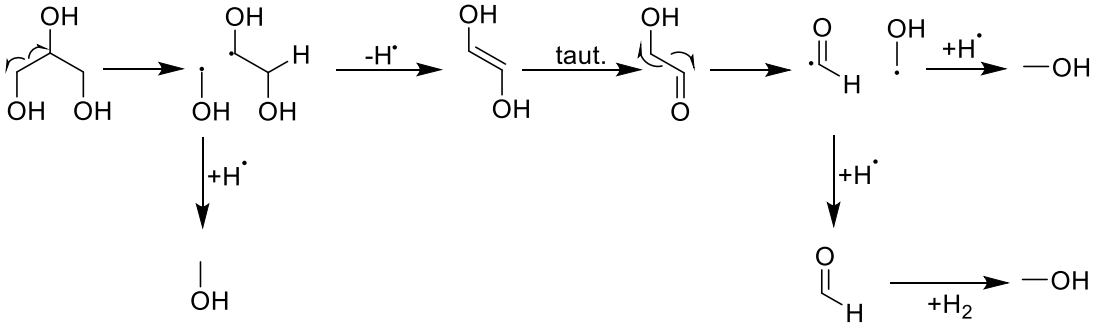

C-C coupling

2,3-butanedione

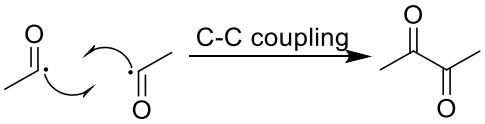

Chapter 3: Glycerol to methanol over metal oxide catalysts

This chapter was partially published in L. R. Smith *et al*., *Catalysis Science & Technology*, 2019, **9**, 1464-1475 and P. J. Smith et al. *Energies*, 2019, **12**, 1359-1372.

Table A3.1a. Catalyst free product list without SiC.			
Temperature (°C)	***320***	***400***	***480***
Product	***Selectivity (%)***		
Acetaldehyde	0.0	3.9	6.4
Propionaldehyde	0.0	0.5	0.7
Acetone	0.0	0.4	0.7
Acrolein	0.0	2.7	2.8
Methanol	0.0	2.5	4.9
Ethanol	0.0	0.0	0.4
2,3-butanedione	0.0	0.0	0.7
1-propanol	0.0	0.0	0.1
3-hexanone	0.0	0.0	0.2
allyl alcohol	0.0	16.2	17.6
Cyclopentanone	0.0	0.0	0.2
Hydroxyacetone	0.0	30.9	26.6
acetic acid	0.0	1.1	1.7
propionic acid	0.0	1.3	2.7
1,2-propanediol	0.0	3.1	3.4
unknown(s)	0.0	22.0	19.4
ethylene glycol	0.0	4.3	8.3
1,3-propanediol	0.0	1.6	0.9
CO	0.0	0.7	0.8
CO_2	0.0	2.3	1.5
CH_4	0.0	0.4	0.1
GLY conversion (%)	0	6	11
Carbon balance (%)	102	95	98

Table A3.1b. Catalyst free product list with SiC.				
Temperature (°C)	***320***	***360***	***400***	***480***
Product	***Selectivity (%)***			
acetaldehyde	0.0	4.0	5.2	12.9
propionaldehyde	0.0	0.0	0.3	0.8
acetone	0.0	0.4	0.4	0.7
acrolein	0.0	1.7	2.3	7.0
butyraldehyde	0.0	0.0	0.0	0.1
methanol	0.0	0.6	1.8	2.1
ethanol	0.0	0.0	0.3	0.5
2,3-butanedione	0.0	0.0	0.5	0.5
1-propanol	0.0	0.0	0.0	0.2
3-hexanone	0.0	0.0	0.1	0.1
2-hexanone	0.0	0.0	0.0	0.3
allyl alcohol	43.1	34.7	30.4	22.3
cyclopentanone	0.0	0.0	0.0	0.1
hydroxyacetone	56.9	37.3	33.5	23.3
3-ethoxy-1-propanol	0.0	0.0	0.3	0.2
acetic acid	0.0	2.5	2.0	1.3
propionic acid	0.0	1.5	1.9	1.1
1,2-propanediol	0.0	1.9	2.0	4.2
unknown(s)	0.0	5.7	9.2	10.3
ethylene glycol	0.0	2.3	3.2	5.9
1,3-propanediol	0.0	1.0	1.0	1.3
phenol	0.0	0.0	0.0	0.3
CO	0.0	0.7	0.7	0.6
CH_4	0.0	0.4	0.1	0.1
CO_2	0.0	3.9	3.3	1.3
GLY conversion (%)	2	4	12	18
Carbon balance (%)	99	97	95	95

Table A3.2 Full product distribution over MgO at a GHSV of 4615 h^{-1}			
Reaction temperature (°C)	***360***	***400***	***440***
Product	***Selectivity (%)***		
Acetaldehyde	9.1	13.3	17.0
Propionaldehyde	0.7	1.6	3.0
Acetone	0.2	0.4	0.6
acrolein	1.3	1.7	3.2
butyraldehyde	0.0	0.1	0.1
methanol	23.4	27.9	25.6
2-propanol	0.1	0.1	0.1
ethanol	1.0	1.5	1.6
2,3-butanedione	1.7	1.9	1.9
2-butanol	0.0	0.1	0.1
1-propanol	0.1	0.3	0.3
3-hexanone	0.2	0.2	0.2
2-hexanone	0.1	0.0	0.0
2-methyl-1-propanol	0.0	0.1	0.0
allyl alcohol	1.0	1.6	2.3
cyclopentanone	0.1	0.4	1.0
hydroxyacetone	25.9	17.9	15.5
3-ethoxy-1-propanol	0.5	0.9	1.3
acetic acid	1.7	2.0	2.0
propionic acid	0.4	0.6	0.7
1,2-propanediol	2.4	1.3	0.9
unknown(s)	10.8	9.5	8.0
ethylene glycol	10.9	5.8	2.5
1,3-propanediol	1.2	0.8	0.5
phenol	0.1	0.2	0.3
CO	3.8	3.9	5.8
CH_4	0.0	2.3	0.4
CO_2	3.3	3.8	5.3
GLY conversion (%)	74	90	100
Carbon balance (%)	74 (77)	73 (77)	68 (73)
Reaction conditions: 50 wt% GLY (0.016 mL min^{-1}), 0.5 g MgO, 50 mL min^{-1} Ar, 3 hours; GHSV = 3615 h^{-1}			

Table A3.3 Full product distribution over MgO with differing feedstock concentrations at 400 °C					
Glycerol concentration	***10 wt. %***	***10 wt. %[b]***	***20 wt. %***	***40 wt. %***	***50 wt. %***
Product	***Selectivity (%)***				
acetaldehyde	18.0	14.6	18.0	17.2	13.3
propionaldehyde	3.8	0.5	3.5	2.1	1.6
acetone	1.0	0.6	0.9	0.4	0.4
acrolein	2.2	2.3	2.5	2.9	1.7
butyraldehyde	0.2	0.0	0.2	0.1	0.1
methanol	34.9	31.6	32.0	29.5	27.9
2-propanol	0.0	0.0	0.1	0.1	0.1
ethanol	3.2	1.2	2.6	1.9	1.5
2,3-butanedione	2.6	0.7	2.3	1.9	1.9
2-butanol	0.1	0.0	0.1	0.1	0.1
1-propanol	0.7	0.0	0.6	0.3	0.3
3-hexanone	0.4	0.1	0.3	0.2	0.2
2-hexanone	0.0	0.0	0.0	0.0	0.0
2-methyl-1-propanol	0.0	0.0	0.0	0.0	0.1
allyl alcohol	2.2	6.2	2.1	2.0	1.6
cyclopentanone	2.2	0.3	1.6	1.0	0.4
hydroxyacetone	3.6	18.7	6.4	14.8	17.9
3-ethoxy-1-propanol	1.7	0.9	1.5	1.1	0.9
acetic acid	0.7	0.8	1.4	1.5	2.0
propionic acid	0.5	0.4	0.8	0.6	0.6
1,2-propanediol	0.2	1.5	0.3	0.8	1.3
unknown(s)	10.1	8.8	10.6	9.6	9.5
ethylene glycol	0.2	7.0	1.0	2.5	5.8
1,3-propanediol	0.3	0.1	0.2	0.5	0.8
phenol	1.3	0.3	0.1	0.3	0.2
CO	3.5	1.5	3.9	4.2	3.9
CH_4	0.2	0.0	0.4	0.9	2.3
CO_2	6.6	1.9	6.8	3.7	3.8
GLY conversion (%)	100	96	100	99	90
Carbon balance (%)	83 (84)	83 (98)	80 (88)	78 (81)	73 (77)
Reaction conditions: 50 wt% GLY (0.016 mL min^{-1}), 0.5 g MgO, 50 mL min^{-1} Ar, 3 hours; GHSV = 3615 h^{-1}					

Table A3.4 Full product distribution over MgO with 50 wt.% glycerol at 400 °C as a function of reaction time					
Time	***2h***	***4h***	***6h***	***24h***	***48h***
Product	***Selectivity (%)***				
acetaldehyde	18.2	14.7	14.8	12.8	14.6
propionaldehyde	2.9	2.1	2.0	1.8	2.1
acetone	0.7	0.5	0.7	0.6	0.5
acrolein	2.4	2.3	2.3	2.0	2.4
butyraldehyde	0.1	0.1	0.1	0.1	0.1
methanol	32.2	27.8	26.9	29.7	26.9
2-propanol	0.0	0.0	0.0	0.0	0.1
ethanol	2.1	1.5	1.5	1.2	1.2
2,3-butanedione	2.7	2.6	2.6	2.3	2.5
2-butanol	0.1	0.1	0.1	0.1	0.1
1-propanol	0.4	0.3	0.3	0.2	0.2
3-hexanone	0.4	0.3	0.3	0.3	0.3
2-hexanone	0.0	0.0	0.0	0.0	0.0
2-methyl-1-propanol	0.0	0.0	0.0	0.0	0.0
allyl alcohol	1.7	1.4	1.4	1.2	1.3
cyclopentanone	0.8	0.6	0.5	0.4	0.4
hydroxyacetone	10.6	17.6	17.3	18.1	19.7
3-ethoxy-1-propanol	1.6	1.4	1.4	1.3	1.3
acetic acid	1.4	2.1	1.8	1.7	1.7
propionic acid	0.6	0.7	0.6	0.6	0.6
1,2-propanediol	0.7	1.4	1.6	1.5	1.5
unknown(s)	7.7	10.5	10.0	10.3	10.1
ethylene glycol	1.4	3.7	4.6	4.5	4.3
1,3-propanediol	0.3	0.3	0.3	0.3	0.3
phenol	0.5	0.0	0.4	0.4	0.4
CO	4.4	3.7	3.9	4.0	3.5
CH_4	0.3	0.2	0.2	0.2	0.2
CO_2	5.8	4.3	4.5	4.3	3.9
GLY conversion (%)	97	87	87	84	85
Carbon balance (%)	62	70	68	65	65
Reaction conditions: 50 wt% GLY (0.016 mL min^{-1}), 0.5 g MgO, 50 mL min^{-1} Ar, 3 hours; GHSV = 3615 h^{-1}					

Table A3.5 Full product distribution over MgO with 50 wt.% glycerol at 400 °C as a function of reaction time		
	Pure glycerol	***Crude glycerol***
Product	***Selectivity (%)***	
acetaldehyde	**17.2**	**14.1**
propionaldehyde	2.1	2.2
acetone	0.4	0.1
acrolein	2.9	3.0
butyraldehyde	0.1	0.1
methanol	**29.5**	**30.1**
2-propanol	0.1	0.0
ethanol	1.9	1.8
2,3-butanedione	1.9	1.1
2-butanol	0.1	0.0
1-propanol	0.3	0.1
3-hexanone	0.2	0.2
2-hexanone	0.0	0.0
2-methyl-1-propanol	0.0	0.0
allyl alcohol	2.0	4.3
cyclopentanone	1.0	0.8
hydroxyacetone	**14.8**	**16.9**
3-ethoxy-1-propanol	1.1	0.9
acetic acid	1.5	1.4
propionic acid	0.6	0.7
1,2-propanediol	0.8	1.1
unknown(s)	**9.6**	**10.4**
ethylene glycol	**2.5**	**1.2**
1,3-propanediol	0.5	0.1
phenol	0.3	0.2
CO	4.2	4.5
CH_4	0.9	0.1
CO_2	3.7	4.4
GLY conversion (%)	99	98
Carbon balance (%)	78	70
Reaction conditions: 40 wt% GLY (0.016 mL min^{-1}), 0.5 g MgO, 50 mL min^{-1} Ar, 3 hours; GHSV = 3615 h^{-1}		

Table A3.6 Full product distribution over CeO_2 calcined at different temperatures with 50 wt.% glycerol at 340 °C				
C. T. (°C)	***400***	***500***	***600***	***700***
Product	***Selectivity (%)***			
acetaldehyde	9.4	8.7	9.4	7.6
propionaldehyde	1.1	1.2	1.4	1.2
acetone	1.0	1.1	1.3	1.1
acrolein	1.9	2.0	1.7	1.2
butyraldehyde	0.1	0.1	0.1	0.1
methanol	8.9	8.6	8.6	7.7
2-propanol	0.1	0.1	0.1	0.1
ethanol	0.6	0.6	0.8	0.6
2,3-butanedione	2.6	2.8	2.1	2.1
2-butanol	0.0	0.0	0.0	0.0
1-propanol	0.0	0.0	0.0	0.0
3-hexanone	0.1	0.1	0.2	0.1
2-hexanone	0.0	0.0	0.0	0.0
2-methyl-1-propanol	0.0	0.0	0.0	0.0
allyl alcohol	1.7	1.6	2.2	2.7
cyclopentanone	0.1	0.1	0.2	0.2
hydroxyacetone	32.5	33.4	29.1	29.4
3-ethoxy-1-propanol	0.3	0.3	0.3	0.3
acetic acid	3.4	3.5	4.0	4.0
propionic acid	4.2	4.3	5.5	5.3
1,2-propanediol	4.1	4.1	4.2	4.9
unknown(s)	16.6	16.1	17.4	16.9
ethylene glycol	4.6	4.6	3.7	5.2
1,3-propanediol	0.1	0.1	0.1	0.1
phenol	0.0	0.0	0.0	0.1
CO	2.7	2.7	3.2	3.6
CH_4	0.0	0.0	0.0	0.0
CO_2	1.6	1.6	1.9	1.9
GLY conversion (%)	83	83	80	84
Carbon balance (%)	82	80	84	81
Reaction conditions; 340 °C, 50 wt.% GLY (0.016 mL min^{-1}), 15 mL min^{-1} Ar, 3 hours, GHSV = 3450 h^{-1}.				

Chapter 4: The effect of ceria morphology on gas phase glycerol valorisations

Catalyst characterisation

Table A4.1 Intensities of observed reflections by PXRD with reference to a database sample

		Ce-C		***Ce-R***		***Ce-P***	
Reflection	***Ref[a] (%)***	***Absolute Intensity***	***Relative Intensity (%)***	***Absolute Intensity***	***Relative Intensity (%)***	***Absolute Intensity***	***Relative Intensity (%)***
111	100	706	100	849	100	947	100
200	27	225	32	216	25	255	27
220	45	470	67	451	53	477	50
311	33	378	54	287	34	414	44
222	6	66	9	51	6	64	7
400	5	75	11	58	7	81	9
311	10	165	23	86	10	138	15
420	6	94	13	30	4	102	11
(200) / (220) ratio	0.60		0.48		0.48		0.53
(111) / (111), (200), (220) ratio	0.58		0.50		0.56		0.56
(200)/(111) ratio	0.27		0.32		0.25		0.27

a) Relative intensities from reference file (JCPDS 01-089-8436)

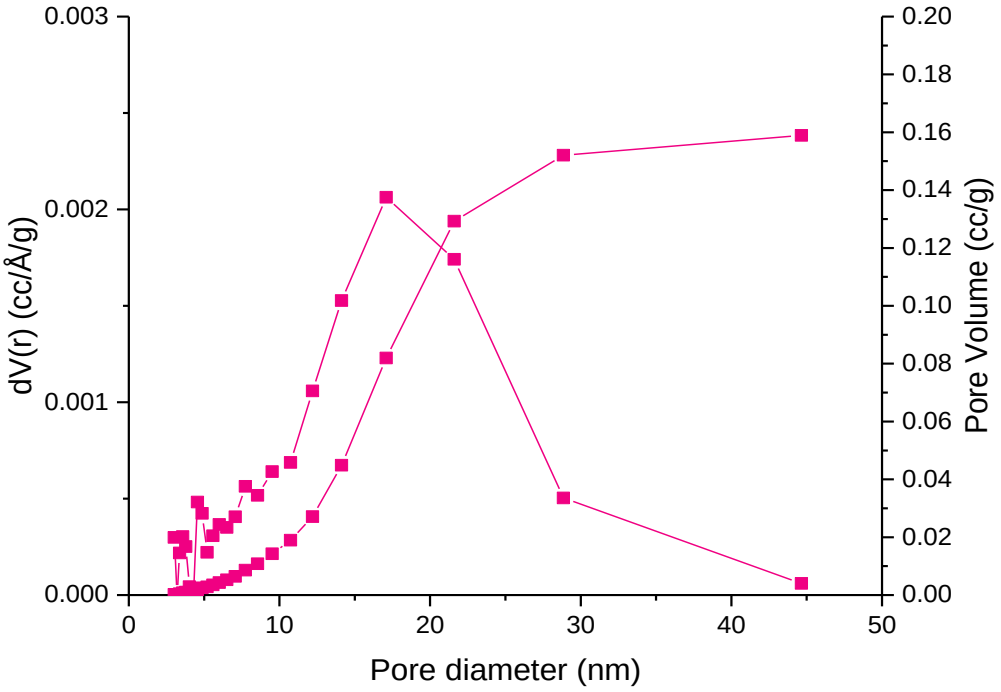

Figure A4.15a. Pore size distribution and pore volume for Ce-C

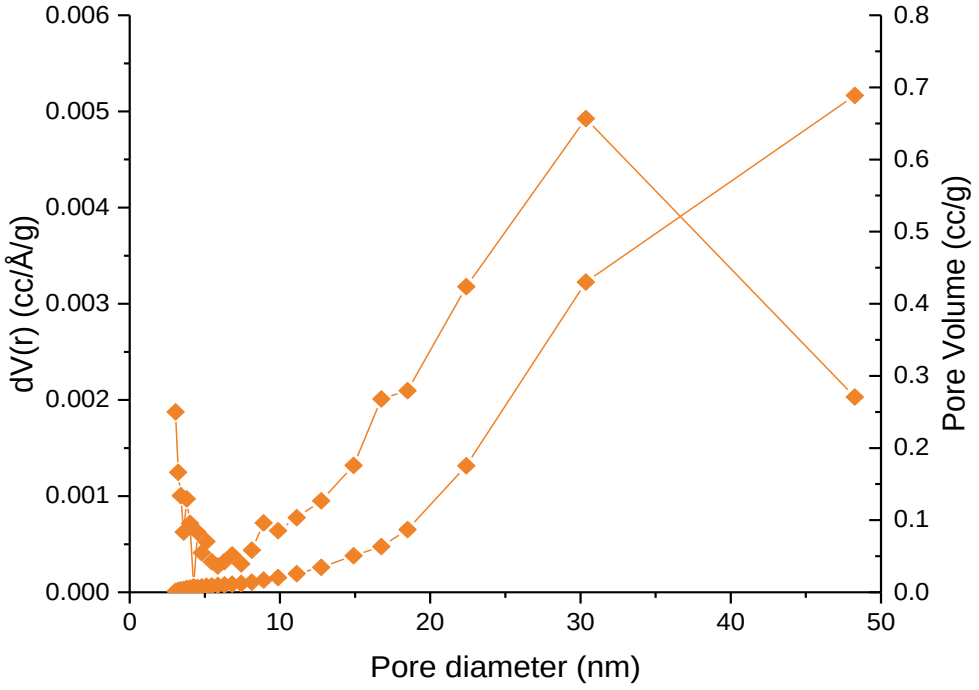

Figure A4.1b. Pore size distribution and pore volume for Ce-R

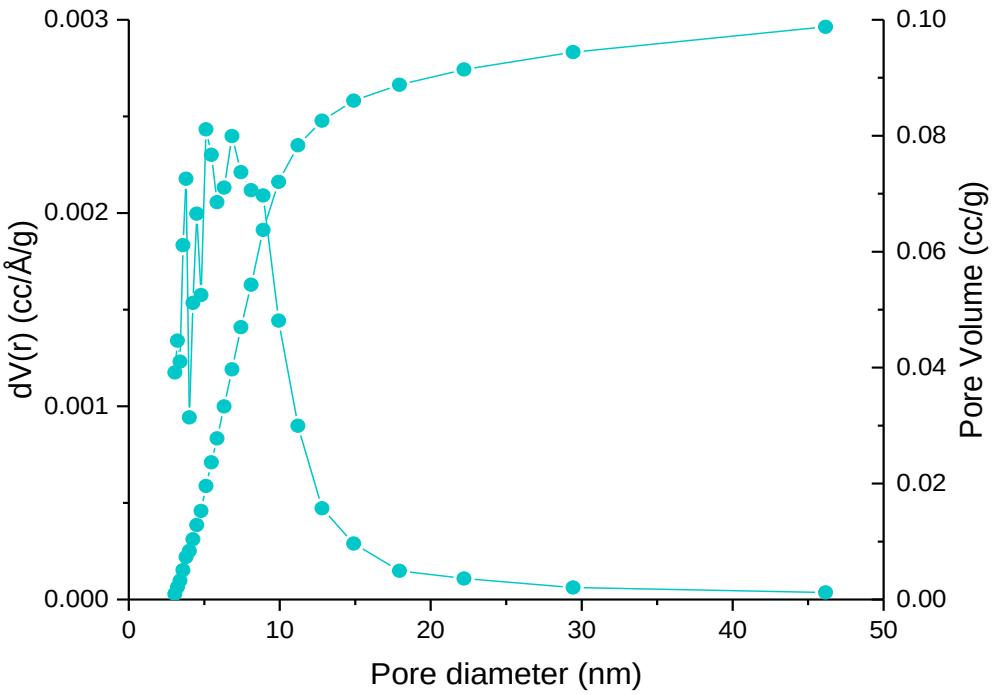

Figure A4.1c. Pore size distribution and pore volume for Ce-P

Glycerol testing

Table A4.2 Full product distribution over Ce-C, Ce-R and Ce-P at a space velocity of 3600h^{-1}

	Ce-C			***Ce-R***			***Ce-P***		
Temperature (°C)	***320***	***360***	***400***	***320***	***360***	***400***	***320***	***360***	***400***
Product	***Selectivity (%)***								
acetaldehyde	4.2	6.9	8.2	4.5	6.9	5.8	5.4	9.9	1.6
propionaldehyde	0.4	1.6	1.3	0.9	1.6	5.6	0.9	2.7	2.6
acetone	0.4	0.7	1.2	0.7	2.2	11.1	0.8	3.8	13.9
acrolein	14.5	12.7	1.1	2.4	1.9	0.8	1.8	1.5	0.3
butyraldehyde	0.0	0.0	0.1	0.1	0.1	0.4	0.1	0.2	0.2
methanol	3.5	6.0	10.0	7.2	10.5	22.6	7.0	12.0	25.5
2-propanol	0.1	0.1	0.1	0.1	0.2	1.6	0.0	0.2	1.7
ethanol	0.9	0.8	1.6	0.6	0.9	2.3	0.6	1.5	3.1
2,3-butanedione	0.5	1.1	1.0	2.2	2.4	3.7	2.0	1.1	5.5
2-butanol	0.0	0.1	0.0	0.0	0.0	0.0	0.1	0.2	0.2
1-propanol	0.3	0.3	0.4	0.2	0.3	1.0	0.1	0.4	1.6
3-hexanone	0.1	0.2	0.2	0.5	0.5	0.3	0.4	0.1	0.4
2-hexanone	0.0	0.0	0.1	0.0	0.0	0.4	0.0	0.0	0.7
2-methyl-1-propanol	0.1	0.1	0.0	0.0	0.0	0.1	0.0	0.0	0.2

allyl alcohol	1.2	2.4	1.7	1.0	1.4	2.7	1.3	2.2	1.4
cyclopentanone	0.2	0.3	1.0	0.2	0.5	1.6	0.2	0.7	1.6
hydroxyacetone	14.1	21.8	8.0	29.8	21.1	0.4	30.2	7.3	0.3
3-ethoxy-1-propanol	0.7	1.3	2.1	1.9	0.4	1.0	0.2	0.3	0.8
acetic acid	1.0	1.4	1.9	3.2	3.7	0.3	3.1	4.2	0.2
propionic acid	3.2	3.2	6.0	7.5	8.3	1.9	4.7	9.5	2.9
1,2-propanediol	2.4	2.7	5.5	7.1	6.0	0.3	6.0	7.9	0.1
unknown(s)	36.5	18.0	27.9	15.4	15.8	10.5	21.6	17.7	6.5
ethylene glycol	6.8	10.2	4.6	8.0	6.4	0.6	7.6	6.5	0.2
1,3-propanediol	2.6	1.4	1.6	0.5	0.2	0.1	0.3	0.0	0.1
phenol	0.0	0.0	0.5	0.0	0.2	0.3	0.0	0.0	0.2
CO	1.2	1.6	7.3	2.0	3.3	8.3	2.6	4.7	10.2
CO_2	5.0	5.0	6.5	4.3	5.1	16.1	3.0	5.5	17.9
CH_4	0.1	0.1	0.1	0.0	0.0	0.2	0.0	0.0	1.6
GLY conversion (%)	17	29	91	65	98	>99	58	96	>99
Carbon balance (%)	93	83	61 (62)	82	76	62 (64)	91	91	67 (67)

Table A4.3a Full product distribution over Ce-C, Ce-R and Ce-P at an iso-conversion of ca. 15% and a reaction temperature of 320 °C			
	Ce-C	***Ce-R***	***Ce-P***
Space velocity (h^{-1})	**3600**	**11250**	**9000**
Product	***Selectivity (%)***		
Acetaldehyde	4.2	4.8	5.2
Propionaldehyde	0.4	1.0	0.6
Acetone	0.4	0.6	0.5
Acrolein	14.5	3.2	1.5
Butyraldehyde	0.0	0.0	0.0
Methanol	3.5	7.7	8.4
2-propanol	0.1	0.1	0.0
Ethanol	0.9	1.1	0.3
2,3-butanedione	0.5	1.4	1.3
2-butanol	0.0	0.0	0.0
1-propanol	0.3	0.5	0.1
3-hexanone	0.1	0.3	0.2
2-hexanone	0.0	0.0	0.0
2-methyl-1-propanol	0.1	0.1	0.0
allyl alcohol	1.2	1.4	0.7
Cyclopentanone	0.2	0.3	0.1
hydroxyacetone	14.1	37.4	43.3
3-ethoxy-1-propanol	0.7	0.9	0.1
acetic acid	1.0	1.3	2.1
propionic acid	3.2	2.3	3.1
1,2-propanediol	2.4	7.5	5.3
unknown(s)	36.5	16.1	16.4
ethylene glycol	6.8	7.0	7.3
1,3-propanediol	2.6	0.6	0.3
phenol	0.0	0.0	0.0
CO	1.2	0.8	1.5
CO_2	5.0	3.5	1.6
CH_4	0.1	0.0	0.0
GLY conversion (%)	17	14	16
Carbon balance (%)	93	96	96

Table A4.3b Full product distribution over Ce-C, Ce-R and Ce-P at an iso-conversion of > 99 % and a reaction temperature of 400 °C			
	Ce-C	***Ce-R***	***Ce-P***
Space velocity (h^{-1})	***1800***	***3600***	***3600***
Product	***Selectivity (%)***		
acetaldehyde	16.5	5.8	1.6
propionaldehyde	4.1	5.6	2.6
acetone	4.1	11.1	13.9
acrolein	2.7	0.8	0.3
butyraldehyde	0.2	0.4	0.2
methanol	13.1	22.6	24.5
2-propanol	0.4	1.6	1.7
ethanol	1.3	2.3	3.1
2,3-butanedione	1.8	3.7	5.5
2-butanol	0.2	0.0	0.2
1-propanol	0.0	1.0	1.6
3-hexanone	0.4	0.3	0.4
2-hexanone	0.1	0.4	0.7
2-methyl-1-propanol	0.0	0.1	0.2
allyl alcohol	4.1	2.7	1.4
cyclopentanone	0.5	1.6	1.6
hydroxyacetone	2.8	0.4	0.3
3-ethoxy-1-propanol	1.4	1.0	0.8
acetic acid	2.1	0.3	0.2
propionic acid	4.2	1.9	2.9
1,2-propanediol	1.4	0.3	0.1
unknown(s)	27.3	10.5	6.5
ethylene glycol	0.8	0.6	0.2
1,3-propanediol	1.0	0.1	0.1
phenol	0.8	0.3	0.2
CO	3.5	8.3	10.2
CO_2	5.1	16.0	17.9
CH_4	0.1	0.2	0.1
GLY conversion (%)	99	100	100
Carbon balance (%)	69	62	67

Table A4.5 Full product distribution of a hydroxyacetone/water feedstock at a reaction temperature of 320 °C and a GHSV of 3600 h^{-1}			
	Ce-C	***Ce-R***	***Ce-P***
Space velocity (h^{-1})	***1800***	***3600***	***3600***
Product	***Selectivity (%)***		
acetaldehyde	5.4	3.7	3.8
propionaldehyde	0.8	0.4	0.5
acetone	4.1	2.7	3.5
acrolein	0.0	0.0	0.0
butyraldehyde	0.0	0.0	0.0
methanol	**9.0**	**6.9**	**7.9**
2-propanol	0.0	0.0	0.0
ethanol	0.7	0.5	0.5
2,3-butanedione	4.6	1.4	4.0
2-butanol	0.0	0.0	0.0
1-propanol	0.0	0.2	0.0
3-hexanone	0.4	1.6	0.2
2-hexanone	0.1	0.0	0.1
2-methyl-1-propanol	0.0	0.0	0.0
allyl alcohol	0.6	1.0	0.5
cyclopentanone	0.1	0.1	0.1
hydroxyacetone	0.0	0.0	0.0
3-ethoxy-1-propanol	3.6	1.6	3.1
acetic acid	13.5	12.9	10.9
propionic acid	8.0	10.9	5.4
1,2-propanediol	2.1	14.1	17.5
unknown(s)	30.8	34.3	30.5
ethylene glycol	0.5	0.0	0.4
1,3-propanediol	3.7	0.3	0.4
phenol	0.1	0.2	0.1
CO	4.2	2.1	3.7
CO_2	0.0	0.0	0.0
CH_4	7.8	5.1	6.8
GLY conversion (%)	18	16	16
Carbon balance (%)	86	92	89

Chapter 5: Transition metal doped ceria catalysts for glycerol conversions

Table A5.1 Full product distribution over CeO_2, $CuCeO_x$, $CoCeO_x$, CeO_2 (reduced mass) at a reaction temperature of 320 °C

	CeO_2	$CuCeO_x$	$CoCeO_x$	CeO_2 (300 mg)
acetaldehyde	5.4	4.6	5.1	6.6
propionaldehyde	0.9	0.5	0.6	1.2
acetone	0.8	0.5	0.4	0.8
acrolein	1.8	1.1	1.2	3.7
butyraldehyde	0.1	0.0	0.0	0.0
methanol	5.7	7.2	8.1	6.1
2-propanol	0.0	0.2	0.1	0.0
ethanol	0.6	0.2	0.2	1.1
2,3-butanedione	2.0	3.5	3.5	2.0
2-butanol	0.1	0.0	0.0	0.0
1-propanol	0.1	0.0	0.0	0.4
3-hexanone	0.4	0.5	0.5	0.5
2-hexanone	0.0	0.0	0.0	0.0
2-methyl-1-propanol	0.0	0.0	0.0	0.1
allyl alcohol	1.3	0.6	0.9	1.2
cyclopentanone	0.2	0.0	0.0	0.4
hydroxyacetone	31.5	42.4	39.6	35.8
3-ethoxy-1-propanol	0.2	1.5	0.9	0.9
acetic acid	3.1	1.8	2.4	1.3
propionic acid	4.7	2.5	2.8	3.5
1,2-propanediol	6.0	1.0	2.1	7.2
unknown(s)	21.6	18.6	18.9	16.2
ethylene glycol	7.6	4.8	4.9	6.1
1,3-propanediol	0.3	0.8	0.2	0.8
phenol	0.0	0.1	0.0	0.0
CO	2.6	3.1	3.1	0.7
CH4	0.0	0.0	0.0	0.0
CO2	3.0	4.4	4.4	3.3
Conversion (%)	58	44	48	45
Carbon balance (%)	91	90	89	87
MeOH STY ($g\ h^{-1}\ kg^{-1}$)	31.3	16.7	21.2	52.7

Table A5.2 Full product distribution over CeO_2, $CuCeO_x$, $CoCeO_x$, CeO_2 (reduced mass) at a reaction temperature of 360 °C				
	CeO_2	$CuCeO_x$	$CoCeO_x$	CeO_2 (300 mg)
acetaldehyde	9.4	8.9	9.8	9.6
propionaldehyde	1.6	1.7	1.6	1.4
acetone	1.3	0.8	0.7	1.3
acrolein	1.7	3.8	4.1	1.7
butyraldehyde	0.1	0.0	0.0	0.1
methanol	10.6	8.9	9.4	10.7
2-propanol	0.1	0.1	0.1	0.1
ethanol	0.8	0.4	0.5	0.8
2,3-butanedione	3.1	2.9	2.8	2.1
2-butanol	0.0	0.0	0.0	0.0
1-propanol	0.0	0.0	0.0	0.0
3-hexanone	0.2	0.2	0.2	0.2
2-hexanone	0.0	0.0	0.0	0.0
2-methyl-1-propanol	0.0	0.0	0.0	0.0
allyl alcohol	2.2	1.9	2.0	2.2
cyclopentanone	0.2	0.0	0.0	0.2
hydroxyacetone	22.8	29.8	27.8	31.1
3-ethoxy-1-propanol	0.3	1.2	0.7	0.3
acetic acid	4.0	1.1	1.0	2.0
propionic acid	5.5	1.2	1.8	2.5
1,2-propanediol	5.1	2.2	3.6	6.7
unknown(s)	16.9	17.1	16.9	15.8
ethylene glycol	4.7	4.2	3.1	5.4
1,3-propanediol	0.1	0.8	0.7	0.1
phenol	0.0	0.0	0.1	0.0
CO	3.5	7.9	7.6	2.2
CH4	0.0	0.0	0.0	0.0
CO2	5.8	4.8	4.8	3.4
Conversion (%)	98	78	81	79
Carbon balance (%)	79	87	88	86
MeOH STY ($g\ h^{-1}\ kg^{-1}$)	84.5	70.4	86.9	82.9

Table A5.3 Full product distribution over CeO_2, $CuCeO_x$, $CoCeO_x$, CeO_2 (reduced mass) at a reaction temperature of 400 °C				
	CeO_2	$CuCeO_x$	$CoCeO_x$	CeO_2 (300 mg)
acetaldehyde	11.7	15.5	14.9	10.6
propionaldehyde	2.6	1.9	2.1	1.7
acetone	8.8	1.9	2.0	2.1
acrolein	0.3	5.2	6.3	3.1
butyraldehyde	0.2	0.0	0.0	0.1
methanol	21.3	10.2	11.0	12.9
2-propanol	1.7	0.0	0.0	0.2
ethanol	3.1	0.6	1.1	1.2
2,3-butanedione	5.5	2.8	3.0	3.7
2-butanol	0.2	0.1	0.0	0.1
1-propanol	1.6	0.2	0.1	0.3
3-hexanone	0.4	0.0	0.0	0.6
2-hexanone	0.7	0.0	0.0	0.0
2-methyl-1-propanol	0.2	0.0	0.0	0.0
allyl alcohol	1.4	2.6	3.3	1.9
cyclopentanone	1.6	0.2	0.3	0.7
hydroxyacetone	0.3	16.7	15.7	21.9
3-ethoxy-1-propanol	0.8	1.0	0.7	1.4
acetic acid	0.2	0.1	0.2	2.1
propionic acid	2.9	0.3	0.3	2.8
1,2-propanediol	0.1	2.5	1.9	5.2
unknown(s)	8.6	19.8	19.8	15.4
ethylene glycol	0.2	3.1	2.4	4.1
1,3-propanediol	0.1	0.4	0.5	0.6
phenol	0.2	0.0	0.0	0.2
CO	7.2	10.1	9.8	3.2
CH4	0.1	0.1	0.1	0.1
CO2	17.9	4.9	4.3	3.7
Conversion (%)	100	94	95	95
Carbon balance (%)	67	76	78	73
MeOH STY (g h^{-1} kg^{-1})	161.2	83.3	91.4	158.1

References

1. *Comprehensive Organic Name Reactions and Reagents*, DOI: https://doi.org/10.1002/9780470638859.conrr464, pp. 2062-2066.
2. R. G. W. Norrish and C. H. Bamford, *Nature*, 1936, **138**, 1016-1016.